Precious metal-free bifunctional catalysts for reversible seawater electrolyzers

vorgelegt von:

Diplom-Chemiker
Sören Lennart Dresp
ORCID: 0000-0001-9575-2173

Von der Fakultät II – Mathematik und Naturwissenschaften
der Technischen Universität Berlin
zur Erlangung des akademischen Grades

Doktor der Naturwissenschaften
- Dr. rer. nat. –

genehmigte Dissertation

Promotionsausschuss:

Vorsitzende:	Prof. Dr. Maria Andrea Mroginski
Berichter:	Prof. Dr. Peter Strasser
Berichter:	Prof. Dr. Aliaksandr S. Bandarenka

Tag der wissenschaftlichen Aussprache: 21.12.2018

Berlin 2019

DANKSAGUNG

Ich möchte mich bei allen bedanken, die es mir ermöglicht haben diese Dissertation anzufertigen. Ich möchte mich vor allem bedanken für die vielen wissenschaftlichen Diskussionen, die Unterstützung bei Laboraufbauten, die Einweisung in neue Techniken als auch die Hilfe bei bürokratischen Fragen und bei allen Korrekturlesern und –leserinnen:

Mein ganz besonderer Dank gilt allerdings Herrn Prof. Peter Strasser, der mir die Chance gab diese Dissertation in seinem Arbeitskreis anzufertigen. Mit Freude nutzte ich die vielen Techniken und Möglichkeiten, welche sein Arbeitskreis zu bieten hat. Ebenso möchte ich mich für sein Vertrauen mit der verbundenen großen wissenschaftlichen Freiheit und für die Ermöglichung der vielen inspirierenden internationalen und nationalen Konferenzen, sowie die großartige Unterstützung bei der Einwerbung von Drittmitteln bedanken, ohne die das Anfertigen dieser Arbeit nicht möglich gewesen wäre.

Des Weiteren danke ich Herrn Prof. Aliaksandr S. Bandarenka für die Bereitschaft als zweiter Gutachter diese Arbeit zu lesen und zu bewerten. Ich bedanke mich ebenso bei Frau Prof. Maria Andrea Mroginski den Prüfungsvorsitz zu übernehmen.

Ferner möchte ich Herrn Prof. Holger Dau und seinem ehemaligen Mitarbeiter Stefan Loos für die Kooperation auf dem Gebiet der Röntgenabsorptionsspektroskpie (XAS) danken.

Ein ganz besonderer Dank gilt außerdem Dr. Fabio Dionigi für die einzigartige Unterstützung während der gesamten Zeit im Arbeitskreis, der immer ein offenes Ohr für mich hatte und mit dem ich inspirierende und aufklärende wissenschaftliche Gespräche führen konnte.

Ich bedanke mich außerdem bei Fang Luo für die Bereitstellung ihres Katalysators. Für die Durchführung der Rasterelektronen Mikroskopie möchte ich mich insbesondere bei Camillo Spöri bedanken. Für die TEM Aufnahmen bedanke ich mich bei Manuel Gliech und Roman Schmack. Für die tatkräftige Unterstützung beim Aufbau des Meerwasserelektrolyse Teststands möchte ich mich bei Benjamin Paul bedanken. Für die Hilfe beim Einrichten des Massenspektrometers bedanke ich mich bei Jorge Ferreira de Araujo. Außerdem bedanke ich mich ganz herzlich bei Carsten Hirschfeld für seine unvergleichlichen Glasbläser Fertigkeiten, Astrid Müller-Klauke für die ICP-OES Messungen, der gesamten Belegschaft der Werkstatt für ihre fantastischen Fähigkeiten Dinge zu reparieren und zu bauen und allen Kollegen und Mitarbeitern der Arbeitsgruppe von Prof. Peter Strasser, die den Arbeitsplatz erst zudem gemacht haben, zu dem man gerne hingegangen ist.

Zu guter Letzt möchte ich noch Elisa Rath danken, welche mir bei der Finalisierung dieser Dissertation geholfen hat und ein ganz besonderer Dank gilt auch meinem Vater, der mich während des gesamten Studiums immer unterstützt hat.

ZUSAMMENFASSUNG

Regenerativer Wasserstoff, welcher mit erneuerbarem Strom über Wasserelektrolyseure hergestellt wird, gilt als ein idealer, da umweltfreundlicher, Energieträger der Zukunft. Während übliche Elektrolyseure nur hochreines Wasser oder Elektrolyte nutzen können, stellt die selektive Spaltung von Meerwasser in Sauerstoff und Wasserstoff eine vielversprechende Alternative dar. Reversibel eingesetzt könnte ein Meerwasserelektrolyseur bei der Rückverstromung des hergestellten Wasserstoffs neben erneuerbarer Elektrizität auch Trinkwasser gewinnen. Thermodynamisch betrachtet stehen in der Meerwasserelektrolyse lediglich die anodische Chlorevolutionsreaktion (CER) und die gewünschte Sauerstoffevolutionsreaktion (OER) in direkter Konkurrenz zueinander.

Ziel dieser Arbeit war die Identifikation und Analyse eines Katalysatorsystems, welches nicht nur selektiv Meerwasser in Sauerstoff oxidieren, sondern ebenfalls reversibel in einer Brennstoffzelle für die Sauerstoffreduktionsreaktion (ORR) genutzt werden kann. Der Fokus lag dabei auf edelmetallfreien Materialien, welches durch die Tatsache der begünstigten Meerwasserspaltung bei hohem pH-Wert ermöglicht wird. Dazu wurden verschiedene Oxide basierend auf Co, Mn, Fe und Ni hergestellt und in Hinsicht auf ihre elektrochemischen OER und ORR Aktivität in Verbindung mit dessen Kristallstruktur und Komposition getestet und kategorisiert. Im Vergleich zeigten jedoch alle hergestellten Materialien keine hinreichenden ORR Aktivitäten, was auf eine favorisierte OER Aktivität von Oxiden schließen lässt. So wurde bei der Entwicklung eines bifunktionalen Katalysatorsystem das Konzept eines Zweikomponenten Systems angewendet und der beste OER Katalysator (NiFe-LDH) mit einem bekannten ORR Katalysator (Fe-N-C) kombiniert. So zeigte die Mischung von (1:3) in 0.1 M KOH bis zu diesem Zeitpunkt unerreicht hohe bifunktionelle OER/ORR Aktivitäten. Auch in reversiblen Elektrolysezelltests konnte unter der Verwendung einer Anionen Austauschmembran (AEM, Tokuyama A201) diese Aktivität bestätigt werden und eröffnete dadurch ein Designkonzept für spätere bifunktionelle Katalysatorsysteme. Lediglich das Fe-N-C zeigte Einschränkungen bei hohen Elektrolysezellpotentialen und die AEM deutete darauf hin nicht stabil gegenüber einer reversiblen Fahrweise zu sein. NiFe-LDH als anodisches Katalysatormaterial in einem Meerwasserelektrolyseur bestätigte aber dessen Eignung und zeigte hohe Selektivitäten wie auch Aktivitäten in einem Meerwasserelektrolyseur. Bei weiteren Untersuchungen wurde ein starker Einfluss des NaCl auf die Membran konstatiert. Auch stetig sinkende Elektrolyseurleistung deuteten eher auf einen Membraneffekt hin, da katalytische Tests und quasi in-situ Röntgenabsorptionsspektroskopie (XAS) NiFe-LDH als geeignetes Material für zukünftige Meerwasserelektrolyseures bestätigten.

ABSTRACT

Regenerative hydrogen, which is produced by renewable electricity used in water electrolyzers, is considered as ideal energy carrier of the future. The selective splitting of seawater into oxygen and hydrogen seem to be a promising alternative compared to established water electrolysis technologies, which typically use highly purified water and electrolytes only. In addition, the back transformation of the produced hydrogen from seawater could generate in fuel cells not only electricity but also fresh water. From a thermodynamic perspective and using a seawater electrolyzer, just the anodic chlorine evolution (CER) competes with the desired oxygen evolution reaction (OER).

The overall goal of this work was the identification and analysis of a catalyst system suitable not only for the selectively oxidation of seawater into oxygen, but also suitable for the oxygen reduction reaction (ORR) in fuel cells. The main focus was set to precious metal free materials, which enables the fact that selective seawater splitting is favored in alkaline media. To reaching the goal various metal oxides based on Co, Mn, Fe and Ni were synthesized, tested in 0.1 M KOH and categorized with regard to their OER and ORR activity associated with their crystal structure. In comparison, every synthesized oxide showed no sufficient ORR activity, which indicates a favored OER activity of oxides. Consequently, a two-component catalyst system was designed to fulfill the requirement of a bifunctional catalyst. While one component consists of the most active OER catalyst (NiFe-LDH), the other component consists of a known precious metal-free ORR catalyst (Fe-N-C). This physical catalyst mixture in a ratio of 1:3 showed to this date unachieved bifunctional activity in 0.1 M KOH. Additional reversible electrolyzer tests using an anion exchange membrane (AEM, Tokuyama A201) confirmed this extraordinary bifunctional activity and opened a design concept for future bifunctional catalyst systems. Just Fe-N-C indicated limitations at elevated potentials and also the AEM appears not reversible.

Testing NiFe-LDH as anode catalyst in a seawater electrolyzer verified its suitability, showing high selectivities and activities. Constantly decreasing electrolyzer performance indicated rather the AEM as bottleneck for seawater electrolyzers than a catalyst induced, which was demonstrated by a strong recovery effect. Supporting this, quasi in-situ X-ray absorption spectroscopy (XAS) showed no influence of Cl^- on the local structure of NiFe-LDH, which verified the suitability of NiFe-LDH as catalyst for seawater electrolyzer anodes.

List of Publications

First authorship

SD-I

Non-noble metal oxides and their application as bifunctional catalyst in reversible fuel cells and rechargeable air batteries [1]

S. Dresp*, P. Strasser*

ChemCatChem, 2018, 10, 4162 DOI: https://doi.org/10.1002/cctc.201800660

SD-II

An efficient bifunctional two-component catalyst for Oxygen Reduction and Oxygen Evolution in reversible fuel cells, electrolyzers and rechargeable air electrodes [2]

S. Dresp, *F. Luo, F., Schmack, R., Kühl, S., Gliech, M. & Strasser, P,*

Energy & Environmental Science, 2016, 9, 2020–2024; DOI: https://doi.org/10.1039/C6EE01046F

SD-III

Direct electrolytic splitting of seawater: Activity, Selectivity, degradation, and recovery studied from the molecular catalyst structure to the electrolyzer cell level [3]

S. Dresp, *F. Dionigi, S. Loos, J. F. de Araujo, C. Spöri, M. Gliech, H. Dau, P. Strasser*

Advanced Energy Materials, 2018, 1800338; DOI: https://doi.org/10.1002/aenm.201800338

SD-IV

Simplified Microwave Assisted Solvothermal One Pot Synthesis of Highly Active Nickel-Iron Layered Double Hydroxide as Oxygen Evolution Reaction Catalyst [4]

***S. Dresp**, P. Strasser*

ECS Transaction, 2016, 75 (14), 1113-1119; DOI: https://doi.org/10.1149/07514.1113ecst

SD-V

Direct Electrolytic Splitting of Seawater: Opportunities and Challenges

***S. Dresp**, F. Dionigi, M. Klingenhof, P. Strasser*

ACS Energy Letters, 2019, 4, 933-942, DOI: https://doi.org/10.1021/acsenergylett.9b00220

Other publications

VII

Oxygen evolution reaction dynamics, faradaic charge efficiency, and the active metal redox states of Ni-Fe oxide water splitting electrocatalysts

*M. Görlin, P. Chernev, J. F. de Araújo, T. Reier, **S. Dresp**, B. Paul, R. Krähnert, H. Dau, P. Strasser*

Journal of the American Chemical Society, 2016, 138 (17), 5603 – 5614; DOI: https://doi.org/10.1021/jacs.6b00332

VIII

Dynamical changes of a Ni-Fe oxide water splitting catalyst investigated at different pH

*M. Görlin, M. Gliech, J.F. de Araújo, **S. Dresp**, A. Bergmann, P. Strasser*

Catalysis Today, 2016, 262, 65-73; DOI: https://doi.org/10.1016/j.cattod.2015.10.018

IX

Tracking catalyst redox states and reaction dynamics in Ni-Fe oxyhydroxide oxygen evolution reaction (OER) electrocatalysts: The role of catalyst support and electrolyte pH

*M. Görlin, J.F. Araújo, H. Schmies, D. Bernsmeier, **S. Dresp**, M. Gliech, Z. Jusys, P. Chernev, R. Krähnert, H. Dau, P. Strasser*

Journal of the American Chemical Society, 2017, 139 (5), 2070-2082 DOI: https://doi.org/10.1021/jacs.6b12250

X

Efficient Electrochemical Hydrogen Peroxide Production from Molecular Oxygen on Nitrogen-Doped Mesoporous Carbon Catalysts

*Y. Sun, I. Sinev, W. Ju, A. Bergmann, **S. Dresp**, S. Kühl, C. Spöri, H. Schmies, H. Wang, D. Bernsmeier, B. Paul, R. Schmack, R. Kraehnert, B. Roldan Cuenya, P. Strasser*

ACS Catalysis, 2018; 8 (4), 2844-2856 DOI: https://doi.org/10.1021/acscatal.7b03464

Patents

I

European Patent (18167304.7 – 1108):

Katalysatormaterial für eine regenerative Brennstoffzelle, sowie Herstellungsverfahren

S. Dresp, M. Klingenhof, P. Strasser

Aktenzeichen: P19057EP (angemeldet am 13.04.2018)

All results were presented as oral or poster presentation at conferences, workshops and special events. The list of scientific contributions can be found in ***Appendix - List of Scientific Contributions*** *on* ***page 133****.*

Table of Contents

LIST OF ACRONYMS

Abbreviation	Explanation
AEM	Anion exchange membrane
BP	Before present (before the year 1950)
CA	Chrono-amperometry
CCM	Catalyst coated membrane
CCS	Carbon capture and storage
CCS	Catalyst coated substrate
CCU	Carbon capture and utilization
CE	Counter electrode
ClER	Chlorine evolution reaction
CNL	Carbon and Fuel Cell (company)
CPE	Non ideal capacitor
CV	Cyclic voltammetry
E	Potential
e^-	Electron
EXAFS	X-ray absorption fine structure
Fe-N-C	Fe nitrogen doped carbon
GDL	Gas diffusion layer
GHG	Greenhouse gases
HER	Hydrogen evolution reaction
HHV	Higher heating value
HOR	Hydrogen oxidation reaction
ICP-OES	Inductively coupled plasma optical emission spectrometry
LDH	Layered double hydroxide
LHV	Lower heating value
MEA	Membrane electrode assembly

Me-N-C	Metal and nitrogen doped carbon
MS	Mass spectrometer / mass spectrometry
OCV	Open circuit potential
OER	Oxygen evolution reaction
ORR	Oxygen reduction reaction
PEIS	Potentio electrochemical impedance spectroscopy
PEM	Proton exchange membrane
PtG	Power to gas
PTL	Porous transport layer
QA	Quaternary ammonium ion
RDE	Rotating disc electrode
RE	Reference electrode
RHE	Reversible hydrogen electrode
RRDE	Rotating ring disc electrode
SEM	Scattering electron microscopy
SHE	Standard hydrogen electrode
TEM	Transmission electron microscopy
UNFCCC	United Nations Framework Convention on Climate Change
WE	Working electrode
wt%	Weight percentage
XANES	X-ray absorption near edge spectroscopy
XAS	X-ray absorption
XRD	X-ray diffraction

SYMBOL DIRECTORY

Symbol	Description	Unit
$\dot{n}$	molar gas flow	mol s^{-1}
$\Delta_R G$	Free enthalpy	$kJ\ mol^{-1}$
$\Delta_R H$	Reaction enthalpy	$kJ\ mol^{-1}$
$\Delta_R S$	Reaction entropy	J K^{-1}
C_{O_2}	Gas concentration of O_2	%
$\dot{V}$	gas flow	m_3 s^{-1}
w_{el}	Electrical work	Wh
c	Concentration	mol L^{-1}
d	Distance	m
E	Potential	V
E^0	Thermodynamic standard potential	V
F	Faraday constant	96485.3 s A mol^{-1}
I	Current	A
j	current density	A cm^{-2}
K	Equilibrium constant	-
n	Amount of substance	mol
p	pressure	Pa
Q	Charge	C
R	Ideal gas constant	R = 8.314 J mol^{-1} K^{-1}
R_s	resistance	Ω
t	Time	s
T	Temperature	K
z	Numbers of electrons transferred	-
θ	theta	°
λ	wavelength	nm

Chapter 1

Introduction and Motivation

This chapter will outline the importance and future role of a hydrogen based economy and will motivate the research and development work on the concept, material science, and technology of seawater electrolysis conducted over the course of this PhD thesis. It will show, how important an energy change from the fossil fuels to renewable energy sources will be. It will further outline the necessity of new and highly efficient electrocatalysts as well as novel approaches and techniques for the storage of renewable energies that is essential for a sustainable energy economy.

In this context, this cumulative thesis will explore a novel electrolysis concept using seawater directly as alternative electrolyte to commonly used alkalinized or acidified but purified freshwater as shown in **SD III**[3] (*Chapter 6*). At the same time, this thesis research also focuses on the extension of this seawater electrolyzer device to the usage as a fuel cell as presented in **SD II**[2] (*chapter 5)*. Accordingly, different non-noble materials were investigated for the suitability as bifunctional catalyst for the oxygen electrode in reversible electrolyzers in **SD I**[1] (*chapter 4*). A final discussion (*Chapter 7)* will evaluate all findings and compare the efficiencies with established technologies (**SD V**[5]).

1.1 The importance of a low carbon energy future

The impact of non-stopping consumption of fossil fuels with their associated emissions of greenhouse gases (GHG) becomes a continuously increasing problem. Air pollution, climate change, sea-level rise and energy-security problems are just some examples.[6, 7] To overcome these problems major transformations in the energy community and an acceptance of the society for a low carbon energy economy is required. Only a sustainable energy policy and a

drastic reduction of greenhouse gas emissions will realize the necessary adjustments for a worth wide future.

Started in England at the 2nd half of the 18th century, the industry revolution spread over first to the EU and latter to the U.S.A. The increasing demand for energy lead to an increased global fossil fuel consumption all over the world. This higher consumption of fossil fuels for the production of energy and later also for using in cars resulted in dramatic emissions of the greenhouse gas CO_2. Taking CO_2-concentration level data from 800,000 years before present (BP: before 1950) the overall atmospheric CO_2 concentration has never been higher than 300 ppm until early 1900 as shown in Figure 1-1.

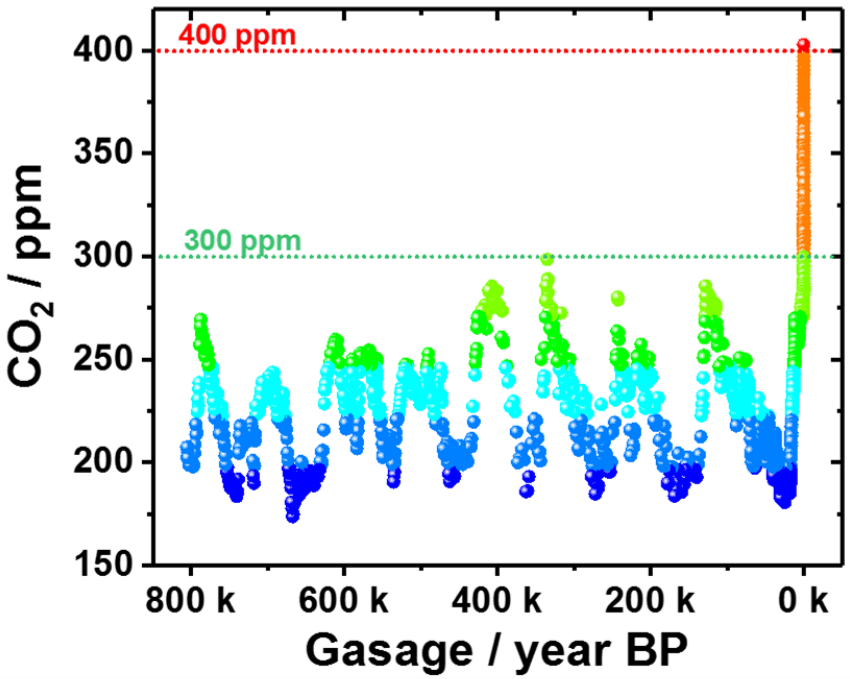

Figure 1-1: CO_2 gas concentration over the past 800 k years before present (BP) until 2016. The data is taken from 800 k – (-51) BP was taken from [8] and the data from 1980 – 2016 was taken from [9]

Since then, the CO_2 concentration did not only exceed 300 ppm, but also passed the 400 ppm threshold in 2016. The problem of this high CO_2 concentration is the strong relation between CO_2 concentration and world average temperature. The temperature fluctuation, also called as temperature anomaly, and the corresponding CO_2 concentration level between 1880 - 2016 is shown in Figure 1-2.

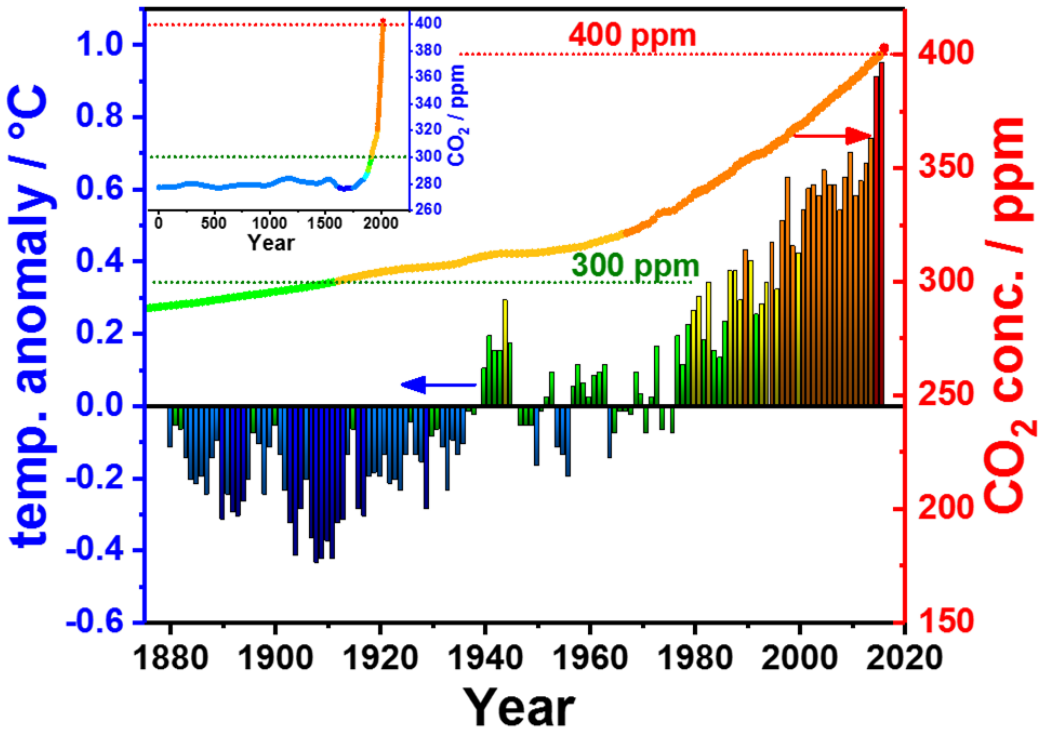

Figure 1-2: Temperature anomaly and CO_2 gas concentration from 1880 – 2016. The data for the temperature was taken from [10] and for the CO_2 concentration from [9]

From this figure, the temperature anomaly increased to positive temperature values similar to the CO_2 concentration, indicating a strong relation between these observables. In fact, the seven warmest years between 1880 – 2016 were all measured in the last 10 years, when the CO_2 concentration already passed the threshold of 350 ppm. In 2016, the CO_2 concentration reached the first time a higher value than 400 ppm. This threshold was a major concern from scientists, pointing out that passing this concentration level would lead to a concentration level we would not be able to reduce it back to concentrations below 300 ppm. Furthermore, the CO_2 concentration is still increasing and studies revealed that even changing the CO_2 emissions to zero would still not stop the global temperature increase. Likewise, the sea level is a major result of elevated temperature caused by glacier melting and water expansion. A study from 2018 revealed that even after a net-zero CO_2 emissions and a temperature stabilization, the sea-level will persist rising until the year 2300.[6] These scientists said further that a stringent emission reduction could only be seen as a first step to stop sea level rise, but is on the other hand highly important to reduce the risk of low-probability high-end sea-level rise. However, the impact of elevated temperature and an increased sea-level is not as strong in Europe as in other nations. Especially the population of the Asian nations will be affected most.[11] The major impacts of climate change can be summed up in changes in microclimate and weather

patterns, worldwide glacier recessions and associated sea level rise and coastal flooding, , sedimentation in river basins, glacial lake outburst floods, changes in the vegetation patterns and phenology, agricultural yield, food security, and damage and loss to populations and economies.[12] Any of this changes is connected to the CO_2 emissions, which drastically started in 1850, when the industry revolution started as shown in Figure 1-3.

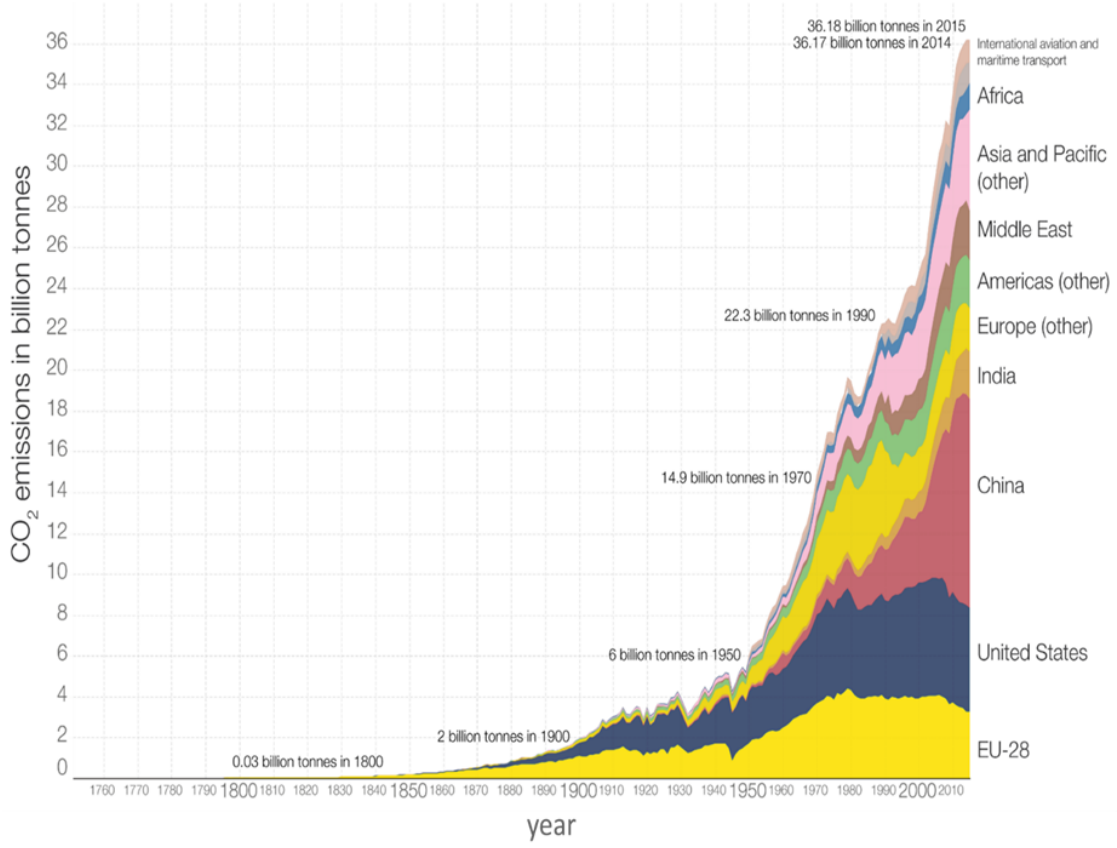

Figure 1-3: Annual CO_2 emissions per region. Reprinted from [13]

While the world CO_2 emission in 1900 was only based on the emissions of the EU and United States with only 2 billion tons, today's global CO_2 emissions are about 36 billion tons. In 1970, Chinas industry revolution started and became, as a consequence, today's global main CO_2 emission producer with about 10 billion tons CO_2 per year. Also, other nations in Asia and Africa release more CO_2 every year, since their industry is growing too. It is estimated that CO_2 emissions should be reduced by 50 % to limit the rise of the global average temperature to 2 °C by 2050.[14] As a consequence, in November 2015 at 21st UNFCCC climate conference in Paris countries all over the world agreed on a global commitment to combat climate change and reduce greenhouse gas emissions.[15] In Europe a consciousness for lower CO_2 emissions emerge around year 2000, while in other countries regulations are less strict. However, the

effects of air pollution are currently so dramatically that even China, where CO_2 emissions drastically increased in recent years, invest in new sustainable and CO_2 free energy and transportation technology to become the new world leader in renewable energy.[16] Accordingly, first regulations and support for sustainable projects of the EU-28 and the United states lead to a reduction of CO_2 emissions in the last years. But it is important to reduce this growing CO_2 emissions worldwide and develop a low carbon based industry future for any nation.

Even though the linkage between CO_2 greenhouse gas emission and the world climate change seem to be obvious, various scientists and politics believe still that there is no anthropogenic reason for climate change at all.[17] They majorly believe in a naturally induced climate change, claiming the earth is situated in a warming period. Overall, the problematic of the greenhouse gas emissions will be our future companion that needs to be combat.

This subchapter presented the linkage between anthropogenic CO_2 emission and global warming. The result of the annual greenhouse gas emissions lead to drastic increase of the global average temperature and related climate changes and sea-level rise. It states that a sustainable and low carbon future is necessary to stop high-end climate change. An approach for a low carbon future is shown in the next section.

1.2 Energy in the future: Hydrogen and its competitors

To combat the greenhouse gas emission it is important to understand its origin. Where does the emissions come from and how could a proper solution be provided? In Figure 1-4 all sectors for the causing greenhouse gas emissions are displayed between the years 1990 - 2010.

Over the whole time span the sector relation remain the same. At any time, the sector with the highest CO_2 emissions is represented by the energy sector with more than 15 Mio. Gg CO_2 in 2010, directly followed by the transportation sector with about 5 Mio. Gg CO_2. Due to higher population resulting in increasing car number and a higher demand for food and energy this sectors will most likely increase over the next years. So, the energy and the transportation sectors are the major fields that are important for a sustainable low CO_2 emission future.

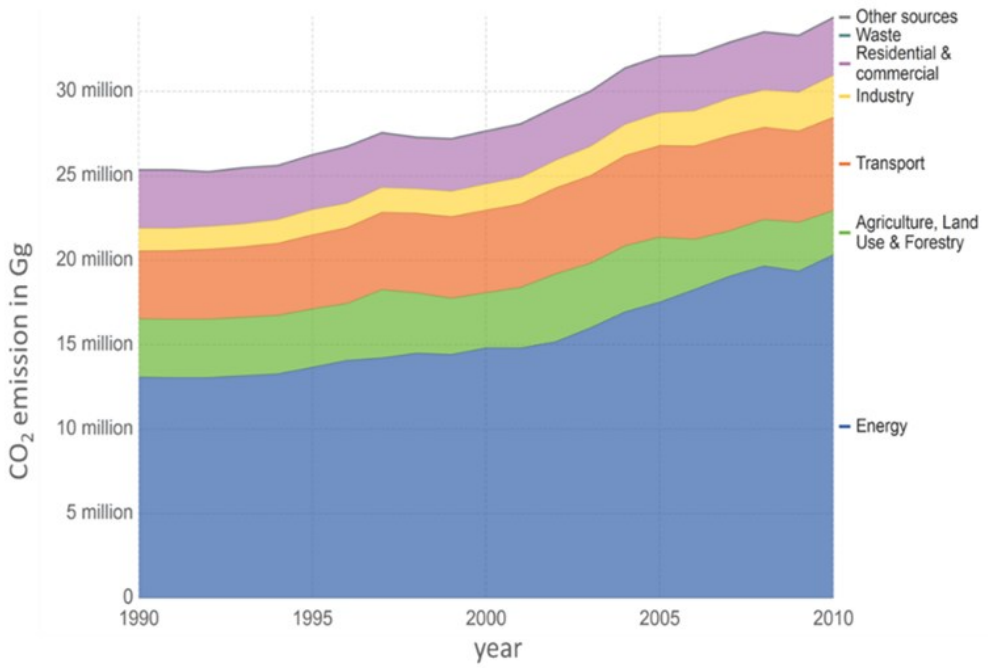

Figure 1-4: Annual global CO_2 emissions by sector in Gg CO_2. Reprinted and modified from [13]

To tackle the energy sector, especially in Germany renewable energy like photovoltaic and wind turbine became most popular among sustainable energy resources and photovoltaic plants and windmill are widely spread across the country. In fact, the major renewable energies in Germany are solar, wind, biomass and water power in that order. A cake diagram of different electricity production methods and respective percentage in Germany are shown in Figure 1-5.

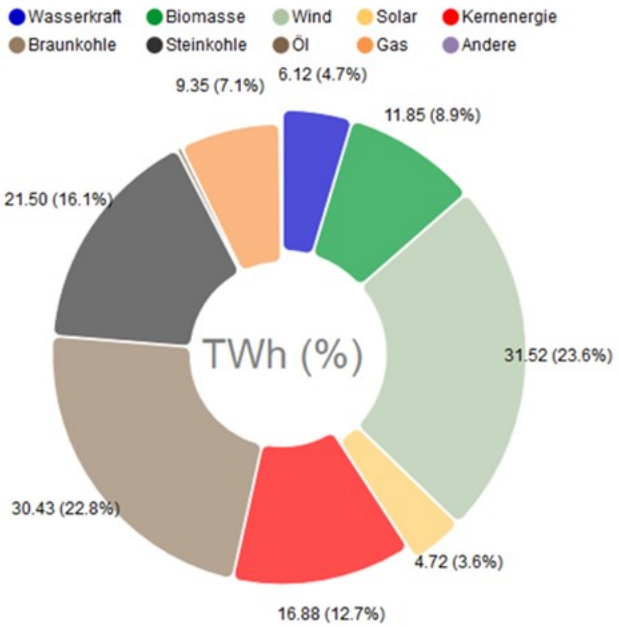

Figure 1-5: Electricity production percentage in Germany 2018. State: March 22nd. Reprinted with permission from [18]

The diagram shows that wind energy already outpaced the commonly used brown coal in 2018. Nevertheless, electricity production using coal-fired power station represents still the major proportion in electricity production. Since nuclear phase-out in 2011 the nuclear power has just a little proportion of only 13 %. In this scenario, the only alternative to burning fossil fuels are the renewable energies. Germany put a lot of effort in making that vision a reality. So, the proportion of renewable energies constantly increased over the last years and already surpassed the 40 % in 2018 as shown in Figure 1-6.

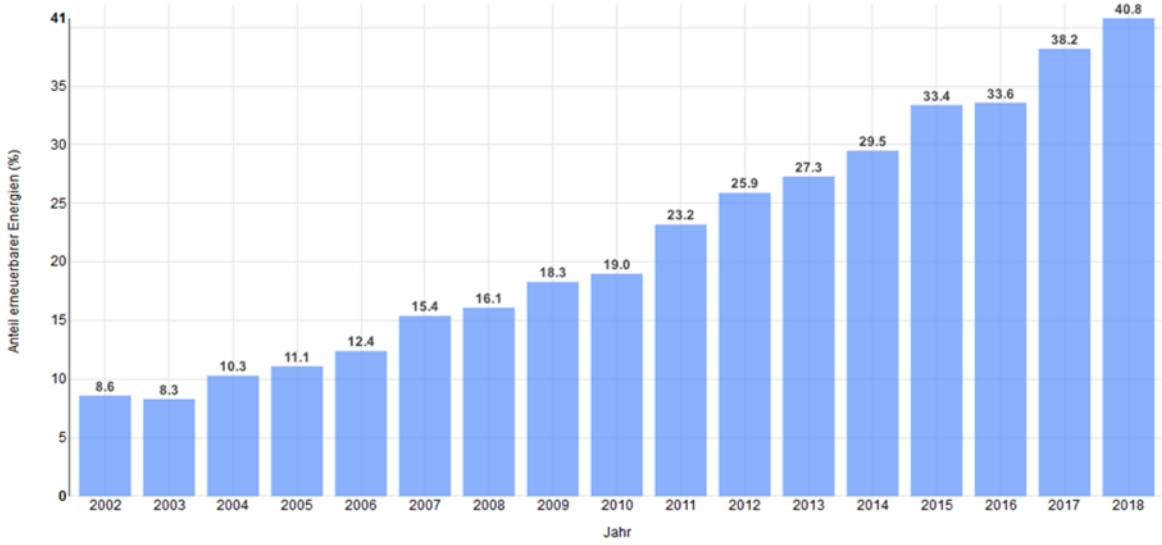

Figure 1-6: Proportion of renewable energy between 2002-2018. Reprinted with permission from [18]

Beside the advances of renewable energies due to their CO_2 free energy production, these technologies raise also a problem. Renewable energies fluctuate due to their dependence on environmental factors. In Figure 1-7, the renewable energy supply of wind and solar energy over a time span of 6 days is shown.

It is noticeable that the photovoltaic plants peak at daytime, when the sun shines and the photovoltaic plants are able to produce electricity. Not as uniform and more chaotic appears the wind power production. This naturally and highly irregular availability of electricity from renewables is not predictable and not easy to control. Consequently, renewable energy plants cannot react on peaks of power demand and cannot provide continuous power supply. Likewise, at low demand the overproductions cannot be stored. In other words, renewable energy is not necessarily following the energy demand which is a major problem for a sustainable and low carbon energy future. In this context, the efficient storage and release of renewable electricity are the major challenge in sustainable low carbon energy future. In order to address these challenge, different approaches are being pursued.

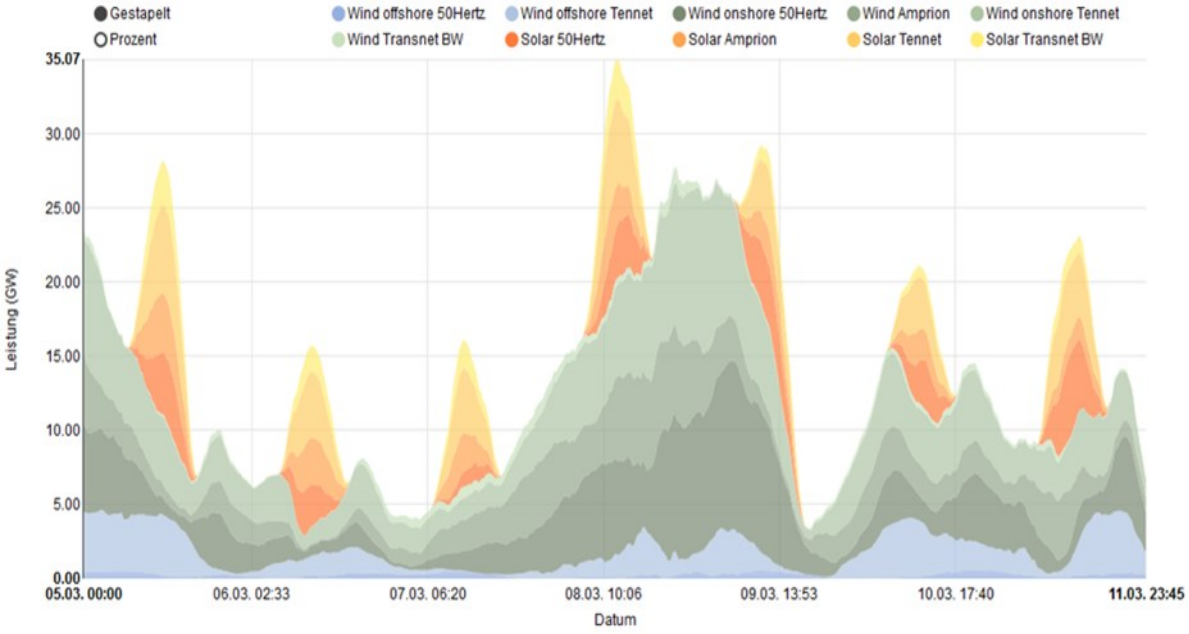

Figure 1-7: Wind and solar electricity production in Germany 2018. Reprinted with permission from [18]

The electricity storage in batteries seem to be practical due to high electricity transfer efficiency. But its low energy density synonymous with a low energy capacity in contrast to the storage demand of high energy amounts for several MW makes the battery storage of large scale electricity unattractive. The better solution is the electrochemical power to X or power to gas (PtG) transformation. Especially the electrochemical splitting of water to hydrogen and oxygen reaction (1-1) is one of the most attractive reactions, since the energy cycle works complete without any carbon emissions involved.

$$2\ H_2O + \text{Electricity} \rightarrow 2\ H_2 + O_2 \quad ; \Delta H_0 = +285.8\ \text{kJ}\ mol_{H_2}^{-1} \qquad (1\text{-}1)$$

The reaction enthalpy ΔH_0 shows that for the production of 1 M H_2 a minimum of 285.8 kJ are necessary. This energy can be used vice versa in a fuel cell to produce electricity. The only side product is water instead of CO_2 that evolves during fossil fuel combustion. This high energy density of H_2 makes it as an ideal energy storage molecule. Additionally, the energy amount storage from water electrolysis is only limited by the volume of the hydrogen container and not by the total capacity like in batteries. For this, the water electrolysis seemed to be the ideal solution for future large-scale renewable electricity/energy storage. Producing substantial amounts of hydrogen would evolve a “hydrogen economy” which is the term that became more and more popular in the last years.[19-21] A hydrogen economy could especially make the transportation sector more sustainable and greener, since the established electric battery

vehicles lack of long distance performance (200 – 400 km / Tesla Model S), which is caused by limiting energy density of batteries that are used in cars.[22] Fuel cell cars using hydrogen as a vector to electric energy overcome this limiting factor reaching easily distances of 800 km as shown in 2018 for the new released Hyundai Nexo.[23] Moreover, filling hydrogen into the fuel cell car needs less than 5 min,[23] which compared with the complete battery charging of at least 1 h, makes fuel cell technology much advantageous. But the future of hydrogen is still controversially discussed and the world wide future establishment of hydrogen is not certain yet.

In 2017, Hanley et al. gave a perspective of the presumable role of hydrogen in low carbon energy futures. They took several national and international studies and prepared a timeline when hydrogen would emerge as shown in Figure 1-8.[24]

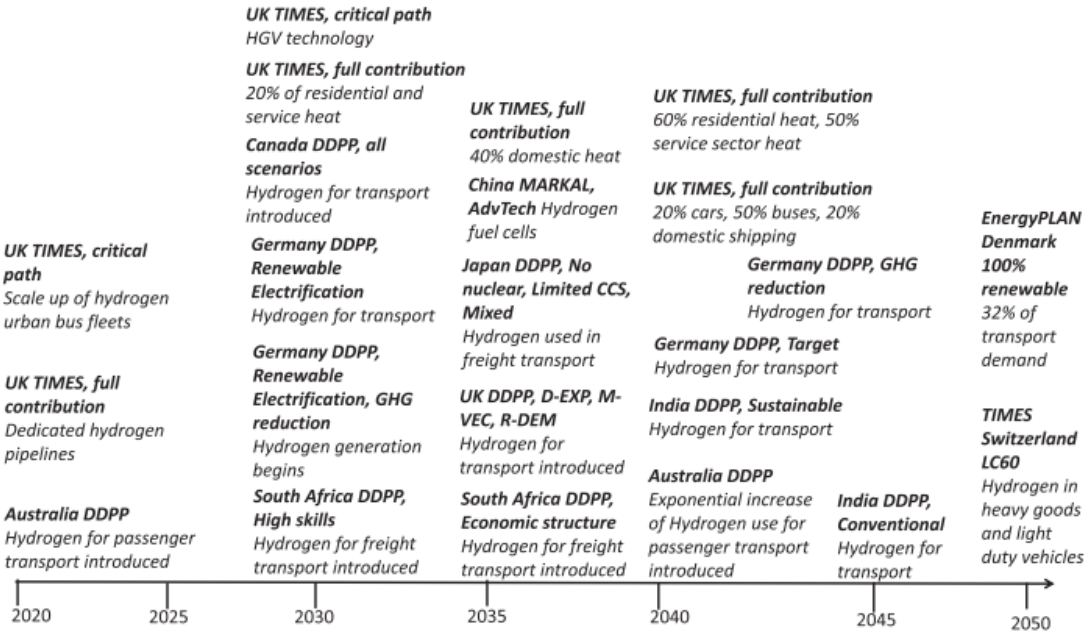

Figure 1-8: Timeline of the emergence of hydrogen in national energy studies (Reprinted with permission from [24]. Copyright 2018 Elsevier)

From this study, hydrogen will emerge in Germany at around 2030. Based on these studies, the proposed main future usage of hydrogen will be exclusively for the freight and transport sector. Only a few studies in the United Kingdom consider hydrogen for heating and other applications like the production of synthetic methane or methanol from CO_2. Hanley et al. also pointed out that not only the electrification, increasing energy efficiencies, hydrogen economy technologies and the expansion of renewable energies would help for a low carbon energy future, but also carbon capture and storage technologies (CCS) could be possible solution in the energy

sector.[25-28] These technologies capture the CO_2 directly from their emission sources like power plants and could either be stored or directly used to synthesis artificial carbohydrates. However, carbon capture and storage technologies focus on long-term storing CO_2 for example in the ground to reduce the GHG emissions. A better solution would be the carbon capture and utilization technology (CCU) when the captured CO_2 is transformed into usable products like methanol or urea. Other nations count on a higher electrification and using battery cars.

The requirement of hydrogen in future is undisputed, but the source for renewable hydrogen is still under an ongoing debate. To compete with CO_2 based technologies, a higher efficiency of hydrogen production is necessary. In other words, renewable hydrogen needs to become cheaper (cf. *chapter 2.1 Water Electrolysis: Bottleneck of the hydrogen economy*). This would be feasible with the development of low cost materials with improved manufacturing capability at lower capital cost requirements and at the same time by improving the efficiency and durability of the system. In this context the U.S. DOE published current hydrogen production program activities, namely: Reforming of renewable, bio derived feedstock, electrolysis, solar thermochemical, photo-electrochemical and biological.[22]

Since the efficiencies of biological and solar driven photo-electrochemical approaches are still too low, biomass and water electrolysis could become the main sustainable sources for hydrogen.[24] Hence, the current main competitor to water electrolysis, is the biomass as renewable hydrogen source. But while biomass require carbohydrate containing materials that directly competes with the food industry, water electrolysis seemed to be the better alternative, although the low efficiencies of electrolyzers and fuel cells, the high cost of existing technologies and the current missing availability of infrastructure hampering the process of a successful assertion of a hydrogen economy, yet. New efficient catalyst materials for fuel cells and electrolyzers could therefore make hydrogen technologies competitive to current competing technologies and pave the way to a hydrogen economy.

This subchapter showed the growing establishment of renewable energies worldwide and revealed the related problems of these technologies. Since the energy and transportation sectors cause the highest CO_2 emissions, especially this field needs to be tackled by replacing them with sustainable energy concepts. The problematic fluctuation of renewable energies makes the replacement difficult and the reversible storage of surplus produced electricity mandatory. A hydrogen economy seems to be the most suitable approach for large scale storage since batteries lack in energy densities and MW capacities. However, studies show that the future of hydrogen will be rather located in the transportation sector than in any other. Finally,

new efficient catalyst materials are necessary to make hydrogen technologies competitive and pave the way for a hydrogen economy establishment. In this context, the next chapter will introduce current used catalysts and the associated problems.

1.3 Hydrogen economy catalysts: The platinum group metal (PGM) problem

For a sustainable hydrogen based energy economy the catalysts are of crucial importance. Catalyst for the hydrogen production and the hydrogen consumption are equally important. Especially the automotive industry invest tremendous amounts of money and time for the development of high efficient catalysts for their fuel cell cars. Currently, there are no better catalysts than platinum based catalysts especially for the fuel cell.[29] To replace platinum with its excellent properties appears highly challenging. It can be used at high temperatures and is even stable in many aggressive chemical environments, e.g. concentrated acids. In 2011 a fuel cell car contained about 46 g of Platinum.[30] In comparison, current car catalysts for their exhaust have about 1-4 g of this metal that accounts already for more than one-third of total global platinum demand.[30, 31] Five years later in 2016 the approximate platinum group metal (PGM) loading is about 22.5 g vehicle$^{-1,}$ which could be translated to a total catalyst loading of 0.25 mg_{PGM} cm^{-2} on the corresponding fuel cell electrodes.[32] Usually the cathode side in the membrane electrode assembly in a fuel cell needs higher amount of PGM and is expressed as bottleneck in fuel cell catalyst research (*see chapter 2.2.3 Oxygen electrode chemistry*). The DOE target for 2020 points out a maximum usage of 9 g_{PGM} vehicle^{-1} (0.125 mg_{PGM} cm^{-2}) that is still the double amount of current exhaust catalysts. Figure 1-9 shows the global map of PGM project locations. The main resource of PGMs are located in South Africa, Russia and North America.

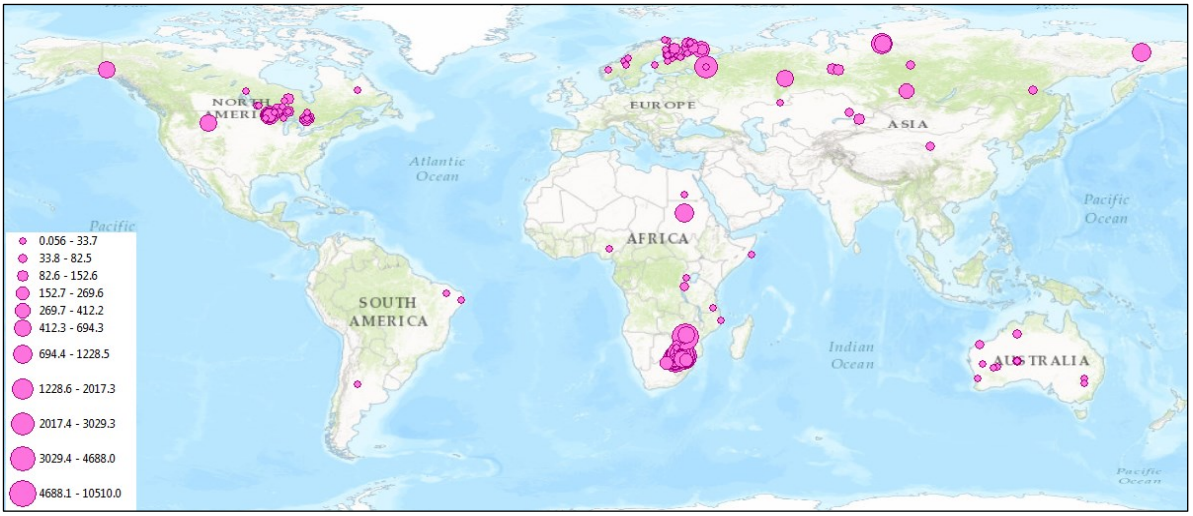

Figure 1-9: Global map of PGE project locations (Reprinted with permission from [33]. Copyright 2018 Elsevier)

But the main mine supplier are by far south Africa and Russia. The mine supply of platinum group elements (PGE) with its market price is shown in Figure 1-10.

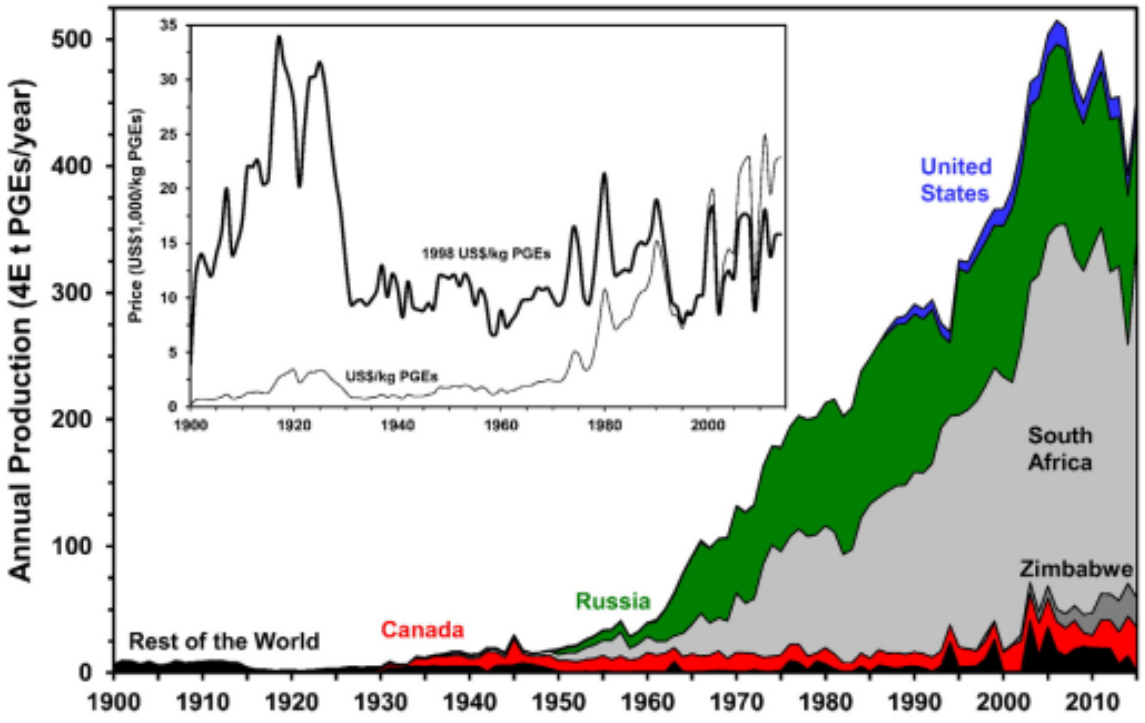

Figure 1-10: Global PGE mine supply. Reprinted with permission from [33]. Copyright 2018 Elsevier

These data indicate that cumulative world mined supply by 2015 is ~16,120 t PGEs. The half was sourced from South Africa, one third from Russia and most of the rest from Canada, the

USA and Zimbabwe. This locality of the PGM resources would make the development of other originated and highly abundant catalysts desirable to gain independency from other countries resources.

In addition to their local appearance, the PGMs are also extremely rare. In 2002, the United States Geological Survey (USGS) published abundancies for almost every element of the periodic table. Figure 1-11 shows the abundancies of the elements over their atomic numbers. Of particular note is that the noble metals including Pt are the rarest elements in earth crust. Especially iridium that is considered as most suitable material for the electrolyzer, is by far the least abundant element on earth. Several theories have been published about this phenomenon concluding all of an extraterrestrial impact event, bringing iridium on earth crust.[34, 35] Considering this, it would be desirable using other elements, especially catalysts made from highly abundant rock-forming elements appear most covetous as the rarest elements in earth crust will not provide a sustainable catalyst resource.

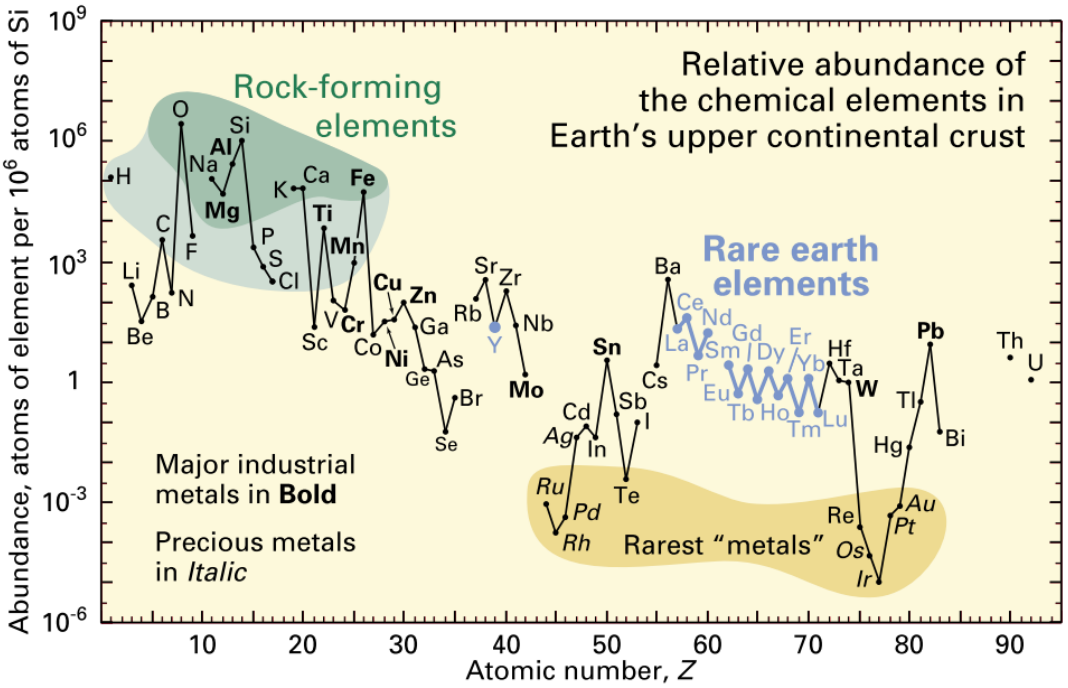

Figure 1-11: Abundance (atom fraction) of the chemical elements in Earth's upper continental crust as a function of atomic number [Taken from [36]]

However, in case of a global change to fuel cell vehicles the global platinum demand would drive up significantly, which directly might even increase the current platinum price so that the technology with all the advantages will again become unattractive due to high raw material prices.

Summarized, current industrial used catalysts for fuel cells and electrolyzers are based on highly rare and expensive elements like Pt and Ir. The fact, that the resources of those elements are mainly located in Africa, Russia and North America only, makes the search for new efficient catalysts based on highly abundant rock-forming elements highly desirable and to avoid monopolism even necessary. A discussion of sources of renewable energy, which is another important point in development of these technologies, will be presented in the next chapter.

1.4 Global distribution of renewable energy potential and freshwater

While the locality for PGM's could hamper the process for a sustainable and renewable energy future, also the resource of renewable electricity are important to consider, since the various renewable energy sources like sunlight or wind streams are not evenly distributed. In that context, Figure 1-12 and Figure 1-13 shows the photovoltaic and the wind power potential of the Globus.

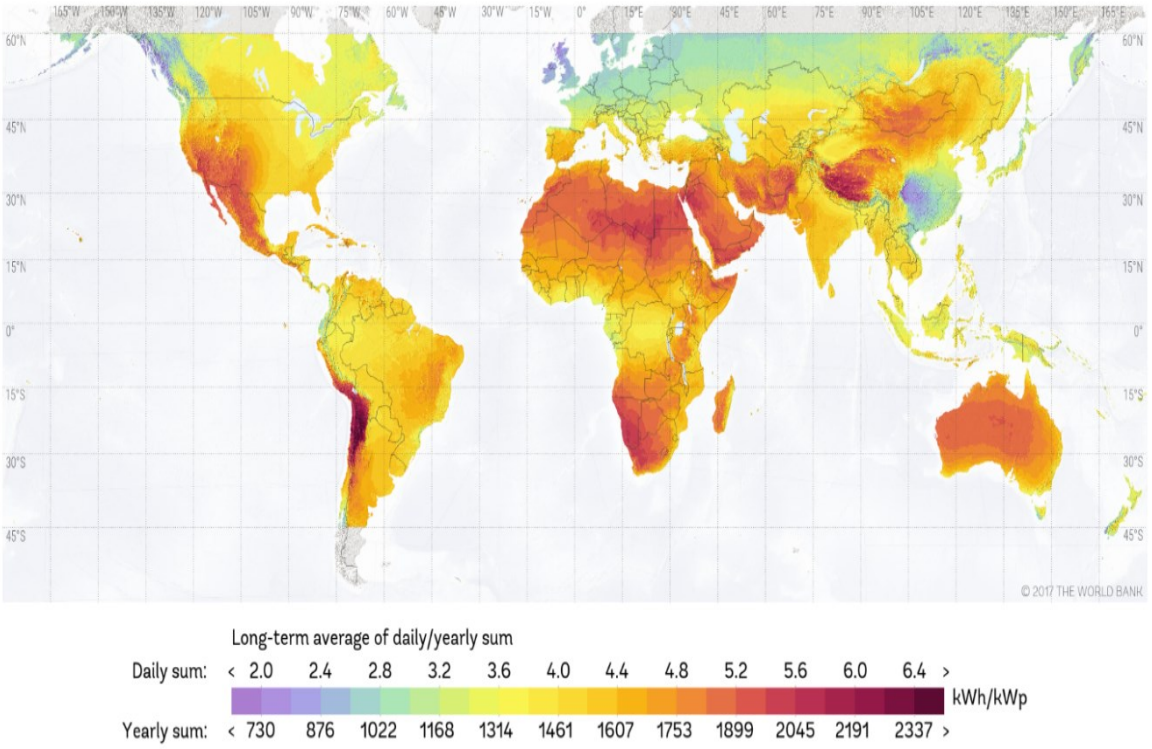

Figure 1-12: Distribution of Photovoltaic energy on the earth. [Taken and Modified from © 2017 The World Bank, Solar resource data: Solargis [37]]

Accordingly, Figure 1-12 shows that the maximum photovoltaic potential of the Globus is mainly located in the Arab world, South Africa, the west coast of America, Australia and the west of China.

In contrast, Figure 1-13 shows that the wind power is mainly concentrated at coastal regions such as the north coast of Europe, south coast of Alaska, the tip of South America and some other small coastal sections in Australia and Asia. These regions appear as the greatest regions for harvesting wind power. Although this would stoke the problematic monopoly and locality at this spots, these facts suggest the production of renewable electricity exactly at this locations. A political consent would therefore be necessary, since global warming affects any country on the globe.

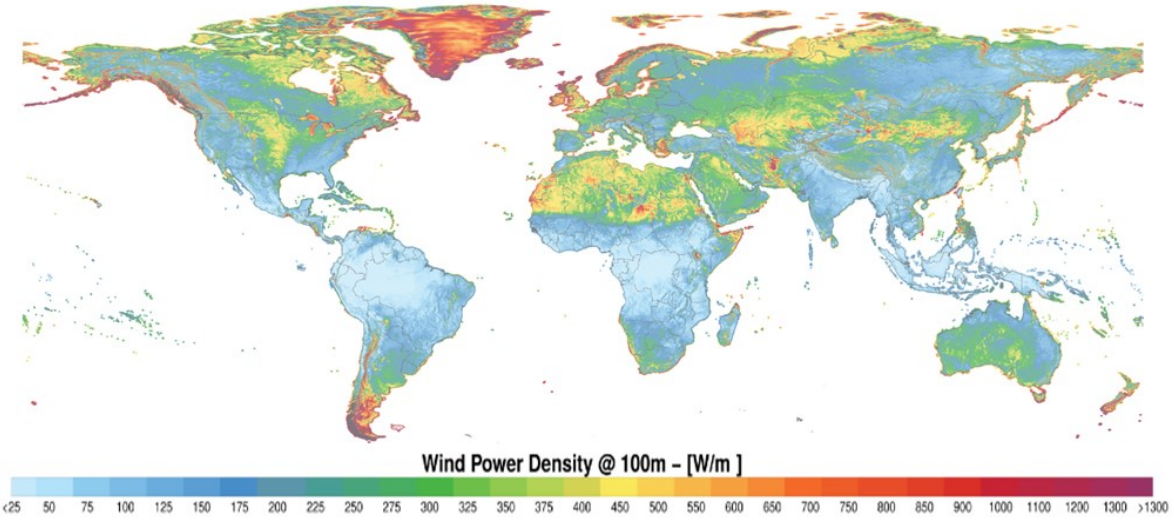

Figure 1-13: Wind Power Density of the world [[Data/information/map obtained from the] "Global Wind Atlas 2.0, https://globalwindatlas.info"[38]]

In any case, large scale production of renewable electricity will result in extremely high local excess of electricity. Water electrolysis to hydrogen with its associated storage and transportation would be the best approach to store and distribute this surplus energy. But current electrolyzer concepts work with either highly alkalized or acidified electrolyte made from highly purified freshwater that does not exist at many of those locations as shown in Figure 1-14.

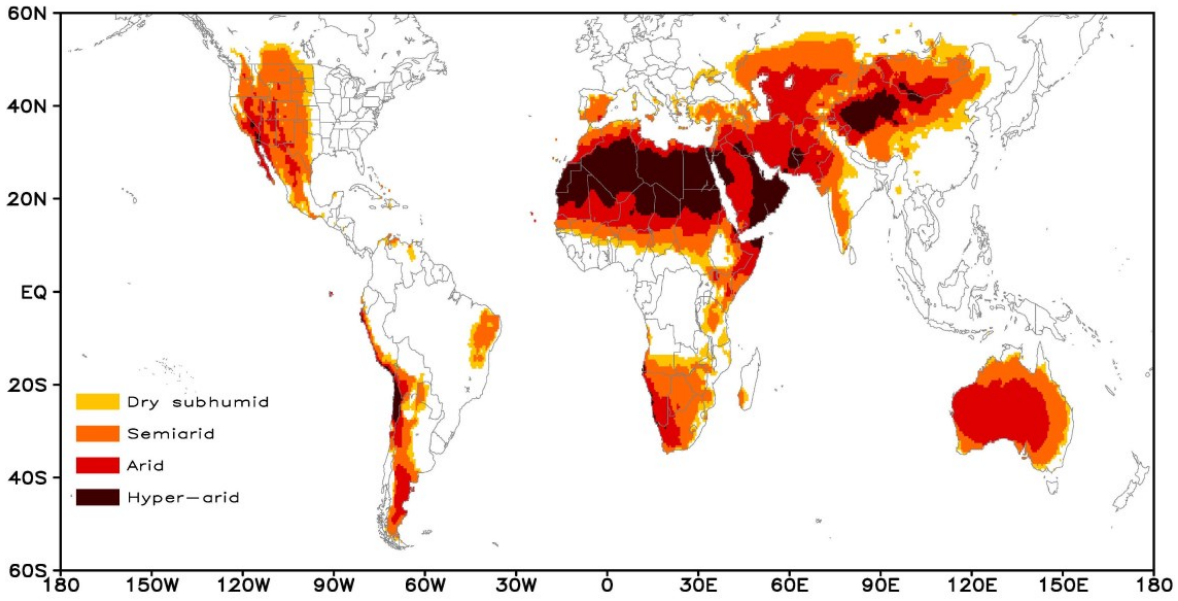

Figure 1-14: Global distribution of drylands for 1961–1990 climatology derived from P / PET ratio based on observations arid Zones. (Reprinted from [39])

Especially the west coast of South and North America or central Africa are mainly hyper-arid zones. Compared with renewable energy resources, the most arid zones are the regions with the highest energy potential. Coastal regions with high photovoltaic and wind power could consequently not provide the necessary fresh water that current electrolysis technologies require. Even though seawater is present at coastal regions, it is not suitable for current electrolyzer technologies.

The reason is that seawater contains many of interfering ions, mainly Na^+ and Cl^- which malfunction current electrolyzer systems (cf. *chapter 2.3, Seawater Electrolysis*). Moreover, additional pre-purification of seawater would reduce the robustness of the system, since reverse osmosis systems require frequent maintenance and other methods need high energies and therefore reduce the overall efficiency. Therefore, the direct usage of seawater for the production of hydrogen would be highly desirable and would make this technology extremely flexible. Existing offshore wind parks and especially sun rich coastal desert regions would benefit from this simple technology, since the produced hydrogen could back transformed into electricity and freshwater, which could be an additional aspect in future water provision. Furthermore, the oceans contain an almost unlimited reservoir of seawater so that this represents an ideal candidate as future water resource for electrolyzer technologies.

In conclusion, a revised simplified electrolyzer with a novel catalyst material that splits directly seawater into hydrogen and oxygen could help boosting the era of a hydrogen economy. It could

further gain the access to freshwater in coastal hyper-arid zones, when back transforming the hydrogen to electricity and water. Looking at the renewable power potential on the Globus like sun and wind compared with the availability of freshwater that is mandatory for electrolysis technologies reveal that the most arid zones are the regions with the highest energy potential. For sun rich coastal desert regions this suggest the direct splitting of seawater into hydrogen and oxygen. Using a fuel cell to back transform hydrogen into electricity and freshwater, this could enable a novel source for freshwater and could help these nations in future freshwater provision.

1.5 Thesis Outline and Objective

In the context of a hydrogen economy and a low carbon energy future, and considering the challenges of pure water electrolysis and the opportunities of seawater electrolysis, the present cumulative thesis has the goal to investigate the feasibility of a reversible seawater electrolyzer as a novel and promising concept for a sustainable and low carbon energy future. The concept of the reversible seawater electrolysis is displayed in Figure 1-15.

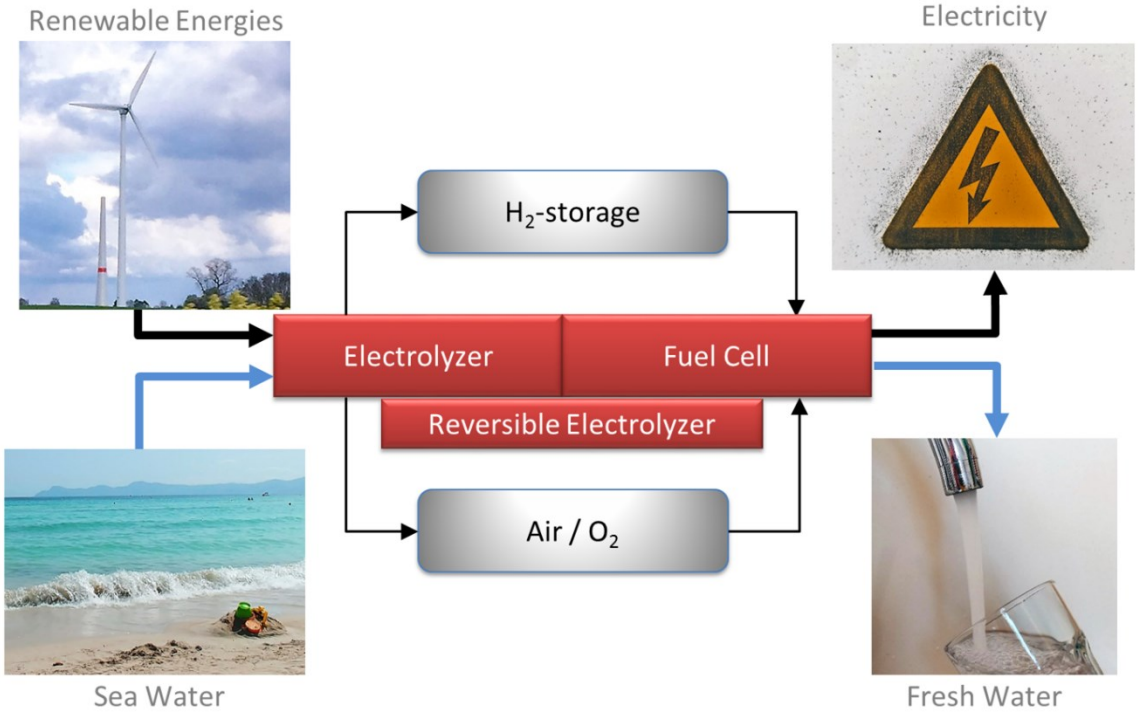

Figure 1-15: Scheme for the overall goal of this project. Renewable electric energy splits seawater into hydrogen and oxygen. The stored hydrogen can back transformed into fresh water and electricity

At first, renewable electricity used in an electrolyzer splits seawater selectively into hydrogen and oxygen. The evolved oxygen could either be stored or released in the atmosphere. The

evolved hydrogen can be stored and used at times of energy demand, when the hydrogen can be back transferred to fresh water and electricity in a fuel cell. The necessary oxygen could either come from air or from the oxygen tank. As a side effect, also fresh water is produced.

In this context, this cumulative thesis represents a feasibility study including fundamental aspects of in depth catalyst research and partwise material compartment selection and investigations. The catalyst investigation focus on relations between activity, selectivity and stability as shown Figure 1-16.

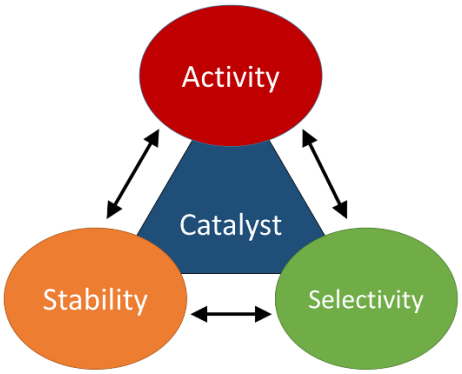

Figure 1-16: Catalyst property relation of electrocatalyst materials

In this context, this study will investigate the aspect of a possible reversible seawater electrolyzer. It will show three major topics with their specific objectives:

- **Bifunctional oxygen evolution reaction/oxygen reduction reaction catalyst**
  - Finding a reversible catalyst suitable for OER/ORR catalyst
  - Understanding the principle of a reversible catalyst on a molecular level
  - Understanding the stability relation due to high OER/ORR potential differences

- **Seawater splitting and selective oxygen evolution reaction**
  - Set-up of a seawater electrolyzer
  - Understanding the parameter in a seawater electrolyzer device
  - Revealing the catalytic relation between activity, selectivity and stability
  - Showing the feasibility of such device
  - Seeking the suitable components and understand the influence of them

Correspondingly, chapter 2 will give important background information for electro catalysts such as current approaches and fundamental knowledge of a reversible electrolyzer and

seawater electrolyzer catalysts. It will reveal the challenges for the catalyst research and will present current designs of reversible electrolyzers**.** Additional to publications **SD I – SD III** [1-3], Chapter 3 gives more detailed information of the experiments that are made to fulfill the objectives. Likewise chapter 4 - 6 summarizes the related publications **SD I - SD III** [1-3]. Accordingly, **SD I** [1] (*chapter 4*) shows the bifunctional electrochemical OER/ORR activity of various self-prepared precious metal free catalysts. It will show the favorable OER activity of non-noble catalyst oxides. In **SD II** [2] (*chapter 5*), we prepared a two-catalyst mixture to overcome the limiting activity of mono-component catalysts and a two- component catalyst concept was developed. The mixture was based on two precious metal free electrocatalysts specialized for only one reaction, which, when combined, give to this date unachieved bifunctional overall activity. It will show the necessity of specialized catalysts that work combined as a mutual bifunctional material. In the context of a specialized material, **SD III**[3] (*Chapter 6*) investigates NiFe-LDH as a highly active oxygen evolution reaction catalyst, which is implemented into an anion exchange membrane based electrolyzer to split directly and selective seawater into hydrogen and oxygen. Finally, Chapter 7 will discuss the feasibility of a reversible seawater electrolyzer based on the results of **SD I -SD III**[1-3] (*chapter 4-6*) and compares a direct and a reversible seawater electrolyzer to already established technologies **SD V**. At the end in chapter 8, all aspects are compiled to an overall conclusion and give a final outlook for reversible seawater electrolyzers.

1.6 Summary of Chapter 1

This chapter presented the linkage between anthropogenic CO_2 emission and global warming. The result of the annual greenhouse gas emissions lead to drastic increase of the global average temperature and related climate changes and sea-level rise. It states that a sustainable and low carbon future is necessary to stop high-end climate change. It also showed the growing establishment of renewable energies worldwide and revealed the related problems of these technologies. Since the energy and transportation sectors cause the highest CO_2 emissions, especially these fields needs to be tackled by replacing them with sustainable energy concepts. The problematic fluctuation of renewable energies makes the replacement difficult and the reversible storage of surplus produced electricity mandatory. A hydrogen economy seems to be the most suitable approach for large scale storage since batteries lack in energy densities and MW capacities. However, studies show that the future of hydrogen will be rather located in the transportation sector than in any other. New efficient catalyst materials are necessary to make hydrogen technologies compatible and pave the way for a hydrogen economy

establishment. In this context, current industrial used catalysts for fuel cells and electrolyzers are based on highly rare and expensive elements like Pt and Ir. The fact, that the resources of those elements are mainly located in Africa, Russia and North America only, makes the search for new efficient catalysts based on highly abundant rock-forming elements highly desirable. Looking at the renewable power potential on the Globus like sun and wind compared with the availability of freshwater which is mandatory for electrolysis technologies reveal that the most arid zones are the regions with the highest energy potential. Consequently, this suggests for especially sun rich coastal desert regions the direct splitting of seawater into hydrogen and oxygen. Using a fuel cell to back transform this hydrogen into electricity and freshwater would additionally enable a novel source for freshwater and could help these nations in future freshwater provision. In this context, this study will investigate the aspect of a possible reversible seawater electrolyzer with a special focus on a bifunctional catalyst for the oxygen electrode.

Chapter 2

Hydrogen Chemistry and Technology

Chapter 2 will give a detailed analysis of the project related technologies, background information and put hydrogen into the focus for a renewable and sustainable energy in future. It will discuss the historical background of electro-catalytically produced hydrogen including electrolyzer and fuel cell concepts and the challenges of reversible working electro-catalysts from atomic scale and theoretical perspectives.

2.1 Water Electrolysis: Bottleneck of the hydrogen economy

When the Dutch scientists Trostweijk and Daiman discovered the electrochemical splitting of water in 1789 they were not aware that their finding would make such an impact in the 21st century.[40] Also, Michael Faraday would not have dreamed about the eager investigating researchers for better hydrogen technologies, when he first introduced the water electrolysis and decomposition process in the first half of the 18th century.[41] Water electrolysis separates the constituent elements of water to ultimately produce hydrogen and oxygen by just using electricity as chemical force. Hydrogen with its enormous energy density is proposed as one of the best energy alternatives since its only side product is water. Today in 2018, a whole society is seeking for better catalysts and improved technologies for hydrogen production, hydrogen usage and hydrogen storage. The advantages of hydrogen compared to other technologies are undisputed (see *chapter 1.2 Energy in the future: Hydrogen and its competitors*). The emergence of the idea of an hydrogen economy goes back to the year 1968, when at a dinner in Stockholm during a scientific meeting the scientists were talking about the transmission of hydrogen through pipes.[42] The reason was, that it might be cheaper to send energy in the form of hydrogen through pipelines than sending electricity through copper wires. Since then, many contributions on the way realizing the hydrogen economy were made. Especially at the point

when CO_2 emissions were identified as major greenhouse gas contributing to the climate change and global warming, which supported and accelerated the vision of a hydrogen economy (cf. *chapter 1.1 The importance of a low carbon energy future).*

Even though water electrolysis using renewable electricity would be the greenest and most sustainable production route, today, water electrolysis compared to other current hydrogen production routes makes just about 4 % worldwide [43]. Most of the hydrogen is produced from fossil fuels by steam methane reforming (48 %), Crude oil cracking (30 %), and coal gasification (18 %).[43] The continuous use of fossil fuels even for the production of hydrogen can be explained by two major reasons.

First, since storing the small molecules of hydrogen was problematic for long time, the industries produced their hydrogen at their site and on demand. At the same time, they directly consumed the entire produced hydrogen. This is the case for almost any hydrogen utilizing industry. In Figure 2-1 the proportions of hydrogen consumption is shown for the year 2012.[44]

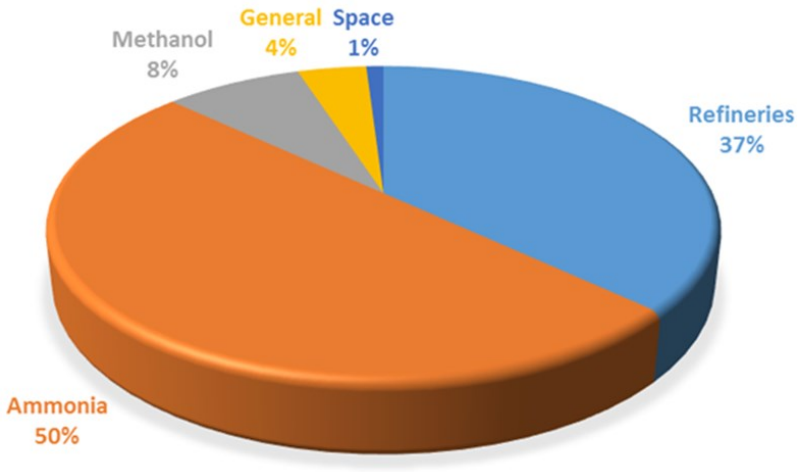

Figure 2-1: Proportions of hydrogen consumption in 2012 (Numbers taken from [44])

The refineries used 37 % of the produced hydrogen. Simultaneously in the refineries large amounts of hydrogen naturally arise, which can directly be consumed for the crude oil refinement. Consequently, an alternative hydrogen resource for the refinery sector would be entirely superfluous. In contrast, 50 % of the current hydrogen production is consumed by the ammonia (NH_3) production industry that require highly purified N_2 and H_2 as resource to form under high pressure and temperatures NH_3. Typically, the ammonia industry use on-site syngas production from methane, water and air. But in contrast to the refineries the use of methane is not required and could be replaced easily by a more sustainable technology such as water

electrolysis. But electrolysis compared to steam reforming is much more expensive, which lead to the second reason responsible for current electrolysis making just about 4 % of hydrogen production worldwide.

In fact, hydrogen produced by conventional methods like natural gas reforming costs about 1.34-2.27 $/kg compared to renewable hydrogen produced via electrolysis costs about 4-24 $/kg.[45] In order to establish a renewable hydrogen economy in future, renewable hydrogen needs to become cheaper to compete with these established methods. Albeit, when a hydrogen economy would emerge the proportions of hydrogen consumption would change drastically due to novel hydrogen related industry sectors, so that the demand of hydrogen would increase equally. The higher demand would perhaps increase the hydrogen price of any production route and could adjust the current higher price of renewable hydrogen.

In order to get to the bottom of renewable hydrogen price made by electrolysis, the proportions of the total price is shown in Figure 2-2.

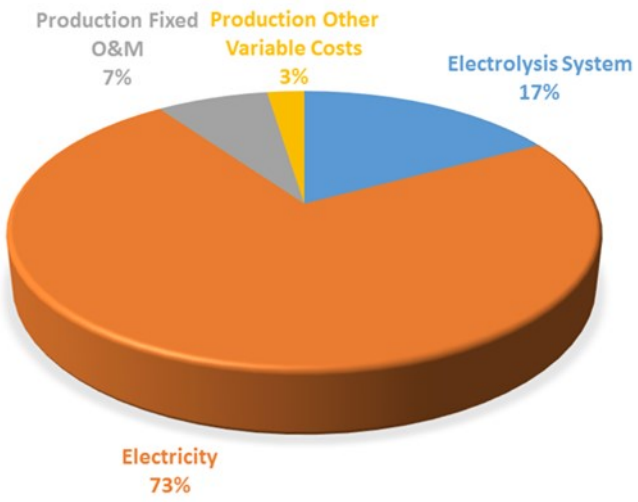

Figure 2-2: Cost Proportion of electrolysis based hydrogen in 2015 (Numbers taken from: [46])

Almost three quarter of the hydrogen price is mainly dependent on the electricity price. Beside the high costs of electricity the electrolyzer system makes about one fifth of the total hydrogen price. Accordingly, only with a minimization of the electricity prices, renewable hydrogen could become cheaper and likewise competitive to fossil fuel based hydrogen production routes. But also improvements in electrolyzer efficiencies could combat the high electricity prices by avoiding high energy losses due to inefficiencies in water electrolysis. This could be done by the development of novel catalysts and electrolyzer systems that make water splitting with a

minimum of energy close to their thermodynamic limits (cf. *chapter 2.2.1 Fundamental thermodynamics of hydrogen chemistry*).

The high cost of electricity and the capital cost of current hydrogen technology, are the reasons for a non-appearance of widespread hydrogen economy, yet. To combat the problems remain quiet challenging. But a reduction of electricity prices and efficiency improvement by using novel electro-catalysts based on cheap and abundant materials could face current problems and strive the path for a sustainable energy future. The hydrogen chemistry and the thermodynamic limits are described in the next section in detail.

2.2 Electro-catalysis and hydrogen chemistry

To understand the chemistry behind the hydrogen economy, the cycle of water splitting via electrolysis and the back transformation to water and electricity in a fuel cell is shown in the next section.

2.2.1 Fundamental thermodynamics of hydrogen chemistry

Water splitting and the back reaction are based on the electrochemical equilibrium reaction displayed in reaction (2-1).

$$H_2\,(g) + \tfrac{1}{2}\,O_2\,(g) \rightleftarrows H_2O\,(l)\ ;\ \Delta_R H = 285.8\ \text{kJ}\ mol^{-1} \qquad (2\text{-}1)$$

While splitting of water is also termed as water electrolysis, the back reaction of hydrogen and oxygen to form water and energy is also called “Knallgas” reaction, which is the same reaction that happens in a fuel cell in a controlled way. The reaction enthalpy $\Delta_R H$ = + 285.8 kJ mol^{-1} gives the necessary energy to split one mole liquid water into hydrogen and oxygen at standard conditions (T = 25 °C, p = 1 atm). The reaction enthalpy is defined from the Gibbs Helmholtz equation as the sum of the free enthalpy $\Delta_R G$ and the thermal term including the temperature T and the entropy $\Delta_R S$ as shown in formula **(2-2)**:*[47]*

$$\Delta_R H = \Delta_R G + T\Delta_R S \qquad (2\text{-}2)$$

Where $\Delta_R G$ is the free enthalpy in [kJ mol^{-1}], $\Delta_R H$ is the reaction enthalpy [kJ mol^{-1}], T is the temperature [K] and $\Delta_R S$ is the entropy [J K^{-1} mol^{-1}]. If the reaction is spontaneous and energy is released $\Delta_R G$ is negative. If the reaction require energy the sign switches to positive. The same applies for the reaction enthalpy $\Delta_R H$. For a better visualization, the reaction coordinate for the hydrogen chemistry in an electrolyzer ($0 < \Delta_R G$) and a fuel cell ($0 > \Delta_R G$) is shown in **Figure 2-3**.

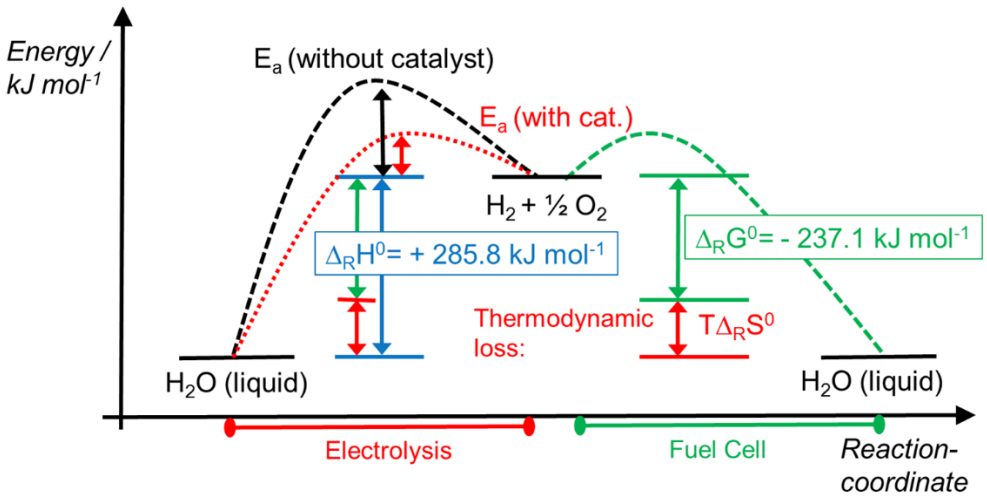

Figure 2-3: Reaction coordinate for water electrolysis and hydrogen back transformation in a fuel cell at standard conditions

Starting from liquid water, at least + 285.8 kJ are necessary to split one mole water into hydrogen and oxygen. The activation energy E_a is the additional energy that needs to be applied to run the reaction and can be varied due to different catalyst materials. Novel and efficient catalysts are important to decrease the activation energy E_a of such reactions. The overall goal for an efficient catalyst is the reduction of E_a to a minimum and run the reaction close to the thermodynamic limits. In contrast, only - 237.1 kJ mol^{-1} are released from the recombination of H_2 and O_2 or more specifically can be gained in form of useful mechanical or electrical work in a fuel cell at standard conditions. The term T $\Delta_R S$ are the thermodynamic heat losses. Consequently, the free enthalpy $\Delta_R G$ = - 237.1 kJ mol^{-1} gives the maximum work that can be extracted from that system. It is defined as

$$\Delta_R G = -RT \ln K \qquad (2\text{-}3)$$

Where R = 8.314 J mol^{-1} K^{-1} is the gas constant, T is the temperature in [K] and K is the equilibrium constant of the reaction. The electrical work w_{el} in [Wh] is expressed as:

$$w_{el} = I \cdot E \cdot t = Q \cdot E \qquad (2\text{-}4)$$

Where I is the current [A], E is the potential [V] and t is the time [s]. Michael Faraday discovered the quantitative relation of electrical charge and the amount of substance:

$$Q = n \cdot z \cdot F \qquad (2\text{-}5)$$

where Q is the total charge [C], n is the amount of substance [mol], z is the transferred electrons and F is the Faraday constant with 96485.3 s A mol^{-1}.

Combining Formula (2-3) with Faraday's law (equation (2-5)) results into the relation:

$$w_{el} = -zFE \tag{2-6}$$

where the energy or electrical work w_{el} can be related to a potential E [V]. Considering the free energy as the maximum electrical energy gained the potential E^0 could be calculated according to the formula (2-7):[47]

$$E^0 = -\frac{\Delta_R G}{z \cdot F} \tag{2-7}$$

Where $\Delta_R G$ is the free enthalpy, z are the electrons transferred and F is the Faraday constant with 96485.3 s A mol^{-1}. This potential E^0 is called standard electrode potential of the reaction and defines the thermodynamic equilibrium potential of the reaction at standard conditions. Vice verse to $\Delta_R G$, if $E^0 > 0$, then the reaction is spontaneous (galvanic cell/fuel cell) and if $E^0 < 0$, then the reaction is nonspontaneous (electrolytic cell). In case of water splitting ($\Delta_R G = +237.1\ kJ\ mol^{-1}$) E^0 is about -1.23 V, which means that the reaction is nonspontaneous and the electrolyzer cell ideally requires a potential difference of +1.23 V (cf. equation (2-8) in *chapter 2.2.2 Fundamental kinetics of hydrogen chemistry*).

Replacing the free enthalpy with the reaction enthalpy $\Delta_R H$ ($+285.8\ kJ\ mol^{-1}$) that includes the thermodynamic proportion, the electrolyzer cell requires a potential difference of +1.48 V. At standard temperature and pressure, this is called the higher heating voltage and coincides with the thermo-neutral voltage (or potential). This potential represents the value, at which heat is neither accepted nor rejected by the water splitting process, as the Gibbs free energy in form of electrical energy matches the required overall enthalpic energy to generate humidified hydrogen and oxygen gas [48]. In other words, this potential is required to split water maintaining a constant temperature. If the potential of the electrolyzer cell is below +1.48 V the reaction is endothermic and the system cools down. If the potential is above +1.48 V the process is exothermic and the temperature of the cell will increase. The relation between temperature, cell potential and energy is exemplary shown in Figure 2-4.

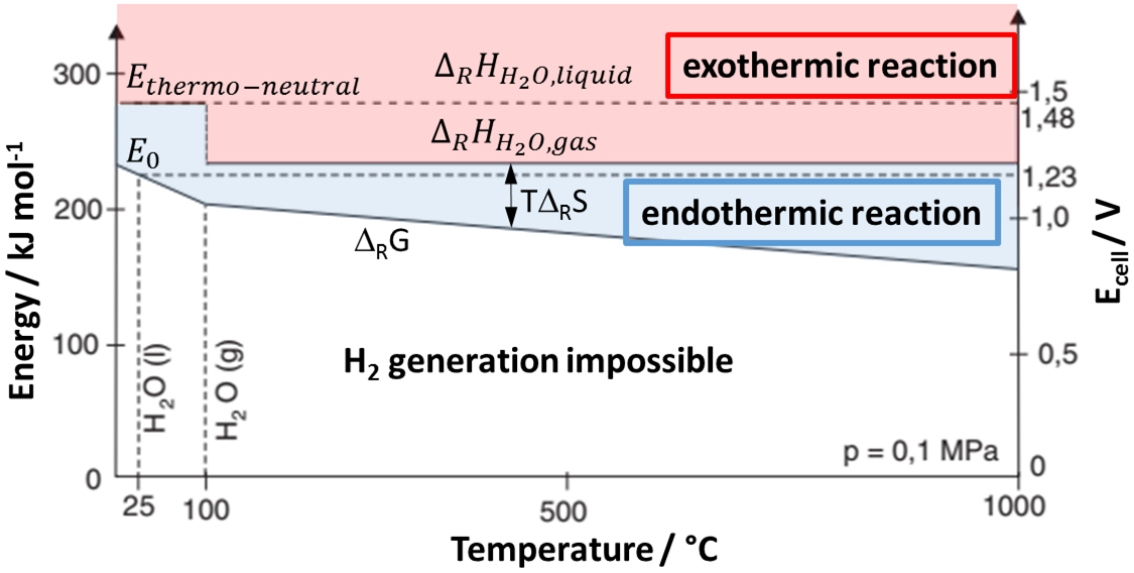

Figure 2-4: Temperature dependence of water electrolysis at standard pressure (Reprinted and modified from [47]). For simplicity, the temperature dependency of the reaction enthalpy $\Delta_R H$ and the corresponding cell potentials are represented by straight lines. A detailed relation at untypical conditions can be found in [48].

For simplicity, the temperature dependency of the reaction enthalpy $\Delta_R H$ and the corresponding cell potentials are represented by straight lines. A detailed relation of enthalpies, thermo-neutral voltage, higher heating voltage, enthalpic voltage at conditions which are not typical (e.g. high temperatures, high pressures, high electrolyte concentrations) can be found in reference [48]. Here, the top line represents the standard reaction enthalpy $\Delta_R H$ = +285.8 kJ mol^{-1} equal to the cell potential of +1.48 V which is at standard conditions also the thermo-neutral voltage and higher heating voltage. At 100 °C the reaction enthalpy drops to +241.83 kJ mol^{-1} due to the phase transition from liquid to gaseous water. This two reaction enthalpies are tantamount with the higher heating value (HHV) and the lower heating value (LHV) depending on the state of the original and generated water. The HHV refers to the heat released from the fuel combustion with the original and generated water in a condensed state while the lower heating value (LHV) refers to water in a gaseous state.[49]

The bottom line represents the free enthalpy $\Delta_R G$ of the system that strongly decreases with increasing temperature. Below this line the hydrogen generation becomes impossible. Typical cell efficiencies are related to the minimal energy that can be extracted from that system or are necessary to produce one mole at standard conditions and the difference between $\Delta_R G$ and $\Delta_R H$ is expressed by $T\Delta_R S$.

Accordingly, the minimal cell potential to split one mole of H_2O at standard conditions is about +1.23 V. At this potential the reaction is in any case endothermic and the cell cools down. Correspondingly, at cell potentials above +1.48 V the reaction is exothermic and the cell needs cooling.

This subchapter described the necessary thermodynamic background information of water splitting and the fuel cell reaction at standard conditions. It indicated the requirement for efficient electro-catalysts that run the reaction close to the thermodynamic limits. Finally, this subchapter introduced the minimal potential necessary to split one mole of water (+1.23 V at standard conditions) and the corresponding thermo-neutral potential (+1.48 V at standard conditions) and related the reaction enthalpies with the higher and lower heating values.

2.2.2 Fundamental kinetics of hydrogen chemistry

Seeking for more efficient catalysts, also the kinetics of the reaction needs to be discussed, since catalysts can directly influence the reaction pathway and simultaneously reaction kinetics, as it was already indicated by the activation energy E_a in Figure 2-3 (*chapter 2.2.1 Fundamental thermodynamics of hydrogen chemistry*). The goal in catalyst research is to proceed reactions close to their thermodynamic limits and maximize the kinetic reaction. This could be enabled by highly efficient catalysts. To maximize the efficiency in an electrolyzer or in a fuel cell it is important to understand the reaction mechanisms first.

In general, the electrochemical redox reactions in electrolyzers and fuel cells split into two electrode reactions, while the overall cell potential is calculated by

$$E^0_{cell} = E^0_{cathode} - E^0_{anode} \qquad (2\text{-}8)$$

Figure 2-5 gives an exemplary sketch of the redox reaction of a water electrolyzer and a fuel cell in alkaline media. The hydrogen evolution reaction (HER) consists of a two electron mechanism. In contrast, during the oxygen evolution reaction (OER) four electrons are transferred. In a fuel cell the direction of the reactions are simply reversed and the hydrogen electrode become the anode with the hydrogen oxidation reaction (HOR) and the oxygen electrode become the cathode with the oxygen reduction reaction (ORR). The double number of electrons in the oxygen redox chemistry complicates the proceeding reaction. Hence, the oxygen electrode became the prominent bottleneck in water splitting and fuel cell research. Accordingly, both electrodes cause energy losses, resulting in higher potentials that needs to be applied compared to the thermodynamic standard potentials (cf. *chapter 2.2.1 Fundamental thermodynamics of hydrogen chemistry*).

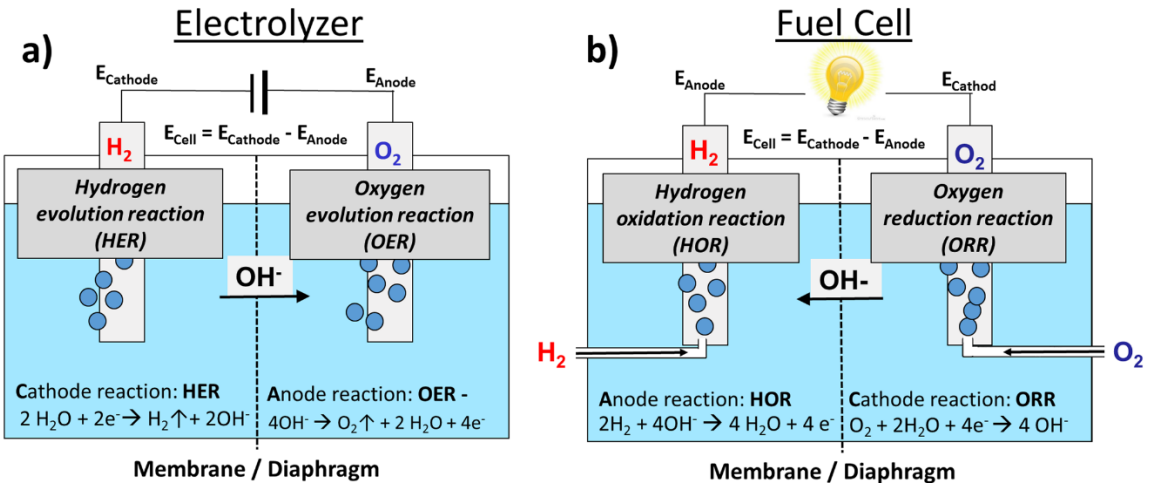

Figure 2-5: Sketch of electrochemical cells with the corresponding electrode reactions in alkaline media (a) electrolyzer and (b) fuel cell

The difference between standard potential and applied potential is called overpotential and is noted as η. The thermodynamic standard potentials represents the case for a reaction in equilibrium only. In case of a proceeding reaction that is comparable to a running current in an electrochemical reaction, the energy losses or overpotentials become larger. The trend for the current [A] or current density [A cm^{-2}] for increasing overpotential is described by exponential Butler-Volmer equation (Formula (2-9)).

$$j = j_0 \cdot \left\{ exp\left[\frac{\alpha_a \cdot z \cdot F}{R \cdot T} \cdot \eta \right] - exp\left[-\frac{a_c \cdot z \cdot F}{R \cdot T} \cdot \eta \right] \right\} \qquad \textbf{(2-9)}$$

Where j_0 is the exchange current density in [A m^{-2}], α_a is the anodic charge transfer coefficient, a_c is the cathodic charge transfer coefficient, z is the number of electrons involved in the electrode reaction , F is the Faraday constant [96485.33 C mol^{-1}], R is the universal gas constant [8.314 J mol^{-1} K^{-1}], T is the temperature [K] and η is the overpotential in [V]. Following the Butler-Volmer relation, an exemplary UI - diagram for an electrolyzer and a fuel cell including the corresponding overpotential is shown in Figure 2-6.

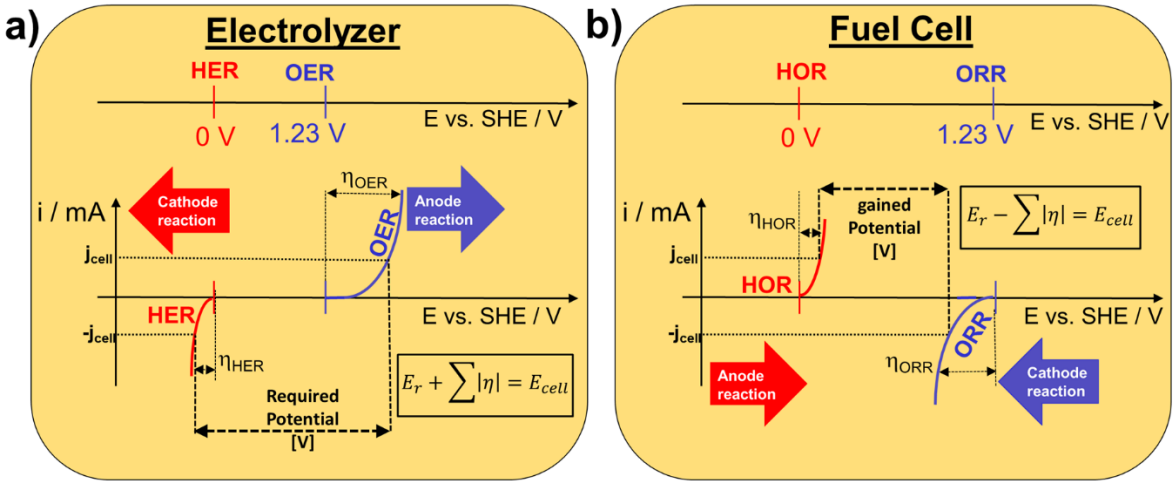

Figure 2-6: Potential scheme related to the standard hydrogen electrode (SHE) for (a) electrolyzer and (b) a fuel cell

In general, each electrode contribute to the energy loss. The overpotential for the ORR and the OER are higher compared to the hydrogen electrode reactions due to the sluggish kinetics. While in the electrolyzer the required potential is the sum of the thermodynamic potential and the additional overpotentials, for the fuel cell the overpotential needs to be subtracted from the standard potential as indicated in Figure 2-6 by the notation "gained potential". Additional, the overall resistance of the cell has a big impact to the total cell potential. This is described as IR-drop. Finally, the cell potential can be described as shown in Formula (2-10):

$$E_{cell} = \Delta E_{electrode} + \sum \eta + iR_{cell} \qquad (2\text{-}10)$$

While iR_{cell} is called as IR-drop, which results from the overall resistance of the system, $\sum \eta$ is the sum of all intrinsic overpotential losses. The goal of the catalyst research is the reduction of the kinetically induced overpotential.

This chapter introduced the first details about the fuel cell and electrolysis reaction mechanisms. It further introduced the Butler-Volmer reaction as the description for the kinetics of an electrochemical reaction and brought the context into a relation for an electrolyzer and a fuel cell. The next chapter will have a stronger focus on the oxygen electrode mechanism, which is the prominent bottleneck in fuel cell and electrolyzer research and will describe the details in greater depth.

2.2.3 Oxygen electrode chemistry

As already indicated the oxygen electrode chemistry holds the highest potential for improving the cell efficiency. The oxygen electrode in water electrolysis or the fuel cell reaction is still under a massive spotlight for catalyst research, since the sluggish four electron transfer causes high-energy losses. One of the most accepted reaction mechanism for the HER and the OER on oxides in alkaline media are given in the following reactions:[50]

Cathode (alkaline):

$$2H_2O + 2e^- \rightarrow 2OH^- + H_2 \quad (2\text{-}11)$$

Anode (alkaline):

$$4OH^- \rightarrow HO^* + 3OH^- + e^- \quad (2\text{-}12)$$

$$\rightarrow O^* + H_2O + 2OH^- + 2e^- \quad (2\text{-}13)$$

$$\rightarrow HOO^* + H_2O + OH^- + 3e^- \quad (2\text{-}14)$$

$$\rightarrow O_2 + 2\,H_2O + 4e^- \quad (2\text{-}15)$$

It is important to mention that the fuel cell reaction involves the same intermediates that are proposed for the electrolysis. For this work the alkaline electrolyte and in special case the oxygen electrode is of major interest, but in the following discussion the acidic case is taken as exemplary. The mechanism for the acidic media is proposed as follows:[50]

Cathode (acidic):

$$2H^+ + 2e^- \rightarrow H^* + H^+ + e^- \rightarrow H_2 \quad (2\text{-}16)$$

Anode (acidic):

$$2H_2O \rightarrow HO^* + H_2O + H^+ + e^- \quad (2\text{-}17)$$

$$\rightarrow O^* + H_2O + 2H^+ + 2e^- \quad (2\text{-}18)$$

$$\rightarrow HOO^* + 3H^+ + 3e^- \quad (2\text{-}19)$$

$$\rightarrow O_2 + 4H^+ + 4e^- \quad (2\text{-}20)$$

It is conspicuous that the proposed intermediates in both environments remain the same for the anodic reaction. The three main intermediates of the oxygen evolution reaction are HO^*, O^*, HOO^*. Due to theoretical considerations the intermediate binds with different free energies to

the catalyst surface. The free binding energies of an ideal catalyst of the three intermediates at 0 V and at 1.23 V are shown in Figure 2-7a.

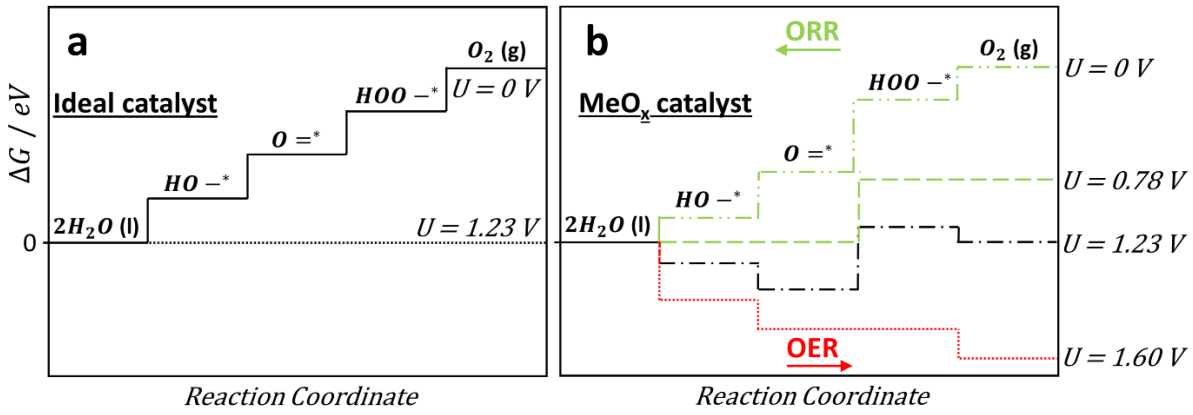

Figure 2-7: The water splitting reaction from left to right and the oxygen reduction reaction from (right to left) at (a) 0 V and at 1.23 V for an ideal catalyst and (b) for an exemplary metal oxide (MeO_x) catalyst (Figure was inspired by [50])

Starting with the OER from the left to the right, water is illustrated as the ground state at 0 eV. Each following step increases the binding energy for the expressed intermediates finally resulting in O_2. Figure 2-7a presents an ideal catalyst so that at 0 V each energy difference for any intermediate perfectly matches with the former. The necessary potential to remove the protons and electrons is predefined by the difference in free energy between the reaction intermediates. At the thermodynamic minimal OER potential 1.23 V, the energy difference becomes a straight line at 0 eV. For a reaction taking place, all steps have to be downwards. In comparison, in Figure 2-7b the free energies of a realistic metal oxide catalyst is presented, showing an upward free energy difference for the intermediate *-OOH at 1.23 V. Consequently, this intermediate represents the potential determining step. As a result, the potential is increased to 1.6 V so that all steps are downhill in free energy. The objective of catalyst research is the reduction of the free energy difference for each intermediate step resulting in a reaction taking place close to the thermodynamic limits. This is done by changing the catalyst material and likewise changing the free binding energy of the intermediate at the catalyst surface. Unfortunately, the binding energies of the different intermediates cannot be varied independently. In fact, the binding energies of similar intermediates scale with each other, which is known as scaling relations.[50-52] Accordingly, the two OER intermediates *-OH and *-OOH interact in a similar way with any catalyst surface, which limits the activity of even the best performing catalyst.[53]

Using the binding energy for intermediates as descriptor for the activity typically results in a volcano curve. This is also known as the Sabatier principle.[54] For the OER activity, the energy of the second step from *-OH to *=O is a suitable descriptor due to the linear scaling relation between *-OH and *-OOH. Thus, this single descriptor can describe the potential-determining step for both strong and weak binding catalysts towards the OER. This is presented in Figure 2-8a.

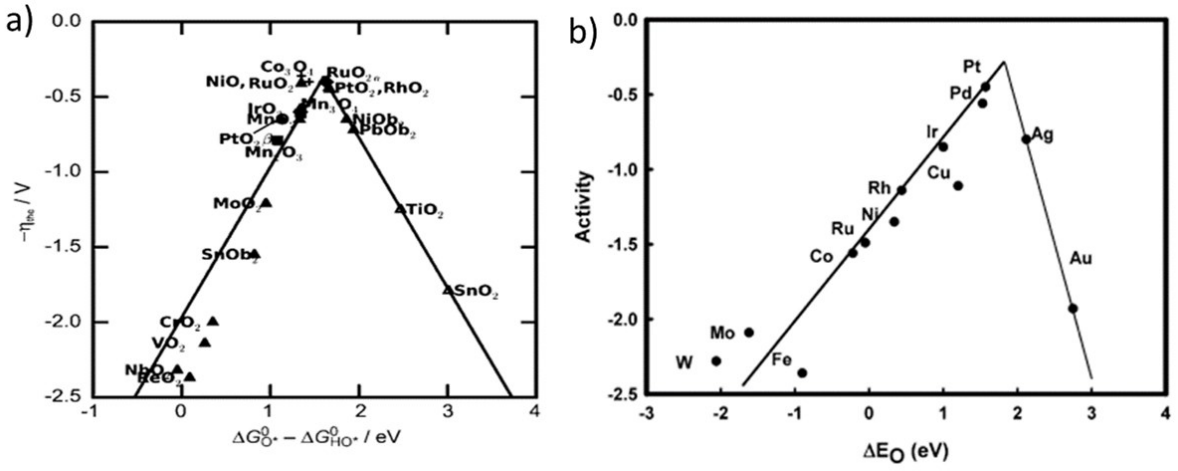

Figure 2-8: (a) Activity trends towards oxygen evolution, for rutile, anatase, Co_3O_4, Mn_xO_y oxides. (Reprinted with permission from [52]. Copyright 2011 John Wiley & Sons) (b) Trends in oxygen reduction activity (Reprinted with permission from [55]. Copyright 2004 American Chemical Society)

For catalyst surfaces that bind too strongly, the overpotential originates from breaking a bond between the intermediates and the surface. For surfaces that bind too weakly the overpotential is related to bonds forming to the surface. The most suitable catalyst is located at the top of this volcano curves.[53] Vice versa, the most suitable descriptor for the ORR is the Oxygen adsorption *-O, since each intermediate scales linearly with the oxygen binding energy.[56] This is shown in Figure 2-8b. Important to mention, even though the scaling relations and the volcano plots are highly restricting with overpotentials far from the thermodynamic limits the group of Rossmeisl postulates approaches going beyond this volcano plots and bypass the scaling relations by introducing so called “special active sites” [57, 58]. This modified active sites consists of 3D sites which would make different intermediate binding energies possible. Different approaches to circumvent scaling relations are shown in Figure 2-9.

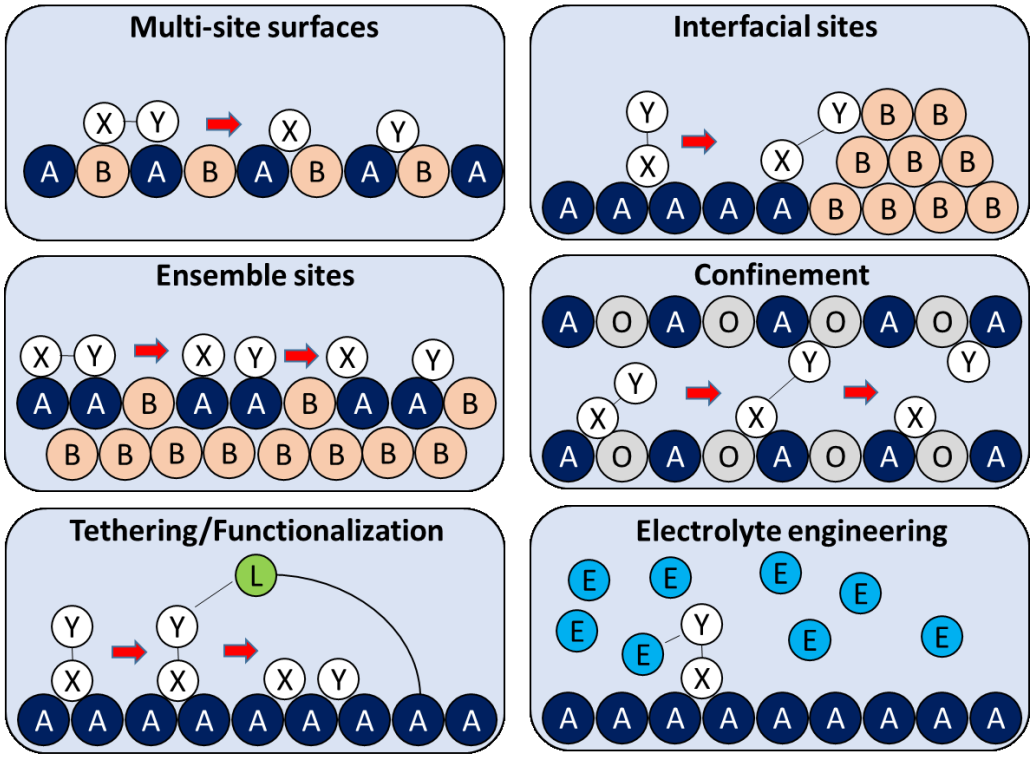

Figure 2-9: Different approaches to circumvent the scaling relations. Inspired from [59-61]

The different approaches include material tuning as well as modifications of the environment, like electrolyte engineering that realize different binding energies at sites close to each other. Consequently, it should be possible to modify the active site by using 3D modifications to go beyond the volcano plot. Every approach could theoretical circumvent scaling relations, even though, it is not sure if it's experimentally possible. Multi-site surfaces, interfacial sites and ensemble sites seem to be the most realistic approaches, since confinement by realizing those 3D active site layers seems most challenging. In this context it should also be possible to develop a bifunctional catalyst material that is active for the OER and the ORR having multi-sites with adjusted binding energies for both reactions. A bifunctional catalyst could enable new possibilities in future device design in a hydrogen based economy. For example, loaded with solar panels cars could be filled with water and produce hydrogen during parking. Additionally, it would further enable new space savings in aerospace.

This subchapter focused on the oxygen electrode chemistry in a fuel cell and electrolyzer, since the energy losses at the hydrogen electrode are comparably small, and showed the important proposed mechanism and kinetics of the oxygen electrode chemistry. It presented the Sabatier principle and showed the first classification and descriptors for a catalyst in a fuel cell and in an electrolyzer and introduced the limiting scaling relations. Several approaches to circumvent

this scaling relations are shown and suggested for a preparation of a bifunctional oxygen electrode catalyst. The set-up of electrolyzer, fuel cells and a unitized regenerative fuel cell are shown in the next chapter.

2.2.4 Device concept: Electrolyzer, Fuel Cell, Unitized Regenerative Fuel Cells

While Trostweijk and Daiman started with just a simple electrolysis set-up, using a U shaped glass tube with enclosed gold wires as electrodes, today's electrolyzer concepts are much enhanced version. The first commercial electrolyzers, which are almost still state of the art electrolyzers, are based on Nickel electrodes used in highly alkaline (37 wt% KOH) electrolyte and asbestos as separator. Still, today's set-up for a polymer electrolyte membrane electrolyzer, fuel cells or unitized regenerative fuel cell (URFC) resembles the design of yore. This set-up is exemplary shown in Figure 2-10.

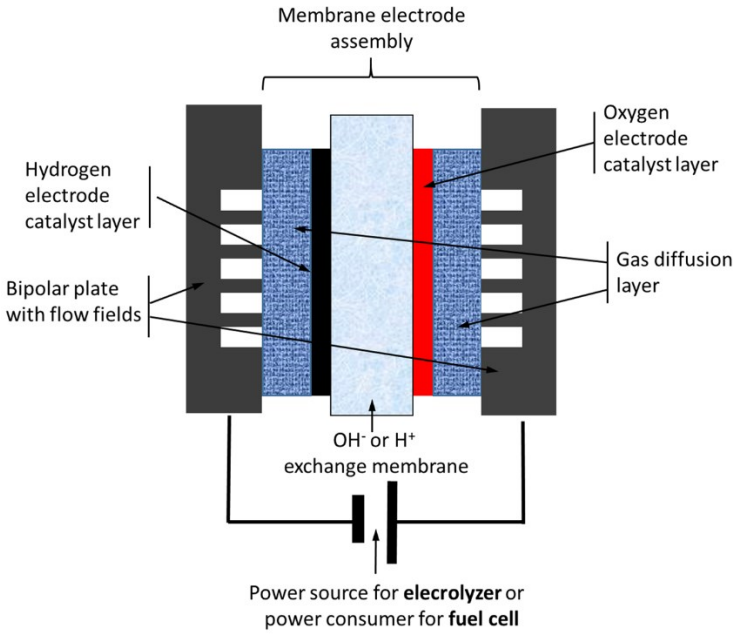

Figure 2-10: Exemplary sketch of a polymer exchange membrane electrolyzer or a fuel cell in a zero gap configuration

At the outside typically the endplates are equipped with bipolar plates which has so called flow channels for an optimal transport of gas and liquids. Flow channels can have different geometries. The most popular are serpentines and parallel configurations. While for fuel cells bipolar plates consists of graphite, electrolyzers have anodic bipolar plates made typically from titanium. The reason for this is the carbon corrosion happening at high anodic potentials.

Reaction (2-21) and (2-22) show the corresponding reactions with their thermodynamic standard potential:

$$C + H_2O \rightarrow CO_2 + 4\,H^+ + 4e^-\,, E^0 = 0.207\,V_{SHE} \qquad (2\text{-}21)$$

$$C + H_2O \rightarrow CO + 2\,H^+ + 2e^-\,\,, E^0 = 0.518\,V_{SHE} \qquad (2\text{-}22)$$

The rate of carbon corrosion up to a standard potential of 1.0 V_{SHE} is however negligible.[62-65] But at electrolyzer relevant potentials about 1.7 – 2.5 V_{SHE} the carbon corrosion is taking place. Thus, the anodic carbon materials are replaced with corrosion resistant but conductive metals like titanium. This also applies for the gas diffusion layer (GDL) also called porous transport layer (PTL). While in fuel cells typically a PTFE coated carbon cloth with a microporous layer is used, in electrolyzers metal meshes are used at the anode to avoid anodic carbon corrosion. In the middle the ion exchange membrane is located. Ion exchange membranes are distinguished between proton exchange membranes (PEM) and anion exchange membranes (AEM). Current PEMs are much better developed compared to current AEM (see also the discussion in *chapter 7.1.2 Reversible seawater electrolyzer: Membrane*). At each side of the membrane a catalyst layer is situated, each layer specialized for the desired reaction.

In contrast to industrial used alkaline electrolyzers, PEM-electrolyzers and fuel cells use ion exchange membranes. This enables a so called zero-gap configuration that enable a reduction of the overall resistance of the cell, which usually causes high energy losses equal to the IR-drop (see *chapter 2.2.2 Fundamental kinetics of hydrogen chemistry*). In this context, each cell component of fuel cells and electrolyzers cause an additional resistance to the total cell resistance. The sum of all resistances is given by Formula (2-23).

$$R_{total} = R_{electric} + R_{anode} + R_{bubble,O2} + R_{ions} + R_{membrane} + R_{bubble,H2} + R_{cathode} \qquad (2\text{-}23)$$

The research goal of electrolyzer and fuel cells is the reduction of all cell resistances to a minimum, which simultaneously minimize the cell performance losses. These resistances are classified into three categories. The first electrical resistance is dependent on the external circuit, the second is the reaction resistance which belong to the electrode resistance influenced by the overpotential of the catalyst for the corresponding reaction at the surface. The third transport resistance originates from the partial coverage of the electrode by gas bubbles so that the contact between electrode and electrolyte separates.[66] Also, R_{ion} belongs to this last group

and is given by the conductivity of the electrolyte. Closely related is the resistance of the membrane $R_{membrane}$, which is given by the membrane conductivity by itself.

Each of these resistances can be tackled by different approaches. The electrical resistance can be easily optimized by improved electrical contacts. One of the most important resistances, the reaction resistance, is optimized by the specified catalyst. The catalyst presets the reaction efficiency, the overpotential of the reaction and all kinetic limits. The optimization of catalysts is one of the most important topics in electrolyzer or fuel cell research. The transport resistance can be optimized by higher ion concentration or better membranes. Overall, the approaches to improve the energy efficiency of water electrolyzers must involve the understanding of these resistances so as to minimize them.*[66]*

This subchapter briefly presents the set-up of current membrane based electrolyzer, fuel cells and reversible electrolyzers and discuss specific material selection to overcome known carbon corrosion. It further introduced electrical resistances occurring in these devices and highlights the importance of reducing the resistances to increase overall cell efficiency.

2.3 Seawater Electrolysis

As already mentioned, common water electrolyzers use highly purified freshwater (see *chapter 1.4 Global distribution of renewable energy potential and freshwater*). This purified water is then either alkalinized for alkaline electrolysis or directly used in PEM electrolyzers. Seawater represents with oceans 96.5 % of the total water occurrence on earth. Further, it is an almost unlimited resource so that it would be desirable to utilize this reserve. Since current electrolyzers split highly purified freshwater only, the major problem of seawater are their interfering ions. Although the composition of seawater varies dependent on the region, the overall average salt concentration is estimated to be 3.5 wt% with a pH~8.[67-70] An overall mean composition of seawater is shown in Table 2-1.

Noticeable are the great shares of Na^+ and Cl^- so that 0.5 M NaCl solution appears as a good adoption for natural seawater. Supporting this, mainly the chlorine chemistry is a serious competitor to the OER since their thermodynamic potentials are very close.

Table 2-1: Standard mean chemical composition of seawater (Taken from [71])

Species	Concentration in [mol / kg H_2O]	Concentration in [g / kg H_2O]
Cl^-	0.56576	20.0579
SO_4^{2-}	0.02927	2.8117
Br^-	0.00087	0.0695
F^-	0.00007	0.0013
Na^+	0.48616	11.1768
Mg^{2+}	0.05475	1.3307
Ca^{2+}	0.01065	0.4268
K^+	0.01058	0.4137
Sr^+	0.00009	0.0079
$B(OH)_3$	0.00033	0.0204
$B(OH)^{4-}$	0.00010	0.0079
CO_2*	0.00001	0.0004
HCO^{3-}	0.00183	0.1117
CO_3^{2-}	0.00027	0.0162
OH^-	0.00001	0.0002

Accordingly, Dionigi et al. presented a pourbaix diagram based on the anodic seawater electrochemistry as shown in Figure 2-11.[72] The main reactions are the chlorine evolution reaction (ClER) at low pH and the hypochlorite formation at high pH. The related reactions with their thermodynamic standard potential are shown in the following reactions:

Chlorine evolution reaction (ClER):

$$2Cl^- \rightarrow Cl_2 + 2e^-_2 \quad ; E^0 = 1.36 \text{ V vs. SHE at pH 0} \quad (2\text{-}24)$$

Hypochlorite formation:

$$2Cl^- + 2OH^- \rightarrow ClO^- + H_2O + 2e^- \quad ; E^0 = 0.89 \text{ V vs. SHE at pH 14} \quad (2\text{-}25)$$

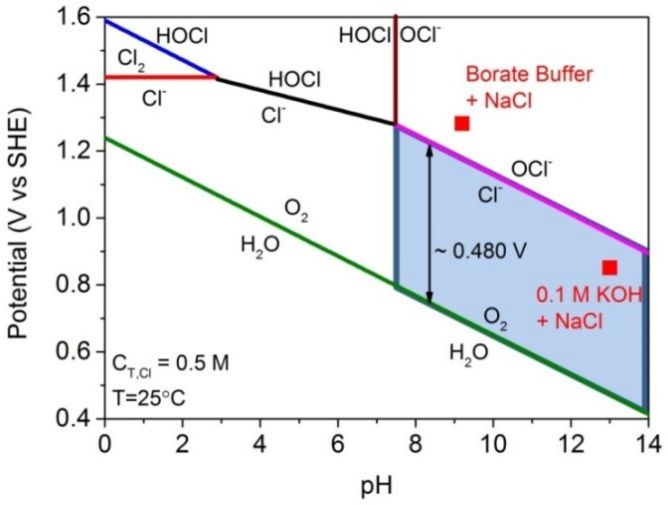

Figure 2-11: Pourbaix diagram of oxygen evolution reaction and chloride chemistry. [Picture taken with permission from [72]. Copyright 2016 John Wiley and Sons]

In contrast to the $4e^-$ transfer reaction of the OER the chloride chemistry involves only $2e^-$. Even though the thermodynamic favors the OER the kinetics are much faster for the chloride reactions, which lead to smaller overpotentials. Consequently, the difference of the thermodynamic potential of the OER and the chloride chemistry should be maximized. At low pH the difference of ClER (E^0 = 1.36 $V_{SHE\ at\ pH\ =\ 0}$) and OER (E^0 = 1.23 $V_{SHE\ at\ pH\ =\ 0}$) is smallest with only $\Delta E_{ClER\text{-}OER}$ = 130 mV. At higher pH values the difference becomes larger since the ClER is pH independent. But at pH 3 the formation of hypochlorous acid starts followed by the hypochlorite formation at roughly pH 7.5. Unfortunately, these reactions are pH dependent so that the potential difference will not increase with even higher pH value. The maximum potential difference of ΔE = 480 mV is shown at the alkaline hypochlorite formation at pH > 7.5. Based on this, high pH values facilitates the selective splitting of seawater into H_2 and O_2. In conclusion, the design criteria for a selectively working seawater electrolyzer is the limitation of the working potential below 1.72 V_{RHE} and a pH value higher than 7.5.

This subchapter presented the design criteria for the selective seawater oxidation. Accordingly, the selective formation of oxygen is favored in alkaline media with pH > 7.5, where the standard potential difference between chloride and oxygen chemistry is maximized and the OER thermodynamically starts first. Hence, the design criteria for a selective working seawater electrolyzer is the limitation of the working cell potential below 1.72 V_{RHE} and a pH value higher than 7.5.

2.4 Summary of chapter 2

The high cost of electricity and the capital cost of current hydrogen technology, are the reasons for a non-appearance of widespread hydrogen economy, yet. To combat the problems remain quiet challenging. But a reduction of electricity prices and efficiency improvement by using novel electro-catalysts based on cheap and abundant materials could face current problems and strive the path for a sustainable energy future. Accordingly, this chapter introduced the first details about the fuel cell and electrolysis reaction mechanisms. It further introduced the Butler Volmer reaction as the description for the kinetics of an electrochemical reaction and brought the context into a relation for an electrolyzer and a fuel cell. However, this chapter focused on the oxygen electrode chemistry in a fuel cell and electrolyzer, since the energy losses at the hydrogen electrode are comparably small, and showed the important proposed mechanism and kinetics of the oxygen electrode chemistry. It presented the Sabatier principle and showed the first classification and descriptors for a catalyst in fuel cells and in electrolyzers and introduced the limiting scaling relations. Several approaches to circumvent this scaling relations are shown and suggested for a preparation of a bifunctional oxygen electrode catalyst. This chapter also briefly presented the set-up of current membrane based electrolyzer, fuel cells and reversible electrolyzers and discuss specific material selection to overcome known carbon corrosion. It further introduced electrical resistances occurring in these devices and highlights the importance of reducing the resistances to increase overall cell efficiency. Finally, this chapter presented the theory about the design criteria for a selectively working seawater electrolyzer. It shows the favored seawater splitting in alkaline media higher than pH of 7.5 where the thermodynamic standard potentials of the OER and chloride chemistry are largest. Hence, the design criteria for a selective working seawater electrolyzer is the limitation of the working cell potential below 1.72 V_{RHE} and a pH value higher than 7.5.

In conclusion, the challenge in catalyst design is always to proceed the reactions close to their thermodynamic limits. As it was shown, different reactions need different catalyst properties. The challenge of this project is to find the suitable catalyst property for two reactions in one catalyst material. In chapter 2.2.3 (*Oxygen electrode chemistry*) a concept of scaling relations and the circumvention of them is presented. This are the tools for the research of this project. The next chapter 3 will give additional detailed experimental descriptions for the experiments used for this thesis research, which are not sufficiently presented in the related publications ***SD I - III*** *[1-3]*.

Chapter 3
Experimental Methods

This chapter describes experimental methods and techniques used in this cumulative work that were not as detailed in the publications. It will give additional technical instructions supported by schemes and photographs. In general, the focus of this work was set to precious metal free catalyst material for the oxygen electrode in reversible electrolyzer. As shown in publications **SD I-IV**[1-4], different precious metal free oxides were prepared using a solvothermal microwave assisted synthesis route, while for Fe-N doped carbons (Fe-N-C) a polyaniline synthesis route was used as presented in **SD II**[2] (*chapter 5*). The materials were characterized by several physico-chemical techniques. Namely, X-ray diffraction (XRD), inductively coupled plasma-optical emission spectroscopy (ICP-OES), transmission electron microscopy (TEM), scatter electron microscopy (SEM) and x-ray absorption (XAS). To study the electrochemical activity, stability and selectivity rotating disk electrodes (RDE), rotating ring disk electrode (RRDE) and an electrolyzer and reversible electrolyzer equipped with an anion exchange membrane (AEM) with preceding membrane electrode assembly (MEA) were applied.

However all techniques and preparation methods are described in the publications, additional information in this chapter are referred to:

- Membrane electrode assembly (MEA)
    - MEA Preparation
    - (reversible) Electrolyzer assembly
    - In-house electrolyzer test station for seawater electrolyzer measurements
    - In-house electrolyzer selectivity measurement using online mass spectrometry (MS)
- 4-probe membrane conductivity measurement
- Preparation of quasi in-situ X-ray absorption samples

3.1 Membrane electrode assembly (MEA) and electrolyzer cell set-up

The preparation of the MEA, the set-up and the MEA measurement is also shown in the corresponding publications. The preparation of a membrane electrode assembly (MEA) consisting of a Tokuyama A201 membrane, 46.7 wt% Pt on Vulcan XC 72R (TKK) as cathode and synthesized NiFe-LDH as anode material is described in **SD III**[3] (*Chapter 6*), while the preparation for a reversible working membrane electrode assembly using 46.7 wt% Pt on Vulcan XC 72R (TKK) as hydrogen and various non-noble materials (e.g. : NiFe-LDH/C and Fe-N-C) as oxygen electrode catalyst is described in **SD II**[2] (*Chapter 5*). Therefore, this chapter will give a more detailed description supported by images.

3.1.1 MEA preparation via spray coating

The MEA's for this work are prepared via a spray coating procedure. For safety reasons, the equipment is kept in a fume hood. Figure 3-1 shows the spray coating set-up including a commercial heated vacuum table and temperature controller (Carbon and FuelCell), a timer, a lamp and a vacuum pump/compressor (Welch 2511).

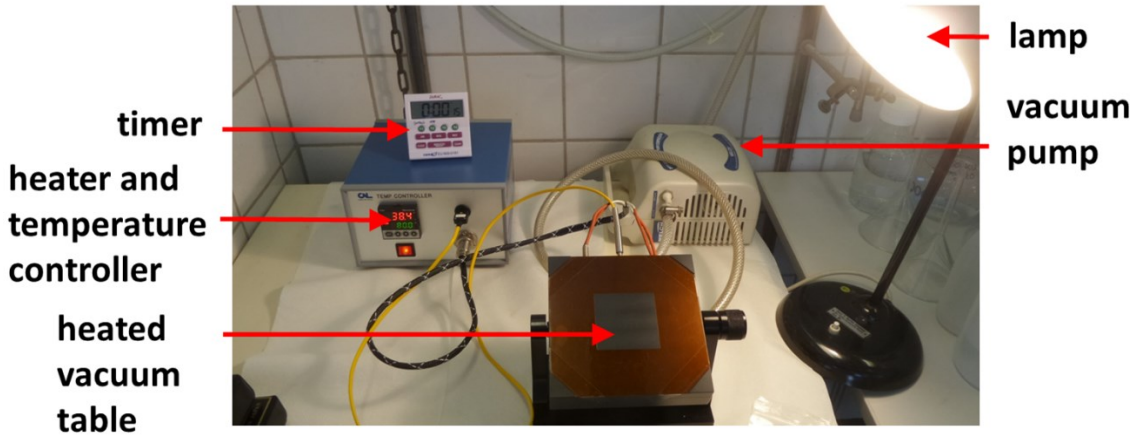

Figure 3-1: Spray coating set-up for preparation of membrane electrode assemblies (MEA)

The dry vacuum pump/compressor and the heat sticks of the temperature controller are connected to the vacuum table that is, dependent on the used membrane, typically heated to 50°C. However, there are other membranes that can resist higher temperatures of up to 120°C as shown for the anion exchange membranes from the group of Holdcroft.[73] The lamp gives a better illumination during the spray coating process. A Kapton® template is placed on top of the vacuum table with a preset space for the membrane and covering the non-used areas of the vacuum table. For a defined catalyst area on the membrane a protection mask with different

areas can be placed on top of the vacuum table. Figure 3-2 shows the protection mask for a 5 cm^2 catalyst area and a Gun Piece SP-2 spray gun (Rich) equipped with a 0.4 mm tip size.

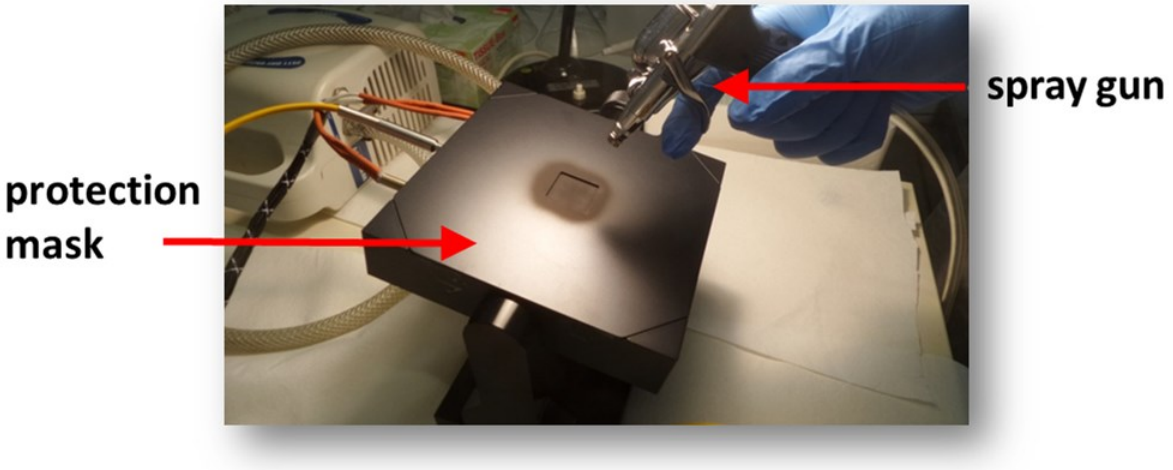

Figure 3-2: Spray coating equipment for defined catalyst area of 5 cm^2

Also, the equipment provides additional protection masks with areas of: 1 cm^2, 10 cm^2 and 25 cm^2. The spray gun operates with a nitrogen gas flow and a pressure of 1-2 bar. Further, the gun is equipped with a predefined ink volume to gain the desired loading.

For ink preparation, 50 mg catalyst, 50 µl ultrapure water (18.2 MΩ cm), 3 ml i-Prop and 460 mg ionomer (5 wt% AS-4, Tokuyama) were ultra-sonicated for 15 min. The resulting catalyst to ionomer ratio is 7:3. Typically, 1 ml for the hydrogen side and 2-4 ml for the oxygen side were spray coated on the membrane. The desired loading were 0.5 mg_{Pt} cm^{-2} for the hydrogen electrode and 1-5 $mg_{cat.}$ cm^{-2} for the oxygen side. Figure 3-3 shows the exemplary MEA preparation procedure using an anion exchange membrane from Fumatech. The total procedure can be divided into 3 steps:

1. Estimation of the constant weight without catalyst
2. Preparation of side A
3. Preparation of side B

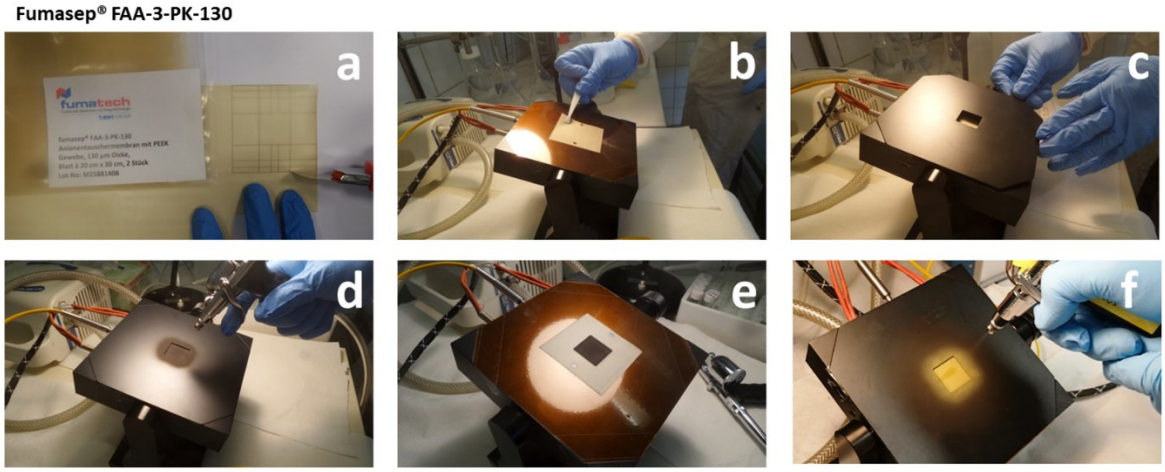

Figure 3-3: Exemplary simplified preparation of a membrane electrode assembly (MEA) using an anion exchange Fumasep® FAA-3-PK-130 membrane: (a) cutting the membrane and using a template (b) attaching the membrane to a heated vacuum table with Kapton® covered sides (c) Covering the unused membrane areas with a mask (d) spray coating the membrane on side A (e) final spray coated side A (f) spray coating side B

1. Estimation of the constant weight without membrane:

a. First the membrane is cut with a scalpel into the right size by using a template that is underneath the membrane (Figure 3-3a). For later protection and storage possibilities, the precisely cut membrane is stored in a small plastic bag.

b. As next step, the membrane transferred from the plastic bag to the heated vacuum table as shown in Figure 3-3b.

c. The membrane is subsequently covered with the protection mask (Figure 3-3c). Then, the temperature of the vacuum table is set to 50 °C. When the set point is reached, the temperature is maintained for another 10 min. For cooling, the temperature controller is switched off for 10 min. Then, the membrane is placed back into the plastic bag and the total weight of the membrane with the plastic bag but without the coating is estimated by using a Sartorius AX224 balance (d = 0.1 mg)

2. Preparation of side A:

d. Although it is not important which side is prepared first, typically the platinum side (or hydrogen side) was prepared first. Accordingly, the unloaded but weighted membrane is placed back on the vacuum table and covered again with the protection mask. Roughly 1 ml of the prepared ink is filled into the reservoir of the spray gun to achieve a loading of 0.5 mg_{Pt} cm^{-2} (Figure 3-3d). The spray coating movement consists of

alternating but continuous sprayed vertical and horizontal serpentines as shown in Figure 3-4. The turning point is outside of the desired area to avoid inhomogeneous catalyst coating at the edges. When the ink is depleted, the temperature (50°C) is maintained for 10 min. Then, the temperature controller is switched off and the membrane is cooled down for another 10 min.

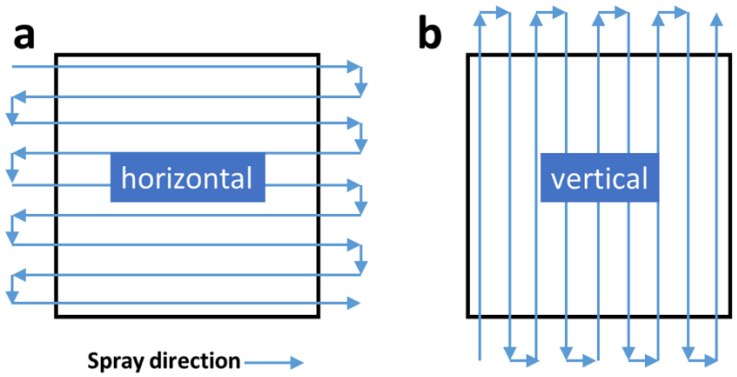

Figure 3-4: Exemplary sketch of spray coating procedure

e. As next step, the protection mask is removed revealing the catalyst coated membrane (Figure 3-3e) which is placed back into the plastic bag. The fresh coated membrane with the bag is weight again. To estimate the loading, the first value of the unloaded membrane is subtracted from the coated value. Based on the ink (ionomer and catalyst content) an additional Table 3-1 helped for the direct catalyst load estimation. If the desired load is to low another layer of ink is spray coated on the membrane accordingly.

Table 3-1: Estimation table for the Pt loading of the hydrogen side based on the typical ink recipie (46.7 wt% Pt/C, (catalst:ionomer) = (7:3)) used for this thesis and a catalyst area of 5 cm^2

Pt loading [mg_{Pt} cm^{-2}]	$m_{cat.}$ on 5 cm^2 [$mg_{cat.}$]	$m_{cat.+ionomer}$ on 5 cm^2 [$mg_{cat.+ionomer}$]
0.1	1.1	1.5
0.2	2.1	3.1
0.3	3.2	4.6
0.4	4.3	6.1
0.5	5.4	7.6

3. Preparation of side B.

f. After successful coating of side A side B is coated analogous (Figure 3-3f). Important is the right fit of the membrane to precisely coat side B on the counterpart as shown in Figure 3-5. Typically coatings for the oxygen side are between 1-5 mg_{cat} cm^{-2}. For practical estimation Table 3-2 gives the defined numbers.

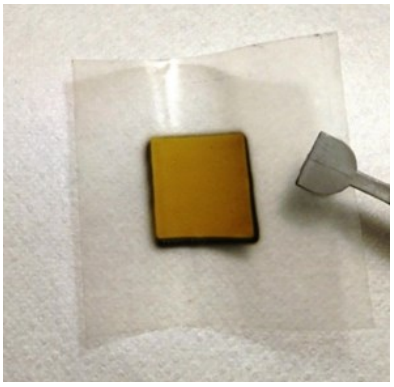

Figure 3-5: Final catalyst coated membrane with Pt/C catalyst on side A and NiFe-LDH on side B

Table 3-2: Estimation table for the catalyst loading of the oxygen side based on the typical ink recipie ((catalst:ionomer) = (7:3)) used for this thesis and a catalyst area of 5 cm^2

Catalyst loading [mg_{Pt} cm^{-2}]	$m_{cat.}$ on 5 cm^2 [$mg_{cat.}$]	$m_{cat.+ionomer}$ on 5 cm^2 [$mg_{cat.+ionomer}$]
0.1	0.5	0.7
0.2	1	1.4
0.3	1.5	2.1
0.4	2	2.9
0.5	2.5	3.6
1	5	7.1
2	10	14.3
3	15	21.4
4	20	28.6
5	25	35.7

The final coated membrane can directly assembled in the electrolyzer or reversible electrolyzer cell as shown in the next chapter.

3.1.2 (Reversible) electrolyzer cell assembly cell set-up

A commercial available (reversible) electrolyzer cell (Carbon and FuelCell) was used for testing the MEA. Figure 3-6 shows an exemplary manual for the typical assembly of a (reversible) electrolyzer cell in detail.

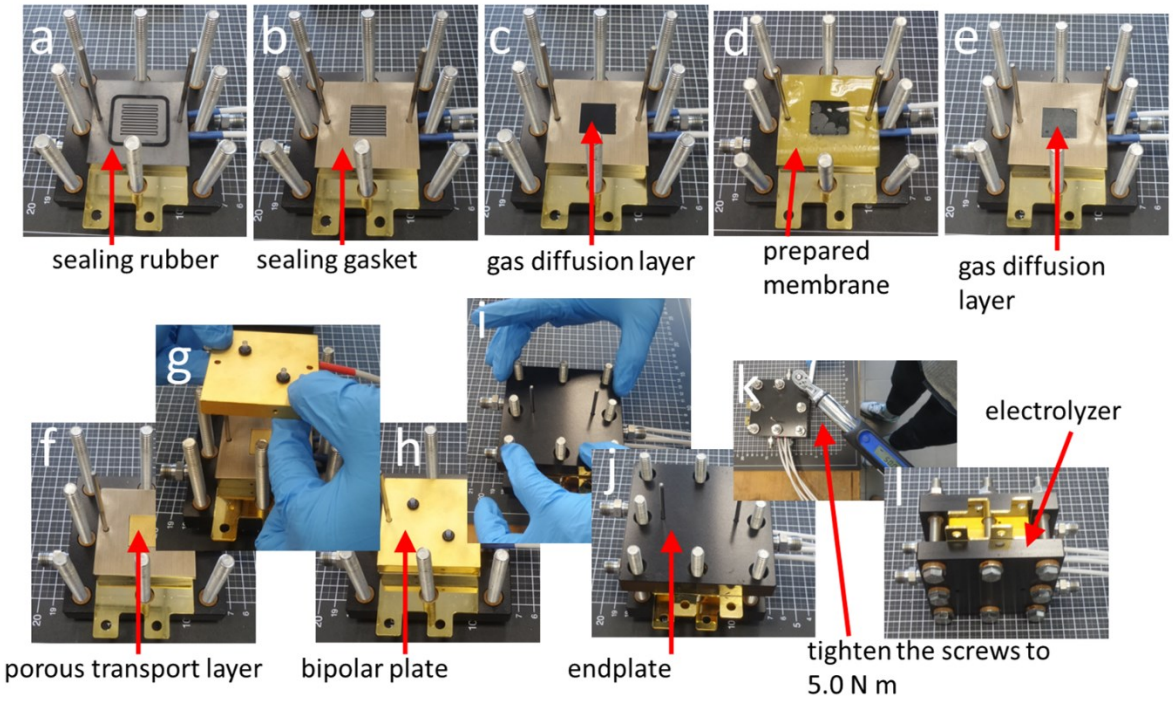

Figure 3-6: Exemplary manual for the assembly of a (reversible) electrolyzer cell

The electrolyzer is assembled layer by layer. For simplification, two removable rods help the accurate stacking of each component (Figure 3-6).

a. First, the endplate then the current collector and the bipolar plate equipped with flow channels are plugged together (Figure 3-6a). An additional sealing gum (Carbon and FuelCell) is place directly on the provided notch.

b. A precisely cut gasket (Carbon and FuelCell, 250 µm) is placed on the bipolar plate.

c. A gas diffusion layer (GDL) (Sigracet® 10BC) is placed in the gap of the gasket

d. The catalyst coated membrane is placed on the gasket

e. Another gasket is placed on the membrane

f. A gold coated titanium mesh used as porous transport layer (PTL) from Carbon and FuelCell is placed in the gap of the gasket

g. The second bipolar plate with the sealing rubber is placed on the gasket and PTL

h. It is important to double check that the bipolare plate is in contact with the membrane electrode assembly

i. The final endplate is placed on the bipolar plate

j. Also here, the endplate has to fit perfectly on the bipolar plate

k. Then, the screws has to be tightened with a torque wrench to 5.0 N m

l. The final electrolyzer cell has to be checked for any failures

For chemical stability regarding the KOH and NaCl electrolyte solution, the inlet, outlets and the flow channels of the endplates were modified with PEEK and Teflon Swagelok connectors as shown in Figure 3-7.

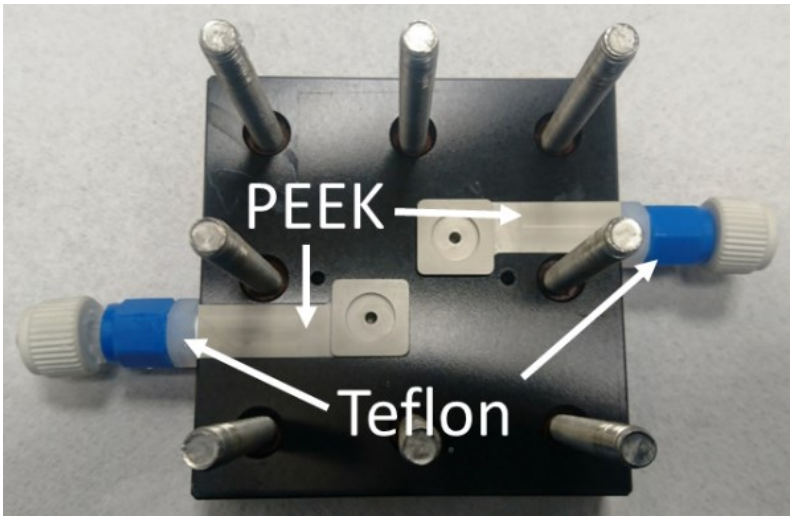

Figure 3-7: (Reversible) electrolyzer endplate with modifications for higher chemical stability

3.1.3 In-house seawater electrolyzer set-up

The used electrolyzer set-up used in **SD III**[3] (*Chapter 6*) is described in detail in the following section. Since the electrolytes used for the publication contain Cl^- ions, the seawater electrolysis could not conducted in a commercial electrolyzer test stand. Also, possibly evolving chlorine could harm the instruments so that an in-house seawater electrolyzer test stand was built and used. To avoid glass corrosion induced by KOH containing electrolyte all tubing and container are made out of Teflon.

Accordingly, the in-house seawater electrolyzer set-up consists of a peristaltic pump (Ismatek), a Gamry 3000 potentiostat, Teflon tubing, two separated Teflon made electrolyte container for each electrode and a temperature controller as shown in Figure 3-8.

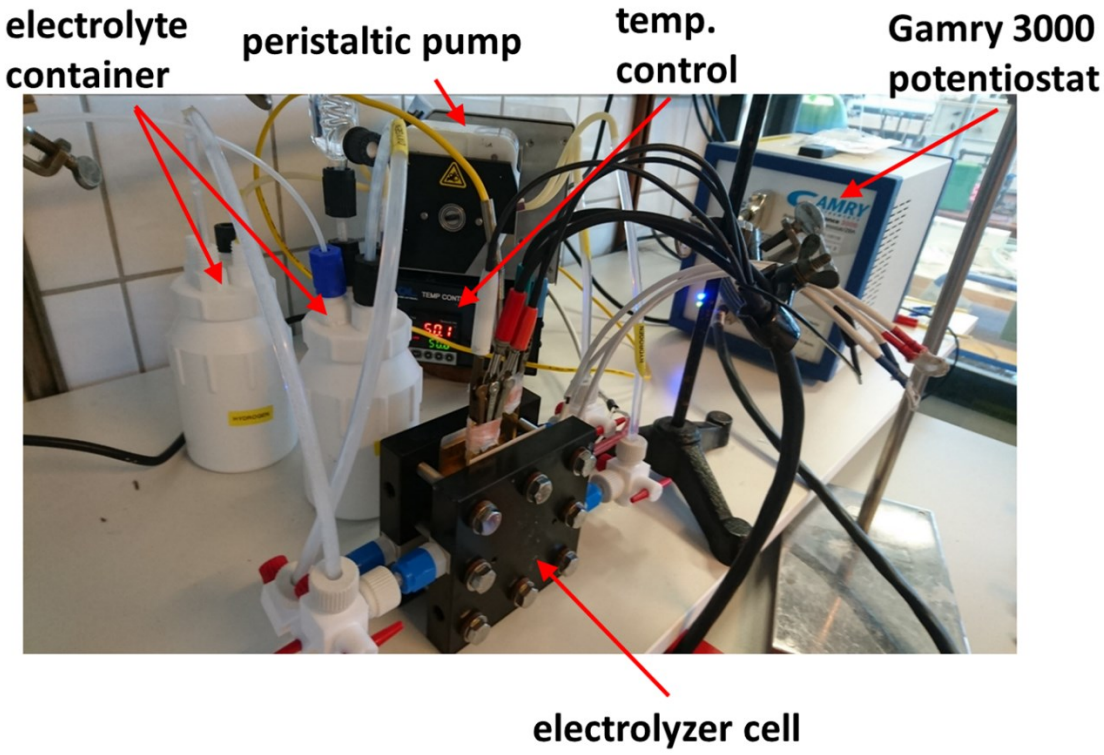

Figure 3-8: In-house bench top seawater electrolyzer set-up

The measurement is conducted in a two-electrode set-up using a Gamry 3000 potentiostat, where the working electrode and working sense is connected to the anode and the counter electrode, counter sense and reference electrode is connected to the cathode. The crocodile clips are fixed to the current collectors by using additional copper tape. The potentiostat is operated by using a laptop which is located outside the walkable fume hood.

3.1.4 In-house electrolyzer selectivity measurement using online mass spectrometry (MS)

For the selectivity measurement in **SD III**[3] (*Chapter 6*), the electrolyzer set-up is extended with an additional mass spectrometer (Pfeiffer Thermostar: GSD 320 TC2), a gas flow controller (N_2), a pre-cooler for gas dehumidification and a MS headspace for detecting the gas composition in the stream as shown in Figure 3-9.

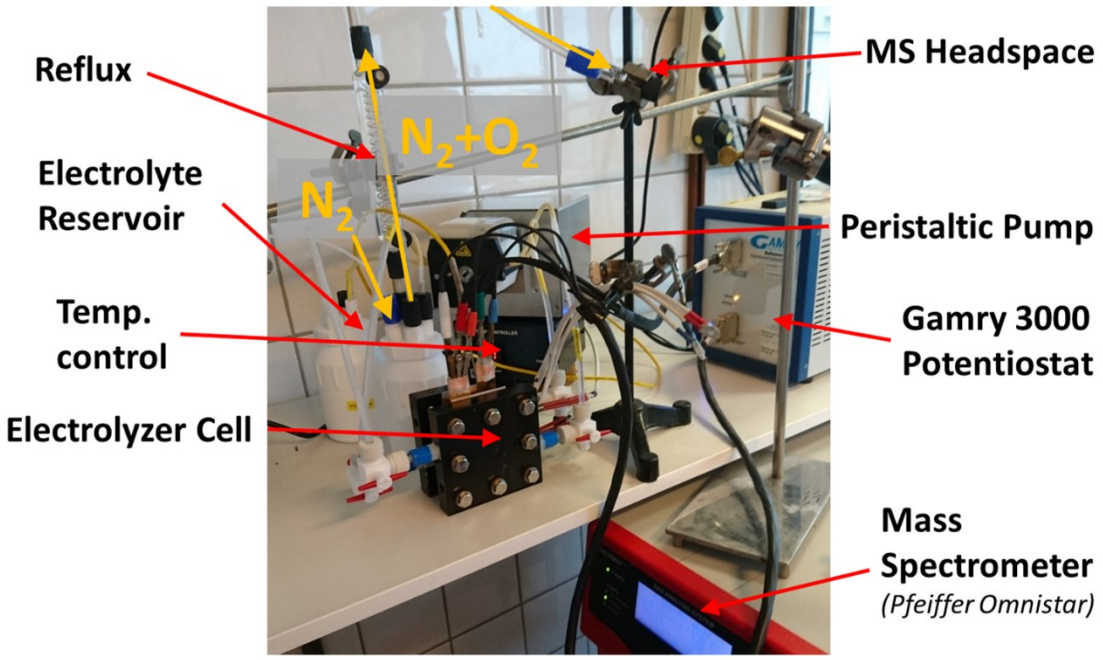

Figure 3-9: Electrolyzer selectivity set-up for online detection of evolved gases from the electrolyzer cell

The gas flow controlled N_2 stream is immersed into the solution of the electrolyte container. The container is completely sealed and autoclavable. The gas stream is set to 100 sccm N_2 flow, which is used as carrier gas. The cycled electrolyte transport the occurring gases into the container, while the carrier gas collect the evolved gas (O_2). The gas mixture flow through the pre-cooler which condense water and dehumidify the gas. The dried gas stream flows further to the MS headspace where the tip of a (150/220 µm) fused silica tubing of the MS is placed. To ensure a constant gas concentration level the constant current was hold for 30 min. For determination of the faradaic efficiency the average concentration level of oxygen of the last 5 min was taken and used for further calculation.

To calculate the faradaic selectivity, the molar gas streams were estimated by modifying the ideal gas equation as shown in equation (3-1):

$$\dot{n} = \frac{\dot{V} \cdot p}{R \cdot T} \qquad (3\text{-}1)$$

Where $\dot{n}$ is the molar stream [mol s^{-1}], $\dot{V}$ is the flow rate [m^3 s^{-1}], p is the pressure [Pa], T is the temperature [K] and R is the ideal gas constant with R = 8.314 J K^{-1} mol^{-1}. Since the gas flow is in an open system and the pre-cooler cools the gas to room temperature, standard conditions are assumed for pressure (p = 1.01 hPa) and temperature (T = 298.15 K). Accordingly, a molar N_2 gas stream of $\dot{n}_{N_2} = 6.81\, mol\, s^{-1}$ is calculated. Based on Faraday's law and the

corresponding currents a molar gas stream produced at the electrodes can be calculated using equation (3-2).

$$\dot{n}_{O_2} = \frac{I}{z \cdot F} \tag{3-2}$$

With the transferred electrons during the oxygen evolution reaction of z = 4 and the Faraday constant F = 96485 s A mol^{-1} results in current depending molar gas streams. Combined with the N_2 flow, the theoretical oxygen gas concentration proportion [%] for a 100 % faradaic efficiency can be calculated using equation (3-3).

$$C_{O_2} = \frac{\dot{n}_{O_2}}{\dot{n}_{N_2} + \dot{n}_{O_2}} \cdot 100 \tag{3-3}$$

The results of the calculation are shown in Table 3-3. Based on the theoretical compared to the determined values a total efficiency can be calculated.

Table 3-3: Currents and the corresponding oxygen production rates and concentrations in the gas stream based on Faraday

I [A]	$\dot{n}_{O_2}$ [mol s^{-1}]	C_{O_2} [%]
0.05	$1.296 \cdot 10^{-7}$	0.190
0.25	$6.478 \cdot 10^{-7}$	0.942
0.5	$1.296 \cdot 10^{-6}$	1.866
0.75	$1.943 \cdot 10^{-6}$	2.773
1	$2.591 \cdot 10^{-6}$	3.664
1.5	$3.887 \cdot 10^{-6}$	5.397
2	$5.182 \cdot 10^{-6}$	7.069
3	$7.773 \cdot 10^{-6}$	10.241

3.2 Four-Probe membrane conductivity set-up

Inspired by Lei[74] an in-house ex-situ membrane conductivity set-up was designed, to determine the membrane conductivity in **SD III**[3] (*Chapter 6*). Some additional information will be given in this section, although the main part of the text is adopted from the publication **SD III**[3]. The glass cell was constructed as shown in Figure 3-10.

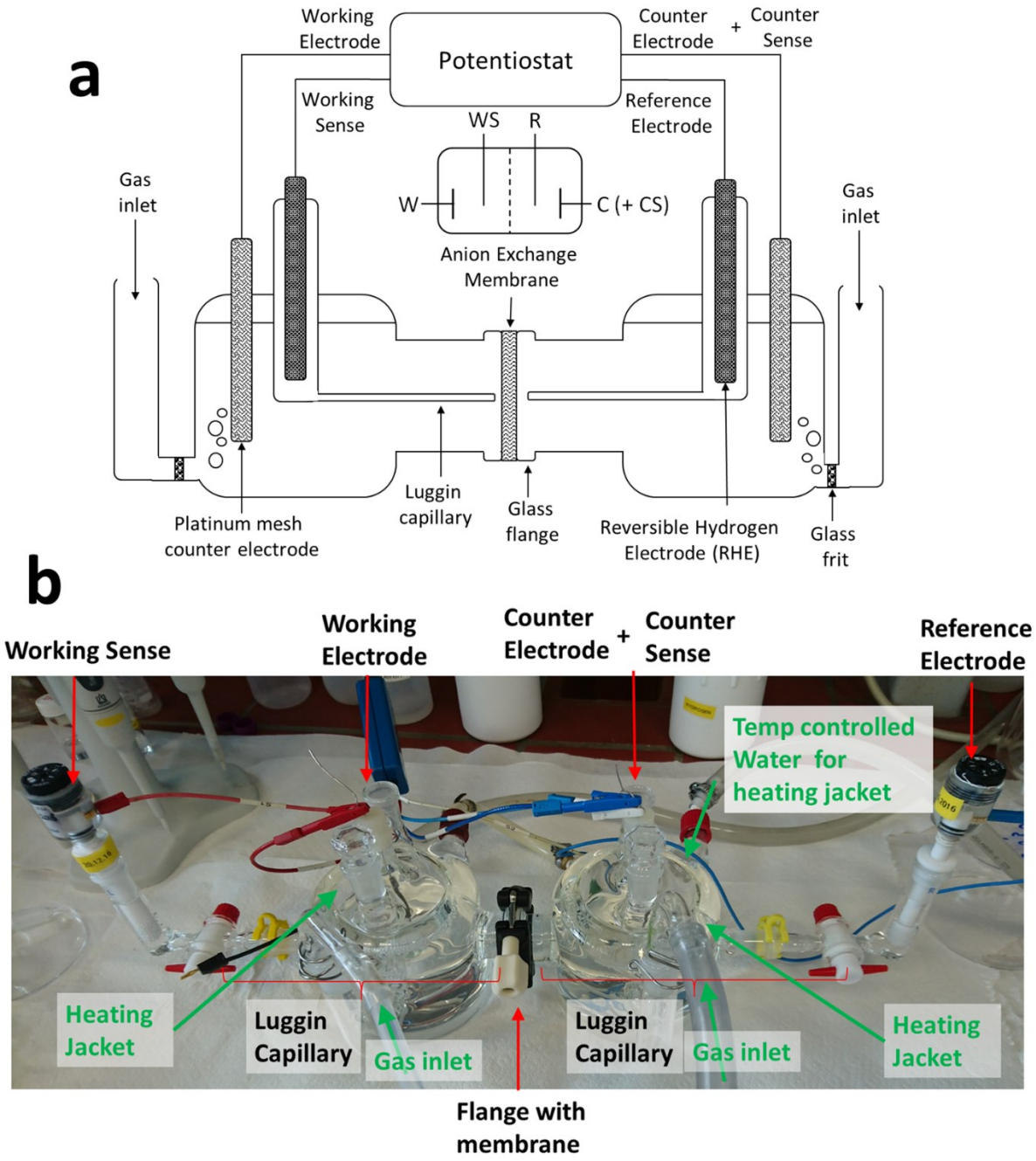

Figure 3-10: 4-Probe membrane conductivity set-up with two chambers (a) detailed sketch (Reproduced with permission from **SD III**[3]. Copyright 2018 Wiley-VCH Verlag GmbH & Co. KGaA. Reproduced with permission) (b) picture of the cell

The membrane was fixed between to identical half-cells. The conductivity was measured using 0.1 M, 0.5 M, 1 M KOH with and without additional 0.5 M NaCl. The electrolyte was N_2 saturated and 50 °C heated to ensure equal conditions. Two Luggin capillaries were located equally close to the membrane, to measure the membrane induced potential drop, while a current was set between the two platinum mesh electrodes acting as working and counter electrodes. The connection of the electrodes is presented in Figure 3-10a. Inspired by Fontananova[75] we applied two approaches for membrane conductivity determination:

1.) Ohm's law approach:

In Ohm's law approach, the potential drop at 1 mA, 2 mA, 3 mA, 4 mA, 5 mA, 10 mA, 20 mA, 50 mA, 100 mA, 200 mA and 230 mA were measured with and without the membrane. The slope of the potential drop and the current density represents the resistance shown in the inset of Figure 3-11. The difference of the membrane-free resistance and the resistance with membrane results into an apparent membrane resistance, which includes the capacitive resistance as shown in the equivalent circuit in the inset of Figure 3-11.

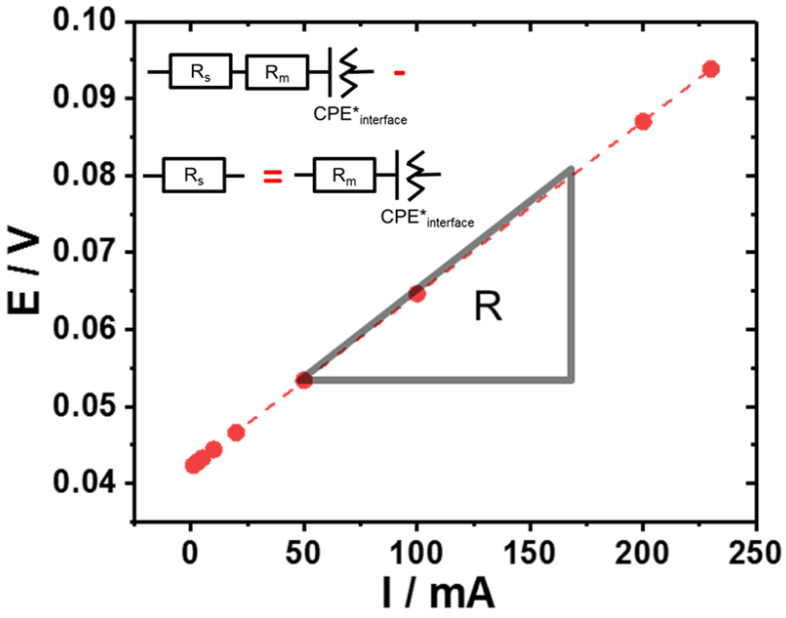

Figure 3-11: Sketch of ohms law approach. The slope gives the corresponding resistance. The inset shows the equivalent resistances with and without membrane, where R_s is the solution resistance, R_m is the membrane resistance and $CPE^*_{interface}$ is the interface capacity of a non-ideal capacitor. Reprinted with permission from **SD III**[3]. Copyright 2018 Wiley-VCH Verlag GmbH & Co. KGaA. Reproduced with permission.

2.) Impedance spectroscopy approach:

After the ohm's law approach the impedance was measured at OCV between 50 – 200 kHz. With this method the resistance of the membrane is obtained without the contribution of the capacitive resistance.[75]

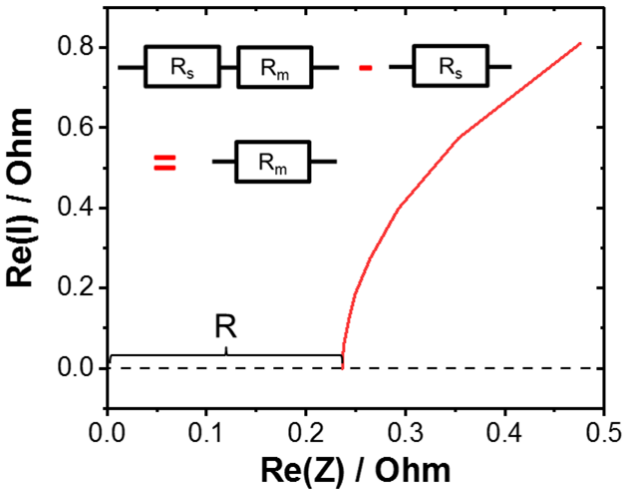

Figure 3-12: Sketch of impedance spectroscopy approach. The inset shows the equivalent resistances with and without membrane. Where R_s is the solution resistance and R_m is the membrane resistance. Reprinted with permission from **SD III**[3]. Copyright 2018 Wiley-VCH Verlag GmbH & Co. KGaA. Reproduced with permission.

3.3 Quasi in-situ X-ray absorption (XAS) – Sample preparation

For **SD III**[3] (*Chapter 6*), X-ray absorption near edge (XANES) and fine structure spectroscopy (EXAFS) was performed at BESSY by Dr. Stefan Loos from the Freie Universität Berlin and at this date group member of Prof. Holger Dau. Based on long experience, we used a freeze-quench technique to imitate an in-situ experiment. In former investigation, the validity of this technique could be verified by comparing freeze quench samples to real in-situ measurements showing identical results.[76] This process is also called quasi in-situ XAS. The details for the experiments at BESSY are described in detail in the publication **SD III**[3] (*Chapter 6*) by Dr. Stefan Loos. However, the sample pretreatment at Technische Universität Berlin is described in detail in this section.

First, the samples are spray coated on glassy carbon substrates (2 x 1 x 0.1 mm) with a catalyst area of 1 cm^2. The routine is similar to the described membrane coating in chapter 3.1.1 (*MEA preparation via spray coating*). After spray coating, the glassy carbon substrate is connected to a copper tape and attached into a frame, which is designated for the XAS set-up. Kapton® tape

at the frame edges provide a proper sealing. Finally, the prepared sample is assembled in the electrochemical assembly as shown in Figure 3-13.

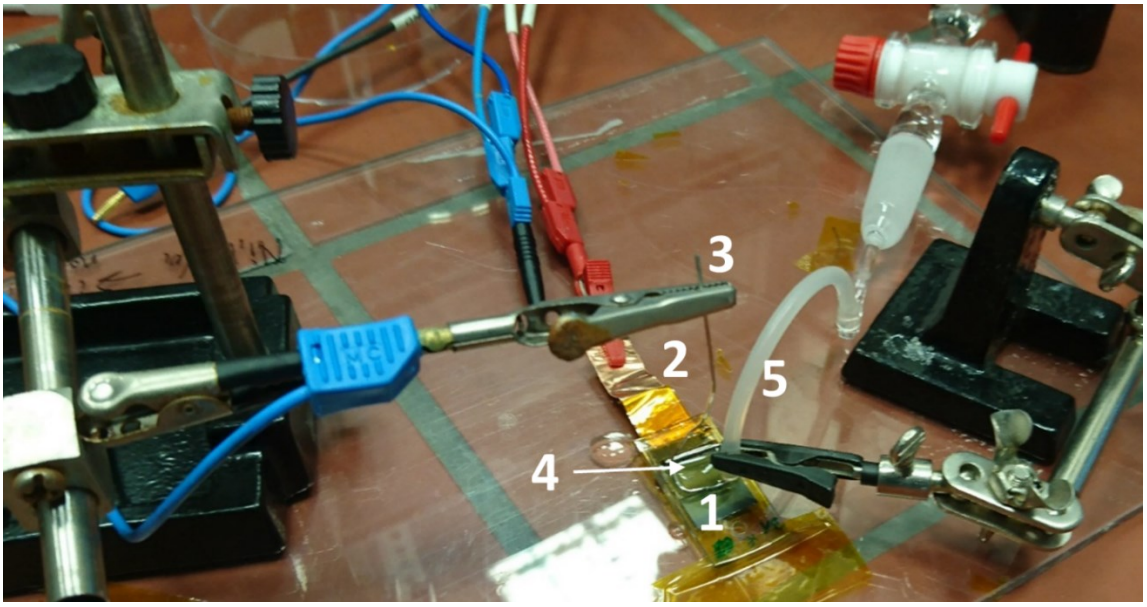

Figure 3-13: Freeze quench set-up for freezing the XAS samples under potential. The samples are coated on a (1) glassy carbon plate mounted on a sample holder using kapton® tape. The plate is connected to the working electrode by using a (2) copper tape. The (3) Pt-wire counter electrode is immersed in an (4) electrolyte drop that is also in contact with a (5) Luggin capillary tube equipped with a reversible hydrogen electrode (RHE)

Then, the test is performed using a BioLogic SP 200 potentiostat. After connecting the electrodes according to Figure 3-13 an electrolyte drop is placed on the catalyst surface. Then the electrochemical sequence was initiated (Figure 3-14).

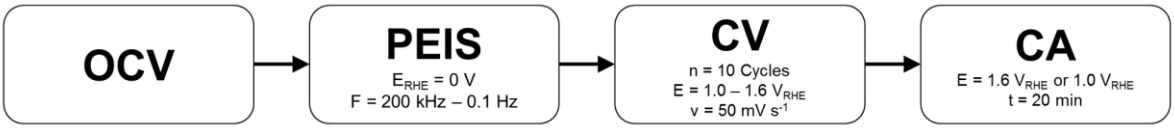

Figure 3-14: Electrochemical pretreatment sequence for BESSY-samples with open circuit potential (OCV), potentio electrochemical impedance spectroscopy (PEIS), cyclic voltammetry (CV) and chronoamperometry (CA)

The open circuit potential (OCV) start the measurement, followed by an impedance measurement to determine the resistance. 10 cycles between 1.0 – 1.6 V_{RHE} activates the sample, followed by a 20 min chronoamperometry measurement at the desired potential. After 15 min at the corresponding potential the sample is freeze quenched by using liquid N_2. After the freeze quenching step the sample is stored immediately into a liquid N_2 filled Dewar

container. The Dewar was used as transportation box and brought to the BESSY II synchrotron facility for XAS measurement performed by Dr. Stefan Loos.

Chapter 4

Non-noble metal oxides as bifunctional catalyst

This chapter is based on and reproduced from publication **SD I**[1]

Non-Noble Metal Oxides and their Application as Bifunctional Catalyst in Reversible Fuel Cells and Rechargeable Air Batteries

Sören Dresp. *Peter Strasser**

ChemCatChem. , 2018, 10, 4162; DOI: https://doi.org/10.1002/cctc.201800660

It will give a reprint of the abstract and summarizes the most important results. Detailed information can be found in the publication reprint in **Appendix II**

4.1 Abstract

"Bifunctional catalyst materials for oxygen electrodes in unitized reversible fuel cells (URFC) or rechargeable metal air batteries have received much attention due to their fundamental scientific challenges and their practical applications. Recent reported data on bifunctional electrochemical activities of the oxygen evolution reaction (OER) and the oxygen reduction reaction (ORR), have shown major inconsistencies and discrepancies largely due to the lack of standardized ORR/OER testing protocols. In contrast to the common procedure of separated OER and ORR measurements, the current protocol includes a series of combined successive ORR and OER activity tests. These exemplary test protocol provide useful data about the catalyst performance reversibility and stability especially regarding the oxidative effects of high OER potential, which is one of the major challenges for URFC catalysts. Our experimental data enables us to classify bifunctional catalysts in terms of a synoptic overpotential diagram. Non-

noble metal oxides show favorable OER than ORR performances and uncover synergistic effects for the combination of MnFe and MnCo towards the ORR and NiFe for the OER. The highest bifunctional activity was found for a novel mixed spinel phase of Co and Mn and the highest OER performance was demonstrated for a mixed metal NiFe layered double hydroxide catalysts, from which practical guidance for the design of bifunctional fuel cell or metal-air battery electrodes ensure." Published in **SD I**[1]

4.2 Project summary

Precious metal free oxides and hydroxides are the ideal candidate to work as catalyst in alkaline reversible electrolyzers, because they are cheap, abundant and stable at high pH. To gain insights for the catalytically behavior and probable suitability of those materials, this publication aims the categorization and classification of mono- and bimetallic oxide/hydroxide combinations of the elements Ni, Fe, Mn and Co towards their OER and ORR activity. As reference materials commercial Pt/C and Ir/C were used and tested. An additional focus was set to the influence of high OER potentials towards the resulting ORR activity, revealing novel insights for bifunctional catalyst stabilities.

4.2.1 Experiment:

A set of bi- and monometallic Co, Mn, Ni and Fe oxygen electrode catalysts were prepared, using a one-pot microwave assisted solvothermal synthesis route using a mixture of DMF and H_2O as solvent. The corresponding crystal phase and elemental composition of the samples were analyzed by XRD and ICP-OES. In order to gain insights of the corresponding bifunctional activity and stability, the materials are tested using a novel testing protocol that subsequent measures the ORR and OER as shown in Figure 4-1.

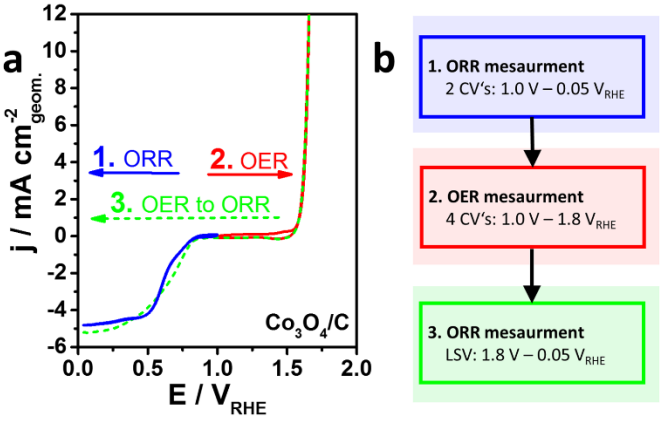

Figure 4-1 : Electrochemical bifunctional testing sequence for the oxygen electrode in O_2 saturated 0.1 M KOH, 1600 rpm and a scan rate of 5 mV s^{-1}. (a) Example for Co_3O_4/C (b) detailed sequence description. Reprinted from **SD I**[1]. Copyright Wiley-VCH Verlag GmbH & Co. KGaA. Reproduced with permission.

While the first two cycles represent the initial ORR activity determination, the four following cycles will give the OER activity with an additional slightly stress test. After OER cycling the ORR is tested again by linear sweep voltammetry (LSV) to detect the influence of OER potentials on the ORR activity.

4.2.2 Results and discussion:

The one-pot microwave assisted synthesis provides catalysts in various phase structures, mainly oxides, hydroxides and layered double hydroxides (see Figure 4-2).

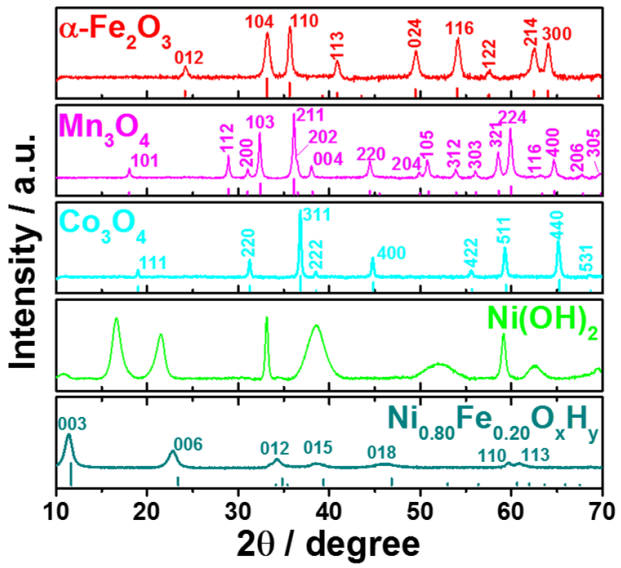

Figure 4-2: Powder X-ray diffraction (XRD) pattern of selected non-noble metal oxide samples supported on Vulcan XC-72r prepared by solvothermal microwave assisted one-pot synthesis route. Reprinted from **SD I**[1]. Copyright Wiley-VCH Verlag GmbH & Co. KGaA. Reproduced with permission.

The electrochemical testing showed novel trends for bifunctional oxygen electrode catalyst. Especially the monometallic catalysts showed different trends for their OER and ORR activity and stability as shown in Figure 4-3.

Even though Fe_2O_3 shows high OER and ORR stability, it presents the lowest performance for both reactions. Ni-based catalyst demonstrates the best OER performance, but simultaneously shows the lowest ORR activity. In contrast, Mn-based catalyst were not stable under OER conditions decreasing activity per cycle, albeit increased the ORR activity. For mono-metallic materials, the Co_3O_4/C exhibit the most promising bifunctional activity.

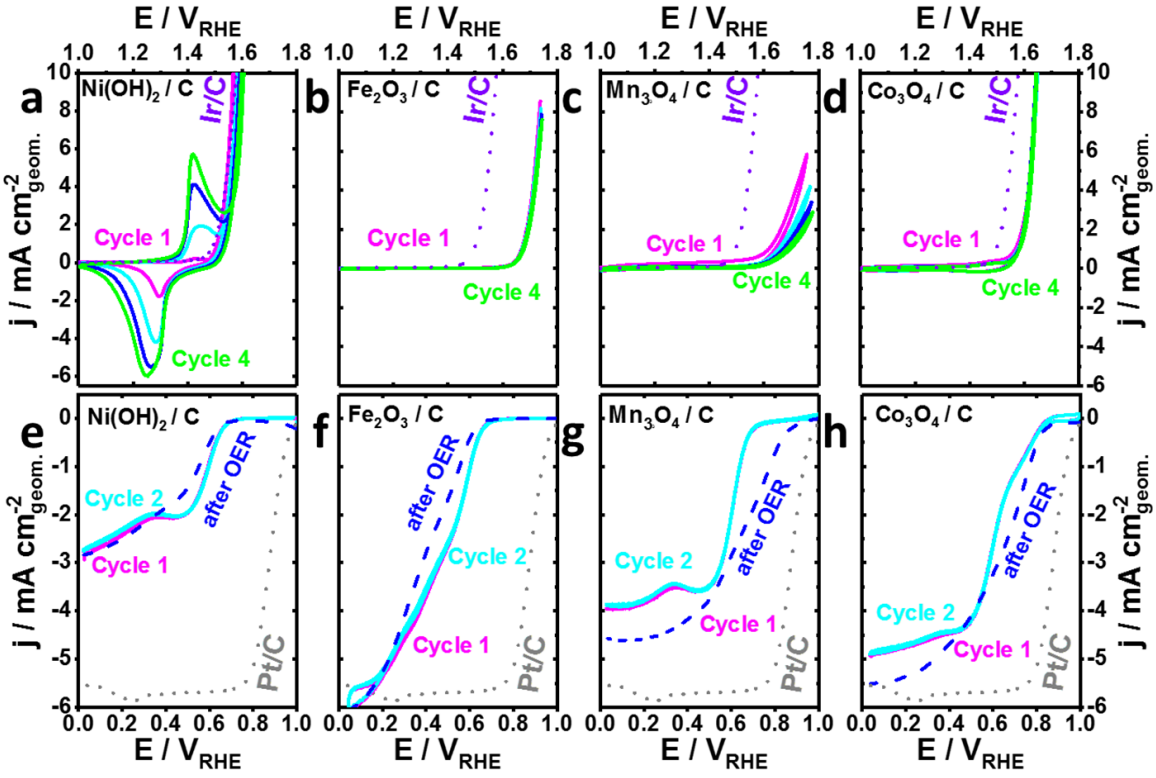

Figure 4-3: Cyclic voltammogram of supported monometallic oxide catalysts in O_2 saturated 0.1 M KOH, 1600 rpm, a scan rate of 5 mVs^{-1} and a cat load 0.2 mg cm^{-2}. Reprinted from **SD I**[1]. Copyright Wiley-VCH Verlag GmbH & Co. KGaA. Reproduced with permission.

The electrochemical performance of mono- and bimetallic catalysts were summarized in synoptical 2D-activity diagrams based on overpotential, mass activity and ECSA normalized activity. Figure 4-4 shows the 2D-overpotential related diagram with regard to the thermodynamic standard potential of 1.23 V_{RHE} taken at a current density of 1 mA cm^{-2} for the OER and -1 mA cm^{-2} for the ORR before and after OER testing.

The diagonal split the area into an ORR favored and an OER favored region. Of particular note is that all catalyst showed a favored OER activity. After OER cycling most of the catalysts showed an activity decrease, except for the Mn and Co based materials which show also the greatest bifunctionality. In addition, the major synergistic effects were determined for the combination of Mn and Co referred to the ORR. The combination of Ni and Fe which resulted in highly crystalline double layered hydroxide (LDH) showed by far the greatest activity referred to the OER.

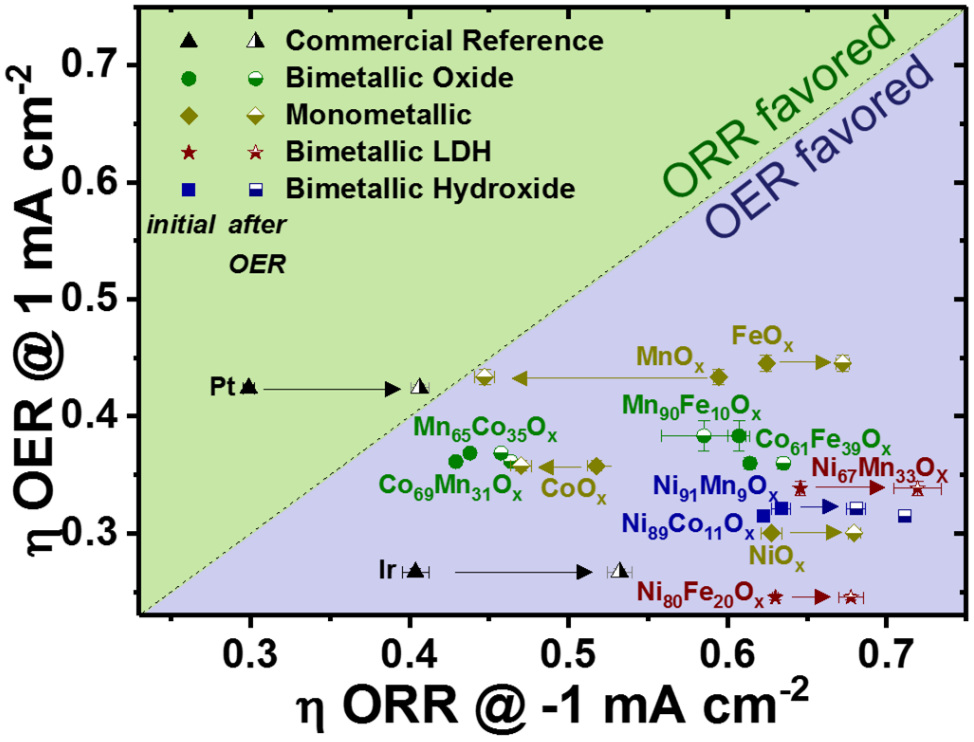

Figure 4-4: Diagram of different catalyst materials for their initial and OER treated on-set potential at -1 mA cm^{-2} for ORR and 1 mA cm^{-2} for OER. Reprinted from **SD I**[1]. Copyright Wiley-VCH Verlag GmbH & Co. KGaA. Reproduced with permission.

All other 2D-diagrams normalized to the ECSA and the elementary metal mass supported the results of Figure 4-4. Nevertheless, none of these materials show sufficient bifunctional activity, indicating limitations of mono-component catalysts associated with a single active site (see also discussion in *chapter 7.1.1 Reversible seawater electrolyzer: Catalyst*)

4.2.3 Conclusion

This study showed the limitations of a mono-component catalyst regarding the suitability as bifunctional catalyst (*cf. chapter 7.1.1 Reversible seawater electrolyzer: Catalyst*). Even though

combinations of MnCo seem to be most promising bifunctional catalyst, the performance seems not sufficient for usage in commercial reversible electrolyzers. However, this study supported the known and extraordinary high catalytic activity of NiFe-LDH catalyst materials, which makes it a promising material as anode catalyst material in future electrolyzers.

Chapter 5

Bifunctional two-component catalyst system

This chapter is based on and reproduced from publication **SD II**[2]

An efficient bifunctional two-component catalyst for Oxygen Reduction and Oxygen Evolution in reversible fuel cells, electrolyzers and rechargeable air electrodes

Dresp, S*. Luo, F., Schmack, R., Kühl, S., Gliech, M. & Strasser, P,*

Energy & Environmental Science, 2016, 9, 2020–2024; DOI: https://doi.org/10.1039/C6EE01046F

---

with permission from The Royal Society of Chemistry

It will give a reprint of the abstract and summarizes the most important results. Detailed information can be found in the publication reprint in **Appendix II**

5.1 Abstract

"We report on a non-precious, two-phase bifunctional oxygen reduction and evolution (ORR and OER) electrocatalyst with previously unachieved combined roundtrip catalytic reactivity and stability for use in oxygen electrodes of unitized reversible fuel cell/electrolyzers or rechargeable metal–air batteries. The combined OER and ORR overpotential, total, at 10 mA cm_{-2} was a record low value of 0.747 V. Rotating Ring Disk Electrode (RRDE) measurements revealed a high faradaic selectivity for the 4 electron pathways, while subsequent continuous MEA tests in reversible electrolyzer cells confirmed the excellent catalyst reactivity rivaling the state-of-the-art combination of iridium (OER) and platinum (ORR)."

Published in **SD [II]**[2]

5.2 Project summary

SD I[1] (*chapter 4*) showed the limitations of mono-component catalyst materials associated with a non-suitability as bifunctional catalyst. However, NiFe-LDH showed highly promising OER activity. Accordingly, study **SD [II]**[2] focused on a two-component catalyst using NiFe-LDH as highly specialized OER catalyst and Fe N doped carbon materials as a known ORR active material. The concept of a two component mixture, each component specialized for one reaction forms most likely multi-sites to circumvent limitations based on a single active site. In fact, this physical mixture shows to this date unachieved overall bifunctional OER/ORR activities.

5.2.1 Experiment

Seeking for the ideal bifunctional catalyst, in this study NiFe-LDH and Fe-N doped carbon (Fe-N-C) were just physically mixed and tested as bifunctional two-component catalyst system. The NiFe-LDH was prepared via a one-pot microwave assisted solvothermal synthesis route and Fe-N-C was prepared via a wet chemical polymerization of aniline in a solution of Ketjen and $FeCl_3$. Repetitive acid leaching resulted in purified Fe-N-C catalysts. For physicochemical characterization the materials are analyzed via XRD, TEM and ICP-OES. For electrochemical testing RDE, RRDE and reversible electrolyzer tests were performed using Tokuyama A201 as AEM.

5.2.2 Results and Discussion

Physical mixing of NiFe-LDH and Fe-N-C resulted in a combined phase, revealing XRD and TEM features of both phases (see Figure 5-1 and **SD [II]**[2]).

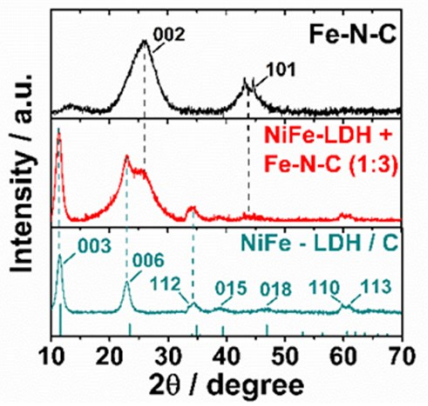

Figure 5-1: X-ray diffraction profiles of the Fe N-doped carbon catalyst (Fe-N-C) (top), the mixture of NiFe-LDH and Fe-N-C catalyst (middle) and the carbon-supported NiFe-layered double hydroxide catalyst (NiFe-LDH/C) in an atomic ratio of $Ni_{0.78}Fe_{0.22}(OH)_x$ (bottom). Reproduced from **SD II** [2] with permission from The Royal Society of Chemistry

Figure 5-2 shows the electrochemical OER and ORR activity measurement of each catalyst in 0.1 M KOH.

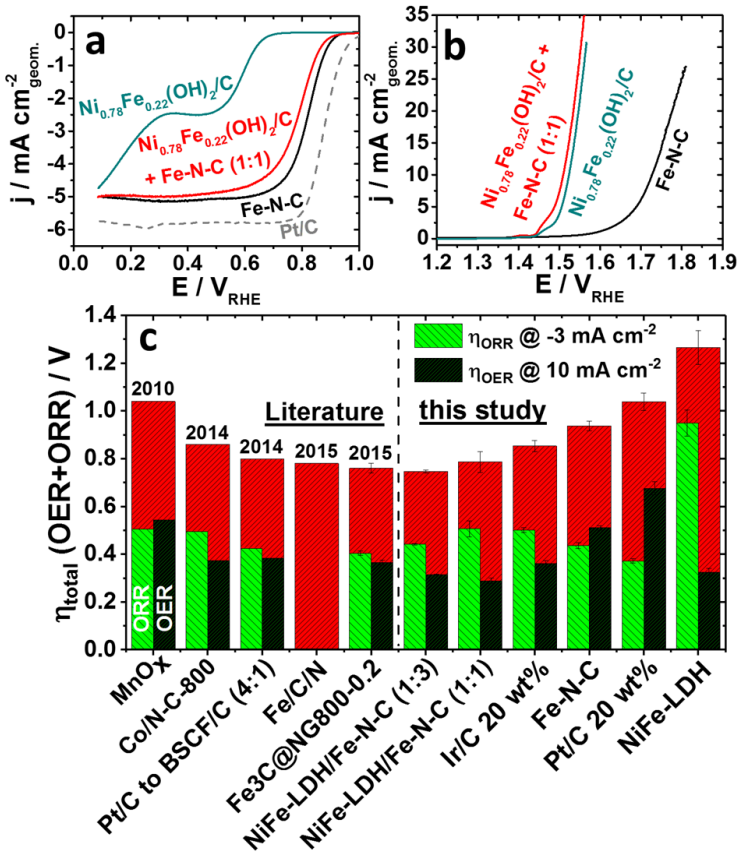

Figure 5-2: Catalytic ORR (a) and OER (b) voltammetric profile and activity of the pure NiFe-LDH, pure Fe-N-C catalysts, and of their two-component mixture in O_2 -saturated 0.1 M KOH at 5 mV/s scan rate, 1600rpm rotation speed and 0.2 mg cm-2 total catalyst loading; (c) Individual ORR and OER, and total overpotentials for six different catalysts of this study (right side) in comparison to published literature [[77-81]] (left side). Fe-N-C/NiFe-LDH(X:Y) denote novel two-phase catalysts reported here. Reproduced from **SD II** [2] with permission from The Royal Society of Chemistry

While the Fe-N-C and NiFe-LDH show either high OER or ORR activity the mixture show a combined bifunctional activity without significant activity losses. Compared to other binfunctional catalysts the mixture of Fe-N-C and NiFe-LDH in a ratio of 3:1 showed to this date unachieved activities (Figure 5-2c). To explain the observed combined performance of a physical mixture, a simple two-phase system provides two distinct and spatially separated ORR and OER catalytic sites that are sufficiently homogeneous to act as a contiguous catalyst film, yet are spatially separated enough not to interfere with each other (see also discussion in *chapter 7.1.1 Reversible seawater electrolyzer: Catalyst*).

Additional RRDE selectivity measurement showed selectivities of >90 % for the ORR, which are almost comparable to the Pt/C reference measurement (cf. **SD [II]**[2]) and OER RRDE tests showed almost 100 % faradaic efficiency (cf. **SD [II]** [2]).

A final reversible electrolyzer test confirmed the high initial bifunctional activity of the two component system (Figure 5-3a). However, the presented system lack in long-term stability, which is demonstrated by the decreased activity per cycle for the reversible electrolyzer test (Figure 5-3c). Figure 5-3d shows additional 24h galvanostatic RDE tests and confirmed the ORR instability, which we attribute to the electrochemical oxidation of Fe-N-C active sites associated with electrochemical carbon corrosion (see also discussion in *chapter 7.1.1 Reversible seawater electrolyzer: Catalyst*).

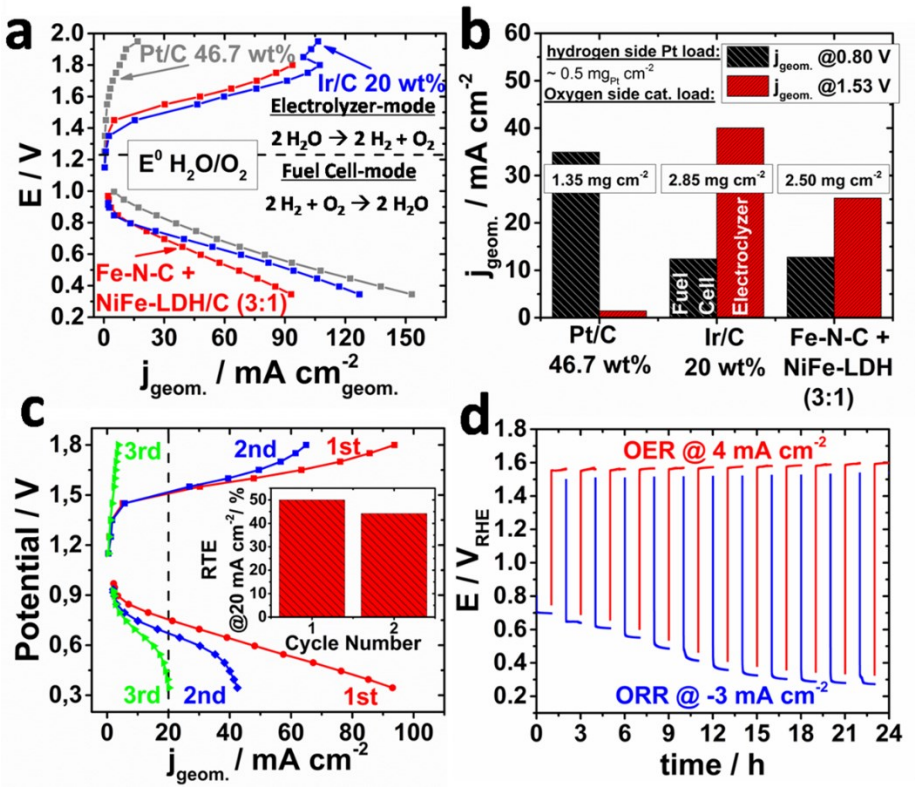

Figure 5-3: Full alkaline exchange membrane (AEM)-based unitized MEA fuel/electrolysis cell measurements: (a) Polarization curves for the first fuel cell / electrolysis cycle with platinum as hydrogen catalyst, and platinum (grey), iridium (blue) and the Fe-N-C/NiFe-LDH(3:1) as oxygen catalysts (b) Comparison of geometric activities of the three unitized cells (c) Three consecutive fuel cell/ Electrolyzer cycles using the Fe-N-C/NiFe-LDH(3:1) catalyst, inset: round trip efficiency (RTE) for the first two cycles; (d) 24h stability measurement of unitized fuel/electrolysis cell using the Fe-N-C/NiFe-LDH(3:1) catalyst. Unitized Fuel Cell / Electrolyzer performance. Reproduced from SD II[2] with permission from The Royal Society of Chemistry

In contrast, the OER activity for the mixture almost remain after 24 h. Since the OER activity in the reversible electrolyzer cell decreased per cycle, we believe that the instability of the cell measurement can also partly be attributed to the membrane instability which is highly sensitive to changing environmental condition (see also discussion *chapter 7.1.2 Reversible seawater electrolyzer: Membrane*). Nevertheless, this study verified the material concept of a two-component catalyst system and NiFe-LDH proofed its suitability as OER catalyst for future alkaline electrolyzers.

5.2.3 Conclusion

This study showed the possibility for a highly active bifunctional material by just mixing NiFe-LDH and Fe-N-C catalyst materials, while the first is highly specialized for OER and the latter for ORR. Although, Fe-N-C lack in stability towards high OER potentials and the membrane seems not optimized for repetitive changing fuel cell/electrolyzer environments, the electrochemical measurement showed by this time unachieved overall bifunctional activity in 0.1 M KOH. Therefore, this study showed a promising approach to gain simultaneous high catalytic activity for ORR and OER and opens a concept for future multi-site catalyst design (see also discussion *chapter 7.1.1 Reversible seawater electrolyzer: Catalyst*).

Chapter 6
Direct Seawater Splitting

This chapter is based on and reproduced from publication **SD III**[3]

Direct electrolytic splitting of seawater: Activity, selectivity, degradation, and recovery studied from the molecular catalyst structure to the electrolyzer cell level

Sören Dresp,[a] *Fabio Dionigi,*[a] *Stefan Loos,*[b] *Jorge Ferreira de Araujo,*[a] *Camillo Spöri,*[a] *Manuel Gliech,*[a] *Holger Dau,*[b]* *Peter Strasser*[a]*

Adv. Energy Mater., ***2018****, 1800338; DOI: https://doi.org/10.1002/aenm.201800338*

It will give a reprint of the abstract and summarizes the most important results. Detailed information can be found in the publication reprint in **Appendix II**

6.1 Abstract

"Seawater electrolysis faces fundamental chemical challenges, such as the suppression of highly detrimental halogen chemistries, which has to be ensured by selective catalyst and suitable operating conditions. In the present study, nanostructured NiFe-layered double hydroxide and Pt nanoparticles are selected as catalysts for the anode and cathode, respectively. The seawater electrolyzer is tested successfully for 100 h at maximum current densities of 200 mA cm−2 at 1.6 V employing surrogate sea water and compared to fresh water feeds. Different membrane studies are carried out to reveal the cause of the current density drop. During long-term dynamic tests, under simulated day-night cycles, an unusual cell power performance recovery effect is uncovered, which is subsequently harnessed in a long-term diurnal day-night cycle test. The natural day-night cycles of the electrolyzer input power can be conceived as a reversible catalyst materials recovery treatment of the device when using photovoltaic electricity sources.

To understand the origin of this reversible recovery on a molecular materials level, in situ extended X-ray absorption fine structure and X-ray near-edge region spectra are applied."

Published in **SD [III]**[3]

6.2 Project summary

Based on **SD [II]**[2] (*chapter 5*), the design concept of a two component catalyst for bifunctional catalysts demonstrated its validity and showed sufficient bifunctional activity for a reversible electrolyzers. The focus of this study was set on selective seawater splitting using a seawater electrolyzer device. The former investigations **SD [I-II]**[1, 2] (*chapter 4-5*) exhibited high OER activity of NiFe-LDH. Thus, NiFe-LDH appeared as suitable material for seawater electrolyzer anodes and selectively oxidize seawater into oxygen. In fact, this study will give first insights of a seawater electrolyzer using direct but alkalinized seawater in a membrane based electrolyzer device and split NaCl containing electrolyte selectively into oxygen and hydrogen.

6.2.1 Experiment

The assembly of the seawater electrolyzer which is used for this study is described in detail in the additional experimental part (*chapter 3.1 Membrane electrode assembly (MEA) and electrolyzer cell set-up*). In short, NiFe-LDH is used as anode and commercial 46.7 wt% Pt/C (TKK) as cathode catalyst material. To obtain the MEA, both catalysts are spray coated on a Tokuyama A201 membrane using Tokuyama AS-4 as ionomer. As electrolyte 0.1 M, 0.5 M and 1 M KOH were tested with and without the addition of 0.5 M NaCl, which is considered as a good adaption of seawater (see *chapter 2.3 Seawater Electrolysis*). The cell temperature was kept at 50 °C. In order to perform selectivity tests, we used an in-house selectivity set-up equipped with an online mass spectrometer (see *chapter 3.1.4 In-house electrolyzer selectivity measurement using online mass spectrometry (MS)*). For testing the separated parts of the electrolyzer cell such as catalyst layer, PTL, membrane, etc., we conducted additional RDE, SEM, 4-probe conductivity (*chapter 3.2 Four-Probe membrane conductivity set-up*) and quasi in-situ tests (*chapter 3.3 Quasi in-situ X-ray absorption (XAS) – Sample preparation*).

6.2.2 Results and Discussion

Testing the different electrolytes 0.1 M, 0.5 M and 1 M KOH with and without the addition 0.5 M NaCl revealed a strong performance drop after adding 0.5 M NaCl (Figure 6-1). Increasing the KOH concentration slightly compensates this effect, although electrolyzer performance using NaCl containing electrolyte remains lower compared to pure KOH.

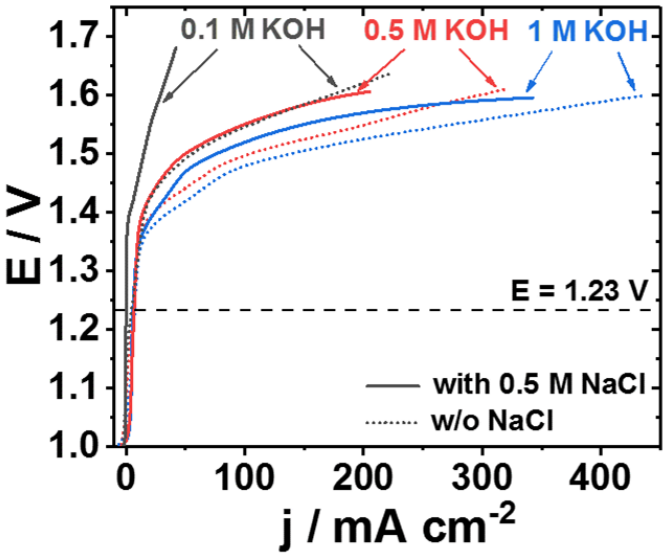

Figure 6-1: Polarization curves extracted from the cyclic voltammetry in different electrolytes using NiFe-LDH as anode material, 46.7 wt% Pt on Vulcan (TKK) as cathode material, and Tokuyama A201 as membrane. Reprinted from **SD III**[3] Copyright Wiley-VCH Verlag GmbH & Co. KGaA. Reproduced with permission.

To identify the origin of this performance drop we performed additional RDE tests of Pt/C 46.7wt% for the HER and NiFe-LDH for the OER in different electrolytes (*cf.* ***SD III****[3]*). Since the performance loss fail to appear in the RDE tests, we concluded rather a membrane based issue than a catalytically. Supporting this, additional impedance measurements show higher cell resistances for NaCl containing electrolytes, which indicates an influence of the Cl^- ions on the membrane. (*cf.* ***SD III****[3]*). We believe that Cl^- might influence the OH^- transport channels which could explain the overall performance drop in Cl^- containing electrolyte (see also discussion *chapter 7.1.2 Reversible seawater electrolyzer: Membrane*).

Potentiostatic 100 h stability tests at 1.6 V resulted in the same electrolyte related performance distribution (Figure 6-2). After an activation time of roughly 12 h, pure 0.1 M KOH showed the highest stability. All other electrolyte compositions revealed a decreasing performance with time. After the 100 h, the final performance dropped to about 50-70 % of the initial performance. Compensating the NaCl with increasing KOH concentration presented a convergence of 0.5 M and 1.0 M KOH concentrated seawater electrolyte. For this 0.5 M KOH appeared as ample concentration to compensate the presumable NaCl induced OH^- transport loss. Also, the membranes are known to be unstable at high KOH concentrations, which could explain the performance drop (see discussion in *chapter 7.1.2 Reversible seawater electrolyzer: Membrane*).

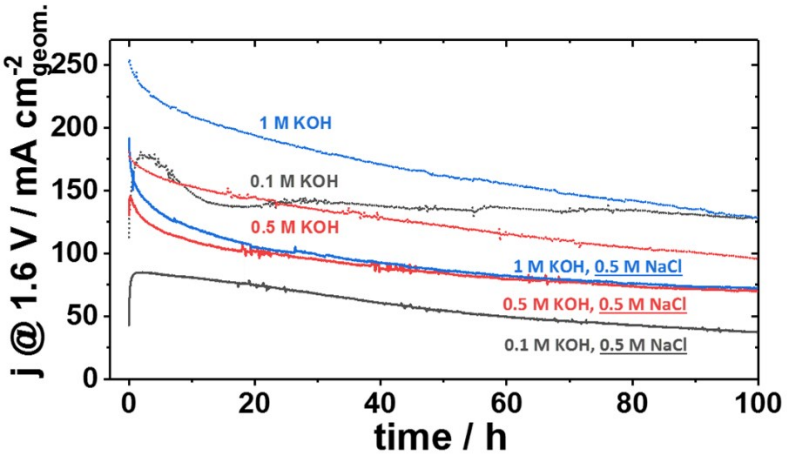

Figure 6-2: 100 h longtime measurement at +1.6 V in different electrolytes using a loading of 0.5 mg_{Pt} cm^{-2} 46.7 wt% Pt on carbon (TKK) on the cathode and 2.5 mg cm^{-2} NiFe-LDH at the anode, a Tokuyama A201 as membrane in different KOH concentrations with and without 0.5 M NaCl. Reprinted from **SD III** [3] Copyright Wiley-VCH Verlag GmbH & Co. KGaA. Reproduced with permission.

However, after 100 h operation at +1.6 V the cell measurement was restarted and a performance recovery effect could be detected (*cf.* ***SD III****[3]*). Although this effect was absent for 0.1 M KOH seawater electrolyte, the effect increases with increasing KOH concentration (*cf.* ***SD III****[3]*). Mimicking electricity provision based on photo voltaic energy sources revealed the possibility to exploit this effect in a diurnal day/night interval. We simulated the daytime for 20 h with a cell potential of +1.6 V and 4 h at OCV which imitates the night (Figure 6-3).

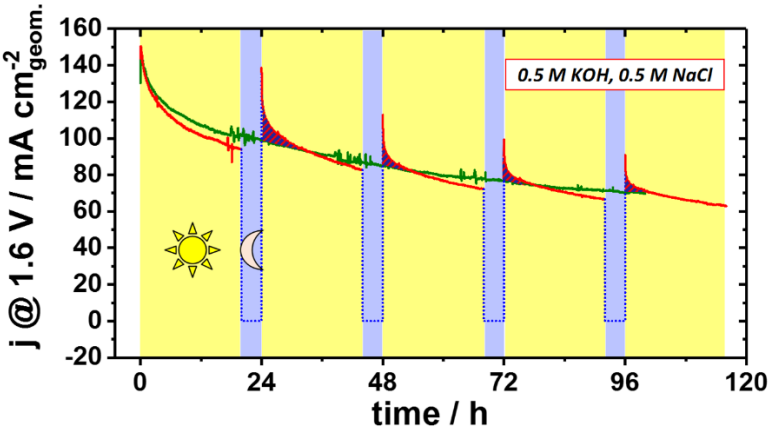

Figure 6-3: Current density versus electrolysis time for a continuous 100 h measurement (green) and a 20 + 4 h day/night interval measurement (red) mimicking a 4 h night cycle at open circuit potential. The electrolysis potential for the continuous and the day time measurement was kept at 1.6 V. The blue red hatched area expresses the advantageous current density in contrast to the 100 h measurement. A loading of 0.5 mg_{Pt} cm^{-2} 46.7 wt% Pt on carbon (TKK) on the cathode and 2.5 mg cm^{-2} NiFe-LDH at the anode, a Tokuyama A201 as membrane and a 0.5 M KOH and 0.5 M NaCl electrolyte was used. Reprinted from **SD III** [3]. Copyright Wiley-VCH Verlag GmbH & Co. KGaA. Reproduced with permission.

After every 4 h OCV, the potential recovered to about 80-90% of the former initial current density, but the performance decreased more strongly. Although the overall stability is almost comparable to the continuous measurement, the red blue patterned areas show an advantageous current density compared to the continuously 1.6 V held cell potential.

Important fact for seawater splitting is the selectivity, which we measured in an in-house selectivity set-up equipped with an online mass-spectrometer, which is described in detail in the experimental section (*chapter 3.1.4 In-house electrolyzer selectivity measurement using online mass spectrometry (MS)*). The galvanostatic testing protocol increased the current stepwise every 30 min. Since we used alkalinized seawater, ClER is not possible to detect due to the direct formation of free chlorine to hypochlorite at high pH (cf. *chapter 2.3 Seawater Electrolysis*). Nevertheless, the O_2 concentration baselines appear identical in pure and 0.5 M NaCl containing 0.5 M KOH (Figure 6-4).

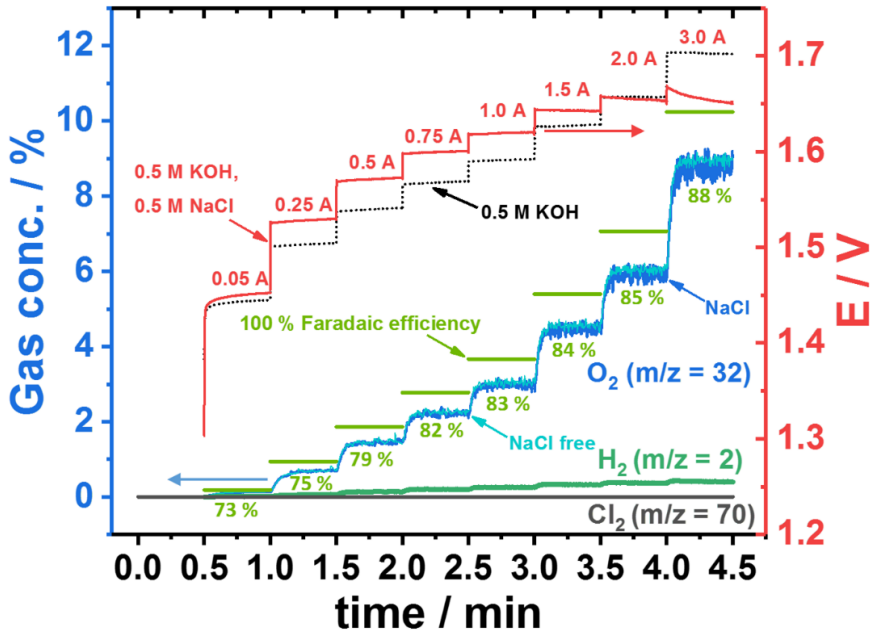

Figure 6-4: Online selectivity measurements of a 5 cm^2 seawater electrolyzer. The volumetric gas concentration in % of the left (blue) y-axis and the cell voltage at the right (red) y-axis is plotted against the measurement time, shown at the bottom x-axis. The applied currents are given in red numbers over the resulting electrode potentials that are shown for an electrolyte concentration of 0.5 M KOH with 0.5 M NaCl in red and for a concentration of 0.5 M KOH as black dotted line. Concurrent oxygen volumetric concentrations for the NaCl containing are in dark blue and the latter in cyan. The green horizontal bars represent the oxygen level of 100% faradaic efficiencies. The green percent values below the measured gas concentration in green indicate the oxygen faradaic efficiency values at each current. Also shown are the time traces of the chlorine (gray) and hydrogen (dark green) concentrations. Reprinted from **SD III** [3]. Copyright Wiley-VCH Verlag GmbH & Co. KGaA. Reproduced with permission.

Although the overall faradaic efficiency is between 73 – 88 %, we believe in an absence of ClER during the seawater electrolyzer test which is indicated by the identical O_2 concentration and the final electrolyzer potential which is still below 1.72 V and thus within the required design criteria for selective seawater splitting (cf. *chapter 2.3 Seawater Electrolysis*). The increasing faradaic efficiency can be explained with the hydrogen and oxygen crossover which is first supported by H_2 detection and second proportional decreasing with higher production rates.

Finally, we investigated the electrode catalyst using a quasi in-situ XANES and EXAFS technique, freeze quenching NiFe-LDH under potential (*cf. chapter 3.3 Quasi in-situ X-ray absorption (XAS) – Sample preparation*). XANES indicate a slightly higher oxidation state of the catalyst under operating conditions, as indicated by a positive shift of the energy of the edge position (*cf.* ***SD III****[3]*). While NiFe-LDH water splitting catalyst, when operated at +1.0 V_{RHE} in KOH, had not yet reached the same high oxidation state it attained at +1.6 V_{RHE} in KOH, the NiFe-LDH catalyst operated in seawater took on its highest experimentally observed oxidation state already at +1.0 V_{RHE}. No further oxidation was observed when the potential was increased to +1.6 V_{RHE} in seawater (*cf.* ***SD III****[3]*).

Additional EXAFS analysis, indicate an influence of the electrolyte on the NiFe-LDH. Figure 6-5 shows higher coordination numbers of Ni- and Fe-centers after activation at 1.0 V for the metal centers in alkalinized seawater compared to pure 0.1 M KOH.

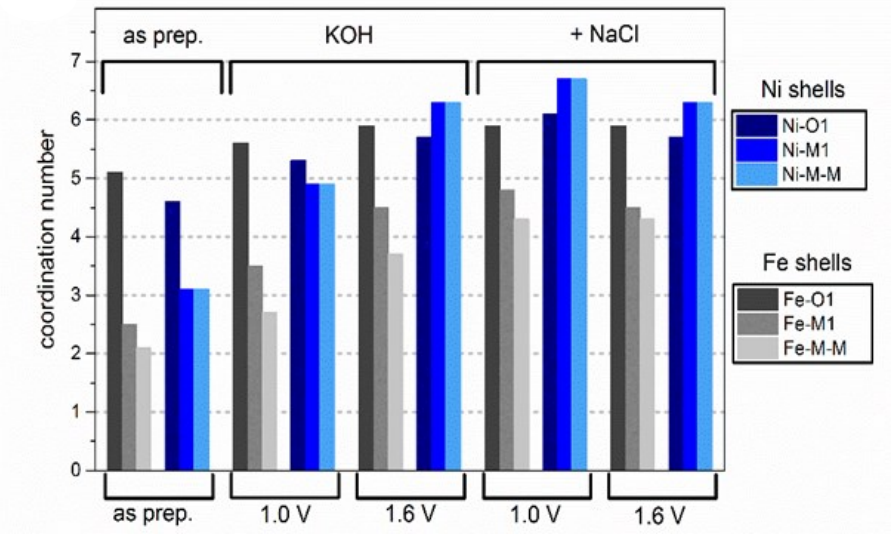

Figure 6-5: Coordination numbers of selected shells as provided from the EXAFS simulation and assignment of structural motifs within the LDH-structure. Reprinted from **SD III** [3]. Copyright Wiley-VCH Verlag GmbH & Co. KGaA. Reproduced with permission.

This suggests a catalyzing oxidation effect by the ionic strength of NaCl. The stronger the ionic strength of the solution the easier the oxidation and the higher the coordination number of the metal centers. This is in agreement with the electrochemical measurement, since the initial $Ni^{ox/red}$ redox features appear larger in higher concentrated electrolytes (see also *chapter 7.1.1 Reversible seawater electrolyzer: Catalyst*). Nevertheless, the results showed no structural decomposition of the NiFe-LDH catalyst in 0.1 M KOH and in 0.5 M NaCl containing electrolyte, supporting the theory that the membrane plays a major role for the stability and activity decrease in high concentrated electrolytes.

6.2.3 Conclusion

This study showed a first selectively working direct seawater electrolyzer. The overall selectivity goals could be achieved, however long-term performance most likely lack in stability of the membrane, since 100 h measurements at 1.6 V result in 30 - 50 % cell performance loss (see also discussion *chapter 7.1.2 Reversible seawater electrolyzer: Membrane*). The addition of NaCl to the pure KOH electrolyte resulted in a strong performance loss, which could not be detected in separated RDE measurements. Additional impedance measurements showing higher cell resistances in NaCl containing electrolyte which indicates a membrane based issue rather a catalytically. Hence, NiFe-LDH proofed its suitability as selective seawater electrolyzer catalyst (see also discussion *chapter 7.1.1 Reversible seawater electrolyzer: Catalyst*). Overall the feasibility of such devices could be shown, but membrane optimization with regard to stability and anion transfer selectivity is still required (see also discussion *chapter 7.1 Is a reversible seawater electrolyzer feasible?*).

Chapter 7

Discussion

This chapter discusses the scientific results presented up to here. It evaluates the physico-chemical feasibility and the practical electrochemical efficiency of a reversible seawater electrolyzer based on the presented scientific data. It also discusses the limitations and future opportunities for research and development of seawater electrolyzers in the context of the overall goal of this thesis. Accordingly, the first part identifies the bottlenecks for this technology based on the experimental data. The second part evaluates the potential for energy storage and freshwater production compared to already established technologies.

7.1 Is a reversible seawater electrolyzer feasible?

The overall goal of this thesis research was, on the one hand, the identification of suitable catalyst materials for the oxygen electrode in reversible seawater electrolyzers, and, on the other hand, the uncovering of qualitative and quantitative relations between structure, activity, selectivity and stability. However, testing the catalyst materials in real cell devices revealed more parameters and components that need to be evaluated for the purpose of assessing the feasibility of an operational reversible seawater electrolyzer. This section will identify the important components of a seawater electrolyzer and evaluate the results with regard to the feasibility of a reversible seawater electrolyzer device.

Conventional reversible electrolyzers combine the properties of an electrolyzer and a fuel cell in a single device.[82] Single fuel cell or electrolyzer devices use specially modified chemical components for the interfacial charge transfer and ionic transport, such as electrocatalysts and membranes, but also suitable cell designs and environments for reactant and product transport, such as flow channel geometry and porous transport layers (PTL). The challenge of a reversible electrolyzer is to realize both the fuel cell and electrolyzer functionalities using shared components inside one single device with high energy efficiencies. Even though this work focused primarily on catalyst design, all cell components like membrane and porous transport layer (PTL) had to be included and evaluated in the tests in order to gain insights into the

feasibility of a single reversible seawater electrolyzer. This is why, in the following discussion, the challenges of the identification of such shared components and their implementation into a reversible seawater electrolyzer will be analyzed.

7.1.1 Reversible seawater electrolyzer: Catalyst

The catalyst layer is one of the most important component of a fuel cell or electrolyzer, as the catalyst determines the charge transfer resistance, the reaction efficiency, the overpotential of the reaction and all kinetic limits, and with it, the overall device performance over large potential ranges. This is why a large number of new material candidates were developed over the past years in search of better performing catalysts [19, 29, 83-85]. The catalysts are compared with benchmark electro-catalysts which are commercially available for both, pure fuel cells or pure electrolyzers. Previously explored bifunctional oxygen catalysts for use in reversible fuel cells are still lacking long-term stability and performance. Also, even though their catalytic activity obtained in a three-electrode rotating disk electrode (RDE) set-up is promising, the translation and realization of those same activities in gas diffusion electrodes or catalyst coated membranes of single electrolyzer remains challenging.[86] Thus, complementing RDE tests, catalytic performance tests using realistic membrane electrode assemblies (MEA) is mandatory.

SD I[1] (*Chapter 4*) reported a number of precious metal-free oxide materials based on Co, Fe, Ni and Mn with respect to the OER and ORR activity and stability using an RDE set-up alone. The data demonstrated the challenge of identifying a single catalyst material that shows a balanced bifunctional OER and ORR activity. All tested precious metal free oxides/hydroxides showed a more active OER than ORR activity. Especially NiFe-LDH showed exceptional OER activity, which was reported before.[87-90] Unfortunately, NiFe-LDH showed almost no ORR and also no other catalyst material showed sufficient ORR activity for use in a reversible electrolyzer. We conclude that oxide materials catalytically favor oxidation reactions rather than reduction reactions. Their limited bifunctional OER/ORR activity may also suggest that one single active site is not suitable for catalyzing the elementary reaction steps of the two opposite chemical reactions. The distinct reaction conditions of OER and ORR may therefore require quite different catalyst properties. In conclusion, the present work demonstrated that the most active and stable cathodic ORR catalysts consisted of metals and metal alloys,[29, 91] while anodic OER catalysts consist of metal oxides.[92-94]

Inspired by Norskov and Rossmeisl et al., we designed in **SD II**[2] (*chapter 5*) a two-component catalyst system that involved a number of different sites with distinct functionalities such as

multi-site surfaces (see *chapter 2.2.3 Oxygen electrode chemistry*) to circumvent the limitations of a single-active site.[59-61] Multi-sites catalytically active ensembles of surface atoms feature specialized surface sites for either the OER or the ORR. To realize such two component catalyst systems, NiFe-LDH as most active OER catalyst material from **SD I**[1] (*Chapter 4*) was brought in atomic proximity to nanostructured Fe-N-C catalyst, a well-known ORR active catalyst material.[95-100] As shown in **SD II**[2] (*chapter 5*), physical mixtures of NiFe-LDH:Fe-N-C in a ratio 1:3 showed unachieved bifunctional OER/ORR activity in 0.1 M KOH. To explain the observed combined performance of a physical mixture, a simple two-phase system provides two distinct and spatially separated ORR and OER catalytic sites that are sufficiently homogeneous to act as a contiguous catalyst film, yet are spatially separated enough not to interfere with each other. Further tests using an AEM (Tokuyama A201) and a commercial reversible electrolyzer confirmed the bifunctional activity and proofed the validity for a two-component mixture even in real reversible electrolyzer devices. Consequently, the two-component concept could open a new catalyst design for future bifunctional electrode applications.

Beside separated multi-site catalyst surfaces, the interaction between the two-components of the catalyst could also influence the mutual electronic and spatial structure at the boundary to form interfacial or ensemble sites (see *Figure 2-9* in *chapter 2.2.3 Oxygen electrode chemistry*). This concept was successfully introduced by theoretical DFT calculations from the group of Rossmeisl, who described Co and Ni modified RuO_2 surfaces which result in enhanced modified active sites that show activities beyond the volcano curve[57].

SD II[2] (*Chapter 5*) also demonstrated a chronopotentiometric instability of the Fe-N-C component of the two component hybrid oxygen catalysts after OER currents. During galvanostatic 24 h stability measurement and alternating hourly the current for ORR (at -3 mA cm^{-2}) and OER (at 4 mA cm^{-2}), the ORR current density decreased each cycle, while the OER performance displayed an almost stable electrode potential during the overall test. To compare this results, we used commercial Ir/C 20wt% and Pt/C 20 wt% in a 1:1 mixture, which showed on the one hand significant higher galvanostatic ORR but less OER stabilities and activites. The better OER activity and stability suggested the suitability of the NiFe-LDH material as a highly promising candidate as reversible electrolyzer catalyst component. The loss in ORR activity was likely due to carbon corrosion and the concomitant decomposition of the Fe-N_4 porphyrin-inspired active site.[101] Previous operando corrosion analysis of Fe-N-C catalysts in acidic electrolyte revealed the dissolution of Fe^{2+} centers at potentials < 0.7 V_{RHE} while carbon corrosion started at potentials > 0.9 V_{RHE} (cf. equation (2-24) and (2-25) in *chapter 2.2.4 Device*

concept: Electrolyzer, Fuel Cell, Unitized Regenerative Fuel Cells). So they concluded a stable potential window between 0.7 V_{RHE} – 0.9 V_{RHE}. Since this investigations used alkaline media, the validity of these stable potential window corresponding with the degradation processes at high pH remain uncertain. Typically, Fe appear stable as Fe_2O_3 at high pH,[102] so that Fe leaching process might be suppressed in alkaline. In contrast, carbon shows even less thermodynamic stability under alkaline conditions and the kinetics for carbon oxidation actually accelerates in alkaline environments due to OH^- anions being excellent nucleophiles.[103] Unfortunately, bifunctional oxygen catalyst materials used in reversibly operating electrolyzers perform at potentials larger than 2.0 V. Therefore, a stable carbon based material at OER potentials does not appear to be feasible. However, some groups have shown high stabilities for carbon based bifunctional catalyst materials. But those groups showed rather metal active sites using carbon as support[85, 104] than carbon-embedded nitrogen-coordinated metal ion centers (porphyrin type motifs),[105] which are still the current best performing precious metal free ORR catalysts.[29] Although the optimal metal center is still under debate, most recent findings indicate ionic Fe-center to be the most active and stable Me-N-C catalyst.[106, 107] Anyway, there is consensus that a non-carbon material should replace the ORR catalyst in future bifunctional two-component catalyst designs. Alternative precious metal free catalyst candidates such as metal oxides, metal nitrides, metal oxynitrides, metal carbonitrides, and metal chalcogenides with ORR activities rivaling those of Me-N-C or platinum are unknown to date.[29] There is only one exception and that is a recently discovered α-MnO_2 catalyst, reaching activities very close to Pt, which could be a promising non-carbon based ORR catalyst candidate,[108] but its OER/ORR suitability and stability is currently being verified.

NiFe-LDH proved very suitable as OER catalyst component for reversible electrolyzers working at high pH values. **SD I**[1] (*Chapter 4*) confirmed the already known outstanding activity and **SD II**[2] (*Chapter 5*) illustrated the stability of this material even after ORR potentials. Nevertheless, one objective was the investigation of a suitable catalyst regarding the selective oxidation of seawater into oxygen. Seawater consists of various anions and cations as shown in Table 2-1, but only chloride chemistry competes electrocatalytically with the oxygen chemistry, since their thermodynamic standard potentials are close. As described in chapter 2.3 (*Seawater Electrolysis*), Dionigi et al. elaborated a thermodynamic design criterion for the selective oxidation of seawater.[72] This design criterion calls for a limitation of the final working cell potential at or below 1.72 V_{RHE}, which is the thermodynamic standard potential of the hypochlorite formation at pH values above 7.5. Electrode potentials anodic of the design criterion likely leads to competing undesired chloride-involving reactions. This chloride

chemistry involves the formation of chlorine, hypochlorous acid (HClO) or hypochlorite (ClO^-) depending on pH (see Figure 2-11 in *chapter 2.3 Seawater Electrolysis*). All these product species are referred to as "free chlorine".

While the design criterion is based on thermodynamics, it does not take into account the kinetic barriers associated with the various chemical reactions. It turns out that not a lot of materials show sufficient kinetic catalytic OER activity at electrode potentials below 1.72 V_{RHE}. Here, NiFe-LDH appears as an ideal OER electrolyzer catalyst as it unfolded its potential before free chlorine was observed. This is why **SD III**[3] (*chapter 6*), investigated a full single cell membrane-based seawater electrolyzer using NiFe-LDH as single anode material. For benchmarking reason typical Pt/C 46.7 wt% (TKK) was used as cathode material.

SD III[3] (*chapter 6*) explored the behavior of a full single cell seawater electrolyzer using Tokuyama A201 as AEM, NiFe-LDH as anode, Pt/C as cathode material. As justified in chapter 2.3 (*Seawater Electrolysis*) a 0.5 M NaCl solution was used to mimic seawater. Since seawater splitting is favored at high pH, and large local pH changes toward more acidic conditions typically occur in unbuffered electrolytes near the reactive electrolyzer OER electrode surfaces,[109] the artificial seawater was alkalinized with 0.1 M, 0.5 M and 1 M KOH.

When the effect of seawater was investigated, 0.5 M NaCl-containing electrolytes showed a strong electrolyzer performance drop compared to pure KOH solutions and additional stability tests have shown, that the overall cell performance decreased to 50-70 % after 100 h at 1.6 V. This was in contrast to isolated, prior catalyst tests in which NiFe-LDH proved its suitability as seawater oxidizing catalyst, because no influence of NaCl on the NiFe-LDH catalyst performance was observed. Also, restarting the measurement revealed a recovery effect of the electrolyzer cell performance. From these results and complementary control tests, we conclude that the experimental instability of the seawater cell was more related to the membrane performance than the catalyst performance. (*Note that this section focus on the catalyst only, the next subchapter 7.1.2 describes the membrane issue in more detail.)*

To get more molecular insights in the chemical redox state and local geometry of the NiFe-LDH OER catalyst material, quasi in-situ XANES and EXAFS measurements were conducted in **SD III**[3] (*Chapter 6*) (cf. *chapter 3.3 Quasi in-situ X-ray absorption (XAS) – Sample preparation*).

The synergistic effect of Ni and Fe is undisputed, but whether Ni or Fe is the active site remains under debate. Using XAS analysis with DFT+U calculations Friebel et al. indicate the incorporated Fe^{3+} as active center in the $Ni_{1-x}Fe_xOOH$ material, since the Fe incorporation into γ-NiOOH changes the chemical bonding between this cation and the intermediates involved in

the OER.[110] Görlin et al. supported this finding [111] and Burke et al. agreed on Fe as active site, but emphasize an additional influence of local geometric structure on activity such as Fe in edge/defect sites versus bulk sites[112]. While Friebel et al. and Görlin et al. see a non-appearance of $Fe^{3+\rightarrow 4+}$ oxidation using XAS methods, especially Bard and Chen et al. have shown evidence for Fe^{4+} using Mössbauer spectroscopy [113, 114].

In contrast, **SD III**[3] (*Chapter 6*) showed already a high oxidation state of Ni in the NiFe-LDH at the activated state and measured at 1.0 V_{RHE}. Especially in seawater, no further oxidation was observed when the potential was increased to 1.6 V_{RHE}. As explanation, the group of Boettcher showed an insulating character of the reduced NiFe-LDH phase below a potential of ~ 1.4 V_{RHE} [88] which might prevent the reduction of the overlying NiFe-LDH film which was oxidized during the activation step in **SD III**[3] (*Chapter 6*). Consequently, a large amount of the metal centers, which were oxidized, remain oxidized and the bulk sensitive XAS, which observes the average valence state of the bulk, cannot directly discriminate among the various centers. To optimize the investigations the catalyst film thickness should be minimized as much as possible.

EXAFS evaluation focused more on coordination number of the metal centers. Consistent with the oxidation state, the Ni- and Fe-centers showed especially for the seawater high coordination numbers (CN) after activation at 1.0 V. The lower CN for the 0.1 M KOH at activated 1.0 V_{RHE} suggests a catalyzing oxidation effect by the higher ionic strength of NaCl. The stronger the ionic strength of the electrolyte the easier the oxidation during the activation step and the higher the coordination number of the activated metal centers. This is in agreement with the electrochemical measurement, since the initial $Ni^{ox/red}$ redox features appear larger in higher concentrated electrolytes. Additional degradation effects by the appearance of Cl^- was not determined. The local structure in both KOH and seawater rather attained identical after prolonged operation. This also supports the idea that membrane degradation processes are largely responsible for the experimental losses in catalytic performance (cf. *chapter 7.1.2Reversible seawater electrolyzer: Membrane*).

While this thesis focused mainly on catalysts for the oxygen electrode, the hydrogen electrode plays an almost equally important role in reversible seawater electrolyzers. This is why in the next section, we will discuss hydrogen electrode catalysts. For this thesis and for benchmarking reasons in every cell measurement of **SD II**[2] (*Chapter 5*) and **SD III**[3] (*Chapter 6*) we used Pt/C 46.7 wt% (TKK) as hydrogen electrode catalyst material. Even though Pt/C is not an optimized HER/HOR catalyst, it shows sufficient activity with acceptable HER/HOR overpotentials.

Even though the efficiency loss of a state of art hydrogen electrode is very low compared to an oxygen electrode,[115] an improved hydrogen evolution catalyst, especially for alkaline pH conditions, would increase the overall cell performance. However, Pt based catalysts show outstanding HER/HOR performances in acid and somewhat lower performance in alkaline conditions, which makes it difficult to replace this catalyst with precious metal free materials. Suitable novel catalysts for the hydrogen electrode catalysts that compete with Pt based catalysts appear highly challenging. Consequently, several approaches follow the path in reducing the Pt amount on the electrode without reducing the overall activity. Reported precious metal free materials for the HER are metal alloys(Ni–Co, Ni–Mo, Ni–Mn), substrates with 3d transition metal (3d-TM=Ni, Co,Fe,Mn) hydroxides (3D-TM$(OH)_2$), 3d–TM phosphides (CoP,NiP), 3d-TM carbides (WC_x, MoC_x), transition, metal sulfides (TMSx=MoS_2, CoS_2, FeS_2, Mo_3S_{13})[116] and also NiFe-LDH shows slight activity towards the HER.[117] For the HOR it is reported that all non-PGM catalysts that are currently known to catalyze the HOR comprise nickel, often alloyed with a one or more non-PGM metals.[118] Hence, only a Ni-based bifunctional hydrogen electrode seem as a possible precious metal free alternative based on the reported materials.

In summary, this subchapter discussed the catalysts materials and concepts explored in this thesis research. For a bifunctional catalyst the concept of a two-component catalyst using NiFe-LDH mixed with Fe-N-C is discussed and presented in **SD II**[2] (*Chapter 5*). This concept employs multi-sites and circumvent the limitations by a single-active site as it was shown in **SD I**[1] (*Chapter 4*). In **SD II**[2] (*Chapter 5*) and **SD III**[3] (*Chapter 6*), NiFe-LDH proofed its electrolyzer catalyst suitability even in membrane based reversible electrolyzer and in a direct seawater electrolyzer, while the used Fe-N-C catalyst suffered strong carbon corrosion at high OER potentials. Thus, α-MnO_2 is suggested to replace the carbon based Fe-N-C catalyst to employ a carbon free OER/ORR bifunctional catalyst in future reversible electrolyzer devices. Although the hydrogen electrode was not investigated in detail, based on literature Ni-based materials are suggested as precious metal free bifunctional HER/HOR catalyst material.

7.1.2 Reversible seawater electrolyzer: Membrane

SD II[2] (*Chapter 5*) and **SD III**[3] (*Chapter 6*), suggest a large impact of the membrane properties and behavior on the overall cell performance and stability of electrolyzers and fuel cells. In **SD II**[2] (*Chapter 5*) the overall cell performance drop per fuel cell/electrolyzer cycle, which was clearly not attributable to catalyst instability alone, instead suggested a large

alkaline membrane-based degradation effect. In addition, **SD III**[3] (*Chapter 6*) highlight the AEM as bottleneck for membrane based electrolyzers.

Unlike alkaline membranes, proton exchange membranes (PEM) have been extensively investigated and optimized, with maximized proton conductivity, high thermal stability and high efficiencies.[119] The hydroxide conductivity and alkaline stability of AEM, however, are still a serious challenge. The disadvantage of PEM are the strong acidic conditions, which require noble metal materials to avoid metal solvation and ensure long-term stability. The best-known PEM is Nafion® showing ionic conductivities at 60 °C of > 0.1 S cm^{-1}, while AEM exhibit ionic conductivities between 0.06 – 0.01 S cm^{-1} only.[120]

The objective of this work to use precious metal free materials (cf. *chapter 1.3 Hydrogen economy catalysts: The platinum group metal (PGM) problem*) and the favored selective seawater splitting in alkaline conditions (cf. *chapter 2.3 Seawater Electrolysis*) required the use of an AEM. Thus, an AEM (Tokuyama A201) is used for the cell measurements in **SD II**[2] (*Chapter 5*) and **SD III**[3] (*Chapter 6*). Based on quaternary ammonia (QA) groups, the Tokuyama A201 is one of the most common class of NaOH-/KOH-free AEMs.[120, 121] Generally, these membranes have reasonable stability in alkaline environments.

However, in **SD III**[3] (*Chapter 6*) the cell performance diminished gradually in KOH solutions higher than 0.1 M and indicated membrane degradation. But known membrane degradation mechanism like the direct nucleophilic displacement or Hofmann elimination of the trimethylammonium groups (see Figure 7-1) are common at elevated temperatures (> 75 °C) and at OH^- concentrations (> 6 mol L^{-1}).[122, 123] Here, we applied a maximum temperature of 50 °C and a maximum anion concentration (Cl^-, OH^-) of 1.5 M.

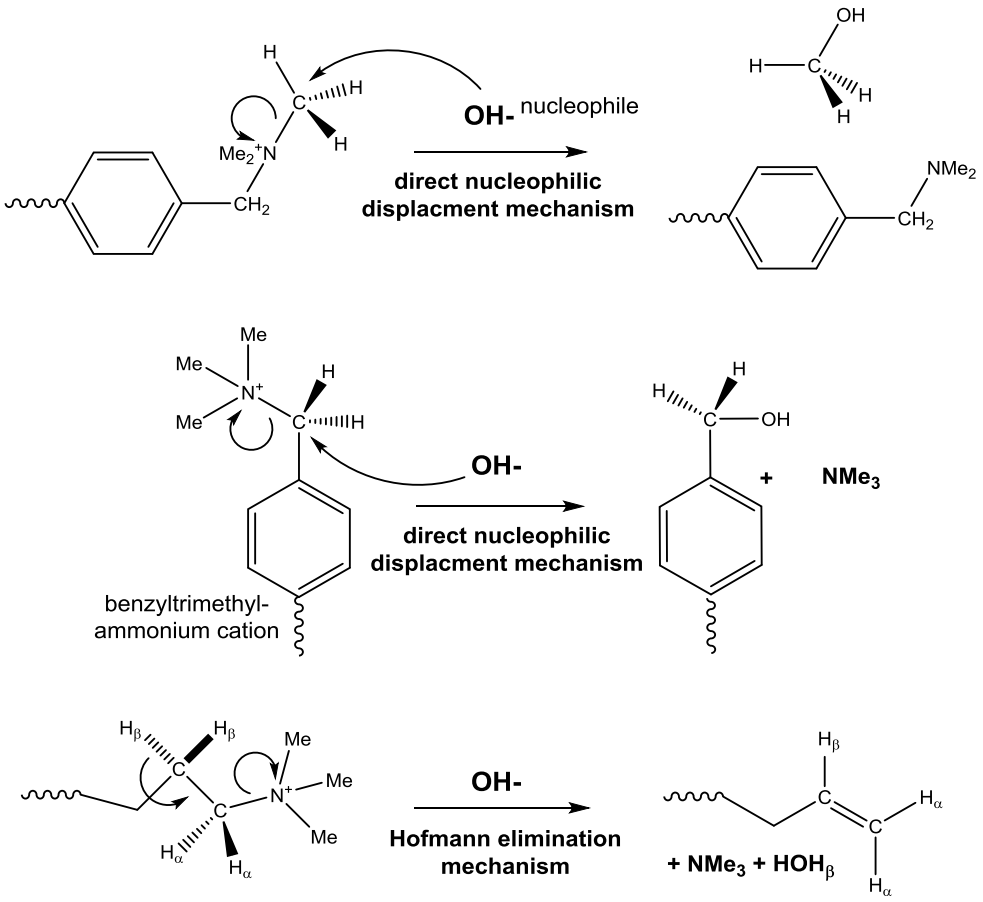

Figure 7-1: Alternative mechanisms for degradation of AEMs by displacement of the quarternary trimethylammonium groups by hydroxide anions. Adapted from [122]

Another traditional AEM fuel cell issue could be the formation of carbonate or bicarbonate in the electrolyte due to the CO_2 content in the atmosphere:[120]

Carbonate formation: $$CO_2 + 2OH^- \rightarrow {CO_3}^{2-} + H_2O \quad (7\text{-}1)$$

Bicarbonate formation: $$CO_2 + OH^- \rightarrow {HCO_3}^- \quad (7\text{-}2)$$

Consequently, Na_2CO_3 and K_2CO_3 could precipitate in the membrane or even in the electrolyte filled pores of the electrode, blocking ion conductive channels and active sites of the catalyst layers. This could also give one explanation of the determined recovery effect after restarting the measurement as shown in **SD III**[3] (*Chapter 6*). The precipitated salt could dissolve during the electrolyzer break due to relaxation inside the MEA and uncover the blocked membrane channels, resulting in on the one hand "recovered" cell performances but on the other hand repeated precipitation after the measurement is started again.

Another important point for reversible fuel cell membranes is the fact that the conditions under electrolyzer and fuel cell operation are entirely different. Fuel cells use humidified gases but electrolyzers require liquid water or electrolyte. Consequently, the electrolyzer membrane conductivity can be enhanced by using KOH containing electrolytes. In contrast, AEMs for fuel cells using humidified gases depend on the ionic conductivity caused by reactive humidification of the membrane across the electrode-membrane interface, which is a function of current density drawn from the fuel cell. In addition, such as PEM also AEM are not conductive in the dry state, which makes water management highly important.

In **SD II**[2] (*Chapter 5*) the reversible electrolyzer cell was switched repeatedly between fuel cell and electrolyzer mode, showing very limited reversibility because the cell performance diminished gradually from cycle to cycle. The fact that, unlike the cell tests, the RDE measurements revealed high OER stability at comparable potentials. This suggests rather membrane-based performance losses as the primary origin of cell degradation, than a catalyst corrosion induced. Notwithstanding this conclusion, other effects such as cell flooding could play also an additional role.

An additional component that affects stability of electrolyzers and fuel cells is the catalyst binder employed. The catalyst binder, required for MEA preparation (cf. *chapter 3.1 Membrane electrode assembly (MEA) and electrolyzer cell set-up*), typically consist of the soluble version of the polymeric ionomer that serves as membrane. Even though Nafion is a common binder for perfluorinated cationic exchange membranes, and is known for high chemical stability. We replaced the Tokuyama AS-4 binder with Nafion in an unpublished test for **SD III**[3] (*Chapter 6*). Figure 7-2 shows the additional MEA electrolyzer tests using a Tokuyama AS-4 and Nafion on a Tokuyama A201 membrane in 0.5 M KOH and 0.5 M NaCl.

As **SD III**[3] (*Chapter 6*) demonstrated and as discussed above, the electrolyzer test using an alkaline Tokuyama AS-4 ionomer showed a high initial activity but a sharp decrease in performance. Since the MEA with Nafion as binder showed a significant higher stability, but a comparably low initial performance. Interestingly, the prolonged current densities of both long term measurements realigned after 100 h. Surprisingly, the performance recovery of the Tokuyama AS-4 binder measurement analyzed in detailed in **SD III**[3] (*Chapter 6*) fell below that of the Nafion binder cell, indeed indicating a strong influence of the binder regarding the recovery effect. This binder test showed that alternative binders even based on cation exchange ionomers can affect stability and overall cell performance of AEM electrolyzers.

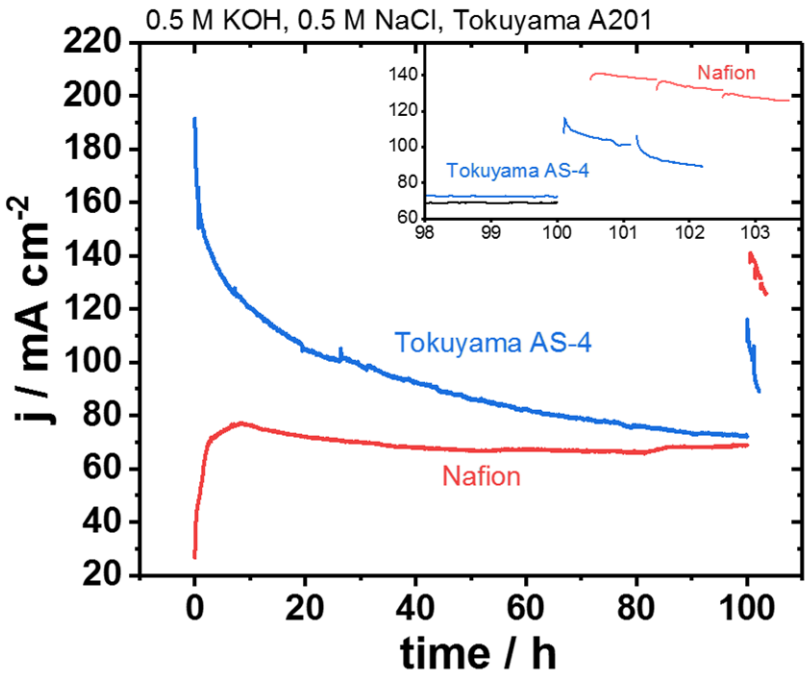

Figure 7-2: Potentiostatic seawater electrolyzer stability test in 0.5 M KOH and 0.5 M NaCl using Nafion and Tokuyama AS-4 as binder on a Tokuyama A201 membrane with NiFe-LDH as anode and 46.7 wt% Pt/C (TKK) as cathode material.

Besides the membrane stability, **SD III**[3] (*Chapter 6*) showed a significant lower cell performance for 0.5 M NaCl containing KOH electrolyte compared to pure 0.1M, 0.5 M and 1.0 M KOH electrolyte. A higher membrane resistance of the NaCl containing electrolyzer test evidenced an influence of the Cl^- anions on the overall ohmic conductivity. To explain this, we hypothesize that Cl^- ions coordinate at QA and partially block OH^- from the anion transport channels of the membrane, which resulted in lower total electrolyzer cell performance. An anion selective membrane or separator could help to circumvent this challenge, even though the design and realization of such a selective membrane has remained very challenging.[124]

In short, this subchapter discussed the membrane based issues of AEM, indicated by **SD II**[2] (*Chapter 5*) and **SD III**[3] (*Chapter 6*). Typical membrane degradation mechanisms like nucleophilic replacement or Hofmann elimination is taking place at temperatures and KOH concentrations beyond the applied conditions in **SD III**[3] (*Chapter 6*). Hence, the precipitation of carbonate salts in the membrane might block ion conducting channels. Relaxation of the MEA at OCV help dissolving the precipitated salts which could explain the determined recovery effect. To overcome the cell performance drop in NaCl containing electrolyzer cells in **SD III**[3] (*Chapter 6*) an OH^- selective membrane is suggested.

7.1.3 Reversible seawater electrolyzer: Cell components

This subchapter will focus on the remaining cell components of a reversible seawater electrolyzer, namely:

- Porous transport layer (PTL) (electrolyzer) / gas diffusion layer (GDL) (fuel cells)
- Bipolar plates
- Flow fields

Although primarily the PTL and GDL was investigated, for completion also the bipolar plate and the flow field will be discussed briefly at the end of this subchapter.

Chapter 2.2.4 (*Device concept: Electrolyzer, Fuel Cell, Unitized Regenerative Fuel Cells*) impressively demonstrated how carbon materials significantly start to corrode at potentials higher 1.0 V_{RHE}, which limits the material selection for electrolyzer and reversible electrolyzer cell components, in which typically titanium is employed as common material for bipolar plates, flow fields and PTL. This is why Ti meshes were employed as PTLs. However, unpublished electrolyzer tests for **SD III**[3] (*Chapter 6*) showed that a specific Ti-mesh from a Korean company (Carbon and FuelCells / CNL) was unsuitable as PTL due to poor electrolyzer performance as shown in Figure 7-3.

Looking at the Pourbaix diagram Ti transforms into a protective and passivated TiO_2 layer at potentials > 0.1 V_{RHE} [125] This layer even spontaneously forms in air. We believe that this TiO_2 protection layer prohibit the electrical contact between the catalyst layer and the bipolar plate, so that low charge transfer conductivity at the boundary between catalyst layer and PTL might explain these low current densities.

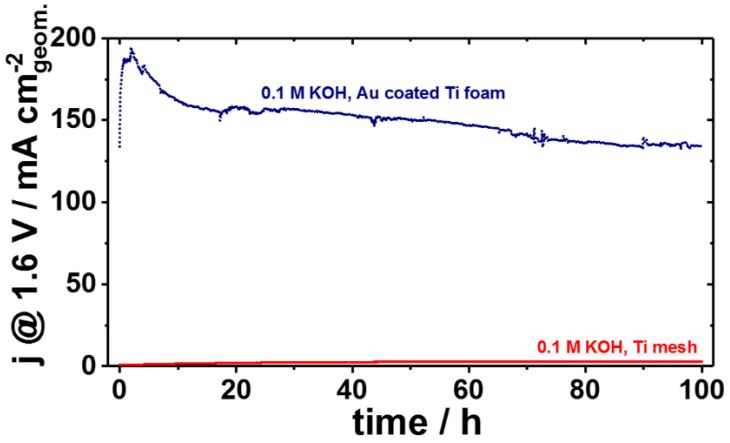

Figure 7-3: Potentiostatic seawater electrolyzer stability test using different anode PTL. The MEA was made from Tokuyama A201, NiFe-LDH as anode and 46.7 wt% Pt/C (TKK) as cathode material using Tokuyama AS-4 as ionomer

The slight elevation of current density during the 100 h electrolyzer test might be due to the initiation of pitting, which might intensify with longer time. To circumvent the insulating passivation layer we used a gold coated Ti mesh instead of pure titanium. Accordingly, Figure 7-3 showed significant performance increase for the 100 h measurement using a gold-coated titanium foam instead of pure Ti-mesh.

Seeking for the optimized PTL we performed additional but unpublished pre-tests. Figure 7-4 shows the simplified sketch of the PTL stability detection for **SD III**[3] (*Chapter 6*).

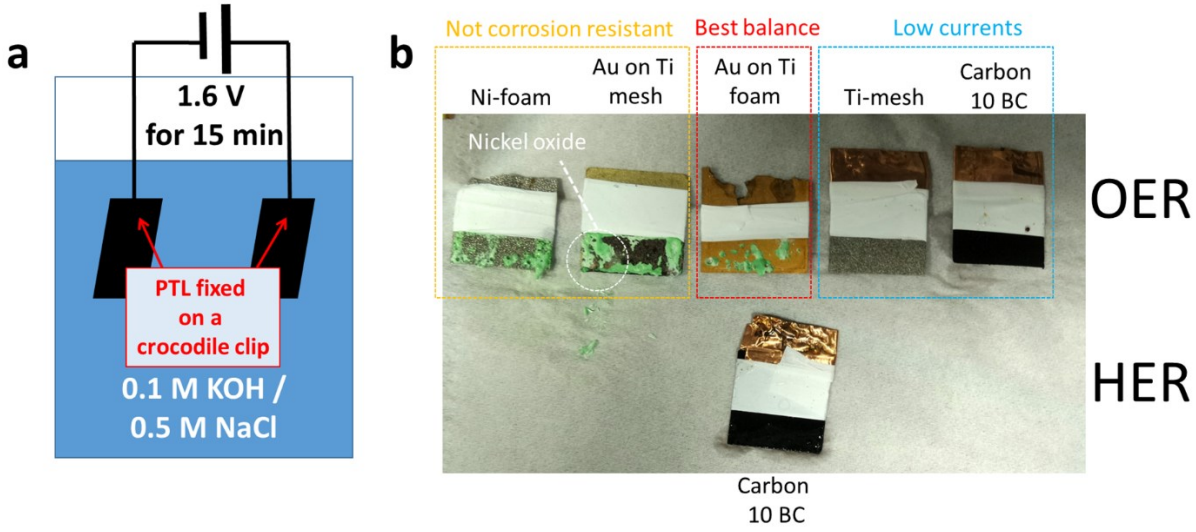

Figure 7-4: (a) GDL pre-tests set-up for testing the GDL stability (b) various GDL after 15 min at 1.6 V in a 0.5 M KOH and 0.5 M NaCl electrolyte solution.

Simulating the electrolyzer conditions, we used a potential of 1.6 V in a two-electrode set-up. The PTLs were fixed with crocodile clips and immersed into the 0.1 M KOH and 0.5 M NaCl electrolyte. At the cathode (HER) a Carbon 10 BC and at the anode (OER) various PTL were used. As already shown in Figure 7-3, uncoated Ti-mesh was not suitable for seawater electrolyzers as it showed insufficient performance. Consistently, the Ti-mesh showed no visible corrosion effect. The same applies for the Carbon GDL, however, carbon corrosion might not be visible after the short testing time of 15 min. The Ni foam and the Au coated Ti-mesh (CNL) showed significant corrosion effects due to green precipitations. Elemental analysis by X-ray fluorescence indicated that the green deposits consist of Ni oxide.

Figure 7-5 shows additional EDX tests on untreated Au coated Ti-mesh (CNL) and revealed Ni in significant amounts in the PTL.

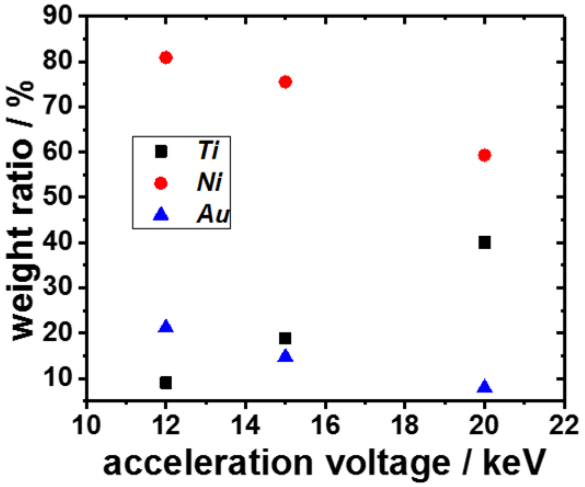

Figure 7-5: Depth resolved EDX compositional analysis untreated gold-coated Ti-mesh. To determine the atomic composition in different material depths beam acceleration voltage are varied to 12 keV, 15 keV and20 keV which roughly correspond to penetration depths of 0.5 µm, 0.7 µm and 1.5 µm.

Even though the Au on Ti foam (CNL) (Figure 7-4b) showed slight NiO_x deposition, EDX showed negligible Ni contents. Accordingly, the gold-coated foam was used in **SD III**[3] (*Chapter 6*).

Bipolar plates and the nature and geometry of the flow fields were not experimentally investigated in this thesis and are consequently not optimized, yet. Still, for completion necessary optimizations will be identified and briefly discussed in the next section.

Bipolar plates that are used in single lab-scale electrolyzer cells are end plates and typically come with integrated flow fields. Accordingly, in **SD II**[2] (*Chapter 5*) a gold coated titanium bipolar plate and **SD III**[3] (*Chapter 6*) a titanium bipolar plate with serpentine flow fields were used for the oxygen side. For the hydrogen side a graphite bipolar plate with integrated serpentine flow field was used. The gold-coated titanium bipolar plate was used to achieve better electrical conductivity and to avoid strong resistivity increase by TiO_2 formation,[126] but after frequent use the gold coating detached easily from the titanium. Nevertheless, additional unpublished tests showed, that in contrast to the PTLs, switching between the gold coated titanium and the titanium bipolar plate did not show any difference in electrolyzer cell performance. Consequently, the electric contact appeared to be sufficient in the electrolyzer even without the gold coating. Hence, in **SD III**[3] (*Chapter 6*) the pure titanium was used for better corrosion resistance. Beside these kind of bipolar plates, also various other bipolar plate materials and other coatings exist, all specified for their final applications.[127] Thus, the bipolar plate might still be improved, but for reversible seawater electrolyzers the titanium bipolar plate as used in industry, seem to be the most suitable.

The last topic of this section is the flow field. As already mentioned, in **SD III**[3] (*Chapter 6*) a single channel serpentine flow field was used, which could still be optimized. Since decades, various investigations have been made, seeking the optimized flow field geometry for fuel cells. Typical geometries are parallel, interdigitated and serpentines. For fuel cells, the serpentine geometry shows superior performance stability and water management compared to other.[128-131] The flow field research for electrolyzers appears smaller, however, parallel flow fields prevailed due to greater cell performances.[132] As a result, in reversible seawater electrolyzer the serpentine geometry might be the best choice, but in future direct seawater electrolyzers without fuel cell abilities, a parallel flow field appears to be more suitable.

This subchapter discussed the optimization process for the residual reversible electrolyzer cell components such as PTL and GDL. While gold coated Ti-foam demonstrated its suitability and a Ti bipolar plate shows sufficient anode stability, the flow fields still provide open potentials to optimize a final reversible electrolyzer device.

7.1.4 Summary: Is a reversible seawater electrolyzer feasible?

This chapter discusses the feasibility of reversible seawater electrolyzer and addressed current challenges based on **SD I**[1] (*Chapter 4*), **SD II**[2] (*Chapter 5*) and **SD III**[3] (*Chapter 6*) with a particular focus on catalysts, membranes and other cell components such as PTL and flow field geometries. The discussion showed the major challenges that needs to be tackled to realize a reversible seawater electrolyzers. The concept of a two-component catalyst with multiple sites appears promising, yet the major challenge remains in identifying a suitable ORR catalyst that is stable even at OER potentials. α-MnO_2 might be a promising candidate, as ongoing studies show. However, this thesis revealed also that it is especially the AEM that lacks long-term stability. The performance drop after adding 0.5 M NaCl indicated a Cl^- induced ionic OH^- transfer conductivity loss of the membrane, suggesting the development of an OH^- selective AEM.

Once these challenges are met, a reversible seawater electrolyzer appear well feasible. However, beside the technical and economic feasibility, there remains the question related to the necessity of this kind of technology? Which possibilities does seawater electrolysis provide and how would be the energy efficiency of direct seawater electrolyzer compared to already established technologies for fresh water or electricity? This important point will be discussed in the next section.

7.2 Reversible seawater electrolyzer as freshwater resource and electrolyzer efficiencies?

This subchapter is based on and reproduced with permission from **SD V** [5].

Direct electrolytic splitting of seawater – Opportunities and challenges

***Dresp, S.**, Dionigi F., Klingenhof, M., Strasser, P,*

ACS Energy Letters, 2019, 4, 933-942, DOI: https://doi.org/10.1021/acsenergylett.9b00220

---

*Detailed and additional information can be found in the publication reprint in **Appendix II***

In contrast to established desalination technologies, an appealing possibility related to seawater electrolysis consists in the production of freshwater when back transforming the hydrogen and oxygen into electricity and water, as indicated in the inset in Figure 7-7. At the beginning of this discussion I like to remind the overall equation for the general water electrolysis. The equation for the water splitting process and its corresponding molar weight and energies are given in Figure 7-6.

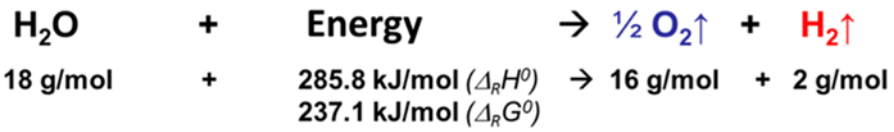

Figure 7-6: Water splitting equation with its corresponding molar weight and energies.

Where $\Delta_R H^0$ is the reaction enthalpy and $\Delta_R G^0$ is the free enthalpy. Accordingly, to produce 1 kg H_2 9 kg of water are required. As already discussed in chapter 2.2.1 (*Fundamental thermodynamics of hydrogen chemistry*), a thermodynamic fuel cell efficiency is given by the relation of the free enthalpy $\Delta_R G$ and the reaction enthalpy$\Delta_R H$. Consequently, the theoretical overall efficiency at the thermodynamic limits at standard conditions is calculated in equation (7-3)):

$$\eta_{theoretical} = \frac{\Delta_R G^0}{\Delta_R H^0} = \frac{237.1\ kJ\ mol^{-1}}{285.8\ kJ\ mol^{-1}} \approx 83\% \qquad (7\text{-}3)$$

Accordingly, the thermodynamic reverse processes of water splitting show a theoretical overall efficiency of ~83 %. Therefore, ~17 % of the energy will be lost during this transformation cycle. The water density at room temperature is $\rho = 0.997\ kg \cdot L^{-1}$, so that 1 Nm^3 of H_2O is about 997 kg. Following this, equation (7-4) results in:

$$n\ (H_2O) = \frac{m(H_2O)}{M(H_2O)} = \frac{997\ kg}{0.018\ kg\ mol^{-1}} = 55\ 389\ mol \tag{7-4}$$

The reaction enthalpy $\Delta_R H^0 = 285.8$ kJ from Figure 7-6 gives the required energy to split 1 mole of H_2O. Equation (7-5) and (7-6) show the necessary energy to split a volume of water corresponding to 1 Nm^3 $\left(1\ Nm^3_{H_2O}\right)$.

$$E\ \left[\frac{kJ}{Nm^{-3}_{H_2O}}\right] = n_{H_2O} \cdot \Delta_R H^0 = 15\ 830\ 144\ \frac{kJ}{Nm^{-3}_{H_2O}} \tag{7-5}$$

$$E\ \left[\frac{kWh}{Nm^{-3}_{H_2O}}\right] = 15\ 830\ 144\ \text{kJ}\ \cdot\ 0.000278\ \frac{kWh}{kJ} = 4401\ \frac{kWh}{Nm^{-3}_{H_2O}} \tag{7-6}$$

Thus, the energy of 4401 $\frac{kWh}{Nm^{-3}_{H_2O}}$ are theoretical necessary to split 1 $Nm^3_{H_2O}$ and the thermodynamic energy loss is in fuel cells is about 17 % which correspond to ~ 750 kWh $\frac{kWh}{Nm^{-3}_{H_2O}}$. The remaining energy content of H_2 is about 3651 kWh based on $\Delta_R G^0$, which can theoretically extracted in fuel cells with a 100 % efficiency. Assuming more realistic efficiencies, such as 79 % for the electrolyzer **SD III**[3] and 50 % for the fuel cell[133] the production of 1 $Nm^3_{H_2O}$ suffers an overall energy loss of 3370 kWh $Nm^{-3}_{H_2O}$.**SD V** [5]

Compared to other established desalination technologies, like the reverse osmosis, the multi-stage flash distillation, multi effect distillation and mechanical vapor compression, the consumption to desalinate 1 $Nm^3_{H_2O}$ for a reversible seawater electrolyzer is about several magnitudes higher as shown in Figure 7-7.[134-136]

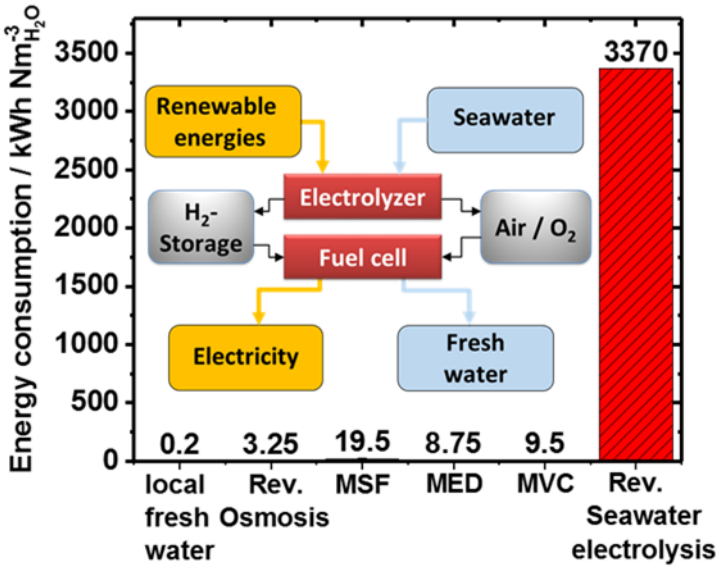

Figure 7-7: Energy consumption of various desalination technologies and the local water treatment supplier per Nm3. MSF = multi-stage flash distillation, MED = Multi effect distillation and MVC = mechanical vapor compression. Values are taken from.[134, 136] The reversible seawater electrolysis is based on a perfect working electrolyzer and fuel cell at the thermodynamic limits. Inset: Sketch for reversible seawater electrolysis based on renewable energy. Reprinted with permission from **SD V**[5]. Copyright 2019 American Chemical Society.

Although the water produced in the fuel cell process is highly purified, the reverse osmosis is by far the current most efficient technology for the production of freshwater. Still, reverse osmosis brings many drawbacks, like the frequent maintenance of the membrane and the exhaust saltwater feed harms the environment. Only the water treatment of local fresh water supplier consumes less energy per 1 $Nm^3_{H_2O}$.

Vice versa, 1 $Nm^3_{H_2O}$ produces H_2 that corresponds to 3651 kWh energy (based on $\Delta_R G^0$) or 2200 kWh (based on 50 % fuel cell efficiency; for more information see **SD V** [5]). This is equal to the electricity demand for an average household in Europe. On the one hand, this illustrates the high energy content of hydrogen and underlines the importance of electrolyzer technologies to store surplus renewable electricity. On the other hand, 1 $Nm^3_{H_2O}$ amounts to the cumulative yearly recommended intake of freshwater of 2–3 L. However, one person consumes significantly more water than 1 $Nm^3_{H_2O}$ per year. As a result, reversible seawater electrolysis should be perceived more as an energy storage technology than a freshwater production technology when transforming the hydrogen back into electricity and water by using the fuel cell.

One possible technological use of seawater electrolysis for the purpose of a constant and sustainable freshwater production by a combination of photovoltaic with reverse osmosis, electrolyzers and fuel cell is shown in Figure 7-8.

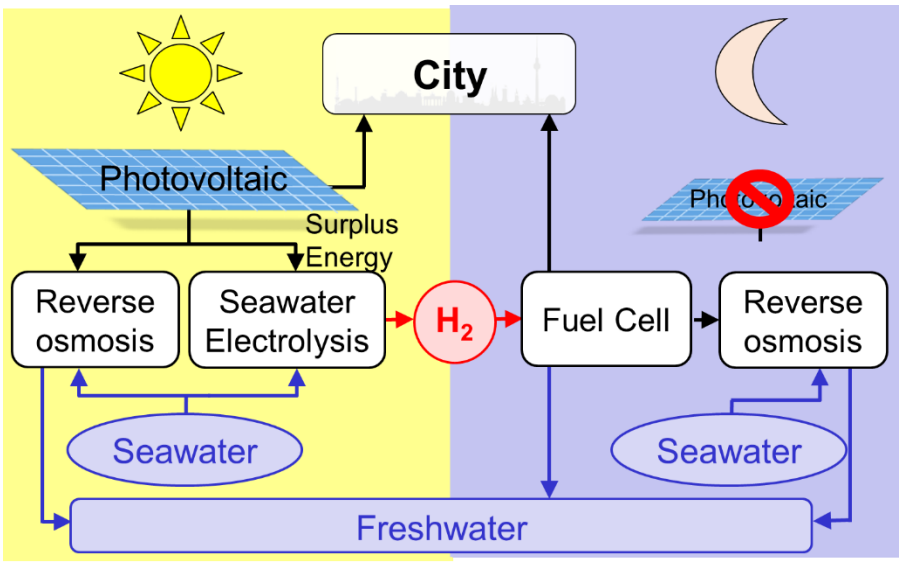

Figure 7-8: Sketch of probable solution for freshwater production based on seawater electrolysis. Reprinted with permission from **SD V**[5]. Copyright 2019 American Chemical Society.

At daytime, the photovoltaic deliver the electricity for reverse osmosis and the electricity demand of the city, while excess energy supply the direct seawater electrolyzer, which produces hydrogen. The reverse osmosis desalinates the seawater and provide the freshwater while the electricity demand of the city is met by the photovoltaic. At nighttime when the photovoltaic process is not possible, the fuel cell can produce freshwater and provide the reverse osmosis with electricity. Surplus electricity from the fuel cell supplies the city with electricity. To conclude, the direct seawater electrolysis overall shows promising potential for the production of hydrogen. As a side effect, water is formed during the fuel cell reaction, which amount is not sufficient for the worldwide fresh water supply; but it could support the established water treatment industry.

7.3 Seawater efficiency and performance compared to established technologies

This subchapter is based on and reproduced with permission from **SD V** [5].

Direct electrolytic splitting of seawater – Opportunities and challenges

***Dresp, S.**, Dionigi F., Klingenhof, M., Strasser, P,*

ACS Energy Letters, 2019, 4, 933-942, DOI: https://doi.org/10.1021/acsenergylett.9b00220

---

*Detailed and additional information can be found in the publication reprint in **Appendix II***

Compared to already established technologies the direct seawater electrolysis shows, however, many advantages. **SD III**[3] (*Chapter 6*) showed voltage efficiencies between 75-79 % of a direct seawater electrolyzer related to the higher heating value (HHV) (see also Table 7-1), which is comparable to current PEM and alkaline electrolyzers. An alternative scenario to direct seawater electrolyzers suggests the combination of a pre-desalination step with a subsequent established PEM or alkaline electrolysis as shown in Figure 7-9.

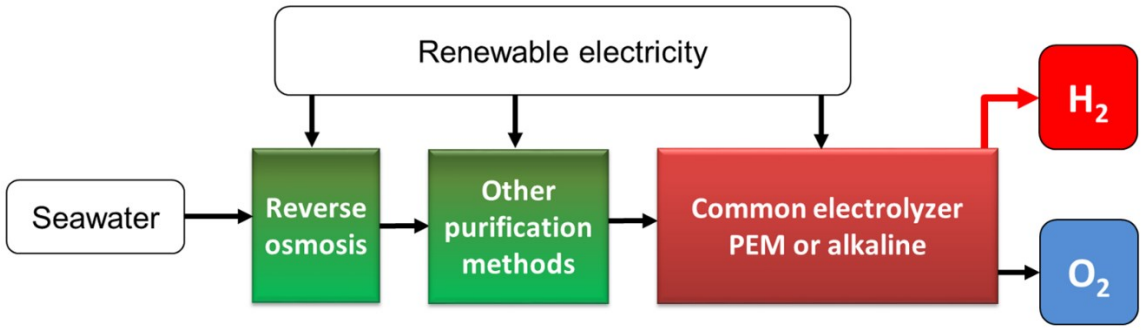

Figure 7-9: Sketch of alternative seawater electrolysis design with common technologies. Reprinted with permission from **SD V** [5]. Copyright 2019 American Chemical Society.

In this concept the seawater could be purified by reverse osmosis which is powered by renewable electricity. After the first desalination another purification step could be added to deliver the suitable water quality for the PEM or alkaline electrolyzer. According to Figure 7-6, 9 kg of water are necessary to produce 1 kg of H_2. Reverse Osmosis use $E_{Rev.\ Osmosis}$ = 3.25

$kWh \cdot Nm_{H_2O}^{-3}$ for the desalination of 1 Nm³ seawater. The resulting desalinated water has a density of 997 $kg \cdot Nm_{H_2O}^{-3}$. Equation (7-7) shows the minimum energy for pre-desalination step via reverse osmosis to produce the water necessary for 1 kg H_2.

$$E\left[\frac{kWh}{kg_{H_2}}\right] = \frac{3.25\ kWh \cdot Nm_{H_2O}^{-3}}{997\ kg_{H_2O} \cdot Nm_{H_2O}^{-3}} \cdot 9\ kg_{H_2O} \cdot kg_{H_2}^{-1} = 0.03\ kWh\ \ kg_{H_2} \qquad (7\text{-}7)$$

Consequently, for the production of 9 kg purified H_2O only 0.03 kWh are required. To get an idea about the production of 1 kg H_2, the literature values for common electrolysis technologies and the direct seawater electrolysis is shown in Table 7-1:

Table 7-1: Performance indicators of different technologies for the production of 1 kg hydrogen and voltage efficiencies of electrolyzers. Data is taken and converted from [137] and **SD III** [3] (*Chapter 6*)

Technology	Specific energy consumption (Stack) [kWh kg_{H2}^{-1}]	Voltage efficiency based on HHV [%]	Literature
PEM-electrolysis	47 - 63	67- 82	[137]
Alkaline electrolysis	47 - 66	62 - 82	[137]
Direct seawater electrolysis	50 - 53	75 - 79	**SD III**[3] (*Chapter 6*)

Although the established systems can reach slightly higher efficiencies of 82 % and lower specific energy consumptions of 47 $kWh\ kg_{H_2}^{-1}$,[137, 138] a direct seawater electrolyzer appear competitive with voltage efficiencies of 79 % and a specific energy consumption of 50 $kWh\ kg_{H_2}^{-1}$. Still, the PEM and alkaline electrolyzer systems would need a pre-desalination step, since interfering ions would malfunction these devices.

For the necessary purification of 9 kg H_2O via reverse Osmosis only 0.03 kWh are required (cf. equation (7-7)). Even with an excess of 10 times and the resulting 0.3 kWh, the energy consumption of the reverse osmosis compared to PEM or alkaline electrolysis is almost negligible. Still, the purity of water produced by reverse osmosis does not reach the required level,[139] since especially the typical PEM membranes require highly purified or even ultra-

purified water. In reality, this combination would need an additional purification step that require higher energy, more space and a third device to purchase.

In contrast, the catalysts and separators (not membranes) of alkaline electrolyzers are more tolerant for impurities than PEM-electrolyzers. But they require high amounts of KOH, since they typically work with KOH concentrations of up to 20 - 40 wt%.[140] In addition, unavoidable traces of chloride ions would be oxidized to hypochlorite ions harming the catalyst and the long-term stability of the system. Nevertheless, this technology comes closest to the suggested alkaline seawater electrolyzer concept **SD III**[3] (*Chapter 6*), but with additional pre-purification that require additional space. Therefore, even those combinations with higher performances do not seem the ideal solution, since the typical application for seawater electrolyzer might be for offshore wind parks without electricity connections or areas without easy access but strong solar irradiation. Consequently, the space is highly restricted and the technology should therefore be as small as possible and the maintenance should be minimized so that the system should work as robust as possible. A single device like the direct seawater electrolyzer with its compact single design shows the smallest even possible space requirement and therefore a minimized maintenance costs. Thereby, the direct splitting of seawater is highly desirable and avoids additional costs in purchase and maintenance costs for additional purification modules at comparable overall efficiencies.

Overall, the direct seawater electrolysis seems to become an important technology of the future. It can be deployed at the most efficient regions where high renewable energy potential is combined with access to seawater. Compared to established PEM and alkaline electrolyzers, the seawater electrolyzer could show competitive efficiencies of 75 - 79 % voltage efficiencies. In addition, due to the simplified and compact design, less challenges needs to be tackled. Additional pre-purification of seawater would reduce the robustness of the system, since reverse osmosis systems require frequent maintenance and other methods need high energies and therefore reduce the overall efficiency. Also, reverse osmosis as pre-purification compete with the main application: to produce fresh water for other human activities. Therefore, the direct usage of seawater for the production of hydrogen would be highly desirable and would make this technology extremely flexible. Existing offshore wind parks and especially sun rich coastal desert regions would benefit from this simple technology, since the produced hydrogen could back transformed into electricity and water, which could support the established water provision industries. Furthermore, the oceans contain an almost unlimited reservoir of seawater so that this represents an ideal candidate as water resource for electrolyzers of the future.

7.4 Summary of chapter 7

The first part of this chapter discussed the feasibility of reversible seawater electrolyzer and addressed current challenges based on **SD I**[1] (*Chapter 4*), **SD II**[2] (*Chapter 5*) and **SD III**[3] (*Chapter 6*) with a particular focus on catalysts, membranes and other cell components such as PTL and flow field geometries. The discussion showed the major challenges that needs to be tackled to realize a reversible seawater electrolyzers.

Based on **SD II**[2] (*Chapter 5*), a bifunctional catalyst concept of a two-component catalyst using NiFe-LDH mixed with Fe-N-C is discussed and presented. This concept employs multi-sites and circumvent the limitations by a single-active site, which was explored in **SD I**[1] (*Chapter 4*). In **SD II**[2] (*Chapter 5*) and **SD III**[3] (*Chapter 6*), NiFe-LDH proofed its electrolyzer catalyst suitability even in membrane based reversible electrolyzer and in a direct seawater electrolyzer, while the used Fe-N-C catalyst suffered strong carbon corrosion at high OER potentials. Thus, α-MnO_2 is suggested to replace the carbon based Fe-N-C catalyst to employ a carbon free OER/ORR bifunctional catalyst in future reversible electrolyzer devices. Although the hydrogen electrode was not investigated in detail, based on literature Ni-based materials are suggested as precious metal free bifunctional HER/HOR catalyst material.

Additional membrane based issues of AEM were discussed, indicated by **SD II**[2] (*Chapter 5*) and **SD III**[3] (*Chapter 6*). Typical membrane degradation mechanisms like nucleophilic replacement or Hofmann elimination is taking place at temperatures and KOH concentrations beyond the applied conditions in **SD III**[3] (*Chapter 6*). Hence, the precipitation of carbonate salts in the membrane might block ion conducting channels. Relaxation of the MEA at OCV help dissolving the precipitated salts which could explain the determined recovery effect. To overcome the cell performance drop in NaCl containing electrolyzer cells in **SD III**[3] (*Chapter 6*) an OH^- selective membrane is suggested.

Finally, additional optimization were suggested for the residual reversible electrolyzer cell components such as PTL and GDL. While a gold coated Ti-foam demonstrated its suitability and a Ti bipolar shows sufficient anode stability, the flow fields still provide open potentials to optimize a final reversible electrolyzer device.

Once these challenges are met, a reversible seawater electrolyzer appear well feasible. However, beside the technical and economic feasibility, there remains the question related to the necessity of this kind of technology, which were discussed in the second part of this discussion.

In sum, the direct seawater electrolysis seems to become an important technology of the future. It can be deployed at the most efficient regions where high renewable energy potential is combined with access to seawater. Due to the simplified and compact design, less challenges needs to be tackled. Additional pre-purification of seawater would reduce the robustness of established electrolyzers and reverse osmosis as pre-purification compete with the main application: to produce fresh water for other human activities. Therefore, the direct usage of seawater for the production of hydrogen would be highly desirable and would make this technology extremely flexible. Furthermore, the oceans contain an almost unlimited reservoir of seawater so that this represents an ideal candidate as water resource for electrolyzers of the future at even comparable efficiencies to established electrolyzers.

Chapter 8
Conclusion and Outlook

In the context of a hydrogen economy for a low carbon energy future, the present cumulative work investigated the feasibility of a reversible seawater electrolyzer. As the high cost of electricity and the capital cost of current hydrogen technology are the reasons for a non-appearance of widespread hydrogen economy, this novel technique which uses cheap and abundant but efficient catalyst materials and seawater as water resource could be a promising concept for the future.

In order to give a more detailed overview of the discovered results, I like to remind the specific compiled objectives of this thesis research which explored the feasibility of reversible seawater electrolyzers.

- **Bifunctional oxygen evolution reaction/oxygen reduction reaction catalyst**
  - Finding a reversible catalyst suitable for OER/ORR catalyst
  - Understanding the principle of a reversible catalyst on a molecular level
  - Understanding the stability relation due to high OER/ORR potential differences

For reaching this goal, **SD I**[1] (*Chapter 4*) categorized a bunch of precious metal free catalyst based on Co, Mn, Fe and Ni regarding their ORR and OER activity**.** Single active sites seem to be not suitable as bifunctional catalyst so that in **SD II**[2] (*Chapter 5*) successfully a novel two-component catalyst concept using a mixture of a highly OER active (NiFe-LDH) and a highly ORR active (Fe-N-C) catalyst material was developed. The principle might base on the development of so called multi-sites, which are formed during the mixing process. While single active-sites are active for only one reaction, these two component catalyst showed to this date unachieved bifunctional activities. To explain the observed combined performance of a physical mixture, a simple two-phase system provides two distinct and spatially separated ORR and OER

catalytic sites that are sufficiently homogeneous to act as a contiguous catalyst film, yet are spatially separated enough not to interfere with each other. Unfortunately, the ORR catalyst suffered strong carbon corrosion resulting in ORR activity losses due to Fe-N-C used as ORR catalyst material. In contrast, NiFe-LDH showed in **SD II**[2] (*Chapter 5*) high stability even after ORR/OER cycling. Thus, NiFe-LDH seems to be a suitable material for reversible seawater electrolyzer, but it is recommended to replace the Fe-N-C catalyst with a non-carbon based ORR material to increase overall ORR stability for a bifunctional working devices. Thus, MnO_x is suggested to replace the carbon based Fe-N-C catalyst to employ a carbon free OER/ORR bifunctional catalyst in future reversible electrolyzer devices. Overall, an approach to produce a bifunctional OER/ORR catalyst that circumvent scaling relations was successfully and experimentally demonstrated.

- **Seawater splitting and selective oxygen evolution reaction**
  - Set-up of a seawater electrolyzer
  - Understanding the parameter in a seawater electrolyzer device
  - Revealing the catalytic relation between activity, selectivity and stability
  - Showing the feasibility of such device
  - Seeking the suitable components and understand the influence of them

To aim the second goal, for **SD III**[3] (*Chapter 6*) an in-house electrolyzer test stand was built, a reversible electrolyzer was modified and a seawater electrolyzer was tested successfully for 100 h. Using potentials at the proposed limits the seawater and non-seawater electrolyzer showed identical oxygen selectivities, excluding any formation of free chlorine. Since the catalyst material seems to be highly robust and the feasibility of such device could be proven, the anion exchange membrane (AEM) revealed a high impact for a final reversible electrolyzer device. The parameter and components were chosen comparable to typical (AEM) electrolyzers, but in order to mimic seawater by adding 0.5 M NaCl to the electrolyte the performance dropped drastically. Also, all tested electrolyte concentrations higher than pure 0.1 M KOH showed performance losses to 50-70% after 100 h compared to the initial value. Typical membrane degradation mechanisms like nucleophilic replacement or Hofmann elimination is taking place at temperatures and KOH concentrations beyond the applied conditions in **SD III**[3] (*Chapter 6*). Hence, the precipitation of carbonate salts in the membrane might block ion conducting channels. Relaxation of the MEA at OCV help dissolving the precipitated salts which could explain the discovered recovery effect. To overcome the cell performance drop in NaCl containing electrolyzer cells in **SD III**[3] (*Chapter 6*) an OH^- selective membrane is suggested.

Beside a gold coated Ti-mesh which was identified as optimized PTL for the anode, possible improvements are suggested for a reversible seawater electrolyzer of the next generation. A modified flow field and an optimized hydrogen catalyst might increase the overall performance. In sum, all tests indicated the AEM for these instability effects and identified the membrane as bottleneck for future seawater electrolyzers.

Comparison between established technologies **SD V** (*chapter 7.2*) supported the seawater electrolysis as an efficient way to produce hydrogen as the efficiency of the seawater electrolyzers show competitive voltage efficiencies of ~75-79 %. In contrast the reversible seawater electrolyzer compared to other desalination technologies, show rather an advanced and efficient way to produce H_2 than to produce specifically fresh water **SD V** (*chapter 7.2*). Nevertheless, the compact design of direct seawater electrolyzers provide a strong simplification in contrast to pre-desalination with subsequent electrolyzer combinations so that less challenges needs to be tackled.

The two component catalyst system can be suggested for future preparation of bifunctional oxygen electrode catalysts that simultaneously split directly seawater into hydrogen and oxygen. In a hydrogen based economy, this bifunctional catalyst concept could enable new possibilities in future device design such as reversible seawater electrolyzers. Used as a fuel cell to back transform the hydrogen into electricity and freshwater would additionally enable a novel source for freshwater which could help these nations in future freshwater provision. However, for water production alone the reversible seawater appears not sufficiently effective. The energy loss compared to state-of-the-art reverse osmosis is too large. Therefore, a novel probable solution for freshwater production based on seawater electrolysis could additional be presented. Nevertheless, the simplified set-up and the direct usage of seawater makes the seawater electrolysis for the production of hydrogen extremely flexible and attractive for the hydrogen production of the future.

As a forecast, the seawater electrolysis could be an attractive technology for prospective hydrogen production. The additional fuel cell property makes it to a universal working device for renewable energy transformations. Following the concept of a two-component catalyst, but with improved overall stabilities, MnO_x could be a suitable and carbon-free ORR catalyst component. In fact, in a follow-up project with Klingenhof a novel two component catalyst mixture of NiFe-LDH with MnO_x was invented. The mixture resulted in competitive high bifunctional ORR/OER activity and most importantly an exceptional high stability at similar conditions to **SD II**[2] (*Chapter 5*). This novel catalyst mixture is officially registered as a patent,

but not granted yet. However, further investigations will be done in future using this novel material mixture.

While the catalyst problems are mostly addressed and solved, the most important bottleneck to tackle in future would be the membrane. Necessary collaborations with membrane experts could address the corresponding parameter which are required for suitable future reversible seawater membrane technology. Also, a new electrolyzer design with an alternative separator concept could help to circumvent the membrane induced problems such as in alkaline media commonly used Zirfon® seperator.

Bibliography

LIST OF REFERENCES

[1] Dresp, S. and P. Strasser, *Non-noble metal oxides and their application as bifunctional catalyst in reversible fuel cells and rechargeable air batteries.* ChemCatChem, 2018. **10**: p. 4162.

[2] Dresp, S., et al., *An efficient bifunctional two-component catalyst for oxygen reduction and oxygen evolution in reversible fuel cells, electrolyzers and rechargeable air electrodes.* Energy & Environmental Science, 2016. **9**: p. 2020-2024.

[3] Dresp, S., et al., *Direct Electrolytic Splitting of Seawater: Activity, Selectivity, Degradation, and Recovery Studied from the Molecular Catalyst Structure to the Electrolyzer Cell Level.* Advanced Energy Materials, 2018. **8**(22): p. 1800338.

[4] Dresp, S. and P. Strasser, *Simplified Microwave Assisted Solvothermal One Pot Synthesis of Highly Active Nickel-Iron Layered Double Hydroxide as Oxygen Evolution Reaction Catalyst.* ECS Transactions, 2016. **75**(14): p. 1113-1119.

[5] Sören Dresp, F.D., Malte Klingenhof, and Peter Strasser, *Direct Electrolytic Splitting of Seawater: Opportunities and Challenges.* ACS Energy Letters, 2019. **4**: p. 933-942.

[6] Mengel, M., et al., *Committed sea-level rise under the Paris Agreement and the legacy of delayed mitigation action.* Nat Commun, 2018. **9**(1): p. 601.

[7] Jacobson, M.Z., et al., *100% Clean and Renewable Wind, Water, and Sunlight All-Sector Energy Roadmaps for 139 Countries of the World.* Joule, 2017. **1**(1): p. 108-121.

[8] *National Centers for Environmental Information, Antarctic Ice Cores Revised 800KYr CO2 Data* Available from: https://www.ncdc.noaa.gov/paleo-search/study/17975 [accessed 23.03.2018].

[9] *Historical CO2 Datasets*. Available from: https://www.co2.earth/historical-co2-datasets [accessed 22.03.2018].

[10] *National centers for environmental information*. Available from: https://www.ncdc.noaa.gov/cag/global/time-series/globe/land_ocean/ytd/12/1880-2016, [accessed 20.03.2018].

[11] Bhuiyan, M.A., et al., *The impact of climate change and energy resources on biodiversity loss: Evidence from a panel of selected Asian countries.* Renewable Energy, 2018. **117**: p. 324-340.

[12] Mal, S., et al., *Introducing Linkages Between Climate Change, Extreme Events, and Disaster Risk Reduction*, in *Climate Change, Extreme Events and Disaster Risk Reduction: Towards Sustainable Development Goals*, S. Mal, R.B. Singh, and C. Huggel, Editors. 2018, Springer International Publishing: Cham. p. 1-14.

[13] *Our World in Data*. Available from: https://ourworldindata.org/co2-and-other-greenhouse-gas-emissions [accessed 27.03.2018].

[14] *Intergovernmental panel on climate change; http://www.ipcc.ch/report/ar5/wg1/*. 2013 [accessed: 11.06.2018].

[15] *United Nations, The Paris Agreement*. Available from: http://unfccc.int/paris_agreement/items/9485.php [accessed 29.03.2018].

[16] *Institut for Energy Economics and Financial Analysis*. 2018; Available from: http://ieefa.org/ieefa-report-china-continues-position-global-clean-energy-dominance-2017/ [accessed: June 6, 2018].

[17] Stips, A., et al., *On the causal structure between CO2 and global temperature.* Sci Rep, 2016. **6**: p. 21691.

[18] *Fraunhofer ISE, Energy Charts*. Available from: https://www.energy-charts.de/ren_share_de.htm?year=all&source=ren-share&period=annual# [accessed 22.03.2018].

[19] Katsounaros, I. and M.T.M. Koper, *Electrocatalysis for the Hydrogen Economy*, in *Electrochemical Science for a Sustainable Society: A Tribute to John O'M Bockris*, K. Uosaki, Editor. 2017, Springer International Publishing: Cham. p. 23-50.

[20] Pellow, M.A., et al., *Hydrogen or batteries for grid storage? A net energy analysis.* Energy & Environmental Science, 2015. **8**(7): p. 1938-1952.

[21] Ball, M. and M. Weeda, *The hydrogen economy – Vision or reality?1.* International Journal of Hydrogen Energy, 2015. **40**(25): p. 7903-7919.

[22] *U.S. department of energy*. Available from: HTTPS://WWW.ENERGY.GOV/EERE/FUELCELLS/DOWNLOADS/FUEL-CELL-TECHNOLOGIES-OFFICE-MULTI-YEAR-RESEARCH-DEVELOPMENT-AND-22 [accessed: April 18, 2018].

[23] *Hyundai*. Available from: https://www.hyundai.de/Modelle/NEXO.html?hyucampaign=KMP-01590-R7G0&gclid=Cj0KCQjwu_jYBRD8ARIsAC3EGCKX5P9_3wK3N_p9fhyQ_c0cbesf44Ew9Q3a3g0_R_97BfZ_FUP6qdEaAgmcEALw_wcB [accessed: June 11, 2018].

[24] Hanley, E.S., J.P. Deane, and B.P.Ó. Gallachóir, *The role of hydrogen in low carbon energy futures–A review of existing perspectives.* Renewable and Sustainable Energy Reviews, 2018. **82**: p. 3027-3045.

[25] Aneke, M. and M. Wang, *Energy storage technologies and real life applications – A state of the art review.* Applied Energy, 2016. **179**: p. 350-377.

[26] Blanco, H. and A. Faaij, *A review at the role of storage in energy systems with a focus on Power to Gas and long-term storage.* Renewable and Sustainable Energy Reviews, 2018. **81**: p. 1049-1086.

[27] Brick, S. and S. Thernstrom, *Renewables and decarbonization: Studies of California, Wisconsin and Germany.* The Electricity Journal, 2016. **29**(3): p. 6-12.

[28] Heard, B.P., et al., *Burden of proof: A comprehensive review of the feasibility of 100% renewable-electricity systems.* Renewable and Sustainable Energy Reviews, 2017. **76**: p. 1122-1133.

[29] Shao, M., et al., *Recent Advances in Electrocatalysts for Oxygen Reduction Reaction.* Chemical Reviews, 2016. **116**(6): p. 3594-3657.

[30] Sun, Y., M. Delucchi, and J. Ogden, *The impact of widespread deployment of fuel cell vehicles on platinum demand and price.* International Journal of Hydrogen Energy, 2011. **36**(17): p. 11116-11127.

[31] Saternus, M., A. Fornalczyk, and J. Cebulski, *Analysis of Platinum Content in Used Auto Catalytic Converter Carriers and the Possibility of its Recovery.* Archives of Metallurgy and Materials, 2014. **59**(2).

[32] Kongkanand, A. and M.F. Mathias, *The Priority and Challenge of High-Power Performance of Low-Platinum Proton-Exchange Membrane Fuel Cells.* The Journal of Physical Chemistry Letters, 2016. **7**(7): p. 1127-1137.

[33] Mudd, G.M., S.M. Jowitt, and T.T. Werner, *Global platinum group element resources, reserves and mining - A critical assessment.* Sci Total Environ, 2018. **622-623**: p. 614-625.

[34] *Extraterrestrial iridium, sediment accumulation and the habitability of the early Earth's surface.* Journal of Geophysical Research: Planets, 2001. **106**(E2): p. 3219-3236.

[35] Gostin, V.A., R.R. Keays, and M.W. Wallace, *Iridium anomaly from the Acraman impact ejecta horizon: impacts can produce sedimentary iridium peaks.* Nature, 1989. **340**: p. 542.

[36] Diggles, M., *Rare Earth Elements—Critical Resources for High Technology*. 2002, U.S. Geological Survey

[37] *The World Bank, Solar resource data: Solargis*. 2017; Available from: https://solargis.com/maps-and-gis-data/download/world [accessed: June 12, 2018].

[38] *[Data/information/map obtained from the] "Global Wind Atlas 2.0, a free, web-based application developed, owned and operated by the Technical University of Denmark (DTU) in partnership with the World Bank Group, utilizing data provided by Vortex, with funding provided by the Energy Sector Management Assistance Program (ESMAP). For additional information: https://globalwindatlas.info" [accessed: June 12, 2018]*. 2018.

[39] Feng, S. and Q. Fu, *Expansion of global drylands under a warming climate.* Atmos. Chem. Phys., 2013. **13**(19): p. 10081-10094.

[40] de Levie, R., *The electrolysis of water.* Journal of Electroanalytical Chemistry, 1999. **476**(1): p. 92-93.

[41] Drennan, O.J., *Faraday's contribution to electrolytic solution theory.* Journal of Chemical Education, 1965. **42**(12): p. 679.

[42] Bockris, J.O.M., *The hydrogen economy: Its history.* International Journal of Hydrogen Energy, 2013. **38**(6): p. 2579-2588.

[43] Benoît Decourt, B.L., Roman Debarre, Olivier Soupa, *Hydrogen-Based Energy Conversion, More Than Storage: System Flexibility*. 2014, Paris: SBC Energy Institute.

[44] Lan, R., J.T.S. Irvine, and S. Tao, *Ammonia and related chemicals as potential indirect hydrogen storage materials.* International Journal of Hydrogen Energy, 2012. **37**(2): p. 1482-1494.

[45] Nikolaidis, P. and A. Poullikkas, *A comparative overview of hydrogen production processes.* Renewable and Sustainable Energy Reviews, 2017. **67**: p. 597-611.

[46] *OFFICE-of-ENERGY-EFFICIENCY-&-RENEWABLE-ENERGY, 3.1 Hydrogen Production,* . Fuel Cell Technologies Office Multi-Year Research, Development, and Demonstration Plan, 2015; Available from: https://www.energy.gov/eere/fuelcells/downloads/fuel-cell-technologies-office-multi-year-research-development-and-22 [accessed: June 19, 2018].

[47] Schmidt, V.M., *Elektrochemische Verfahrenstechnik: Grundlagen, Reaktionstechnik, Prozessoptimierung*. 2009: Wiley.

[48] LeRoy, R.L., C.T. Bowen, and D.J. LeRoy, *The Thermodynamics of Aqueous Water Electrolysis.* Journal of The Electrochemical Society, 1980. **127**(9): p. 1954-1962.

[49] Sheng, C. and J.L.T. Azevedo, *Estimating the higher heating value of biomass fuels from basic analysis data.* Biomass and Bioenergy, 2005. **28**(5): p. 499-507.

[50] Rossmeisl, J., A. Logadottir, and J.K. Norskov, *Electrolysis of water on (oxidized) metal surfaces.* Chemical Physics, 2005. **319**(1-3): p. 178-184.

[51] Rossmeisl, J., et al., *Comparing electrochemical and biological water splitting.* Journal of Physical Chemistry C, 2007. **111**(51): p. 18821-18823.

[52] Man, I.C., et al., *Universality in Oxygen Evolution Electrocatalysis on Oxide Surfaces.* Chemcatchem, 2011. **3**(7): p. 1159-1165.

[53] Frydendal, R., et al., *Enhancing Activity for the Oxygen Evolution Reaction: The Beneficial Interaction of Gold with Manganese and Cobalt Oxides.* ChemCatChem, 2015. **7**(1): p. 149-154.

[54] Medford, A.J., et al., *From the Sabatier principle to a predictive theory of transition-metal heterogeneous catalysis.* Journal of Catalysis, 2015. **328**: p. 36-42.

[55] Nørskov, J.K., et al., *Origin of the Overpotential for Oxygen Reduction at a Fuel-Cell Cathode.* The Journal of Physical Chemistry B, 2004. **108**(46): p. 17886-17892.

[56] Stephens, I.E.L., et al., *Oxygen Electroreduction Activity and X-Ray Photoelectron Spectroscopy of Platinum and Early Transition Metal Alloys.* ChemCatChem, 2012. **4**(3): p. 341-349.

[57] Halck, N.B., et al., *Beyond the volcano limitations in electrocatalysis - oxygen evolution reaction.* Physical Chemistry Chemical Physics, 2014. **16**(27): p. 13682-13688.

[58] Busch, M., et al., *Beyond the top of the volcano? – A unified approach to electrocatalytic oxygen reduction and oxygen evolution.* Nano Energy, 2016. **29**(Supplement C): p. 126-135.

[59] Peterson, A.A. and J.K. Nørskov, *Activity Descriptors for CO2 Electroreduction to Methane on Transition-Metal Catalysts.* The Journal of Physical Chemistry Letters, 2012. **3**(2): p. 251-258.

[60] Montoya Joseph, H., et al., *The Challenge of Electrochemical Ammonia Synthesis: A New Perspective on the Role of Nitrogen Scaling Relations.* ChemSusChem, 2015. **8**(13): p. 2180-2186.

[61] Vojvodic, A. and J.K. Nørskov, *New design paradigm for heterogeneous catalysts.* National Science Review, 2015. **2**(2): p. 140-143.

[62] Galeano, C., et al., *Nitrogen-Doped Hollow Carbon Spheres as a Support for Platinum-Based Electrocatalysts.* ACS Catalysis, 2014. **4**(11): p. 3856-3868.

[63] Gallagher, K.G., R.M. Darling, and T.F. Fuller, *Carbon-support corrosion mechanisms and models*, in *Handbook of Fuel Cells*. 2010, John Wiley & Sons, Ltd.

[64] Jixin, C., et al., *Carbon Corrosion in PEM Fuel Cell Dead-ended Anode Operations.* Journal of the Electrochemical Society, 2012. **158**(9): p. 1164-1174.

[65] Kim, J., J. Lee, and Y. Tak, *Relationship between carbon corrosion and positive electrode potential in a proton-exchange membrane fuel cell during start/stop operation.* Journal of Power Sources, 2009. **192**(2): p. 674-678.

[66] Zeng, K. and D.K. Zhang, *Recent progress in alkaline water electrolysis for hydrogen production and applications.* Progress in Energy and Combustion Science, 2010. **36**(3): p. 307-326.

[67] Cuartero, M., et al., *In Situ Detection of Macronutrients and Chloride in Seawater by Submersible Electrochemical Sensors.* Analytical Chemistry, 2018. **90**(7): p. 4702-4710.

[68] Ji, S.M., et al., *Photocatalytic hydrogen production from natural seawater.* Journal of Photochemistry and Photobiology A: Chemistry, 2007. **189**(1): p. 141-144.

[69] Kester Dana, R., et al., *Preparation of artificial seawater* Limnology and Oceanography, 1967. **12**(1): p. 176-179.

[70] Maeda, K., H. Masuda, and K. Domen, *Effect of electrolyte addition on activity of* $(Ga_{1-x}Zn_x)(N_{1-x}O_x)$ *photocatalyst for overall water splitting under visible light.* Catalysis Today, 2009. **147**(3): p. 173-178.

[71] A. G. Dickson, C.G., *Handbook of methods for the analysis of the various parameters of the carbon dioxide system in sea water; version 2*, ed. C.G. Andrew G. Dickson. 1994, San Diego, ORNL/DCIAC-74.

[72] Dionigi, F., et al., *Design Criteria, Operating Conditions, and Nickel–Iron Hydroxide Catalyst Materials for Selective Seawater Electrolysis.* ChemSusChem, 2016. **9**(9): p. 962-972.

[73] Wright, A.G., et al., *Hexamethyl-p-terphenyl poly(benzimidazolium): a universal hydroxide-conducting polymer for energy conversion devices.* Energy & Environmental Science, 2016. **9**(6): p. 2130-2142.

[74] Li, L. and Y. Wang, *Quaternized polyethersulfone Cardo anion exchange membranes for direct methanol alkaline fuel cells.* Journal of Membrane Science, 2005. **262**(1–2): p. 1-4.

[75] Fontananova, E., et al., *Probing membrane and interface properties in concentrated electrolyte solutions.* Journal of Membrane Science, 2014. **459**: p. 177-189.

[76] Risch, M., et al., *Water oxidation by amorphous cobalt-based oxides: in situ tracking of redox transitions and mode of catalysis.* Energy & Environmental Science, 2015. **8**(2): p. 661-674.

[77] Gorlin, Y. and T.F. Jaramillo, *A Bifunctional Nonprecious Metal Catalyst for Oxygen Reduction and Water Oxidation.* Journal of the American Chemical Society, 2010. **132**(39): p. 13612-13614.

[78] Jiang, H., et al., *Iron Carbide Nanoparticles Encapsulated in Mesoporous Fe–N-Doped Graphene-Like Carbon Hybrids as Efficient Bifunctional Oxygen Electrocatalysts.* ACS Applied Materials & Interfaces, 2015. **7**(38): p. 21511-21520.

[79] Su, Y., et al., *Cobalt nanoparticles embedded in N-doped carbon as an efficient bifunctional electrocatalyst for oxygen reduction and evolution reactions.* Nanoscale, 2014. **6**(24): p. 15080-15089.

[80] Zhao, Y., et al., *Efficient Bi-functional Fe/C/N Electrocatalysts for Oxygen Reduction and Evolution Reaction.* The Journal of Physical Chemistry C, 2015. **119**: p. 2583-2588.

[81] Zhu, Y., et al., *A Universal and Facile Way for the Development of Superior Bifunctional Electrocatalysts for Oxygen Reduction and Evolution Reactions Utilizing the Synergistic Effect.* Chemistry – A European Journal, 2014. **20**(47): p. 15533-15542.

[82] Wu, X., et al., *A reversible water electrolyser with porous PTFE based OH− conductive membrane as energy storage cells.* Journal of Power Sources, 2014. **246**(0): p. 225-231.

[83] Zoulias, E., et al., *A review on water electrolysis.* TCJST, 2004. **4**(2): p. 41-71.

[84] He, C., et al., *PEM fuel cell catalysts: Cost, performance, and durability.* Interface-Electrochemical Society, 2005. **14**(3): p. 41-46.

[85] Wang, Y.-J., et al., *A Review of Carbon-Composited Materials as Air-Electrode Bifunctional Electrocatalysts for Metal–Air Batteries.* Electrochemical Energy Reviews, 2018. 10.1007/s41918-018-0002-3.

[86] Martens, S., et al., *A comparison of rotating disc electrode, floating electrode technique and membrane electrode assembly measurements for catalyst testing.* Journal of Power Sources, 2018. **392**: p. 274-284.

[87] Gong, M., et al., *An advanced ni-fe layered double hydroxide electrocatalyst for water oxidation.* Journal of the American Chemical Society, 2013. **135**(23): p. 8452-5.

[88] Trotochaud, L., et al., *Nickel–Iron Oxyhydroxide Oxygen-Evolution Electrocatalysts: The Role of Intentional and Incidental Iron Incorporation.* Journal of the American Chemical Society, 2014. **136**(18): p. 6744-6753.

[89] McCrory, C.C.L., et al., *Benchmarking Hydrogen Evolving Reaction and Oxygen Evolving Reaction Electrocatalysts for Solar Water Splitting Devices.* Journal of the American Chemical Society, 2015. **137**(13): p. 4347-4357.

[90] Yu, X., et al., *A high-performance three-dimensional Ni-Fe layered double hydroxide/graphene electrode for water oxidation.* Journal of Materials Chemistry A, 2015. **3**(13): p. 6921-6928.

[91] Banham, D. and S. Ye, *Current Status and Future Development of Catalyst Materials and Catalyst Layers for Proton Exchange Membrane Fuel Cells: An Industrial Perspective.* ACS Energy Letters, 2017. **2**(3): p. 629-638.

[92] Dau, H., et al., *The Mechanism of Water Oxidation: From Electrolysis via Homogeneous to Biological Catalysis.* Chemcatchem, 2010. **2**(7): p. 724-761.

[93] McCrory, C.C.L., et al., *Benchmarking Heterogeneous Electrocatalysts for the Oxygen Evolution Reaction.* Journal of the American Chemical Society, 2013. **135**(45): p. 16977-16987.

[94] Geiger, S., et al., *Activity and Stability of Electrochemically and Thermally Treated Iridium for the Oxygen Evolution Reaction.* Journal of The Electrochemical Society, 2016. **163**(11): p. F3132-F3138.

[95] Sahraie, N.R., et al., *Noble-Metal-Free Electrocatalysts with Enhanced ORR Performance by Task-Specific Functionalization of Carbon using Ionic Liquid Precursor Systems.* Journal of the American Chemical Society, 2014. **136**: p. 14486-14497.

[96] Fellinger, T.P., et al., *Mesoporous Nitrogen-Doped Carbon for the Electrocatalytic Synthesis of Hydrogen Peroxide.* Journal of the American Chemical Society, 2012. **134**(9): p. 4072-4075.

[97] Chung, H.T., et al., *Direct atomic-level insight into the active sites of a high-performance PGM-free ORR catalyst.* Science, 2017. **357**(6350): p. 479-484.

[98] Ferrero, G.A., et al., *Fe–N-Doped Carbon Capsules with Outstanding Electrochemical Performance and Stability for the Oxygen Reduction Reaction in Both Acid and Alkaline Conditions.* ACS Nano, 2016. **10**(6): p. 5922-5932.

[99] Lin, L., Q. Zhu, and A.-W. Xu, *Noble-Metal-Free Fe–N/C Catalyst for Highly Efficient Oxygen Reduction Reaction under Both Alkaline and Acidic Conditions.* Journal of the American Chemical Society, 2014. **136**(31): p. 11027-11033.

[100] Masa, J., et al., *Eine Stickstoff-dotierte Kohlenstoffmatrix mit eingeschlossenen MnxOy/NC- und CoxOy/NC-Nanopartikeln für leistungsfähige bifunktionale Sauerstoffelektroden.* Angewandte Chemie, 2014. **126**(32): p. 8648-8652.

[101] Choi, C.H., et al., *Stability of Fe-N-C Catalysts in Acidic Medium Studied by Operando Spectroscopy.* Angewandte Chemie International Edition, 2015. **54**(43): p. 12753-12757.

[102] Takeno, N., *Atlas of Eh-pH diagrams.* Geological survey of Japan open file report, 2005. **419**: p. 102.

[103] Varcoe, J.R., et al., *Anion-exchange membranes in electrochemical energy systems.* Energy & Environmental Science, 2014. **7**(10): p. 3135-3191.

[104] Liu, Y., et al., *Transition metals (Fe, Co, and Ni) encapsulated in nitrogen-doped carbon nanotubes as bi-functional catalysts for oxygen electrode reactions.* Journal of Materials Chemistry A, 2016. **4**(5): p. 1694-1701.

[105] Chung, H.T., et al., *Direct atomic-level insight into the active sites of a high-performance PGM-free ORR catalyst.* Science, 2017. **357**(6350): p. 479.

[106] Jaouen, F., et al., *Recent advances in non-precious metal catalysis for oxygen-reduction reaction in polymer electrolyte fuel cells.* Energy & Environmental Science, 2011. **4**(1): p. 114-130.

[107] Rojas-Carbonell, S., et al., *Transition metal-nitrogen-carbon catalysts for oxygen reduction reaction in neutral electrolyte.* Electrochemistry Communications, 2017. **75**: p. 38-42.

[108] Stoerzinger, K.A., et al., *Recent Insights into Manganese Oxides in Catalyzing Oxygen Reduction Kinetics.* ACS Catalysis, 2015. **5**(10): p. 6021-6031.

[109] Kuhn, A.T. and C.Y. Chan, *pH changes at near-electrode surfaces.* Journal of Applied Electrochemistry, 1983. **13**(2): p. 189-207.

[110] Friebel, D., et al., *Identification of Highly Active Fe Sites in (Ni,Fe)OOH for Electrocatalytic Water Splitting.* Journal of the American Chemical Society, 2015. **137**(3): p. 1305-1313.

[111] Görlin, M., et al., *Tracking Catalyst Redox States and Reaction Dynamics in Ni–Fe Oxyhydroxide Oxygen Evolution Reaction Electrocatalysts: The Role of Catalyst Support and Electrolyte pH.* Journal of the American Chemical Society, 2017. **139**(5): p. 2070-2082.

[112] Stevens, M.B., et al., *Reactive Fe-Sites in Ni/Fe (Oxy)hydroxide Are Responsible for Exceptional Oxygen Electrocatalysis Activity.* Journal of the American Chemical Society, 2017. **139**(33): p. 11361-11364.

[113] Chen, J.Y.C., et al., *Operando Analysis of NiFe and Fe Oxyhydroxide Electrocatalysts for Water Oxidation: Detection of Fe4+ by Mössbauer Spectroscopy.* Journal of the American Chemical Society, 2015. **137**(48): p. 15090-15093.

[114] Ahn, H.S. and A.J. Bard, *Surface Interrogation Scanning Electrochemical Microscopy of Ni1–xFexOOH (0 < x < 0.27) Oxygen Evolving Catalyst: Kinetics of the "fast" Iron Sites.* Journal of the American Chemical Society, 2016. **138**(1): p. 313-318.

[115] Hong, W.T., et al., *Toward the rational design of non-precious transition metal oxides for oxygen electrocatalysis.* Energy & Environmental Science, 2015. 10.1039/C4EE03869J.

[116] Strmcnik, D., et al., *Design principles for hydrogen evolution reaction catalyst materials.* Nano Energy, 2016. **29**: p. 29-36.

[117] Chen, G., et al., *Accelerated Hydrogen Evolution Kinetics on NiFe-Layered Double Hydroxide Electrocatalysts by Tailoring Water Dissociation Active Sites.* Advanced Materials, 2018. **30**(10): p. 1706279.

[118] Davydova, E.S., et al., *Electrocatalysts for Hydrogen Oxidation Reaction in Alkaline Electrolytes.* ACS Catalysis, 2018. **8**(7): p. 6665-6690.

[119] Ran, J., et al., *Ion exchange membranes: New developments and applications.* Journal of Membrane Science, 2017. **522**: p. 267-291.

[120] Slade, R.C.T., et al., *Alkaline Membrane Fuel Cells*, in *Fuel Cells: Selected Entries from the Encyclopedia of Sustainability Science and Technology*, K.-D. Kreuer, Editor. 2013, Springer New York: New York, NY. p. 9-29.

[121] Fukuta, K., *Electrolyte Materials for AMFCs Electrolyte Materials for AMFCs and AMFC Performance. Available from: http://www1.eere.energy.gov/hydrogenandfuelcells/pdfs/amfc_050811_fukuta.pdf [accessed: October 02,2018].* 2011.

[122] Rhodri Jervis, D.J.L.B., *Alkaline Anion Exchange Membrane Fuel Cells*, in *Materials for Low-Temperature Fuel Cells*, B.L.S.P.J.Y. Yan, Editor. 2014, 2015 Wiley-VCH Verlag GmbH & Co. KGaA.

[123] Robert C.T. Slade, J.P.K., Simon D. Poynton, Rong Zeng, and John R. Varcoe, *Chapter 2 Alkaline Membrane Fuel Cells*, in *Encyclopedia of Sustainability Science and Technology*, R.A. Meyers, Editor. 2012.

[124] Dekel, D.R., *Review of cell performance in anion exchange membrane fuel cells.* Journal of Power Sources, 2018. **375**: p. 158-169.

[125] Bhola, S.M. and B. Mishra, *Effect of pH on the Electrochemical Properties of Oxides formed over beta - Ti-15Mo and Mixed Ti-6Al-4V Alloys.* International Journal of Electrochemical Science, 2013. **8**(5): p. 7075-7087.

[126] Asri, N.F., et al., *Coating of stainless steel and titanium bipolar plates for anticorrosion in PEMFC: A review.* International Journal of Hydrogen Energy, 2017. **42**(14): p. 9135-9148.

[127] Tawfik, H., Y. Hung, and D. Mahajan, *Metal bipolar plates for PEM fuel cell—A review.* Journal of Power Sources, 2007. **163**(2): p. 755-767.

[128] Spernjak, D., A.K. Prasad, and S.G. Advani, *In situ comparison of water content and dynamics in parallel, single-serpentine, and interdigitated flow fields of polymer electrolyte membrane fuel cells.* Journal of Power Sources, 2010. **195**(11): p. 3553-3568.

[129] Wang, X.-D., et al., *Local transport phenomena and cell performance of PEM fuel cells with various serpentine flow field designs.* Journal of Power Sources, 2008. **175**(1): p. 397-407.

[130] Kumar, A. and R.G. Reddy, *Effect of channel dimensions and shape in the flow-field distributor on the performance of polymer electrolyte membrane fuel cells.* Journal of Power Sources, 2003. **113**(1): p. 11-18.

[131] Ferng, Y.-M., A. Su, and S.-M. Lu, *Experiment and simulation investigations for effects of flow channel patterns on the PEMFC performance.* International Journal of Energy Research, 2008. **32**(1): p. 12-23.

[132] Lee, B., K. Park, and H.M. Kim, *Dynamic Simulation of PEM Water Electrolysis and Comparison with Experiments.* International Journal of Electrochemical Science, 2013. **8**(1): p. 235-248.

[133] Salameh, Z., *Chapter 4 - Energy Storage*, in *Renewable Energy System Design*, Z. Salameh, Editor. 2014, Academic Press: Boston. p. 201-298.

[134] *Energy requirements of desalination processes*. Encyclopedia of Desalination and Water Resources (DESWARE); Available from: http://www.desware.net/Energy-Requirements-Desalination-Processes.aspx [retrieved July 30, 2018].

[135] Desai, D., et al., *Electrochemical Desalination of Seawater and Hypersaline Brines with Coupled Electricity Storage.* ACS Energy Letters, 2018. **3**(2): p. 375-379.

[136] EPRI, P.A., *Water & Sustainability (Volume 4): U.S. Electricity Consumption for Water Supply & Treatment - The Next Half Century*. 2000: Palo Alto, CA. p. 1006787.

[137] Carmo, M., et al., *A comprehensive review on PEM water electrolysis.* International Journal of Hydrogen Energy, 2013. **38**(12): p. 4901-4934.

[138] Dresp, S., et al., *Direct Electrolytic Splitting of Seawater: Activity, Selectivity, Degradation, and Recovery Studied from the Molecular Catalyst Structure to the Electrolyzer Cell Level.* Advanced Energy Materials, 2018. **0**(0): p. 1800338.

[139] Hanrahan, G., *Chapter 5 - Water Treatment and Related Technologies*, in *Key Concepts in Environmental Chemistry*, G. Hanrahan, Editor. 2012, Academic Press: Boston. p. 155-176.

[140] Smolinka T, G.M., Garche J. , *NOW-Studie: Stand und Entwicklungspotenzial der Wasserelektrolyse zur Herstellung von Wasserstoff aus regenerativen Energien.*, in *Technical report*. 2011, Fraunhofer ISE.

LIST OF FIGURES

LIST OF TABLES

Appendix

The Appendix show additional information and consists of the following sections:

I. List of scientific contributions
II. Publication reprints
III. Author contributions

LIST OF SCIENTIFIC CONTRIBUTIONS

Most of the results were presented as oral presentation at the following conferences and workshops

[I] ***1st* Symposium on Electrocatalysis & Materials for Energy Conversion and Storage**– El Gouna, Egypt, **2015**
S.Dresp, P. Strasser, *Non-precious bifunctional catalysts for the oxygen electrode in membrane based regenerative fuel cells* ***(oral presentation)***

[II] **ECS PRIME 2016** – Honolulu, U.S.A., **2016**
S.Dresp, P. Strasser, *Simplified microwave assisted solvothermal one pot synthesis of highly active Nickel-Iron layered double hydroxide as oxygen evolution reaction* ***(oral presentation)***

[III] **S.Dresp**, P. Strasser, *Utilization of Solar Fuels by Implementation of NiFe-LDH and Fe-N-C as Bifunctional Catalyst for the Oxygen Reduction Reaction and the Oxygen Evolution Reaction* ***(oral presentation)***

[IV] ***2nd* Symposium on Electrocatalysis & Materials for Energy Conversion and Storage** – El Gouna, Egypt, **2016**
S.Dresp, P. Strasser, *Precious metal-free catalysts for the oxygen electrode in reversible alkaline electrolyzers* ***(oral presentation)***

[V] ***Frankfurter Sonderkolloquium*** *„Meere und Ozeane – geschätzt, genutzt und bedroht" zum BMBF-Wissenschaftsjahr 2016/2017 „Meere und Ozeane"* – Frankfurt, Germany, **2017**
S.Dresp, P. Strasser, *Vom Meerwasser zum solaren Brennstoff zum Trinkwasser* ***(oral presentation, Invited)***

[VI] **International Conference of Electrolysis 2017 (ICE17)** – Copenhagen, Denmark, **2017**
S.Dresp, P. Strasser, *Efficient seawater electrolyzer based on Nickel Iron layered double hydroxide as selective Oxygen evolution reaction catalyst* ***(oral presentation)***

[VII] **68th Annual Meeting of the International Society of Electrochemistry (ISE)** – Providence, U.S.A., **2017**
S.Dresp, P. Strasser, *Selective Oxygen Evolution Reaction in Seawater Electrolysers by using NiFe-LDH as Highly Efficient Catalyst Material* ***(oral presentation)***

[VIII] **Electrochemistry 2018** – Ulm, Germany, **2018**
S.Dresp, F. Dionigi, P. Strasser, *Direct electrolytic splitting of seawater: Activity, selectivity, degradation, and recovery studied from the molecular catalyst structure to the electrolyzer cell level* ***(oral presentation)***

Additionally, 6 posters were presented:

[I] **3rd Ertl Symposium -** Berlin, Germany, **2015**
S.Dresp, P. Strasser *Non-precious supported oxygen electrocatalysts for reversible electrolyzer cells* **(poster)**

[II] **3rd International Symposium on Chemistry for Energy Conversion and Storage** - Berlin, Deutschland, **2015**
S.Dresp, P. Strasser, *Non-precious supported Nickel Iron electrocatalysts for the oxygen evolution reaction* **(poster)**

[III] **47. Jahrestreffen Deutscher Katalytiker** - Weimar, Deutschland, **2015**
S.Dresp, P. Strasser , *Non-precious metal oxides as bifunctional catalyst for the electrochemical oxygen reduction and the oxygen evolution reaction in unitized regenerative electrolyzers* **(poster)**

[IV] **Renewable Energy: Solar Fuels - Gordon Research Conferences (GRC) and Seminar (GRS)** – Lucca, Italien, **2016**
S.Dresp, P. Strasser, *NiFe-LDH and Fe-N-C as Bifunctional Two-Component Catalyst for Oxygen Reduction Reaction and Oxygen Evolution Reaction* **(poster)**

[V] **NanoGe Solar Fuels 16** – Berlin, Deutschland
S.Dresp, P. Strasser, *Utilization of solar fuels by implementation NiFe-LDH and Fe-N-C as two-component bifunctional catalyst for the oxygen electrode in reversible electrolyzers* **(poster)**

[VI] 4th **CINF summerschool** (***Reactivity of nanoparticles for more efficient and sustainable energy conversion)*** – Gilleleje, Dänemark, **2016**
S.Dresp, P. Strasser, *An efficient bifunctional and precious metal-free catalyst for the oxygen electrode in reversible alkaline electrolyzers* **(poster)**

PUBLICATION REPRINTS

This section reprints the following five publications on which this dissertation is based on:

I. *Non-Noble Metal Oxides and their Application as Bifunctional Catalyst in Reversible Fuel Cells and Rechargeable Air Batteries*
Dresp, S., Strasser, P.* *ChemCatChem*, **2018**, 10, p. 4162; DOI: https://doi.org/10.1002/cctc.201800660

II. *An efficient bifunctional two-component catalyst for oxygen reduction and oxygen evolution in reversible fuel cells, electrolyzers and rechargeable air electrodes*
Dresp, S. Luo, F., Schmack, R., Kühl, S., Gliech, M. & Strasser, P, *Energy & Environmental Science*, **2016**, 9, 2020–2024; DOI: https://doi.org/10.1039/C6EE01046F

III. *Direct Electrolytic Splitting of Seawater: Activity, Selectivity, Degradation, and Recovery Studied from the Molecular Catalyst Structure to the Electrolyzer Cell Level*
S. Dresp, F. Dionigi, S. Loos, J. F. de Araujo, C. Spöri, M. Gliech, H. Dau, P. Strasser, *Adv. Energy Mater.*, **2018**, p. 1800338; DOI: https://doi.org/10.1002/aenm.201800338

IV. *Simplified Microwave Assisted Solvothermal One Pot Synthesis of Highly Active Nickel-Iron Layered Double Hydroxide as Oxygen Evolution Reaction Catalyst*
Dresp, S., Strasser, P.* *ECS Transactions*, **2016**, 75(14): p. 1113-1119. DOI: https://doi.org/10.1149/07514.1113ecst

V. *Direct electrolytic splitting of seawater – Opportunities and challenges*
Dresp, S., Dionigi F., Klingenhof, M., Strasser, P, ACS Energy Letters, **2019**, 4, 933-942, https://doi.org/10.1021/acsenergylett.9b00220

I. *Non-Noble Metal Oxides and their Application as Bifunctional Catalyst in Reversible Fuel Cells and Rechargeable Air Batteries*

This section reprints the following paper

Dresp, S., Strasser, P.*

ChemCatChem, **2018**, 10, p. 4162; DOI:
https://doi.org/10.1002/cctc.201800660

(21 pages)

ChemPubSoc Europe

DOI: 10.1002/cctc.201800660

CHEMCATCHEM Full Papers

Non-Noble Metal Oxides and their Application as Bifunctional Catalyst in Reversible Fuel Cells and Rechargeable Air Batteries

Sören Dresp[a] and Peter Strasser*[a]

We report on a comprehensive structural and electrocatalytic reactivity study of a diverse set of non-noble monometallic and bimetallic Fe, Mn, Co, and Ni -based oxide bifunctional ORR and OER electrocatalysts. To assess their catalytic activity and suitability for bifunctional operation in a consistent manner, we introduce and apply a standardized successive electrochemical testing protocol. Correlations are established between bifunctional activity and structure, by which the materials are classified. The large set of tested catalyst materials in this study enabled us to unravel entire reactivity trends across material groups and to make conclusions as to their suitability for reversible operating oxygen electrode applications. Our analysis reveals both beneficial synergistic effects of MnFe and MnCo based catalysts towards the oxygen reduction reaction (ORR) as well as favorable trends of NiFe based materials towards the oxygen evolution reaction (OER). We visualize synoptic activity trends in so-called "double overpotential" diagrams to elucidate easily the underlying activity trends. The highest bifunctional activity was found for a novel mixed spinel phase of Co and Mn and the highest OER performance was demonstrated for a mixed metal NiFe layered double hydroxide catalysts, from which practical guidance for the design of bifunctional fuel cell or metal-air battery electrodes ensues.

Introduction

Efficient electrochemical energy storage and conversion is a critical element of a sustainable future energy infrastructure.[1] Electrochemical reactions require catalysts, however, most state-of-art electrocatalysts for fuel cells and electrolyzers consist of noble metals, such as Platinum or Iridium, with high cost and low abundance. Different approaches are being explored to realize lower metal loadings, such as core shell nanoparticles or bulk alloys with high ratios of cheap non-noble metals.[2] Still, entirely noble metal-free catalysts remain the ultimately desirable solution. Figure 1 reproduces the relative abundance of the most prominent noble and non-noble metals in earth crust vs. current price on market in September 2016. Evidently, due to its high abundance and especially the low price, Fe represents the most desirable catalyst element. But other non-noble metal options suits also as catalyst material, since they are also up to 1000 times more abundant than noble metals like Pt and Ir. Such high abundance is considered critical for a world-wide deployment of electrocatalyst materials for future hydrogen energy technologies like fuel cells or electrolyzers.

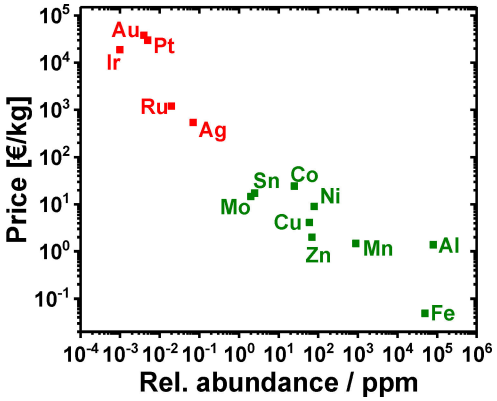

Figure 1. Relative abundance in earth crust vs. current price on market of noble (red) and non-noble (green) metals. The iron price was found for iron ore and molybdenum for molybdenum oxide.[3]

Today's vision of a hydrogen economy is based on electrolyzers splitting electrochemical water into hydrogen and oxygen ($2H_2O + \text{Electricity} \rightarrow 2H_2 + O_2$), but does also include fuel cell technology recovering electricity by transforming hydrogen and oxygen into water ($H_2 + O_2 \rightarrow H_2O + \text{Electricity}$).[4] Merging these two technologies in a single device is highly desirable for energy applications with severely limited space or weight, such as spaceships, aircrafts and other transportation applications. In addition, the use of one single device instead of two has potential to lower the overall cost. A continuous operating device combining the function of fuel cells and electrolyzers is referred to as "reversible fuel cell" or a "unitized regenerative fuel cell" (URFC). In excess of electricity, these device generates hydrogen in the electrolyzer mode, while in times of electricity shortage it generates electric power using hydrogen in the fuel

[a] S. Dresp, Prof. P. Strasser
Department of Chemistry
Chemical Engineering Division
The Electrochemical Energy
Catalysis and Materials Science Laboratory
Technische Universität Berlin
Straße des 17. Juni 124
Berlin 10623 (Germany)
E-mail: pstrasser@tu-berlin.de

Supporting information for this article is available on the WWW under https://doi.org/10.1002/cctc.201800660

cell mode.[5] The key challenge is the availability of active and stable electrocatalysts that can sustain the forward and reverse reaction processes at the negative hydrogen and positive oxygen electrodes of reversible fuel cells (the terms anode and cathode is impractical due to their switching just like for rechargeable batteries).

In electrolyzer mode the electrode reactions consist of the hydrogen evolution reaction (HER) and oxygen evolution reaction (OER) while in fuel cell mode the hydrogen oxidation reaction (HOR) and oxygen reduction reaction (ORR) occur. Equation (1) and (2) display the reversible electrochemical half-cell reactions formulated in alkaline media:[6]

Hydrogen electrode:

HER

$$2H_2O + 2e^- \rightleftarrows 2OH^- + H_2 \quad (1)$$

HOR

Oxygen electrode:

OER

$$4OH^- \rightleftarrows 2H_2O + 4e^- + O_2 \quad (2)$$

ORR

The oxygen electrode exhibits large inefficiencies due to the sluggish 4-electron charge transfer kinetics resulting in high overpotentials (η). This is why new oxygen electrode catalysts are scientifically and practically prioritized for electrolyzer and fuel cell catalyst research and research on rechargeable metal air batteries alike.[7]

First published in 2010, Manganese oxides are the classical example of bifunctional non-noble catalyst materials with an overall ΔOER-ORR overpotential of $>1.0\ V_{RHE}$,[8] yet other promising non-noble metals with lower overpotentials were explored.[9] More recently, cobalt based and cobalt manganese mixed metal oxides received heightened attention showing total overpotentials of less than $0.9\ V_{RHE}$.[10] Even though, these materials achieved high initial performance, they lack in necessary data regarding the durability and flexibility.[11] The literature mainly presents either OER stability or ORR stability only. It would be desirable to present measurements with subsequent mode switching, to see the influence of the one potential range on the other, primarily, the high corrosive OER potentials on the sensitive often carbon based catalysts such as metal N-doped carbon materials.[12] In fact, the carbon lead to possible durability problems at high OER potentials due to carbon corrosion that could degrade the Me–N doped Carbon sites.[13] Nevertheless, carbon is still the most important and prominent support material for metal oxides to increase conductivity and activity.[14]

Accordingly, the present study explores a comprehensive set of carbon supported bimetallic non-noble metal oxides based on Co, Ni, Fe and Mn derived from their mono-metallic parent oxide structures, such as spinels or layered double hydroxides. The carbon matrix adjusts the overall conductivity of metal oxides. It further enables the possibility to study the influence of OER potentials on the carbon metal oxide matrix regarding their durability. The catalysts are characterized, and their performance and suitability as bifunctional oxygen electrode catalyst material is evaluated. The stability focus for this study is set to the influence of the high OER potentials on the ORR activity. For catalyst preparation, a modified microwave-assisted solvothermal synthesis route was applied and provided rapid synthetic access to the studied set of carbon supported non-precious oxides.[15][16],[17] A synoptic comparison and classification of the trends in the experimental activity and stability offer new insight and practical guidance for new candidates for carbon supported bifunctional oxygen electrodes in unitized reversible fuel cells.

Results and Discussion

Our comprehensive comparative study of non-noble catalyst materials considers crystal phase, elemental analysis, and corresponding electrochemical activity as major experimental correlation parameters. The crystal structure was determined by using X-ray diffraction (XRD) and the elemental composition and metal loading by inductively coupled plasma-optical emission spectroscopy (ICP-OES). The catalyst materials are grouped into monometallic metal oxides and bimetallic oxides. Finally, the samples were tested in O_2 saturated 0.1 M KOH electrolyte to determine and categorize their bifunctional activity. For better conductivity, the materials are supported on Vulcan XC72R.

Structure of Non-noble Oxide Materials

Figure 2 shows the powder X-ray diffraction (XRD) patterns of the prepared monometallic and bimetallic mixed oxide catalysts.

The monometallic oxides resulted in highly crystalline phases. The Fe sample shows the typical XRD pattern of α-Fe_2O_3 or Hematite and fits almost perfectly to the pdf pattern JCPDS: 00-089-0598, but with a strongest peak intensity for the (110) reflection instead of (104). The reflections for manganese confirmed the Hausmannite structure (JCPDS: 00-024-0734) which is known as a Jahn-Teller distorted spinel, having the strongest (211) reflection at 2θ 43°. The cobalt oxide pattern is consistent with its spinel structure (JCPDS: 00-043-1003), which has the strongest reflection at 2θ 36.1° corresponding to the (311) plane. In contrast, the $Ni(OH)_2$ sample showed a poorly-defined turbostratic crystalline phase that could be attributed to neither the beta nor the alpha phase. Generally, the beta $Ni(OH)_2$ phase is more crystalline showing stronger reflection than α-$Ni(OH)_2$.[18] However, in 1997 Rajamathi et al. already discovered a mixed phase for $Ni(OH)_2$ and described it as an intermediate phase for $Ni(OH)_2$ which shows almost similar reflections to the present $Ni(OH)_2$-phase.[19] The bimetallic oxides showed high crystallinity (Figure S1–S3), except for the nickel-based oxides (Figure S4). These nickel-based materials

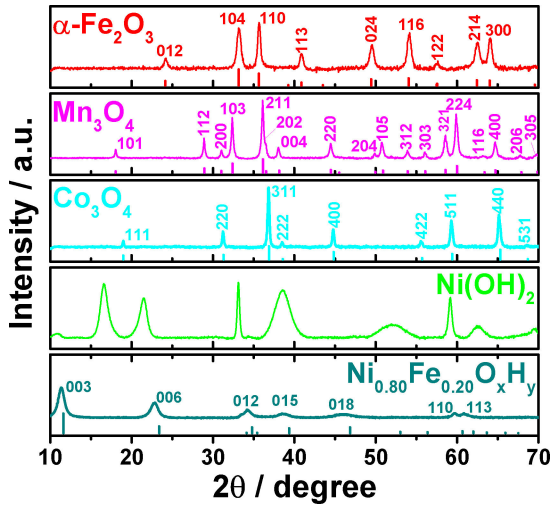

Figure 2. Powder X-ray diffraction (XRD) pattern of selected non-noble metal oxide samples supported on Vulcan XC-72r prepared by solvothermal microwave assisted one-pot synthesis route.

showed a similar turbostratic intermediate phase like the previously discussed $Ni(OH)_2$, but with slightly different reflection width and interlayer distances. The Ni-free bimetallic materials resulted in mixed-phase patterns showing XRD reflections of the parent monometallic oxide structure. Likewise, combinations of manganese and cobalt resulted in a mixed phase showing XRD features of both oxides. This suggests an occurring mixed phase of two oxides (Figure S1–S2). Surprisingly, the combination of nickel and iron resulted in highly crystalline layered double hydroxide (LDH) also known as hydrotalcite ($MgAl_2CO_3(OH)_{16}$*$4H_2O$/JCPDS: 00-014-0191) but with slightly higher interlayer distances, expressed by their characteristic (003) and (006) reflections at 2θ values of 11.4° and 22.7° (Figure 2).[20]

Exemplary Bifunctional Activity Protocol

Typically, a separated OER and ORR activity measurement is established for bifunctional ORR/OER catalyst research. However, since these catalysts will be operated in reversible electrolyzers, a switching between OER and ORR potential is important for a reversibility test. Especially, the high OER potentials could affect the catalyst and the support material dramatically due to carbon corrosion or catalyst oxidation and result in an instant change to the prior determined ORR activity.

This is why this study utilized an exemplary combined scanning voltammetry sequence to enable a first classification for non-noble bifunctional catalyst materials regarding their ORR activity after OER potentials. As an exemplary protocol, the activity trends that are shown might vary from other publications, since activities are highly dependent on the sequence protocol and the materials nature.

For all activity measurements oxygen-saturated, non-prepurified 0.1 M KOH was used as electrolyte. The protocol was based on the successive electrochemical testing of ORR and

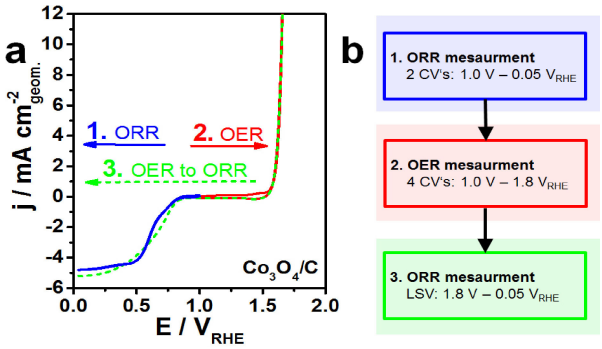

Figure 3. Electrochemical bifunctional testing sequence for the oxygen electrode in O_2 saturated 0.1 M KOH, 1600 rpm and a scan rate of 5 mV s^{-1}. (a) Example for Co_3O_4/C (b) detailed sequence description.

OER as shown in Figure 3. The test protocol started with two cyclic voltammograms (CV) in a potential window between $+1.0\pm0.05$ $V_{RHE.}$ to determine the initial ORR activity. The second cycle was applied to verify the activity of the first cycle. After ORR testing, four cycles in a window between $+1.0\pm1.8$ V_{RHE} were conducted to determine the OER activity. 4 cycles seemed to represent the perfect balance between the OER stability and influence of OER potentials on the ORR activity. More cycles would have affected the structure to strong while a lower cycle number would have not been representative for OER stability. As a result, a significant OER stability observation and a slight impact on the catalyst material could be determined, so that the material will not be affected to strong that an electrochemical analysis due to extreme degradation would have become impossible. In particular, such high oxidizing potentials during the OER test could potentially affect the structure of the catalyst material and likewise the catalytic activity. These four cycles at high potentials were taken as a first indication for OER stability. Lastly, a final linear sweep from $+1.8\pm0.05$ V_{RHE} after the OER cycles was conducted to test changes in the ORR activity due to the prior exposure to OER potentials, from which the ORR stability was derived.

Electrochemical Performance of Noble Metal Reference Catalysts

As reference material, commercially available Iridium on Carbon (Ir/C, 20 wt%, BASF) and Platinum on Carbon (Pt/C, 20 wt%, TKK) was used and tested using the electrochemical protocol as described before. The cyclic voltammetry of these materials is shown in Figure 4.

Ir/C. Iridium is proposed as most suitable OER catalyst in especially acidic and, besides NiFe-LDH, also in alkaline media.[21] Figure 4a support the expected high OER performance for the commercial Ir/C catalyst, showing an overpotential of 350 mV at 10 mA cm^{-2} for the 3rd cycle. In Figure 4c the ORR activity of Ir/C is presented. Even though Ir/C shows a decent ORR activity with an overpotential of 491 mV at −3 mA cm^{-2} for the 2nd cycle, the ORR activity does not remain after the OER

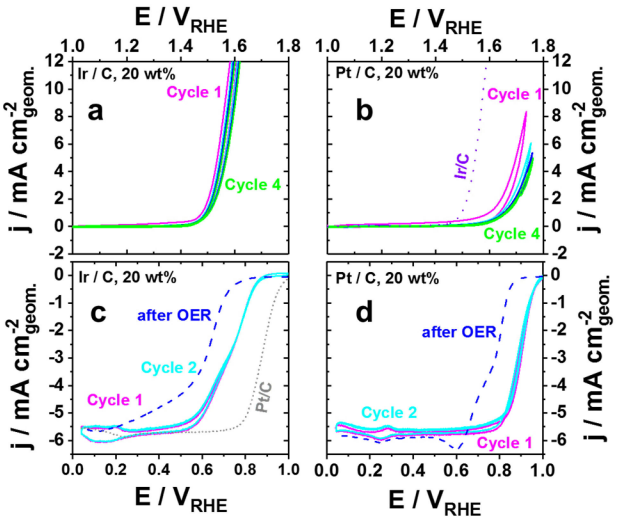

Figure 4. Cyclic voltammogram of commercial reference catalysts in O_2 saturated 0.1 M KOH, 1600 rpm and a scan rate of 5 mV s^{-1}, cat load 0.2 mg cm^{-2}. The corresponding overpotentials are listed in Table 1 and Table S1 in the Supporting Information.

cycling. Thus, the OER cycling have a big influence on the ORR activity even for the noble Ir/C catalyst.

Pt/C. Started in 1964, Pt is studied for longtime as fuel cell catalyst. Many different approaches are being explored for increasing ORR activity and stability.[22] In this work, we used commercial Pt/C as Benchmark catalyst and explore the behavior regarding high OER potentials on the ORR activity. In contrast to the high ORR activity shown in Figure 4d, the Pt/C exhibits a low OER activity. With further cycling the Pt/C catalyst show even an instability towards the low catalytic OER performance. In fact, also the ORR performance drastically decreases after OER treatment.

Both noble metal materials show high catalytic activity towards their specific reaction. But even this noble material suffers ORR activity loss after only 4 cycles of aggressive OER potentials. The influence of OER potentials on bifunctional catalyst seem to be underestimated. Hence, this work will explore further the influence of OER potentials towards common non-noble metal oxides and classify their ability as ORR, OER or as bifunctional catalyst.

Electrochemical Performance of Monometallic Oxides

Figure 5 shows the cyclic voltammetry of carbon supported $Ni(OH)_2$, Fe_2O_3, Mn_3O_4 and Co_3O_4 catalysts. As reference, commercial Ir supported on Vulcan XC72R (20 wt%, BASF) (Ir/C) and Platinum supported on Vulcan XC72R (20 wt%, TKK) (Pt/C) were used.

$Ni(OH)_2$/C. In Figure 5a the OER activity is presented for $Ni(OH)_2$/C. The voltammetry revealed a $Ni(OH)_2$-typical increase of the redox peak charge per cycle. The oxidation peak indicates the Ni^{+II} to $Ni^{+III/IV}$ oxidation.[23] However, $Ni(OH)_2$/C shows high OER activity almost similar to Ir/C, having an overpotential of $\eta_{OER} = 300 \pm 3$ mV at 1 mA cm^{-2}. This is likely due to ppm-level Fe contaminations of the electrolyte that surface dope the Ni hydroxides that show lower overpotentials.[24] This synergistic effect of ppm level of Iron is only found for Nickel based materials and will not affect the other element materials.

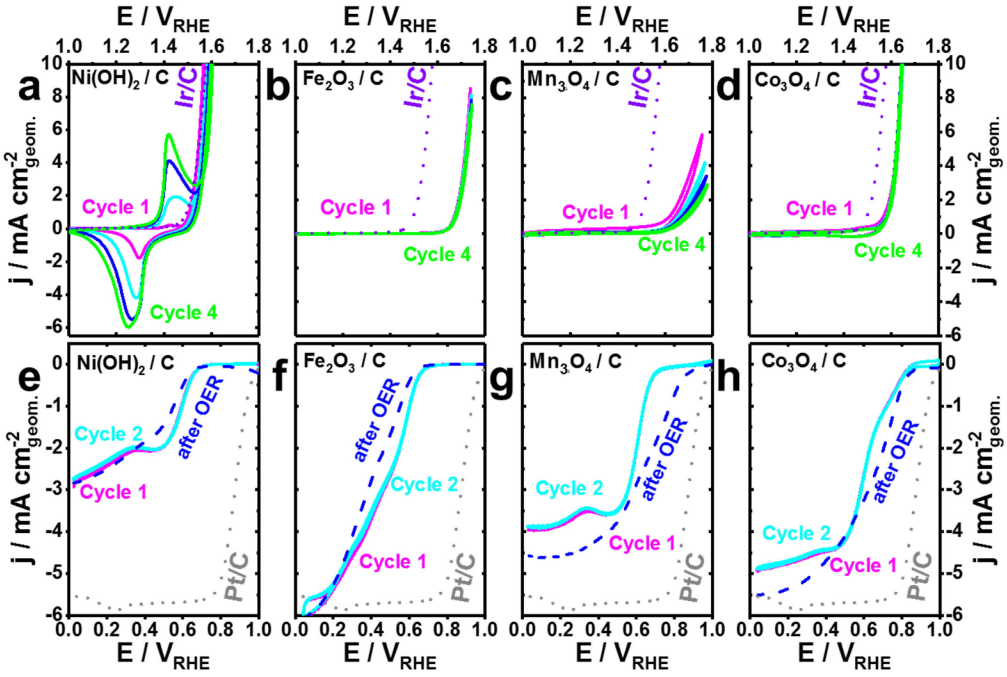

Figure 5. Cyclic voltammogram of supported monometallic oxide catalysts in O_2 saturated 0.1 M KOH, 1600 rpm, a scan rate of 5 mV s^{-1} and a cat load 0.2 mg cm^{-2}. The corresponding overpotentials are listed in Table 1 and Table S1 in the Supporting Information.

In contrast to its OER performance, the $Ni(OH)_2$ showed poor ORR activity in comparison to the platinum reference (Figure 5e). The ORR onset potential of the $Ni(OH)_2$/C catalyst is about 0.603 ± 0.007 V_{RHE} at 1 mA cm^{-2} followed by a plateau at 2 mA cm^{-2}. in a potential range between 0.50–0.35 V_{RHE}. The current plateau at ~2 mA cm^{-2} is less than half of the usual mass-transfer limiting current of the platinum reference catalyst (~6 mA cm^{-2}). This, however, indicates a favored 2 electron process which can be attributed to the production of H_2O_2 or HO_2^-. The formula of the competing oxygen reduction reactions to HO_2^- and H_2O_2 are shown in Equation (3) and (4):

HO_2^- formation at $E^0 = -0.076$ V_{SHE}:

$$O_2 + H_2O + 2e^- \rightarrow HO_2^- + OH^- \quad (3)$$

H_2O_2 formation at $E^0 = -0.146$ V_{SHE}:

$$O_2 + 2H_2O + 2e^- \rightarrow H_2O_2 + 2OH^- \quad (4)$$

Correspondingly, the hydrogen peroxide standard electrode potentials in pH 13 are $E_{O2/HO2-} = +0.691$ $V_{SHE,pH13}$ and $E_{O2/H2O2} = +0.621$ $V_{SHE,pH13}$ which are comparable to the corresponding on-set potentials in Figure 4e. Nevertheless, the plateau vanishes after OER cycling indicating a decrease of the ORR activity to hydrogen peroxide.

α-Fe_2O_3/C. In Figure 4f, the ORR activity of Fe_2O_3/C shows a slightly lower overpotential than the $Ni(OH)_2$/C sample. The onset of $+0.606 \pm 0.005$ V_{RHE} at −1 mA cm^{-2} represents an ORR overpotential of $\eta_{ORR} = -0.624 \pm 0.005$ V with respect to the four-electron path. Although the overpotential is in the hydrogen peroxide production range, no plateau is detected for Fe_2O_3/C. The oxygen reduction current is almost linearly increasing for Fe_2O_3/C reaching diffusion limited currents comparable to Pt/C at overpotentials of about 1.23 V. This indicates a prevalence of the 4 e$^-$ oxygen reduction path despite high ORR overpotentials.[25] In Figure 4b, the Fe_2O_3/C catalysts displayed an OER overpotential of $\eta_{OER} = +0.445 \pm 0.012$ V_{RHE} at +1 mA cm^{-2}. In contrast to $Ni(OH)_2$, the OER activity remained constant after 4 cycles, whereas the final ORR on the final cathodic sweep featured a similar ORR decrease.

Mn_3O_4/C. The activity tests of Mn_3O_4/C are presented in Figures 5g and 5c. Even though the ORR activity is slightly lower compared to other catalysts of this study like 150 mV lower than Fe_2O_3/C, it fell sharply short of some previously reported performance values. Manganese oxides have been intensively studied as bifunctional catalyst and were found highly bifunctionally active.[8,26] In 2012, Gorlin et al. showed ORR electrode potentials of $E_{ORR} = 0.73$ V at −3 mA cm^{-2}, representing an ORR overpotential of −500 mV. In the present study, the ORR overpotential is just $\eta_{ORR} = -0.594 \pm 0.005$ V_{RHE} at −1 mA cm^{-2}. for the Mn_3O_4/C catalyst. The discrepancy can be explained by the initial electrochemical cycling in N_2 saturated 0.1 M KOH (see experimental section). This step might have influenced the activity of Mn_3O_4/C. In addition, since MnO_x occur in very different phase structures and every phase shows different activities the structure aspect should not be underestimated. Especially α-MnO_2 and Mn_2O_3 showed exceptional high ORR activities.[27] In this context, Hausmannite (Mn_3O_4) might not be the most ORR and OER active Mn-phase.

However, our tests confirmed the favorable ORR characteristics as well as their high sensitivity to redox transitions. The most active Mn materials are invariably those that respond most sensitively to the applied electrode potential range. For instance, for α-MnO_2 catalysts to retain their initial activity, the potential cannot exceed +1.1 V_{RHE} or fall below +0.3 V_{RHE}. Otherwise α-MnO_2 changes into higher or lower-valent phases. The OER activity of the present Mn_3O_4/C displayed a similar, albeit less dramatic sensitivity to the applied electrode potentials. The overpotential increased from $\eta_{OER} = +1.617 \pm 0.009$ V_{RHE} to $\eta_{OER} = +1.664 \pm 0.012$ V_{RHE} at +1 mA cm^{-2} (see Figure 5c). The origin is the disproportionation of Mn^{3+} into the quite soluble Mn^{2+} and Mn^{4+} followed by the loss of the former out of the oxide lattice by electrolyte leaching.[28] Along this argument, the strong increase in ORR activity after the anodic OER tests appears perfectly consistent and can be rationalized by Mn reoxidation.

Co_3O_4/C. Figure 5h and 5d show the electrochemical activity of Co_3O_4/C. This material shows the best bifunctional performance and stability of the monometallic oxides under the present conditions. The overpotential at currents of +/−1 mA cm^{-2} $\eta_{ORR} = -0.518 \pm 0.009$ V_{RHE} and $\eta_{OER} = +0.358 \pm 0.007$ V_{RHE} were comparable. However, the combined absolute overpotential $\eta_{total} = 0.876 \pm 0.016$ V_{RHE} was relatively small and no declines were observed during OER potential cycling. Similar to the Mn based catalyst, the ORR activity increased after OER cycling, suggesting the reformation of low valent Co oxide phases during ORR testing after OER potentials.

For a better comparison to literature-based data, Table 1 compares the present OER, ORR and combined overpotential data of the parent monometallic oxide catalysts at −3 mA cm^{-2} and 10 mA cm^{-2}.

Table 1. Monometallic oxides and the corresponding overpotentials at common current densities for the 2nd ORR Cycle and the 3rd OER cycle

Catalyst material	η_{ORR}[a] [V]	η_{OER}[b] [V]	ΔE[c] [V]
$Ni(OH)_2$	1.172	0.367	1.539
α-Fe_2O_3	0.764	–	–
Mn_3O_4	0.682	–	–
Co_3O_4	0.647	0.425	1.072
Ir	0.491	0.350	0.841
Pt	0.342	–	–

[a] Current density −3 mA cm^{-2}; [b] current density +10 mA cm^{-2}; [c] $E_{OER} - E_{ORR}$.

Electrochemical Performance of Bimetallic Metal Oxides

Starting from the parental monometallic oxides, a range of bimetallic oxide catalysts were prepared and investigated. The activities of nickel-based catalysts with a composition of $Ni_{x>0.75}Me_{1-x}O_yH_z$ and nickel-free bimetallic combinations $Me1_{x>0.60}Me2_{1-x}O_y$ are shown in Figure S5 and S6. Table 2 compares the

Table 2. Bimetallic oxides and their corresponding overpotential at common current densities for the 2nd ORR Cycle and the 3rd OER cycle.

Metal comp. of catalyst	η_{ORR}[a] at -3 mA cm^{-2} [V]	η_{OER}[b] at 10 mA cm^{-2} [V]	ΔE[c] ($E_{OER}-E_{ORR}$) [V]
$Ni_{80}Fe_{20}$	0.950	0.297	1.247
$Ni_{85}Co_{15}$	0.907	0.387	1.294
$Ni_{91}Mn_{09}$	0.825	0.375	1.200
$Mn_{31}Co_{69}$	0.597	0.420	1.017
$Mn_{65}Co_{35}$	0.617	0.442	1.059
$Co_{61}Fe_{39}$	0.689	0.419	1.108
$Mn_{90}Fe_{10}$	0.758	0.487	1.245
$Ni_{67}Mn_{33}$	0.983	0.421	1.404

[a] Current density -3 mA cm^{-2}; [b] current density $+10$ mA cm^{-2}; [c] $E_{OER}-E_{ORR}$.

experimental ORR and OER overpotentials at a current density of -3 mA cm^{-2} and 10 mA cm^{-2} respectively. For all nickel-based catalysts, no significant reduced overpotential at -1 or 1 mA cm^{-2} was detected. The OER activity showed no drastic differences in activity, either, except for the combination of Ni and Fe. This underlines the outstanding OER activity of Ni–Fe mixed oxides. The combinations of nickel with cobalt or manganese differed from $Ni(OH)_2$/C largely in their electrochemical redox behavior. Beside the increase in peak charge, the Ni oxidation peak split into two peaks during anodic potential sweeps. Since $Ni(OH)_2$ occurred here in an intermediate phase between α-$Ni(OH)_2$ and β-$Ni(OH)_2$, one explanation is an inhomogeneous phase distribution of those phases resulting in two separated sharp redox peaks each related for either the α- or the β-phase. On the contrary, the nickel-free bimetallic mixed oxide combinations showed a strong improvement compared to their monometallic oxides. By comparison, the combination of Mn–Co showed an overall bifunctional improvement, while Fe–Mn mixed oxides displayed only favorable OER activity and stability. Figure 6 details the cyclic voltammetry of the most active Ni–Fe and Co-based catalysts of the present study.

Ni-derived catalysts. Figure 6a and 6d present the OER catalytically highly active NiFe-LDH material. The bimetallic material showed low OER overpotential of $+297\pm3$ mV at 10 mA cm^{-2} in 0.1 M KOH and just $+219\pm2$ mV at 1 mA cm^{-2}. Consistent with the notion that the presence of Fe mute the redox activity of Ni, the anodic Ni oxidation peak is shifted to higher potentials and deconvolute.[17c,25a] Görlin et al. explained this as the result of a two proton-one electron (PT/ET) process influenced by the Fe^{+3} center during the OER mechanism as shown in Equation (5).[25b]

$$Ni^{+2}Fe^{+3}(OH)(OH) + 2OH^- \rightarrow Ni^{+3}Fe^{+3}(O)(O)^{\delta-} + 2H_2O + e^- \ (PT/ET) \quad (5)$$

The initial proton abstraction from a terminal or bridged OH group at a Fe^{+3} center is hypothesized to be slow and exhibits a kinetic barrier that increase the required overpotential for proton abstraction with increasing Fe content. The subsequent e^- and another proton abstraction from an OH group attached to a redox active Ni^{+2} center is considered as fast resulting in the $Ni^{+3}Fe^{+3}(O)(O)^{\delta-}$ intermediate including the negatively

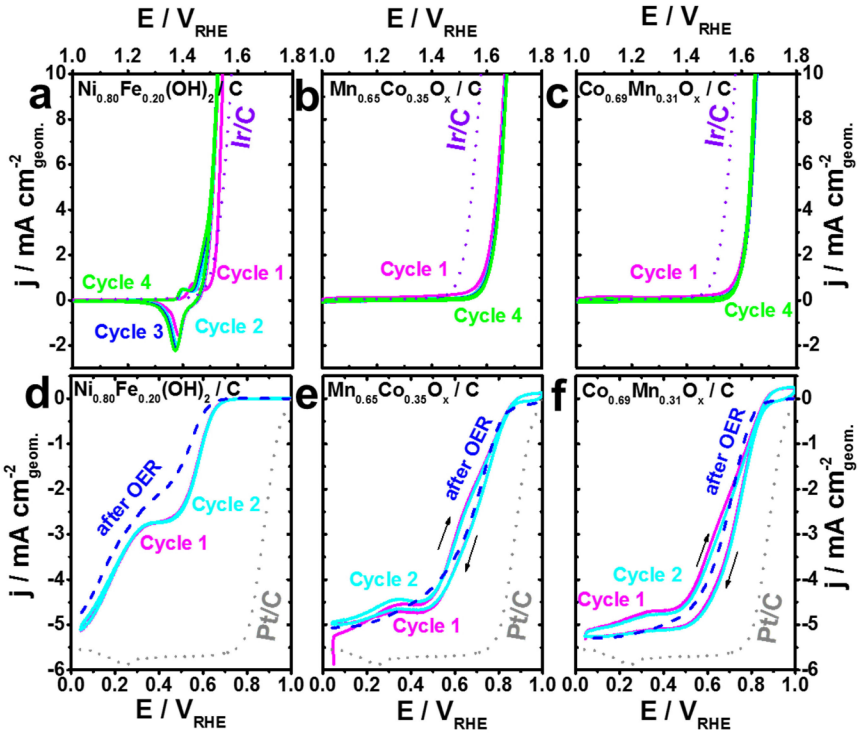

Figure 6. Cyclic voltammogram of supported bimetallic oxide catalysts in O_2 saturated 0.1 M KOH, 1600 rpm,a scan rate of 5 mV s^{-1} and a cat load 0.2 mg cm^{-2}. The corresponding overpotentials are listed in Table 2 and Table S1 in the Supporting Information.

charged oxygen ligands that are considered in literature as "active oxygen".[29]

The ORR cyclic voltammogram of NiFe-LDH looked similar to the parent compound in the kinetic region, yet displayed a somewhat larger transport limited plateau. In comparison to the reference Pt/C catalysts, however, the ORR activity is low, showing an onset potential of only $+0.600 \pm 0.002\ V_{RHE}$ at $-1\ mA\,cm^{-2}$. As a result, the NiFe-LDH catalyst featured a cyclic voltammetric behavior that resembled the superposition of the two monometallic oxides.

Mn- and Co-derived catalysts. The Mn-based and Co-based catalysts showed promising bifunctional activity with additional stability. We note that the two materials in Figure 6c-f consist of distinctly different crystallographic oxide phases, yet showed almost identical activities. Experimental OER overpotentials were $+420 \pm 2$ mV for $Mn_{31}Co_{69}$/C and $+442 \pm 0.5$ mV for $Mn_{65}Co_{35}$/C at 10 mA cm^2. Their OER activity showed better stabilities (sustained activity) compared to their parent Mn_3O_4/C and Co_3O_4/C. In Figure 6e and 5f, the Mn–Co oxide catalyst showed promising ORR overpotentials for non-noble metal materials of 597 ± 7 mV for $Mn_{31}Co_{69}$/C and 617 ± 3 mV for $Mn_{65}Co_{35}$/C at $-3\ mA\,cm^2$, and, noteworthy, the activity remained at comparable levels after OER testing. The present Mn–Co oxide material exhibits the hitherto most promising bifunctional non-noble bimetallic mixed oxide catalyst meeting and exceeding previous reports. In 2014, Zhao et al. investigated spinel Mn–Co in N-doped Carbon Nanotubes as bifunctional catalyst. However, this catalysts showed very low overall activities.[10c] In the same year, Masa et al. reported bifunctional activities for Co- and Mn-based materials.[30] In terms of Masa's total absolute overpotential metric (overpotential at $-1\ mA\,cm^{-2}$ for ORR and $10\ mA\,cm^{-2}$ for OER) our catalysts outperform previous catalyst candidates based on a combined 849 mV loss for $Mn_{31}Co_{69}$ and 880 mV for $Mn_{65}Co_{35}$.

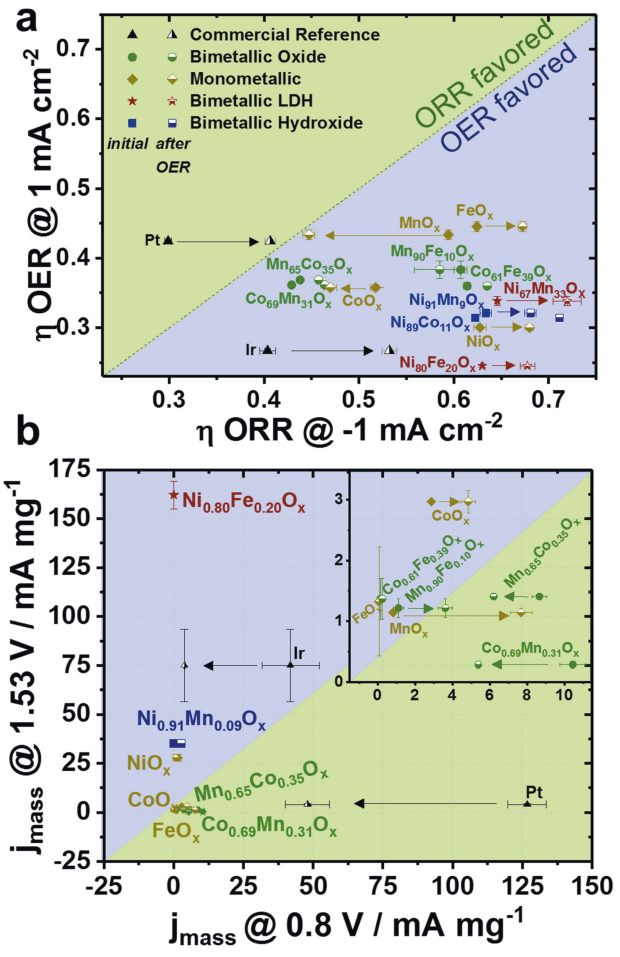

Figure 7. (a) Diagram of different catalyst materials with the corresponding on-set potential at $-1\ mA\,cm^{-2}$ for ORR and $1\ mA\,cm^{-2}$ for OER. (b) Diagram of elemental metal mass activities for different catalyst materials at 1.53 V_{RHE} for OER and at 0.8 V_{RHE} for ORR.

To put all of our catalyst in perspective, Figure 7a displays all of the present data in a comparative 2-dimensional OER-ORR performance trend diagram.

All materials are different colored related to their initial structure appearance. To gain a symmetrical synoptical diagram related to their OER/ORR activity, the ORR overpotential at $-1\ mA\,cm^{-2}$ is plotted at the x-axis and the OER overpotential at $+1\ mA\,cm^{-2}$ is plotted at the y-axis. A diagonal of slope 1 represents the line of balanced bi-functionality. Catalysts located in the upper green region are materials having lower ORR overpotentials than OER overpotentials. Consequently, these materials are favoring the ORR. Catalysts located in the blue region are catalysts that favor the OER. The better the material as closest it is located at the origin of this diagram. Additional bifunctional ORR/OER activities after the 4 OER cycles are added to display the influence of the OER potentials.

Assessing the initial activities, the reference Pt/C catalyst is the only sample located in the ORR favored region. All other materials tested in this study are in the OER favored region. Consequently, every single oxide catalyst of this work favors the OER which is consistent with the notion that high-valent oxides tend to become increasingly unstable under reducing electrochemical conditions, even though the combinations of Mn and Co show comparably high ORR activities. The Ir/C reference showed the best bifunctional activity located closest to the origin. The initial activities of the single metal oxides encircle an area of the diagram, representing the activity limitations of these oxide materials. In contrast, some outliers beyond this area are the NiFe- and MnCo-based catalysts. Although the MnFe-based catalysts featured a significant improvement in the OER activity, they are not located outside of the limiting area. It is fair to say that the group of NiFe, MnCo and MnFe bimetallic oxides resulted in a truly new and synergistic effect towards the OER or ORR. The Fe-doping of Mn or Ni resulted in a joint OER improvement, whereas the combination of Mn and Co improved mainly the ORR activity. The detailed potentials for all the materials at various current densities are listed in Table S1.

Correspondingly, the ORR data after OER overpotential showed interesting various behaviors. While most of the tested materials decreased their performance after 4 cycles between 1.0–1.8 V_{RHE}, Mn_3O_4, Co_3O_4, $Mn_{90}Fe_{10}O_x$ showed a decreased overpotential after OER cycling. Nevertheless, even the noble catalyst materials showed a strong influence regarding the OER potentials indicated by a strong drop in overpotential.

To expand our characterization further, we determined the total metal mass and ECSA normalized activities for the different oxide materials. For comparison, the currents are taken at commonly accepted benchmarking values. For ORR mass activity, the current was taken at 0.8 V_{RHE} ($\eta = -430$ mV) and for the OER at 1.53 V_{RHE} ($\eta = +300$ mV). The final mass activities are represented in Figure 7b and the ECSA normalized diagram is shown in the supporting information in Figure S11. The x-axis represents the normalized current density for the ORR at $+0.8$ V_{RHE} and the y-axis represents the normalized current density for OER at $+1.53$ V_{RHE}. Even though the currents are not taken at symmetrical overpotentials, the blue area indicates that OER outperforms ORR, and the green region indicate that ORR outperforms OER.

Except for the Fe contaminated NiOx catalyst, the monometallic oxides showed low mass activities in a range of 1–3 mA mg^{-1}. The platinum reference catalyst featured again ORR mass activities of around 127 mA mg^{-1} amounting to a two orders of magnitudes advantage. The same applied for NiFe-LDH in case of OER. The mass activity of 162 mA mg^{-1} was two magnitudes higher compared to the other non-noble materials and showed the highest OER activity in this study. Even though the Mn–Co catalyst showed small mass activities, a synergistic effect doubled its mass activity in ORR direction. It is only matched by Iridium, known to be one of the best OER catalysts in acidic media,[21b,31] which also showed comparably high bifunctional activity in alkaline media.[32] The ECSA normalized diagram shown in the supporting information in Figure S11 supports the overall activity trends of the catalyst materials. However, the activity differences are more pronounced. Especially the Ni based material tend to be even more OER active compared to the other catalyst materials due to their small ECSA value, while the Mn based materials shift from the OER into the ORR favored region supporting their bifunctional ORR/OER activity.

Conclusions

This study provides a comprehensive overview of an array of non-precious metal bifunctional OER/ORR oxygen electrocatalysts involving Co, Mn, Ni and Fe and the additional influence of high OER potentials. The study includes monometallic as well as bimetallic mixed metal oxides synthesized by a facile solvothermal one-pot synthesis. By comparing the ORR and OER activity using an exemplary combined voltammetry test protocol, this study reports performance trends and values which are more likely to represent the situation in a unitized fuel cell or rechargeable air battery.

The most promising monometallic materials were the (electrolyte Fe-contaminated) $Ni(OH)_2$ for the OER and the CoO_x for the ORR process. To overcome performance limitations of the monometallic systems metals were mixed to develop a two-phase system with overall higher activity.

All oxide catalysts in this study revealed more favorable OER than ORR performances. Synergistic catalytic effects were observed for combinations of Ni and Fe, and Mn and Fe towards the OER activity, and for the combination of Co and Mn towards the ORR activity. Two-dimensional trend diagrams based on OER/ORR overpotential and mass activity revealed, for the first time, desirable performance regions and current performance limitations of the studied oxide.

The large majority of mixed metal oxide exhibited an intermediate activity between the pure parental oxides; a striking exception was the mixture of nickel and iron that resulted in a layered double hydroxide phase with a drastic improvement in the oxygen evolution reaction kinetics, resulting in highest OER activity of this study, with a sustained ORR onset potential at -1 mA cm^{-2}. In addition, the mixture of Co and Mn showed a dramatic synergistic effect for the ORR activity, with a sustained OER onset at $+1$ mA cm^{-2}.

This study provides new and refines known material candidates for oxygen electrode catalysts to be deployed in unitized fuel cells or aqueous rechargeable air batteries, or other electrochemical applications of the reversible oxygen electrode. Our synoptic comparisons provide intuitive performance trends and performance targets and limitations for future design of oxygen electro-catalysts.

Experimental Section

Sample Preparation

Supported non-noble metal oxide catalysts were synthesized in solvothermal one-pot synthesis route using a microwave assisted autoclave (Anton Paar 300 Monowave), also described elsewhere.[17a] The carbon was used to increase overall sample conductivity and enables a better and more realistic catalytic comparison of the different non-noble metal-based samples in conjunction with a carbon support. In brief, 6 mg Vulcan XC72R (Cabot) were sonicated for 20 min in DMF. Afterwards a total volume of 1440 µl in different ratios of 0.2 M $Ni(OAc)_2 \times 4H_2O$ (99.998% trace metals basis, Aldrich), $Fe(NO_3) \times 9H_2O$ (98% trace metals basis, alfa aeser), $Mn(OAc)_2 \times 4H_2O$ (99% trace metals basis, sigma aldrich) and $Co(NO_3)_2 \times 6H_2O$ (99% trace metals basis, strem chemicals) were added to the solution. To ensure the support impregnation the solution was stirred for at least 1 h. After impregnation 8 ml ultrapure water (>18 MΩ at room temperature) and 4 ml additional DMF were added to the reaction mixture. The solution was then microwave treated at 120 °C for 60 min and subsequently at 160 °C for 60 min. The final product was collected by centrifuging and several times washed with ultrapure water and ethanol.

Material Characterization

Inductively coupled plasma-optical emission spectroscopy (ICP-OES) was used for elemental and compositional analysis using a 715-ES-inductively coupled plasma analysis system with CCD detector (Varian). Prior to detecting, the catalyst materials were dissolved in a mixture of HNO_3/H_2SO_4/HCl in a ratio of 1:1:3. *X-ray diffraction (XRD)* measurements were carried out to study the crystallinity using a D8 Advance Diffractometer (Bruker) equipped with a Lynx Eye Detector and KFL Cu 2 K X-ray tube. The diffraction profiles were collected between 10–70° 2d with a step size of 0.039°. The divergence slit was set to 6 mm, the antiscattering slit to 6° and the Lynx-Iris to 10 mm.

Electrochemical Characterization

Each measurement is conducted in a three-electrode cell consisting of reversible hydrogen electrode (RHE, *Gaskatel*) as reference, a Pt mesh as counter and glassy carbon (GC) disk electrode (PINE) as working electrode. The 0.1 M KOH was prepared by using KOH pellets (>99.99% trace metals basis, sigma aldrich) and millipure water (>18 mΩ at room temperature). All electrode potentials are IR-corrected and given in respect to the reversible hydrogen electrode (RHE). For electrochemical testing a catalyst ink was prepared using 5 mg of catalyst powder, 750 µl i-propanol, 500 µl ultrapure water (>18 MΩ at room temperature) and 5 µl Nafion solution (5 wt%, sigma aldrich). The catalyst ink was sonicated for 15 min. For drop coating, 10 µl of the ink were pipetted onto a previously cleaned and polished glassy carbon electrode (Ø = 5 mm) and subsequent dried for 7 min at 50 °C. Before the catalysts are tested they were electrochemical pretreated for 20 cycles in N_2 saturated 0.1 M KOH between 1.0–0.5 V_{RHE} at 50 mV s^{-1}. After pretreatment, the catalysts were tested towards their bifunctional ORR and OER activity as presented in Figure 3 and explained in detail in the section *activity protocol*. At first, the ORR activity was determined by cycling two times between 1.0–0.05 V at 5 mV s^{-1} in O_2 saturated 0.1 M KOH. Then, the OER activity was determined by cycling 4 times between 1.0–1.8 V_{RHE}. A final linear sweep voltammogram from 1.8–0.05 V_{RHE} at 5 mV s^{-1} concluded the measurement. All measurements are conducted at room temperature.

Acknowledgements

Financial support by the German Research Foundation (DFG) through grant reference number STR 596/8-1 is grateful acknowledged.

Conflict of Interest

The authors declare no conflict of interest.

Keywords: Bifunctional Oxygen Catalyst · Non-Noble oxides · Oxygen Evolution Reaction · Oxygen Reduction Reaction · Reversible Electrolyzer

[1] a) M. A. Pellow, C. J. M. Emmott, C. J. Barnhart, S. M. Benson, *Energy Environ. Sci.* **2015**, *8*, 1938–1952; b) M. Ball, M. Weeda, *Int. J. Hydrogen Energy* **2015**, *40*, 7903–7919; c) I. Dincer, C. Acar, *Int. J. Hydrogen Energy* **2015**, *40*, 11094–11111; d) O. Ehret, K. Bonhoff, *Int. J. Hydrogen Energy* **2015**, *40*, 5526–5533; e) S. E. Hosseini, M. A. Wahid, *Renewable Sustainable Energy Rev.* **2016**, *57*, 850–866; f) S. Sharma, S. K. Ghoshal, *Renewable Sustainable Energy Rev.* **2015**, *43*, 1151–1158.

[2] a) H. N. Nong, H.-S. Oh, T. Reier, E. Willinger, M.-G. Willinger, V. Petkov, D. Teschner, P. Strasser, *Angew. Chem. Int. Ed.* **2015**, *accepted*; b) L. Gan, P. Strasser in *Dealloyed Pt-Based Core–Shell Catalysts for Oxygen Reduction, Vol. 9* (Ed. M. Shao), Springer, London, **2013**, pp. 533–560; c) M. Oezaslan, F. Hasché, P. Strasser, *J. Phys. Chem. Lett.* **2013**, *4*, 3273–3291; d) N. Hahn, S. Koh, P. Strasser, *ECS Trans.* **2006**, *3*, 139–140.

[3] a) K. S. Smith, H. L. Huyck, *The environmental geochemistry of mineral deposits* **1999**, *6*, 29–70; b) E. L. Miller, R. E. Rocheleau, *J. Electrochem. Soc.* **1997**, *144*, 3072–3077.

[4] a) M. Carmo, D. L. Fritz, J. Mergel, D. Stolten, *Int. J. Hydrogen Energy* **2013**; b) C. Song, J. Zhang in *Electrocatalytic Oxygen Reduction Reaction*, (Ed. J. Zhang), Springer London, **2008**, pp. 89–134.

[5] a) M. Gabbasa, K. Sopian, A. Fudholi, N. Asim, *Int. J. Hydrogen Energy* **2014**, *39*, 17765–17778; b) R. E. Clarke, S. Giddey, F. T. Ciacchi, S. P. S. Badwal, B. Paul, J. Andrews, *Int. J. Hydrogen Energy* **2009**, *34*, 2531–2542.

[6] a) J. Durst, A. Siebel, C. Simon, F. Hasche, J. Herranz, H. A. Gasteiger, *Energy Environ. Sci.* **2014**, *7*, 2255–2260; b) M. K. Bates, Q. Jia, N. Ramaswamy, R. J. Allen, S. Mukerjee, *J. Phys. Chem. C* **2015**, *119*, 5467–5477; c) J. Rossmeisl, A. Logadottir, J. K. Norskov, *Chem. Phys.* **2005**, *319*, 178–184.

[7] D. U. Lee, P. Xu, Z. P. Cano, A. G. Kashkooli, M. G. Park, Z. Chen, *J. Mater. Chem. A* **2016**, *4*, 7107–7134.

[8] Y. Gorlin, T. F. Jaramillo, *J. Am. Chem. Soc.* **2010**, *132*, 13612–13614.

[9] M. Risch, K. A. Stoerzinger, S. Maruyama, W. T. Hong, I. Takeuchi, Y. Shao-Horn, *J. Am. Chem. Soc.* **2014**, *136*, 5229–5232.

[10] a) Y. Zhao, R. Nakamura, K. Kamiya, S. Nakanishi, K. Hashimoto, *Nat. Commun.* **2013**, *4*; b) Y. Liang, Y. Li, H. Wang, J. Zhou, J. Wang, T. Regier, H. Dai, *Nat. Mater.* **2011**, *10*, 780–786; c) A. Zhao, J. Masa, W. Xia, A. Maljusch, M.-G. Willinger, G. Clavel, K. Xie, R. Schlögl, W. Schuhmann, M. Muhler, *J. Am. Chem. Soc.* **2014**, *136*, 7551–7554.

[11] S. Dresp, F. Luo, R. Schmack, S. Kuhl, M. Gliech, P. Strasser, *Energy Environ. Sci.* **2016**, *9*, 2020–2024.

[12] a) H. Jiang, Y. Yao, Y. Zhu, Y. Liu, Y. Su, X. Yang, C. Li, *ACS Appl. Mater. Interfaces* **2015**, *7*, 21511–21520; b) D. He, Y. Xiong, J. Yang, X. Chen, Z. Deng, M. Pan, Y. Li, S. Mu, *J. Mater. Chem. A* **2017**, *5*, 1930–1934.

[13] P. Trogadas, T. F. Fuller, P. Strasser, *Carbon* **2014**, *75*, 5–42.

[14] Y.-J. Wang, B. Fang, D. Zhang, A. Li, D. P. Wilkinson, A. Ignaszak, L. Zhang, J. Zhang, *Electrochem. Energy Reviews* **2018**.

[15] I. Bilecka, M. Niederberger, *Nanoscale* **2010**, *2*, 1358–1374.

[16] M. Gong, Y. Li, H. Wang, Y. Liang, J. Z. Wu, J. Zhou, J. Wang, T. Regier, F. Wei, H. Dai, *J. Am. Chem. Soc.* **2013**, *135*, 8452–8455.

[17] a) S. Dresp, P. Strasser, *ECS Trans.* **2016**, *75*, 1113–1119; b) M. Görlin, M. Gliech, J. F. de Araújo, S. Dresp, A. Bergmann, P. Strasser, *Catal. Today* **2016**, *262*, 65–73; c) M. Görlin, P. Chernev, J. Ferreira de Araújo, T. Reier, S. Dresp, B. Paul, R. Krähnert, H. Dau, P. Strasser, *J. Am. Chem. Soc.* **2016**, *138*, 5603–5614; d) C. C. L. McCrory, S. Jung, J. C. Peters, T. F. Jaramillo, *J. Am. Chem. Soc.* **2013**, *135*, 16977–16987.

[18] P. Oliva, J. Leonardi, J. F. Laurent, C. Delmas, J. J. Braconnier, M. Figlarz, F. Fievet, A. Deguibert, *J. Power Sources* **1982**, *8*, 229–255.

[19] M. Rajamathi, G. N. Subbanna, P. Vishnu Kamath, *J. Mater. Chem.* **1997**, *7*, 2293–2296.

[20] F. B. Saiah, B. L. Su, N. Bettahar, *J. Hazard. Mater.* **2009**, *165*, 206–217.

[21] a) T. Reier, D. Teschner, T. Lunkenbein, A. Bergmann, S. Selve, R. Kraehnert, R. Schlogl, P. Strasser, *J. Electrochem. Soc.* **2014**, *161*, F876–F882; b) S. Geiger, O. Kasian, B. R. Shrestha, A. M. Mingers, K. J. J. Mayrhofer, S. Cherevko, *J. Electrochem. Soc.* **2016**, *163*, F3132–F3138; c) S. Cherevko, T. Reier, A. R. Zeradjanin, Z. Pawolek, P. Strasser, K. J. J. Mayrhofer, *Electrochem. Commun.* **2014**, *48*, 81–85.

[22] a) H. Ghanbarlou, S. Rowshanzamir, M. J. Parnian, F. Mehri, *Int. J. Hydrogen Energy* **2016**, *41*, 14665–14675; b) T. J. P. Hersbach, A. I. Yanson, M. T. M. Koper, *Nature Communications,* **2016**, *7*, 12653; c) D. Banham, S. Ye, *ACS Energy Lett.* **2017**, *2*, 629–638.

[23] H. Bode, K. Dehmelt, J. Witte, *Electrochim. Acta* **1966**, *11*, 1079–1087.

[24] a) M. E. G. Lyons, M. P. Brandon, *Int. J. Electrochem. Sci.* **2008**, *3*, 1386–1424; b) L. Trotochaud, S. L. Young, J. K. Ranney, S. W. Boettcher, *J. Am. Chem. Soc.* **2014**, *136*, 6744–6753; c) D. A. Corrigan, *J. Electrochem. Soc.* **1987**, *134*, 377–384.

[25] a) M. W. Louie, A. T. Bell, *J. Am. Chem. Soc.* **2013**, *135*, 12329–12337; b) M. Goerlin, J. Ferreira de Araújo, H. Schmies, D. Bernsmeier, S. Dresp, M. Gliech, Z. Jusys, P. Chernev, R. Kraehnert, H. Dau, P. Strasser, *J. Am. Chem. Soc.* **2017**.

[26] Y. Gorlin, B. Lassalle-Kaiser, J. D. Benck, S. Gul, S. M. Webb, V. K. Yachandra, J. Yano, T. F. Jaramillo, *J. Am. Chem. Soc.* **2013**, *135*, 8525–8534.

[27] a) Y. Meng, W. Song, H. Huang, Z. Ren, S.-Y. Chen, S. L. Suib, *J. Am. Chem. Soc.* **2014**, *136*, 11452–11464; b) K. A. Stoerzinger, M. Risch, B. Han, Y. Shao-Horn, *ACS Catal.* **2015**, *5*, 6021–6031; c) A. S. Ryabova, A. Bonnefont, P. Zagrebin, T. Poux, R. Paria Sena, J. Hadermann, A. M. Abakumov, G. Kéranguéven, S. Y. Istomin, E. V. Antipov, G. A. Tsirlina, E. R. Savinova, *ChemElectroChem* **2016**, *3*, 1667–1677; d) A. S. Ryabova, F. S. Napolskiy, T. Poux, S. Y. Istomin, A. Bonnefont, D. M. Antipin, A. Y. Baranchikov, E. E. Levin, A. M. Abakumov, G. Kéranguéven, E. V. Antipov, G. A. Tsirlina, E. R. Savinova, *Electrochim. Acta* **2016**, *187*, 161–172.

[28] A. Bergmann, I. Zaharieva, H. Dau, P. Strasser, *Energy Environ. Sci.* **2013**, *6*, 2745–2755.

[29] a) M. Zhang, M. de Respinis, H. Frei, *Nat. Chem.* **2014**, *6*, 362; b) B. J. Trześniewski, O. Diaz-Morales, D. A. Vermaas, A. Longo, W. Bras, M. T. M. Koper, W. A. Smith, *J. Am. Chem. Soc.* **2015**, *137*, 15112–15121; c) O. Diaz-Morales, D. Ferrus-Suspedra, M. T. M. Koper, *Chem. Sci.* **2016**, *7*, 2639–2645.
[30] J. Masa, W. Xia, I. Sinev, A. Zhao, Z. Sun, S. Grützke, P. Weide, M. Muhler, W. Schuhmann, *Angew. Chem.* **2014**, *126*, 8648–8652.
[31] H. Dau, C. Limberg, T. Reier, M. Risch, S. Roggan, P. Strasser, *ChemCatChem* **2010**, *2*, 724–761.
[32] T. Reier, M. Oezaslan, P. Strasser, *ACS Catal.* **2012**, *2*, 1765–1772.

Manuscript received: April 21, 2018
Accepted Article published: July 19, 2018
Version of record online: August 9, 2018

Supporting Information

Non-Noble Metal Oxides and their Application as Bifunctional Catalyst in Reversible Fuel Cells and Rechargeable Air Batteries

Sören Dresp and Peter Strasser*

Supporting Information

Non-Noble Metal Oxides and their Application as Bifunctional Catalyst in Reversible Fuel Cells and Rechargeable Air Batteries

Sören Dresp, Peter Strasser*

The Electrochemical Catalysis, Energy, and Material Science Laboratory
Department of Chemistry, Chemical and Materials Engineering Division

Technische Universität Berlin
Straße des 17.Juni 124
10623 Berlin
Germany

E-mail: pstrasser@tu-berlin.de

X-ray diffraction of oxide materials

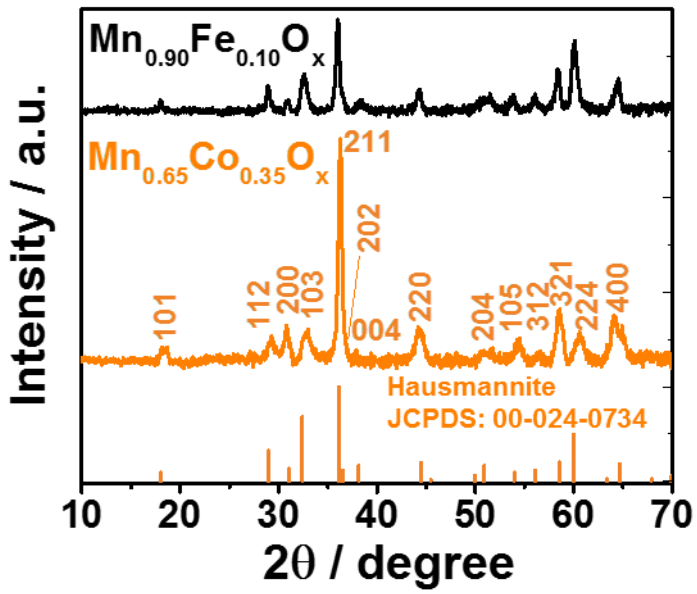

Figure S1: Powder X-ray diffraction (XRD) pattern (hausmannite) of non-noble metal oxides supported on Vulcan XC-72r prepared by solvothermal microwave assisted one-pot synthesis route

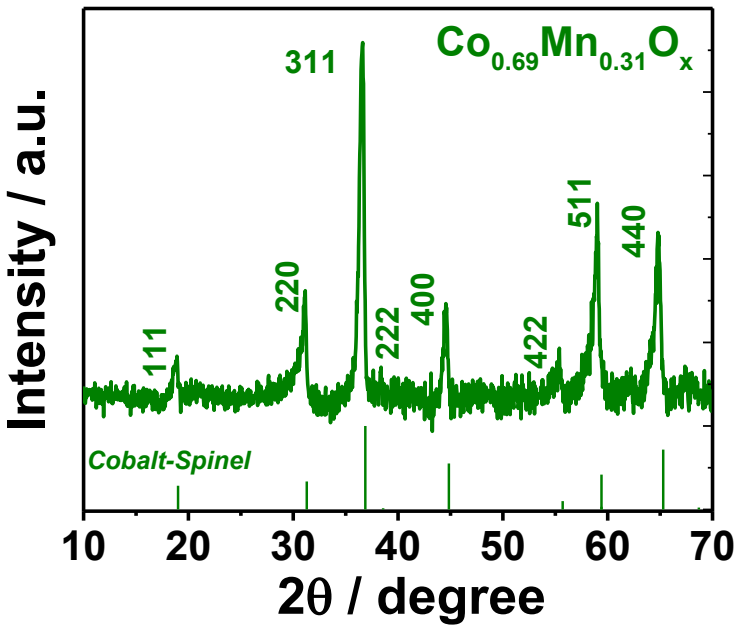

Figure S2: Powder X-ray diffraction (XRD) pattern (Spinel) of non-noble metal oxide supported on Vulcan XC-72r prepared by solvothermal microwave assisted one-pot synthesis route

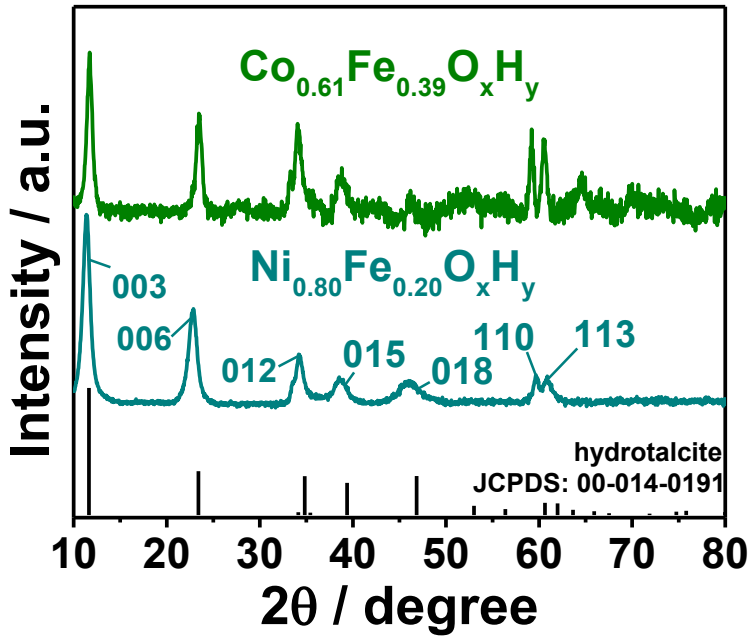

Figure S3: Powder X-ray diffraction (XRD) pattern (hydrotalcite) of non-noble metal oxides supported on Vulcan XC-72r prepared by solvothermal microwave assisted one-pot synthesis route

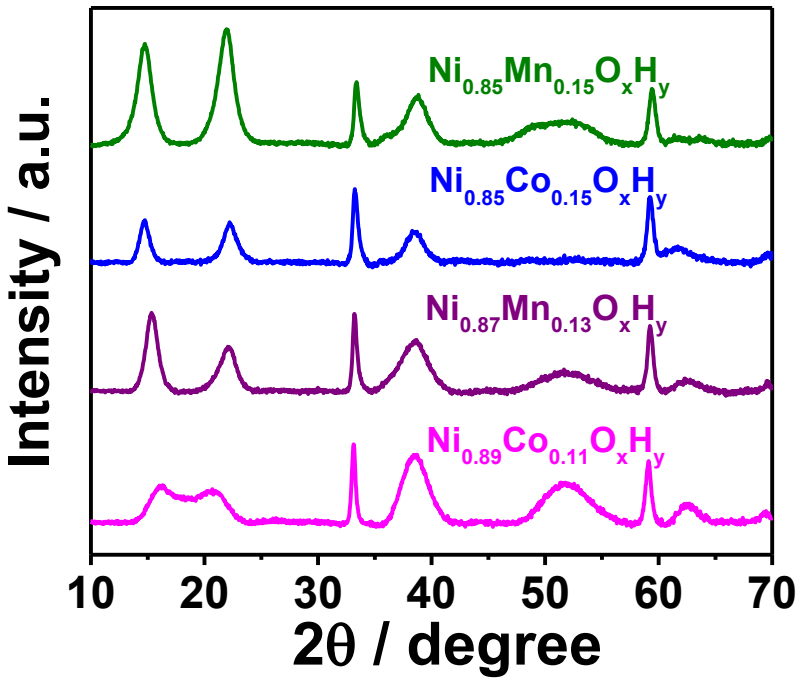

Figure S4: Powder X-ray diffraction (XRD) pattern of non-noble metal oxide samples supported on Vulcan XC-72r prepared by solvothermal microwave assisted one-pot synthesis route

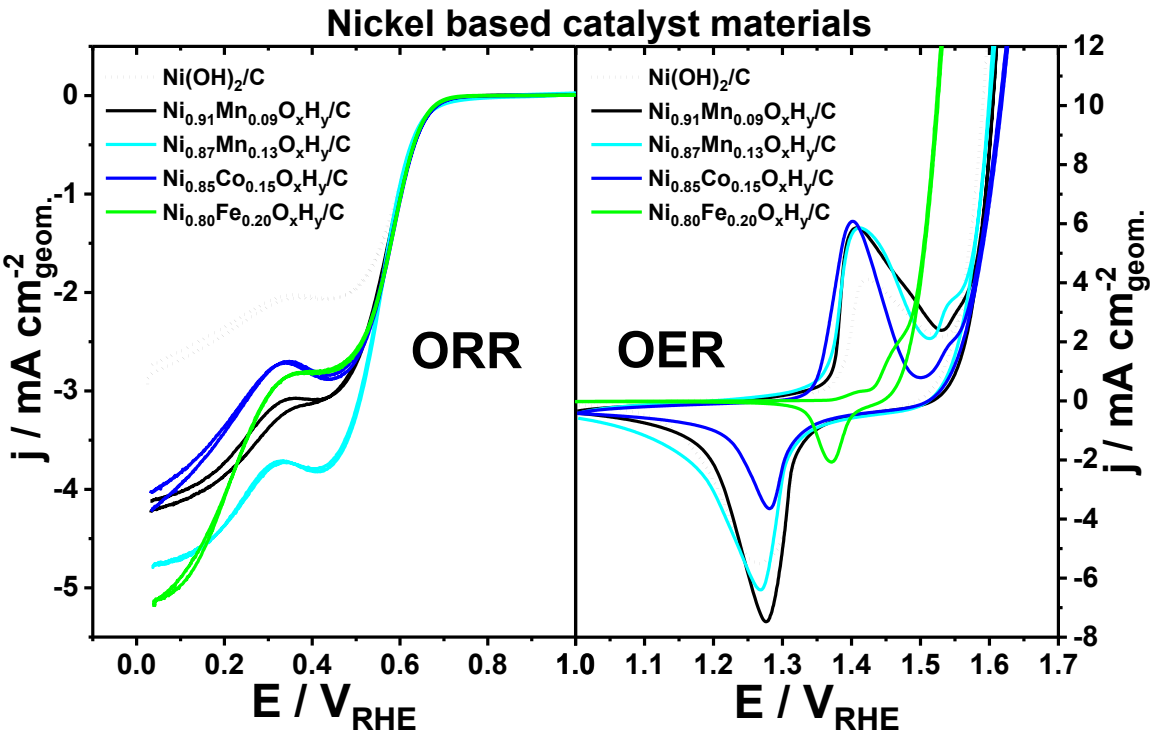

Figure S5: Cyclic voltammogram of Nickel based samples measured in 0.1 M KOH, 1600 rpm, 0.2 mg cm^{-2} cat. load and 5 mV s^{-1} scan rate. $Ni(OH)_2/C$ was included for comparison. The left side shows the ORR activity and the right side the OER activity

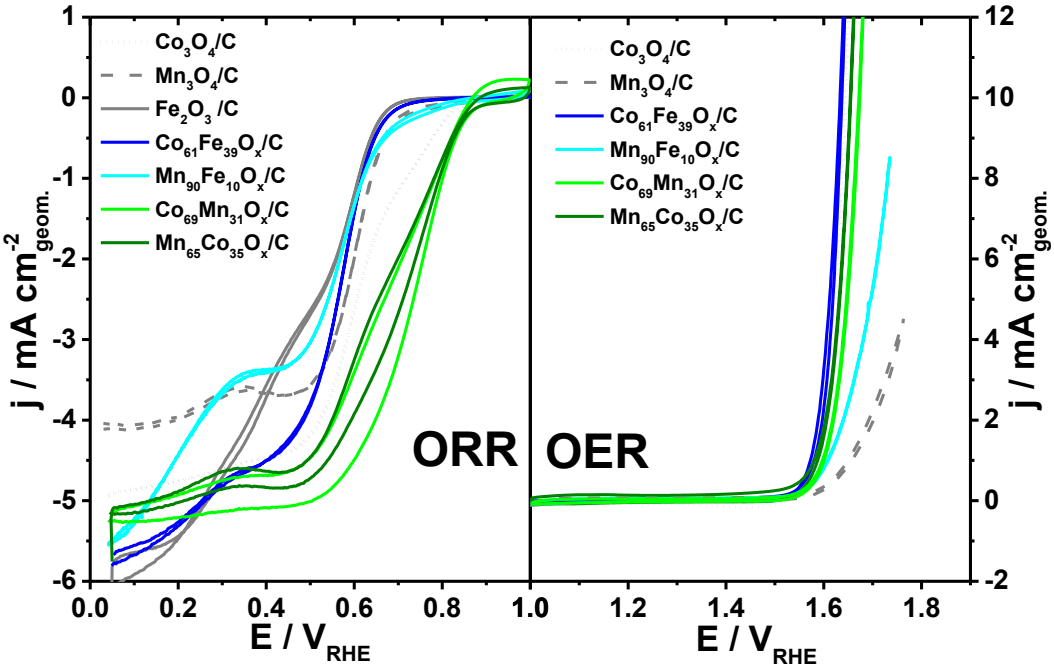

Figure S6: Cyclic voltammogram of non-noble catalysts without Ni measured in O_2 saturated 0.1 M KOH ,1600 rpm and a 5 mV/s scan rate. Co_3O_4/C and Mn_3O_4/C were included for comparison. The left side shows the ORR activity and the right side the OER activity

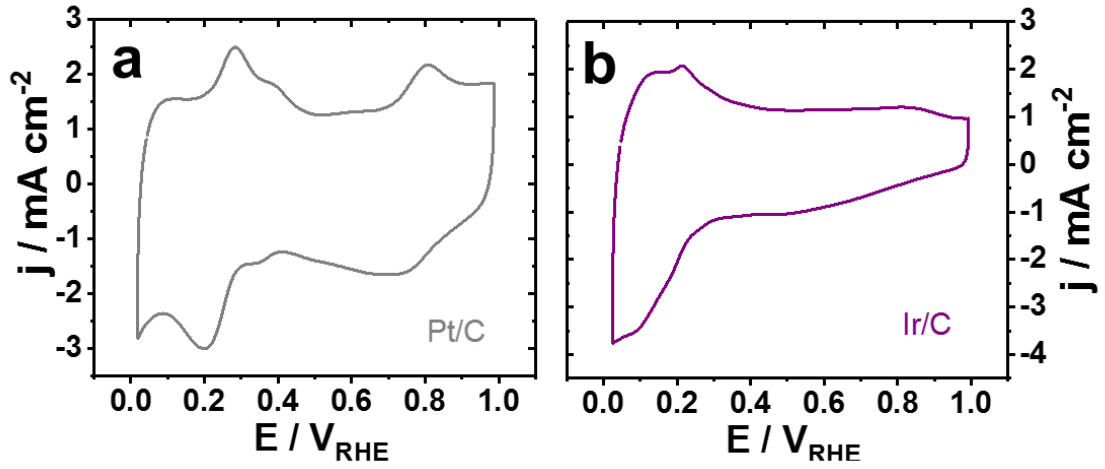

Figure S7: Cyclic voltammogram of commercial Pt-C 20 wt% (TKK) and Ir/C 20 wt% (BASF) catalyst materials measured in N_2 saturated 0.1 M KOH with a rotation speed of 1600 rpm and a scan rate of 100 mV s^{-1}

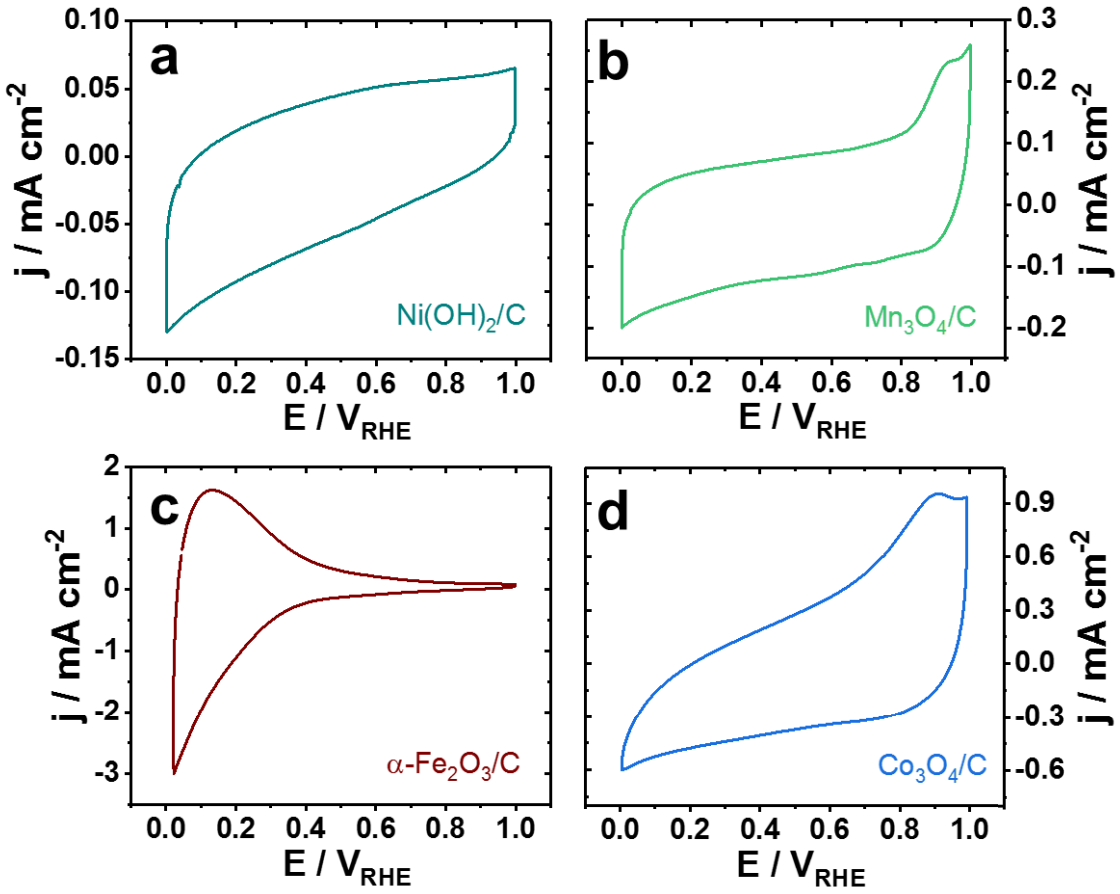

Figure S8: Cyclic voltammogram of solvothermal prepared monometallic catalysts measured in N_2 saturated 0.1 M KOH with a rotation speed 1600 rpm and a scan rate of 100 mV s^{-1}

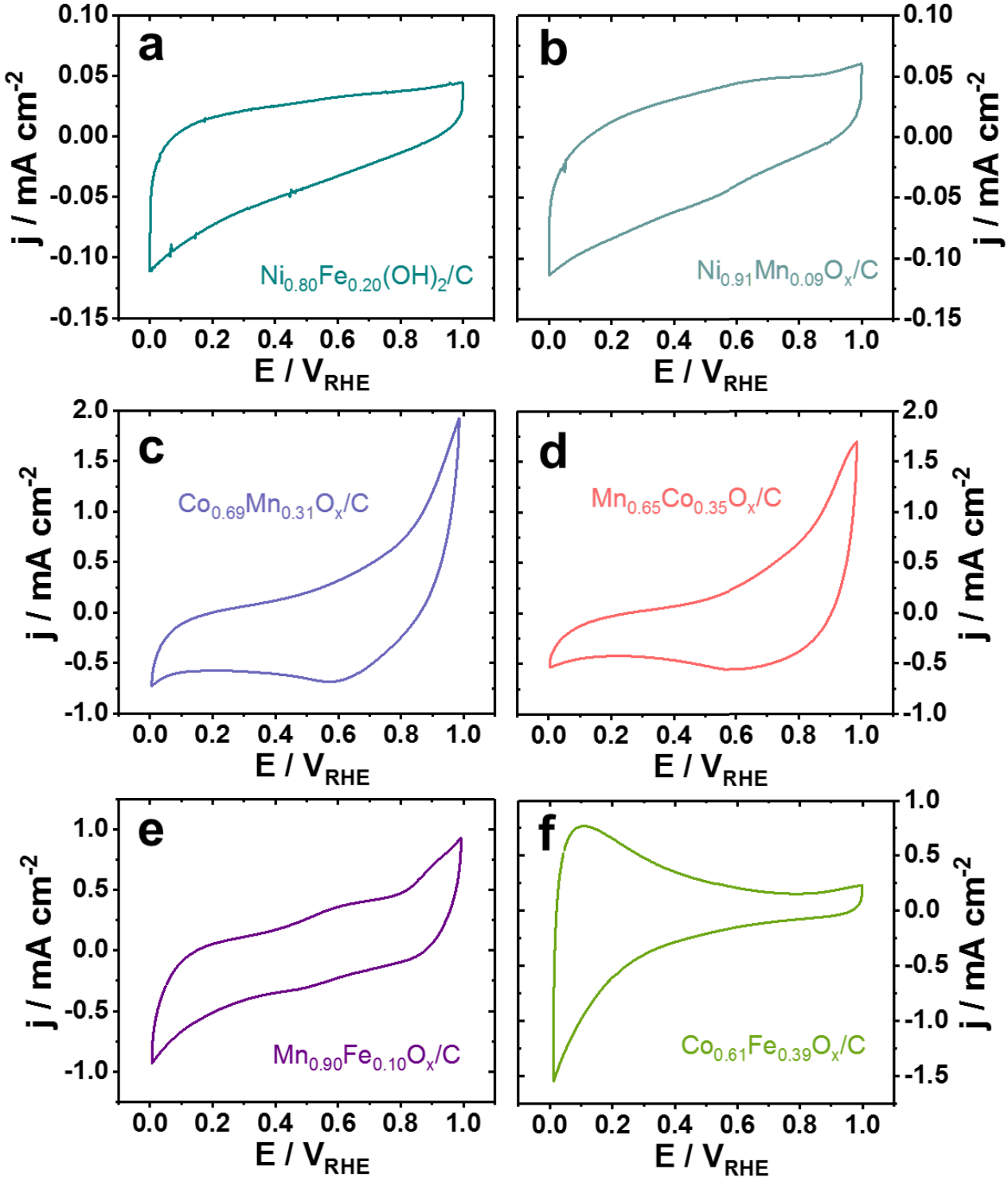

Figure S9: Cyclic voltammogram of solvothermal prepared bi-metallic catalysts measured in N_2 saturated 0.1 M KOH with a rotation speed 1600 rpm and a scan rate of 100 mV s^{-1}

Electrochemical surface area (ECSA) was determined by Impedance spectroscopy following the method by Jaramillo et al.[1]. The impedance spectrum was measured at 1 V in the range of 1 Hz to 100 kHz and the resulting graph was simulated by using an equivalent circuit as shown in the inset in figure S10.

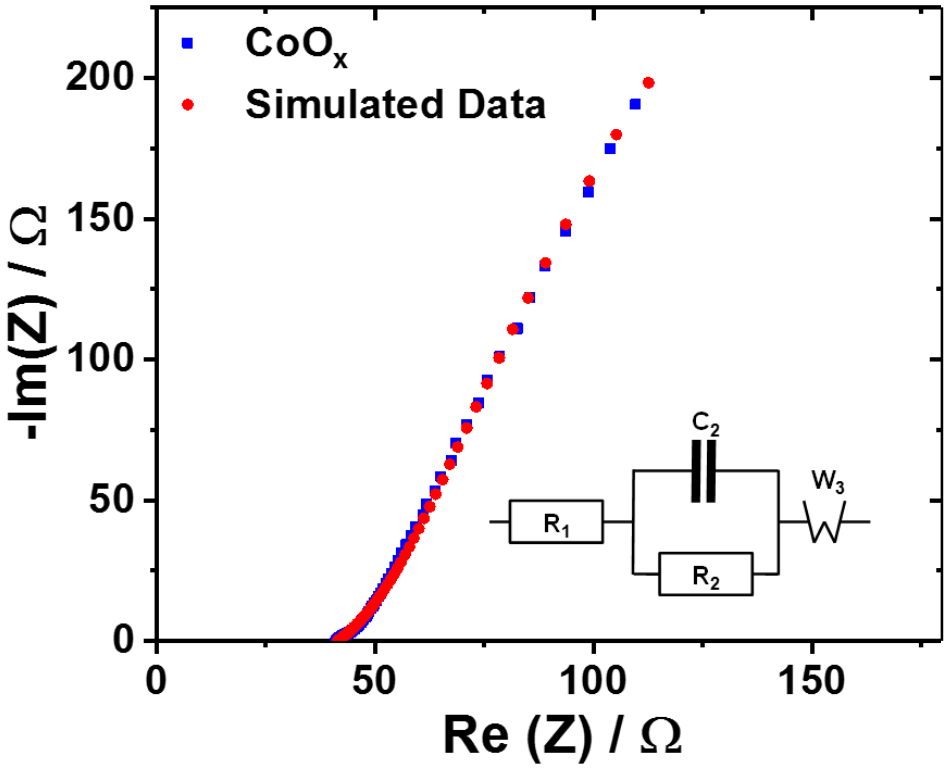

Figure S10: Representative Nyquist plot for CoO_x catalyst in 0.1 M KOH at 1 V vs. RHE in the frequency range 100 kHz to 1 Hz. The red circles represent the simulated data for an equivalent circuit presented in the inset

The simulated data with the corresponding catalyst system (Figure S10) shows the ohmic resistor R_1 = 41.2 Ω, the capacity C_2 = 1.93 mF, the second ohmic resistor R_2 = 5.0 kΩ and the Warburg coefficient W_3 = 103.99 Ω $s^{-1/2}$. Then, the resulting capacity C_2 was used to calculate the ECSA by using the following equation:

$$\mathrm{ECSA} = \frac{C_2}{C_s} \qquad \text{(S1)}$$

where C_s is the specific capacitance of the sample. The specific capacitance C_s is defined as the capacitance of an atomically smooth planar surface of the material per unit area under identical

electrolyte conditions. Since there is a huge range for the value of C_s and the estimation for each catalyst does not seem to be that practical it was decided to choose C_s = 0.04 mF cm^{-2}. The resulted ECSA values for the different catalyst materials are given in table S1 and the corresponding activity diagram is shown in Figure S11.

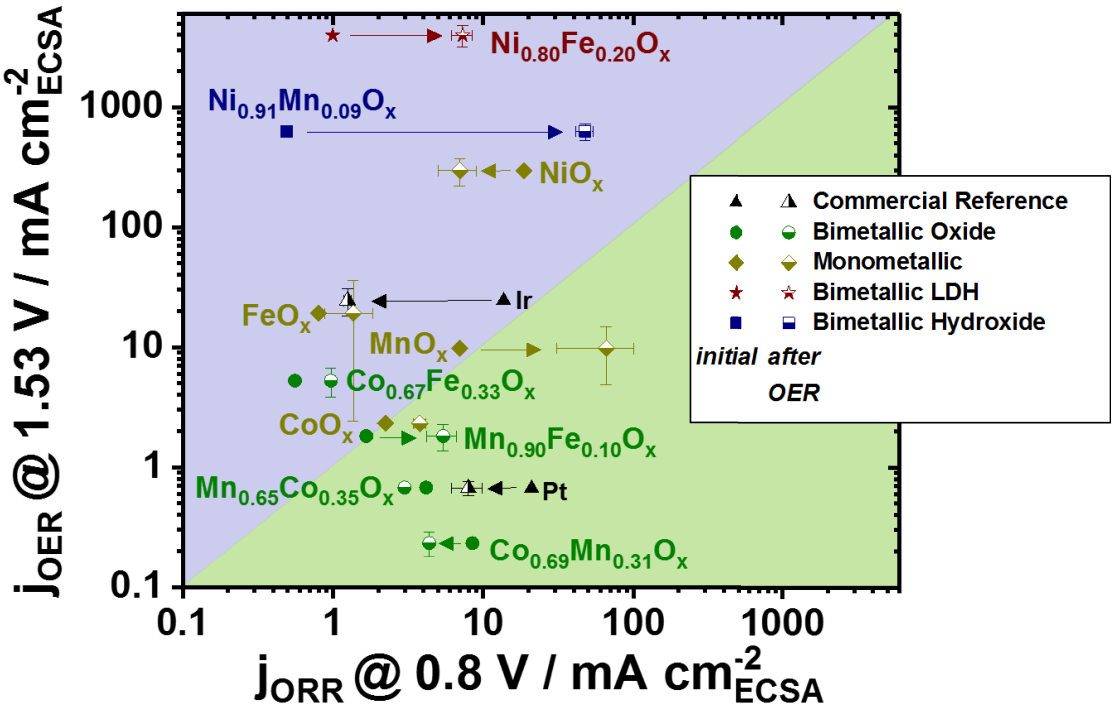

Figure S11: Diagram of elemental metal activities for different catalysts based on their electrochemical ECSA at 1.53 V_{RHE} for OER and at 0.8 V_{RHE} for ORR

Table S1: Catalyst materials and their potentials for the 2nd ORR and the 3rd OER cycle and the corresponding ECSA value

metal composition of catalyst	E_{ORR} @ -1 mA cm^{-2} [V_{RHE}]	E_{OER} @ 1 mA cm^{-2} [V_{RHE}]	E_{ORR} @ -3 mA cm^{-2} [V_{RHE}]	E_{OER} @ 10 mA cm^{-2} [V_{RHE}]	ECSA [cm^2]
Co	*0.712 ± 0.005*	*1.588 ± 0.004*	*0.583 ± 0.001*	*1.655 ± 0.006*	25.73 ± 0.32
Fe	*0.606 ± 0.003*	*1.675 ± 0.007*	*0.466 ± 0.001*	-	1.22 ± 0.24
Ir	*0.826 ± 0.008*	*1.497 ± 0.003*	*0.739 ± 0.009*	*1.580 ± 0.008*	24.46 ± 0.24
Mn	*0.636 ± 0.003*	*1.664 ± 0.007*	*0.548 ± 0.007*	-	2.40 ± 1.09
Ni	*0.627 ± 0.007*	*1.530 ± 0.001*	*0.058*	*1.597 ± 0.002*	1.39 ± 0.27
Pt	*0.931 ± 0.004*	*1.654 ± 0.003*	*0.888 ± 0.006*	-	48.23 ± 3.17
$Ni_{80}Fe_{20}$	*0.600 ± 0.002*	*1.449 ± 0.002*	*0.280 ± 0.012*	*1.527 ± 0.003*	0.59 ± 0.41
$Ni_{85}Co_{15}$	*0.607 ± 0.002*	*1.545 ± 0.003*	*0.323 ± 0.048*	*1.617 ± 0.009*	1.31 ± 0.31
$Ni_{91}Mn_{09}$	*0.596 ± 0.006*	*1.551 ± 0.001*	*0.405 ± 0.055*	*1.605 ± 0.001*	1.11 ± 0.25
$Mn_{31}Co_{69}$	*0.801 ± 0.002*	*1.591 ± 0.0005*	*0.633 ± 0.007*	*1.650 ± 0.002*	23.00 ± 0.30
$Mn_{65}Co_{35}$	*0.792 ± 0.002*	*1.599 ± 0.001*	*0.613 ± 0.003*	*1.672 ± 0.0005*	40.28 ± 1.26
$Co_{61}Fe_{39}$	*0.616 ± 0.001*	*1.590 ± 0.005*	*0.541 ± 0.003*	*1.649 ± 0.006*	5.27 ± 0.15
$Mn_{90}Fe_{10}$	*0.623 ± 0.007*	*1.613 ± 0.013*	*0.472 ± 0.015*	*1.717*	15.60 ± 1.90
$Ni_{67}Mn_{33}$	*0.584 ± 0.001*	*1.568 ± 0.006*	*0.247 ± 0.024*	*1.651 ± 0.009*	0.795 ± 0.08

The standard errors (SE) were estimated by determining the value from at least three independent measurements and calculated by using the following formula:

$$SE = \frac{s}{\sqrt{n}} \tag{S2}$$

with

$$s = \sqrt{\frac{\sum_{i=1}^{n} \left(x_i - \bar{x} \right)^2}{n-1}} \tag{S3}$$

where s is the standard deviation, n is the number of measurements, x_i is the value of the i measurement and $\bar{x}$ is the average of the values.

[1] C. C. L. McCrory, S. Jung, J. C. Peters and T. F. Jaramillo, *J. Am. Chem. Soc.* **2013**, *135*, 16977-16987.

II. *An efficient bifunctional two-component catalyst for oxygen reduction and oxygen evolution in reversible fuel cells, electrolyzers and rechargeable air electrodes*

This section reprints the following paper und is reproduced from

---

Dresp, S*. Luo, F., Schmack, R., Kühl, S., Gliech, M. & Strasser, P,*

Energy & Environmental Science, **2016**, *9, 2020–2024; DOI: https://doi.org/10.1039/C6EE01046F*

(21 pages)

Energy & Environmental Science

COMMUNICATION

View Article Online
View Journal | View Issue

Cite this: *Energy Environ. Sci.*, 2016, **9**, 2020

Received 8th April 2016,
Accepted 18th April 2016

DOI: 10.1039/c6ee01046f

www.rsc.org/ees

An efficient bifunctional two-component catalyst for oxygen reduction and oxygen evolution in reversible fuel cells, electrolyzers and rechargeable air electrodes†

Sören Dresp, Fang Luo, Roman Schmack, Stefanie Kühl, Manuel Gliech and Peter Strasser*

We report on a non-precious, two-phase bifunctional oxygen reduction and evolution (ORR and OER) electrocatalyst with previously unachieved combined roundtrip catalytic reactivity and stability for use in oxygen electrodes of unitized reversible fuel cell/electrolyzers or rechargeable metal–air batteries. The combined OER and ORR overpotential, total, at 10 mA cm^{-2} was a record low value of 0.747 V. Rotating Ring Disk Electrode (RRDE) measurements revealed a high faradaic selectivity for the 4 electron pathways, while subsequent continuous MEA tests in reversible electrolyzer cells confirmed the excellent catalyst reactivity rivaling the state-of-the-art combination of iridium (OER) and platinum (ORR).

Broader context

The transformation of our existing fossil fuel-based energy systems into renewable fuel-based ones will require advances and innovations from chemistry and catalysis science. In particular, efficient, low cost and abundant catalysts for the two-way conversion of electricity into, as well as the generation of electricity from high-energy molecules, such as molecular hydrogen, will be critical. "One way" hydrogen-based devices that facilitate these chemical processes, such as fuel cells and electrolyzers, typically depend on catalyst materials that are high in price and low in abundance, like platinum and iridium oxide. Earth-abundant bifunctional catalysts, on the other hand, that can act as "two-way" catalysts and combine the fuel cell as well as the electrolyzer functions would allow the design of compact (reversible) unitized regenerative fuel cells (URFC). Here, we report on a facile design concept, and the synthesis, activity, selectivity and device performance of bifunctional oxygen electrode (oxygen reduction and oxygen evolution) catalysts. Deployed in gas diffusion electrodes, our heterogeneous two-component catalysts display previously unachieved bifunctional catalytic activity.

Electrochemical energy storage based on the interconversion of renewable electricity and molecular fuels (solar fuels) and solid state structures (aqueous metal–air cells) invariably involves the oxygen/water redox system supplying and consuming water, protons, electrons and oxygen. This is why efficient catalysts for the oxygen evolution reaction (OER: $4OH^- \rightarrow O_2 + 2H_2O + 4e^-$) and the oxygen reduction reaction (ORR: $O_2 + 2H_2O + 4e^- \rightarrow 4OH^-$) are critical.[1–4] Combining the two functionalities in one single bifunctional oxygen redox electrode would greatly simplify the design of energy conversion devices or enhance the mobility and power-to-weight ratio. This plays an important role in spacecraft, aircraft, and ground transportation applications. Active oxygen redox catalysts such as IrO_2 or Pt are rare and expensive, which is why the development of efficient non-precious oxygen catalysts is of interest.[5–10] The layered double hydroxide of Ni and Fe ("NiFe-LDH") is known to be one of the most active non-noble OER catalysts in alkaline solution.[5,11–26] In contrast, nitrogen-doped carbon materials are promising non-precious candidates for the ORR.[27–30] Rather than exploring suitable bifunctional catalytic surface sites, or designing two distinct active sites on the same substrate, we propose the facile heterogeneous mixing of either material to obtain a two-phase bifunctional catalyst. This was shown for noble metal catalysts of iridium and platinum.[31,32] Recently, non-precious metal mixtures of Mn–Co oxides and carbon nanotubes have been tested.[33] Realizing that a two-component surface is necessary for highly active bifunctional catalysts,[34,35] in this contribution, we designed two-component NiFe-LDH – Fe–N–C catalysts resulting in today's most efficient bifunctional oxygen electrodes in 0.1 M KOH. A mutual improving effect between the two components in the two-phase structure with distinct neighbouring active sites appears key to the observed performance.

Using a fast microwave-assisted solvothermal one-pot synthesis route (Fig. S1, ESI†), we prepared a carbon-supported crystalline NiFe-LDH catalyst material in a Ni/Fe ratio of ~3.6 ($Ni_{0.78}Fe_{0.22}(OH)_x$) and a metal loading of ~37 wt%. The X-ray diffraction (XRD) pattern (Fig. 1) is consistent with the data-based reflections of layered double hydroxides (JCPDS: 00-014-0191), but with slightly higher interlayer distances.[36]

TEM images of NiFe-LDH/C show very small (~2–4 nm) plates presumably representing NiFe-LDH flakes. SAED revealed instability of the LDH phase under TEM working conditions

Department of Chemistry, Technical University Berlin, 10623 Berlin, Germany

† Electronic supplementary information (ESI) available. See DOI: 10.1039/c6ee01046f

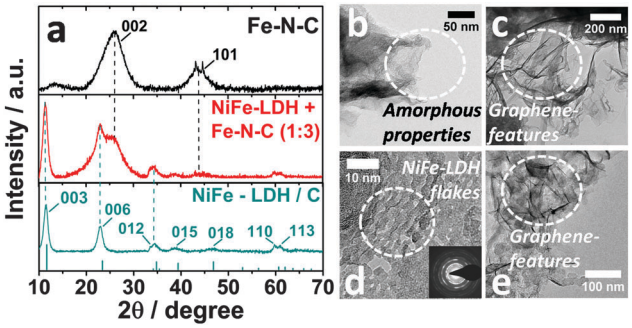

Fig. 1 (a) X-ray diffraction profiles of the Fe N-doped carbon catalyst (Fe–N–C) (top), the mixture of NiFe-LDH and Fe–N–C catalysts (middle) and the carbon-supported NiFe-layered double hydroxide catalyst (NiFe-LDH/C) in an atomic ratio of ~3.6 ($Ni_{0.78}Fe_{0.22}(OH)_x$) (bottom); (b and c) TEM images of Fe–N–C; and (d and e) TEM images of NiFe-LDH/C.

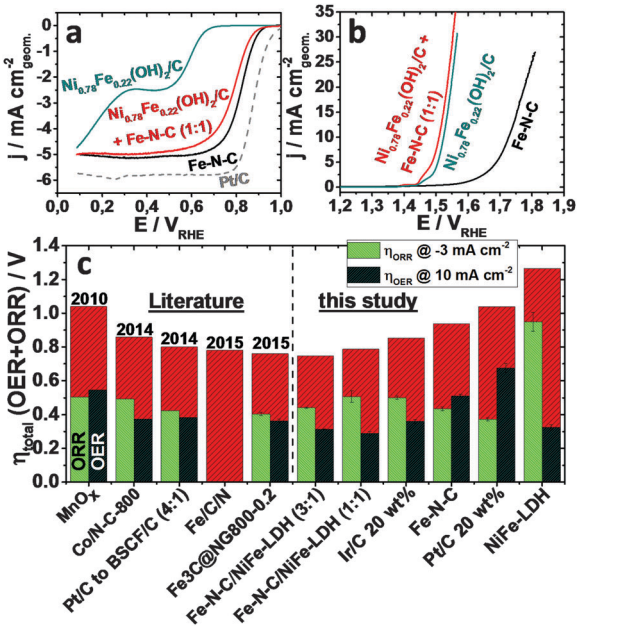

Fig. 2 Catalytic ORR (a) and OER (b) voltammetric profile and activity of the pure NiFe-LDH, pure Fe–N–C catalysts, and of their two-component mixture in O_2-saturated 0.1 M KOH at 5 mV s^{-1} scan rate, 1600 rpm rotation speed and 0.2 mg cm^{-2} total catalyst loading; and (c) individual ORR and OER, and total overpotentials for six different catalysts of this study (right side) in comparison to the published literature (left side). Fe–N–C/NiFe-LDH (*X* : *Y*) denote novel two-phase catalysts reported here. Detailed activity values are given in Table S1 (ESI†).

(high vacuum and e^--beam) since only NiO (JCPDS: 03-065-2901), possibly mixed with FeO (JCPDS: 01-077-2355), was detected. Furthermore, NiFe-LDH/C showed graphene features as shown in Fig. 1e which evolved from the carbon black support. The Fe–N–C material was synthesized using aniline polymerization in the presence of $FeCl_3$, followed by repetitive annealing and acid leaching to dissolve the residual Fe species, which may block the active sites in the catalyst material (see the ESI† and Fig. S2).[37] The XRD pattern showed largely graphene reflections (JCPDS: 98-000-0231) (Fig. 1a). In fact, the graphene morphology is detected by TEM (Fig. 1c). Additional TEM images suggest a strong amorphization of the remaining sample (Fig. 1b), which is in accordance with the XRD data due to non-appearance of strong reflections. When we mixed the samples, the XRD data reveal a two-phase system with reflections of both samples. So we believe that the catalyst system is a mixed two component system with separated phases. Supporting this, TEM images show graphene features as well as a flake like structure almost similar to the features of each of the other samples (Fig. S8, ESI†).

Electrochemical activity

First, we investigated the OER and ORR activity in O_2-saturated 0.1 M KOH at 1600 rpm separately for both catalysts. The results are shown in Fig. 2a and b. Linear sweep voltammetry verified the high OER activity for NiFe-LDH/C and high ORR activity for the Fe–N–C material. As expected, either material showed essentially no activity for the reverse reactions: NiFe-LDH was almost inactive for ORR and Fe–N–C for OER.

We then tested a two-component mixture of the catalysts keeping the total catalyst loading at 0.2 mg cm^{-2} in all measurements. Our data showed that all the beneficial features of NiFe-LDH and Fe–N–C are fully unfolded in the mixture due to the presence of the other component.

Fig. 2b demonstrates that the two-phase Fe–N–C/NiFe-LDH (1 : 1) sample showed a slightly higher OER activity than the identical NiFe-LDH alone. This could be due to a higher surface area or improved conductivity indicated by a higher $Ni^{2+/3+}$ redox peak[11,13,23,38] presented in Fig. S9 (ESI†), which is also indicated by capacitive measurements in N_2 presented in Fig. S10 (ESI†). We further note that the ORR activity of the two-phase powder catalyst, at constant OER activity, could be significantly increased by increasing the Fe–N–C/NiFe-LDH ratio to 3 : 1 (see "Fe–N–C/NiFe-LDH (3 : 1)" catalyst).

Fig. 2c shows the combined overpotentials, $\eta_{total} = \eta_{OER} + \eta_{ORR}$, of our two-phase catalysts and some previously reported materials in a reversible oxygen electrode. The parameter η_{total} describes the effective combined oxygen overpotential of the OER overpotential at 10 mA cm^{-2} and the half-wave ORR potential ($E_{1/2}$) at −3 mA cm^{-2} and 1600 rpm.[39,40] The evolution of reported η_{total} values (Fig. 2c left) compared to those of the present study (Fig. 2c right) demonstrates the superiority of our two-phase catalysts. While in 2010 a single-phase Mn-oxide based catalyst has been shown to have an overpotential of η_{total} = 1.04 V, our Fe–N–C/NiFe-LDH (3 : 1) catalyst reached the value of 0.747 V ± 0.006 V and thus represents the most efficient bifunctional oxygen redox RDE activity to date. It should be mentioned that in 2011 Liang *et al.* prepared Co_3O_4 on N-doped graphene with a lower total overpotential of $\Delta\eta_{total}$ = 0.71 V, this however in 1 M KOH, not 0.1 M KOH.[41] In addition, our material has outstanding individual OER activity with an overpotential of 0.309 ± 0.002 V *vs.* RHE at 10 mA cm^{-2}. This is a lower overpotential than that of IrO_2 and is one of the best bifunctional catalysts in 0.1 M KOH (Fig. 2c, details in Table S1, ESI†). To explain the observed combined performance of a physical mixture, our preliminary studies confirm[34,35] that a

simple two-phase system provides two distinct and spatially separated ORR and OER catalytic sites that are sufficiently homogeneous to act as a contiguous catalyst film, yet are spatially separated enough not to interfere with each other. Based on our available data, we cannot exclude the formation of special 3D structured active sites by physical atomic proximity of OER and ORR sites on either component, as suggested by Rossmeisl and co-workers to overcome restrictive adsorption scaling relations.[42–44] Following this track, the combination of two active sites for the generation of a multisurface site was also suggested by Norskov *et al.* as a new design paradigm for heterogeneous catalysts.[45]

Selectivity

Rotating ring disk electrode (RRDE) measurements were carried out to determine the ORR selectivities under alkaline conditions (Fig. 3a). The ORR reaction diagram (Fig. 3b[46–48]) highlights the direct 4e$^-$ pathway to OH$^-$ and the 2e$^-$ pathway to HO_2^- which may desorb into the solution, subsequently react in a 2e$^-$ process to OH$^-$, or else undergo chemical disproportionation. The ring potential was kept at +1.2 V_{RHE} to monitor the desorbed HO_2^- species upon its re-oxidation to oxygen at the ring (see Fig. 3c). Almost similar to Fe–N–C the RRDE data revealed a high selectivity (>90% at $E > 0.2$ V) towards the direct 4-electron pathway to OH$^-$ for the Fe–N–C/NiFe-LDH (3 : 1) catalyst, compared to glassy carbon (12–17%) or the 20 wt% Pt/C reference (86%). A completely different behaviour of NiFe-LDH that showed a strong increase of H_2O_2 production at low overpotentials was observed. After passing a maximum of ~76% at 0.45 V *vs.* RHE, the production rate of H_2O_2 drops and the kinetics change to a 4e$^-$ transfer reaction to OH$^-$ at 0.1 V *vs.* RHE. Evaluation of the number of transferred electrons during the reaction further revealed an almost ideal 4-electron transfer over the full potential range for all Fe–N–C based catalysts (Fig. 3d). Furthermore, we confirmed O_2 production during OER for NiFe-LDH *via* RRDE measurements as presented in the ESI,† Fig. S11. Therefore we kept the potential at 0.31 V *vs.* RHE to reduce the oxygen to HO_2^-. We further determined an efficiency of almost 100% at 1.5 V *vs.* RHE. At higher potentials the faradaic efficiency drops, which can be explained by mass transfer limitations of the gaseous oxygen produced at the disk.

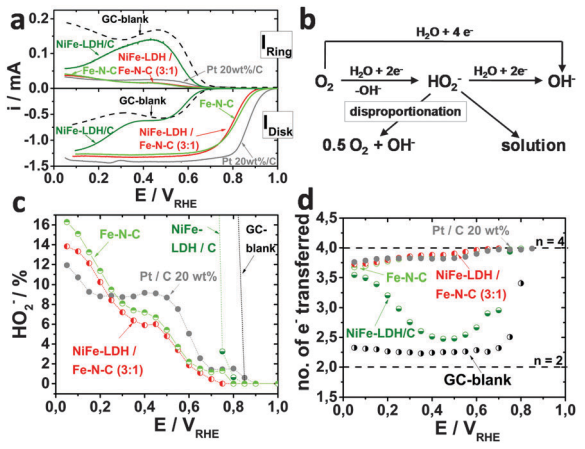

Fig. 3 (a) Rotating Ring Disk Electrode (RRDE) selectivity measurements; (b) reaction pathways of the ORR; (c) faradaic HO_2^- selectivities of Fe–N–C (green), Fe–N–C/NiFe-LDH (3 : 1) (red), Pt (grey), and carbon (dashed line,); and (d) the number of transferred electrons as a function of electrode potential.

Unitized fuel cell/electrolyzer performance

Unitized alkaline exchange membrane-based single-cell fuel cell/electrolyzer measurements were carried out to study the catalyst performance under real conditions (Fig. 4a). Alternating fuel cell/electrolyzer polarization tests revealed an unprecedented activity for the noble metal-free Fe–N–C/NiFe-LDH (3 : 1) positive electrode material rivaling the Ir catalyst. Platinum, as expected, showed excellent fuel cell but poor electrolyzer performance (Fig. 4b).

In Fig. 4c a cell stability test is presented for the Fe–N–C/NiFe-LDH (3 : 1) catalyst, where the polarization curves were recorded in alternating fuel cell and electrolyzer modes. The fuel cell activity decreased gradually after each cycle. The initial round trip efficiency (RTE) decreased from 50% to 45% in the second cycle. This was superior to the performance of the two noble-metal reference catalysts (Fig. S14, ESI†), indicating a higher reversibility of the bifunctional two-component catalyst.

To evaluate stability we conducted a long term RDE measurement. Fig. 4d presents a 24 h galvanostatic RDE stability test of the Fe–N–C/NiFe-LDH (3 : 1) catalyst. Currents were held for 1 h, alternating between the fuel cell and electrolyzer modes.

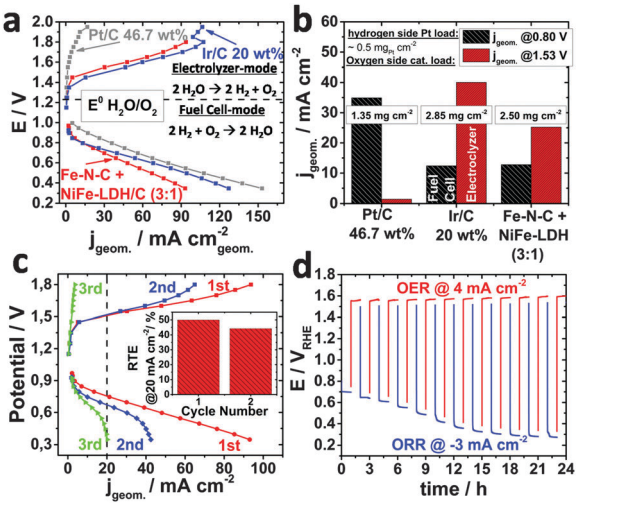

Fig. 4 Full alkaline exchange membrane (AEM)-based unitized MEA fuel/electrolysis cell measurements: (a) polarization curves for the first fuel cell/electrolysis cycle with platinum as the hydrogen catalyst, and platinum (grey), iridium (blue) and the Fe–N–C/NiFe-LDH (3 : 1) as the oxygen catalysts. (b) Comparison of geometric activities of the three unitized cells. (c) Three consecutive fuel cell/electrolyzer cycles using the Fe–N–C/NiFe-LDH (3 : 1) catalyst, inset: round trip efficiency (RTE) for the first two cycles. (d) 24 h RDE stability measurement of unitized fuel/electrolysis cell using the Fe–N–C/NiFe-LDH (3 : 1) catalyst. Unitized fuel cell/electrolyzer performance.

To reduce bubble formation the OER current was held at 4 mA cm^{-2} and the ORR current was held at -3 mA cm^{-2}, which represents approximately the half wave potential ($E_{1/2}$) at 1600 rpm.

Clearly, the OER cell potentials remained constant and stable for the entire 24 h test highlighting the stability of the NiFe-LDH OER system. The slightly larger performance drop in fuel cell mode is consistent with the data from Fig. 4c and the RDE data. The oxygen reduction potential decreased per each OER/ORR cycle until it remained constant at approximately 0.3 V. We attribute this to the electrochemical oxidation of the active Fe–N–C sites combined with electrochemical carbon corrosion which is also indicated by the strong activity decrease during OER for the Fe–N–C catalyst presented in Fig. S13 (ESI†).[49] We believe that stronger graphitization at a higher temperature could prevent the strong degradation of this material. Further TEM and SEAD measurements of the two-component system indicated beside a strong agglomeration an increased crystallinity and nanoparticle formation after the electrochemical treatment (Fig. S8, ESI†).

In conclusion, we present a microwave-assisted synthesis of highly OER active NiFe-LDH. Physical mixing with a Fe–N–C catalyst in a highly active bifunctional oxygen electrode catalyst for use at unitized oxygen electrodes. This catalyst exhibited the lowest combined OER/ORR overpotential ever recorded in 0.1 M KOH. RRDE investigation showed high ORR selectivity. Beyond RDE screenings, we further reported anion exchange membrane electrode assembly tests (AEM-MEA) in a reversible electrolyzer. The non-noble mixture catalysts outperformed Pt and rivaled Ir reference catalysts. During alternating electrolyzer and fuel cell tests the ORR cell performance revealed a larger degradation compared to the OER cell performance, suggesting that the OER potentials damage the carbon-based Fe–N–C ORR active sites, which might be improved by stronger graphitization using a higher annealing temperature or replacing the graphitic Fe–N–C catalyst by Fe–N doped graphene.

Acknowledgements

Financial support by the German Research Foundation (DFG) through grant reference number STR 596/8-1 and the Federal Ministry of Education and Research (BMBF) grant 03SF0433A ''MEOKATS'' are grateful acknowledged. S. K. acknowledges financial support under BMBF grant 03SF0527A ''LOPLAKAT''. Also, we acknowledge the ZELMI for making the TEM micrograph.

Notes and references

1 L. Barreto, A. Makihira and K. Riahi, *Int. J. Hydrogen Energy*, 2003, **28**, 267–284.
2 S. M. Fernández Valverde, *Geofis. Int.*, 2002, **41**, 223–228.
3 G. Marbán and T. Valdés-Solís, *Int. J. Hydrogen Energy*, 2007, **32**, 1625–1637.
4 R. Schlogl, *ChemSusChem*, 2010, **3**, 209–222.
5 C. C. L. McCrory, S. Jung, J. C. Peters and T. F. Jaramillo, *J. Am. Chem. Soc.*, 2013, **135**, 16977–16987.
6 H. A. Gasteiger, S. S. Kocha, B. Sompalli and F. T. Wagner, *Appl. Catal., B*, 2005, **56**, 9–35.
7 M. Heggen, M. Oezaslan, L. Houben and P. Strasser, *J. Phys. Chem. C*, 2012, **116**, 19073–19083.
8 R. Forgie, G. Bugosh, K. C. Neyerlin, Z. C. Liu and P. Strasser, *Electrochem. Solid-State Lett.*, 2010, **13**, D36–D39.
9 E. Ortel, T. Reier, P. Strasser and R. Kraehnert, *Chem. Mater.*, 2011, **23**, 3201–3209.
10 M. Oezaslan, F. Hasche and P. Strasser, *J. Electrochem. Soc.*, 2012, **159**, B394–B405.
11 L. Trotochaud, S. L. Young, J. K. Ranney and S. W. Boettcher, *J. Am. Chem. Soc.*, 2014, **136**, 6744–6753.
12 M. W. Louie and A. T. Bell, *J. Am. Chem. Soc.*, 2013, **135**, 12329–12337.
13 L. Trotochaud, J. K. Ranney, K. N. Williams and S. W. Boettcher, *J. Am. Chem. Soc.*, 2012, **134**, 17253–17261.
14 D. A. Corrigan, *J. Electrochem. Soc.*, 1987, **134**, 377–384.
15 D. A. Corrigan, R. S. Conell, C. A. Fierro and D. A. Scherson, *J. Phys. Chem.*, 1987, **91**, 5009–5011.
16 R. L. Doyle, I. J. Godwin, M. P. Brandon and M. E. G. Lyons, *Phys. Chem. Chem. Phys.*, 2013, **15**, 13737–13783.
17 C.-C. Hu and Y.-R. Wu, *Mater. Chem. Phys.*, 2003, **82**, 588–596.
18 M. E. G. Lyons and M. P. Brandon, *Int. J. Electrochem. Sci.*, 2008, **3**, 1386–1424.
19 C. C. L. McCrory, S. Jung, I. M. Ferrer, S. M. Chatman, J. C. Peters and T. F. Jaramillo, *J. Am. Chem. Soc.*, 2015, **137**, 4347–4357.
20 M. D. Merrill and R. C. Dougherty, *J. Phys. Chem. C*, 2008, **112**, 3655–3666.
21 E. L. Miller and R. E. Rocheleau, *J. Electrochem. Soc.*, 1997, **144**, 3072–3077.
22 E. Potvin and L. Brossard, *Mater. Chem. Phys.*, 1992, **31**, 311–318.
23 X. Yu, M. Zhang, W. Yuan and G. Shi, *J. Mater. Chem. A*, 2015, **3**, 6921–6928.
24 K. Zeng and D. Zhang, *Prog. Energy Combust. Sci.*, 2010, **36**, 307–326.
25 F. Dionigi, T. Reier, Z. Pawolek, M. Gliech and P. Strasser, *ChemSusChem*, 2016, DOI: 10.1002/cssc.201501581.
26 M. Görlin, P. Chernev, J. Ferreira de Araújo, T. Reier, S. Dresp, B. Paul, R. Krähnert, H. Dau and P. Strasser, *J. Am. Chem. Soc.*, 2016, DOI: 10.1021/jacs.6b00332.
27 G. Wu, K. L. More, C. M. Johnston and P. Zelenay, *Science*, 2011, **332**, 443–447.
28 D. Geng, Y. Chen, Y. Chen, Y. Li, R. Li, X. Sun, S. Ye and S. Knights, *Energy Environ. Sci.*, 2011, **4**, 760–764.
29 W. Li, J. Wu, D. C. Higgins, J.-Y. Choi and Z. Chen, *ACS Catal.*, 2012, **2**, 2761–2768.
30 L. Lin, Q. Zhu and A.-W. Xu, *J. Am. Chem. Soc.*, 2014, **136**, 11027–11033.
31 S. Zhigang, Y. Baolian and H. Ming, *J. Power Sources*, 1999, **79**, 82–85.
32 S.-Y. Huang, P. Ganesan, H.-Y. Jung and B. N. Popov, *J. Power Sources*, 2012, **198**, 23–29.
33 A. Zhao, J. Masa, W. Xia, A. Maljusch, M.-G. Willinger, G. Clavel, K. Xie, R. Schlögl, W. Schuhmann and M. Muhler, *J. Am. Chem. Soc.*, 2014, **136**, 7551–7554.

34 M. Risch, K. A. Stoerzinger, S. Maruyama, W. T. Hong, I. Takeuchi and Y. Shao-Horn, *J. Am. Chem. Soc.*, 2014, **136**, 5229–5232.
35 W. T. Hong, M. Risch, K. A. Stoerzinger, A. Grimaud, J. Suntivich and Y. Shao-Horn, *Energy Environ. Sci.*, 2015, **8**, 1404–1427.
36 M. Gabrovska, D. Crisan, N. Stanica, D. Nikolova, L. Bilyarska, M. Crisan and R. Edreva-Kardjieva, *Rev. Roum. Chim.*, 2014, **59**, 447–452.
37 N. R. Sahraie, J. P. Paraknowitsch, C. Göbel, A. Thomas and P. Strasser, *J. Am. Chem. Soc.*, 2014, **136**, 14486–14497.
38 M. Gong, Y. Li, H. Wang, Y. Liang, J. Z. Wu, J. Zhou, J. Wang, T. Regier, F. Wei and H. Dai, *J. Am. Chem. Soc.*, 2013, **135**, 8452–8455.
39 Y. Zhao, K. Kamiya, K. Hashimoto and S. Nakanishi, *J. Phys. Chem. C*, 2015, **119**, 2583–2588.
40 Y. Gorlin and T. F. Jaramillo, *J. Am. Chem. Soc.*, 2010, **132**, 13612–13614.
41 Y. Liang, Y. Li, H. Wang, J. Zhou, J. Wang, T. Regier and H. Dai, *Nat. Mater.*, 2011, **10**, 780–786.
42 N. B. Halck, V. Petrykin, P. Krtil and J. Rossmeisl, *Phys. Chem. Chem. Phys.*, 2014, **16**, 13682–13688.
43 R. Frydendal, M. Busch, N. B. Halck, E. A. Paoli, P. Krtil, I. Chorkendorff and J. Rossmeisl, *ChemCatChem*, 2015, **7**, 149–154.
44 I. C. Man, H. Y. Su, F. Calle-Vallejo, H. A. Hansen, J. I. Martinez, N. G. Inoglu, J. Kitchin, T. F. Jaramillo, J. K. Norskov and J. Rossmeisl, *ChemCatChem*, 2011, **3**, 1159–1165.
45 A. Vojvodic and J. K. Nørskov, *National Science Review*, 2015, **2**, 140–149.
46 N. S. Georgescu, A. J. J. Jebaraj and D. Scherson, *ECS Electrochem. Lett.*, 2015, **4**, F39–F42.
47 C. F. Zinola, A. M. Castro Luna, W. E. Triaca and A. J. Arvia, *J. Appl. Electrochem.*, 1994, **24**, 531–541.
48 Y. Gorlin, C.-J. Chung, D. Nordlund, B. M. Clemens and T. F. Jaramillo, *ACS Catal.*, 2012, **2**, 2687–2694.
49 K. G. Gallagher, R. M. Darling and T. F. Fuller, *Handbook of Fuel Cells*, John Wiley & Sons, Ltd, 2010.

Electronic Supplementary Material (ESI) for Energy & Environmental Science.

Supporting Information for

An efficient bifunctional two-component catalyst for Oxygen Reduction and Oxygen Evolution in reversible fuel cells, electrolyzers and rechargeable air electrodes

Sören Dresp, Fang Luo, Roman Schmack, Stefanie Kühl, and Peter Strasser*

Department of Chemistry

Chemical and Materials Engineering Division,
The Electrochemical Catalysis, Energy, and Material Science Laboratory

Technische Universität Berlin
10623 Berlin
Germany

Catalyst Preparation

Nickel Iron layered double hydroxides (NiFe-LDH) supported on Vulcan XC72R were prepared via a microwave assisted autoclave one-pot synthesis route (Figure S1). 1200 µl of 0.2 M Ni(OAc)2 x 4 H_2O (Sigma Aldrich, 99.998 % purtity) and 240 µl 0.2 M $Fe(NO_3)3$ x 9 H_2O (Alfa Aeser, 98 % purity) prepared aqueous precursor solution were added to a 6 mg Vulcan XC72R (Cabot) in 6 ml Dimethylformamid (Sigma Aldrich) dispersion and subsequent stirred for 1 h. Additional 4 ml DMF and 8 ml ultrapure water (18.2 MΩ cm) were added before a two step synthesis microwave treatment (60 min at 120 °C; 30 min at 160° C and) was conducted by using an Anton Paar Monowave 300. The final product was collected by centrifuge, repetitively washing with Ethanol and ultrapure water and lyophilized. All NiFe-LDH/C materials resulted in 37.7 ± 2.1 wt% metals in a Ni/Fe ratio of 3.62 ± 0.03.

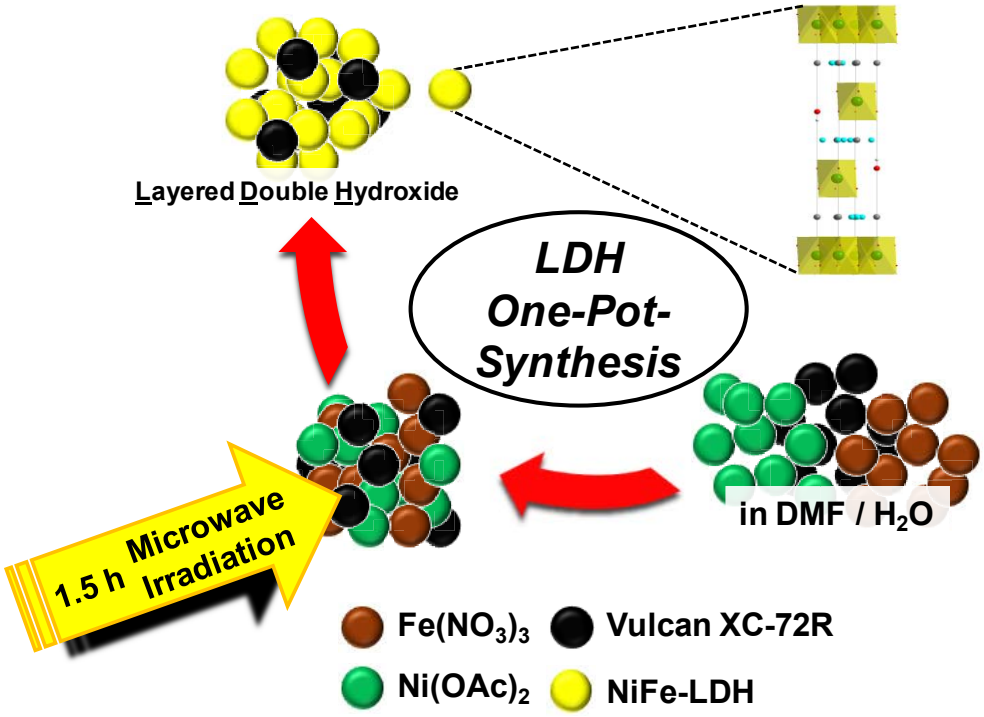

Figure S1: Diagram of one-pot microwave assisted synthesis route

For the Fe/PANI/Ketjen catalyst, Carbon Ketjen was pretreated: As-received commercial carbon support, Ketjen EC 600JC (AkzoNobel) (5 g) was dispersed in 0.5 M HCl (100 ml) for 30 minutes by ultra-sonication. The dispersion was kept for 24 h under continuous stirring condition. The pre-leached carbon was collected by filtering, subsequent washing until neutralization and drying overnight at 60 °C

in air. For activation the carbon powder (5 g) was refluxed in concentrated nitric acid (69 wt%, 10ml) at 90 °C for 5 hours. After activation the carbon was washed again until neutralization and dried overnight at 60 °C.

For the final Fe /PANI/Ketjen catalyst, 2 ml aniline (Sigma-Aldrich, > 99.5 % purity) was first dissolved in 250 ml 0.5 M HCl solution. 3 g FeCl3 (anhydrous, Sigma-Aldrich) was added into the solution and kept stirring for 15 min to ensure a total dissolution of aniline and $FeCl_3$. Then, 5 g ammonium peroxydisulfate ((NH4)2S2O8) (Carl Roth, > 98 % purity) was dissolved in 250 ml 0.5 M HCl solution, and added drop wise (30~45 min) to the ice bath cooled dissolution for in situ polymerization of aniline. The polymerization of aniline was indicated by a color change, from initially light blue to a resulting dark blue. The polymer suspension was kept at low temperature until no color change was observed. Then, the pretreated Ketjen (0.4 g) was mixed with Fe/Polyaniline (Fe/PANI) under constant stirring for 48 h at room temperature to achieve uniformly distributed suspension, which was subsequently refluxed for 5 h at 80-90°C. After overnight drying of the mixture at 80-90°C in N_2, a heat treatment was performed at 900 °C for 1 hour in N_2. The remaining excess of Fe was removed by repetitive acid leaching (2M H_2SO_4) under a reflux at 80-90°C for 7-8 h in N2 followed by washing until reaching a pH of 7. The next heat treatment at 900 °C was performed for 3 h in N_2 until the final Fe-N-C product was achieved.

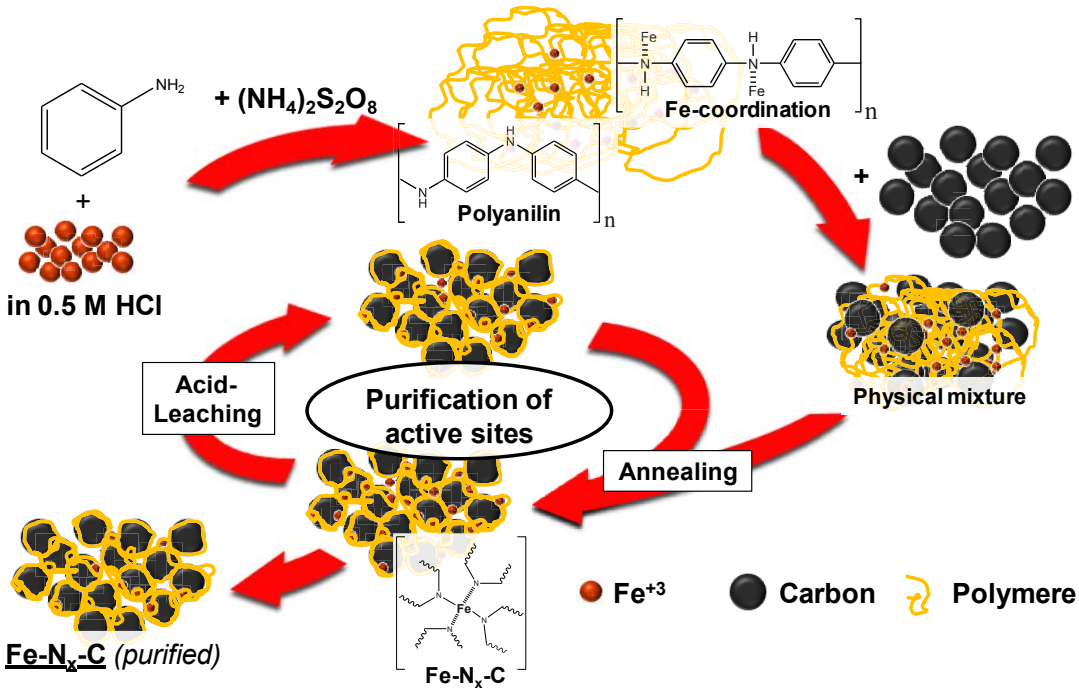

Figure S2: Diagram of synthesis route for preparing Fe in N-doped carbon material

Fabrication of membrane electrode assembly (MEA) and measurement

The membrane electrode assembly (MEA) was prepared by a spray coating technique to obtain a catalyst coated membrane (CCM). Typically, 50 mg catalyst (46.7 wt% Pt/C TKK for the bifunctional Hydrogen electrode), 50 µl ultrapure water (18.2 MΩ cm), 3 ml i-Prop and 460 mg Ionomer (5 wt% AS-4, Tokuyama) were ultrasonicated for 15 min. The membrane (A201, Tokuyama) was fixed on a commercial heatable vacuum table (Carbon and FuelCell) equipped with a dry vacuum pump/compressor (Welch 2511) and a temperature controller (Carbon and FuelCell). Typically, 650 µl of the ink were spray coated on a membrane using 1 bar N_2 stream and a Gun Piece SP-2 spray gun (Rich) equipped with a 0.4 mm tip size to achieve a loading of 0.5 mgPt cm^{-2} for the hydrogen electrode side. To obtain a homogenous 5 cm^2 coating the spraying was conducted in horizontal and subsequent vertical serpentine line and the table temperature was set to 50 °C. A mask was used to protect the protruding part of the membrane and to ensure the optimal vis-à-vis coating. After coating the drying process precedes 10 min. After further 10 min of cooling the mass loading on the membrane was determined. To control the obtained coated catalyst mass the unladen weight were determined before the coating step and compared to the resulted weight.

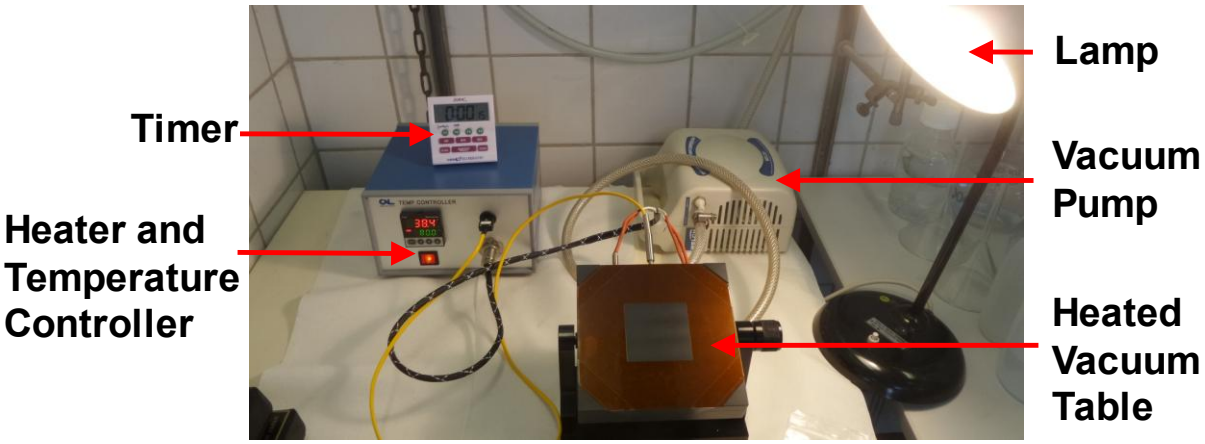

Figure S3: Membrane coating set up for preparing MEA preparation

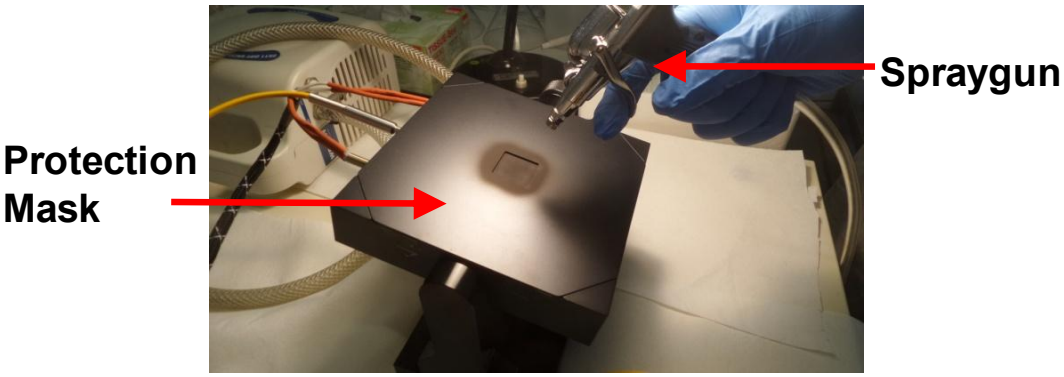

Figure S4: Image of the membrane coating

Physical and chemical characterization of the samples

Powder X-ray diffraction **(XRD)** was carried out in locked mode between 10-70 ° and a step size of 0.039° on a Bruker D8 Advance x-ray Powder diffractometer equipped with a Lynx Eye detector and KFL Cu 2K X-ray tube. The divergence slit was set to 6 mm, the antiscattering slit to 6° and the Lynx-Iris to 10 mm. Transmission electron microscopy **(TEM)** and Energy dispersive x-ray spectroscopy **(EDX)** were conducted to study morphology and composition using a Tecnai G2 20 S-TWIN microscope operated at 200 kV, equipped with a GATAN MS794 P CCD-detector. Inductively coupled plasma-optical emission spectroscopy **(ICP-OES)** was used for elemental and compositional analysis using a 715-ES-inductively coupled plasma analysis system (Varian).

Electrochemical characterization

Every given electrochemical potential is given in respect to the reversible hydrogen electrode **(RHE)**.For all rotating disk electrode (RDE) and rotating ring disk electrode (RRDE) measurements, 5 mg catalyst, 960 µl ultrapure water, 250 µl i-Propanol and 40 µl Nafion (5wt %) were ultrasonicated for 15 min. The electrodes were polished initially with 1 µm Alumina (Buehler) on a Nylon pad and subsequently with 0.05 µm Alumina (Buehler) on a microcloth. The residual Alumina was removed by ultra sonicating the electrode in water and acetone. To obtain a catalyst loading of 0.2 mg cm^{-1}, 10 µl of the ink were drop coated on the RDE (0.1963 cm^2 geometrical disk surface area) and 12.60 µl were drop coated on a RRDE (0.2475 cm^2 geometrical disk surface area). All electrochemical measurements were conducted in at

least 15 min deaerated 0.1 M KOH at room temperature and a three electrode measurement set-up using a glass cell equipped with a large surface area Pt counter electrode and a reversible hydrogen electrode (RHE) (HydroFlex) as reference electrode, which is connected to the main compartment of the glass cell via a Luggin capillary. The RDE measurements were performed using a BioLogic SP 200 and the RRDE measurements were carried out using a bipotentiostat BioLogic VSP.

To activate Fe-N-C based materials, the catalyst was cycled between 0.05 – 1.0 V and 100 mV/s in N2 saturated 0.1 M KOH for 20 Cycles until a constant Cyclic Voltammogram (CV) was achieved. The capacitive current was recorded between 0.05 - 1.0 V and 5 mV/s. Impedance measurement (PEIS) between 0.1 Hz – 100 kHz at 1 V was conducted to determine the IR-drop resistance. All measurements are IR-drop corrected.

The activity measurement were conducted in O_2 saturated 0.1 M KOH. The starting ORR activity measurement was carried out by immersing the electrode at 0.05 V and subsequent cycling for one cycle between 0.05 - 1.1 V at 5 mV/s, followed by 20 Cycles at 50 mV/s and ending with 1 Cycle at 5 mV/s. After the ORR measurement the OER activity measurement was performed between 1.0 – 2.0 V in the same way.

Galvanostatic stability measurement was conducted with RDE at 1600 rpm in O_2 saturated 0.1 M KOH by setting alternate 1 h a constant current of 4 mA cm^{-2} for the OER and -3 mA cm^{-2} for ORR.

RRDE measurement was initially performed in N_2 saturated 0.1 M KOH to clean the Platinum surface area of the ring by cycling between 0.05 – 1.4 V for at least 200 Cycles and 100 mV/s until a constant CV was achieved and secondly cleaning the disk surface area by cycling between 0.05 – 1.0 V for 20 Cycles at 100 mV/s followed by determining the capacitive current and the resistance as described previously for the RDE measurement. The bipotentiostat measurement was finally performed in O_2 saturated 0.1M KOH with a scan rate of 5 mV/s and the ring was set to 1.2 V between 0.05 - 1.1 V at different rotation rates.

The collection efficiency was determined by measuring the current of the ring at 1.55 V in N_2 saturated 0.1 M KOH and 0.01 M $K_3[Fe(III)(CN)_6]$ solution by cycling the disk between 0.2 – 1.4 V at 5 mV/s. The ratio between disk current (i_D) and ring current (i_R) at the same potential resulted in the collection efficiency N ~ 0.37:

$$N = -\frac{i_R}{I_D} \quad \text{(S1)}$$

The HO_2^- production was calculated by using the following formula:

$$X_{HO_2^-} = -\frac{2i_R/N}{I_D + i_R/N} \quad \text{(S2)}$$

And the equation to calculate the **electron transfer** is as follows [1-3]:

$$n = -\frac{4I_D}{I_D + i_R/N} \quad \text{(S3)}$$

Where i_r is the measured current of the ring, i_D is the current of the disc and N is the collection efficiency.

The cell measurement was carried out by using a commercial reversible fuel cell assembly (Carbon and FuelCell) consisting of two endplates with gas ports, two current collectors, two bipotential plates (*Carbon plate for bifunctional hydrogen side, gold coated titanium plate for oxygen side*), a gas diffusion layer (GDL-10BC, Sigracet® GDL) and the prepared MEA. The screws were tightened with a torque of 50 kg cm.

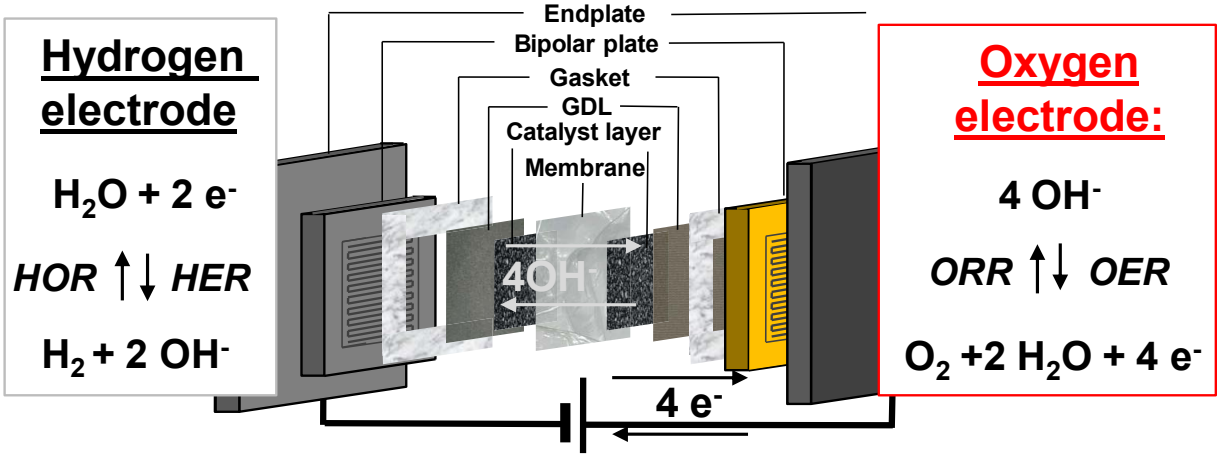

Figure S5: Set-up of reversible electrolyzer cell

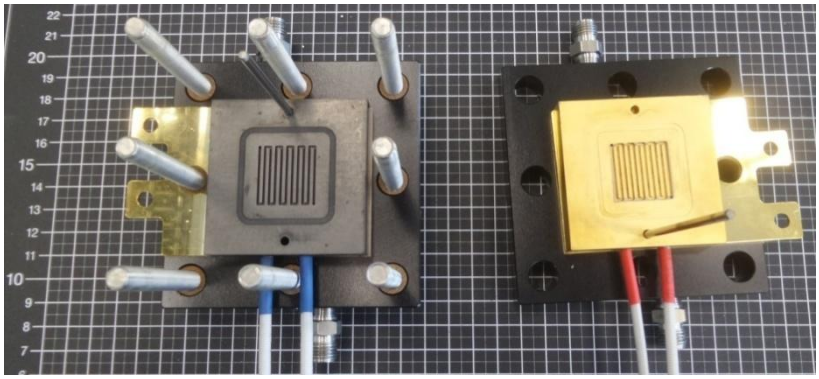

Figure S6: View on the reversible electrolyzer with a carbon based bipolar plate (left) for the bifunctional hydrogen electrode and a gold coated titanium plate (right) for the bifunctional oxygen electrode

At first the reversible electrolyzer cell was tested in a fuel cell mode using a fuel cell test station (Fuel Cell Technologies, Inc.). After a heating procedure and gas purging for 1 h, the VI-curve between 0.35 – 1

V was realized at 50 °C and a gas flow of 200 sccm of H_2 and O_2 was used. Impedanz was recorded after each measurement. For each data point a delay time of 15 s was set. After fuel cell measurement the electrolyzer mode was tested at 50 °C and a flow rate of 0.5 sccm of ultrapure water was set using a Reglo digital MS-2/6 peristalticpump (Ismatec) (Figure S7).

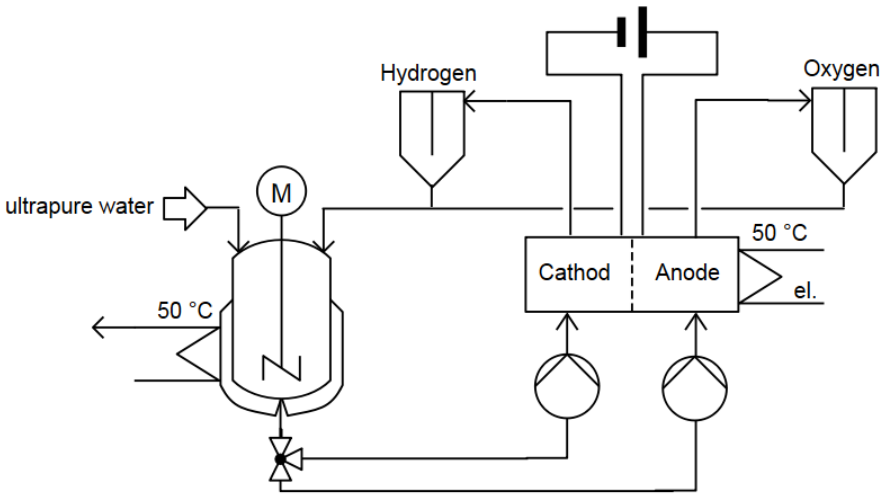

Figure S7: Flowdiagram for Electrolyzer set up

To record the IV-curve a BioLogic SP 200 was used. Each data point was held for 15 s and the last Voltage point was taken. To repeat measuring in fuel cell mode the gases were purged again for at least 1 h at 50 °C to dry the GDL. Afterwards again 3 VI curves were recorded in fuel cell mode.

The standard errors (SE) were estimated by determining the value from at least three independent measurements and calculated by using the following formula:

$$SE = \frac{s}{\sqrt{n}} \tag{S4}$$

with

$$s = \sqrt{\frac{\sum_{i=1}^{n}\left(x_i - \bar{x}\right)^2}{n-1}} \tag{S5}$$

where **s** is the standard deviation, **n** is the number of measurements, $\mathbf{x_i}$ is the value of the i measurement and $\bar{x}$ is the average of the values.

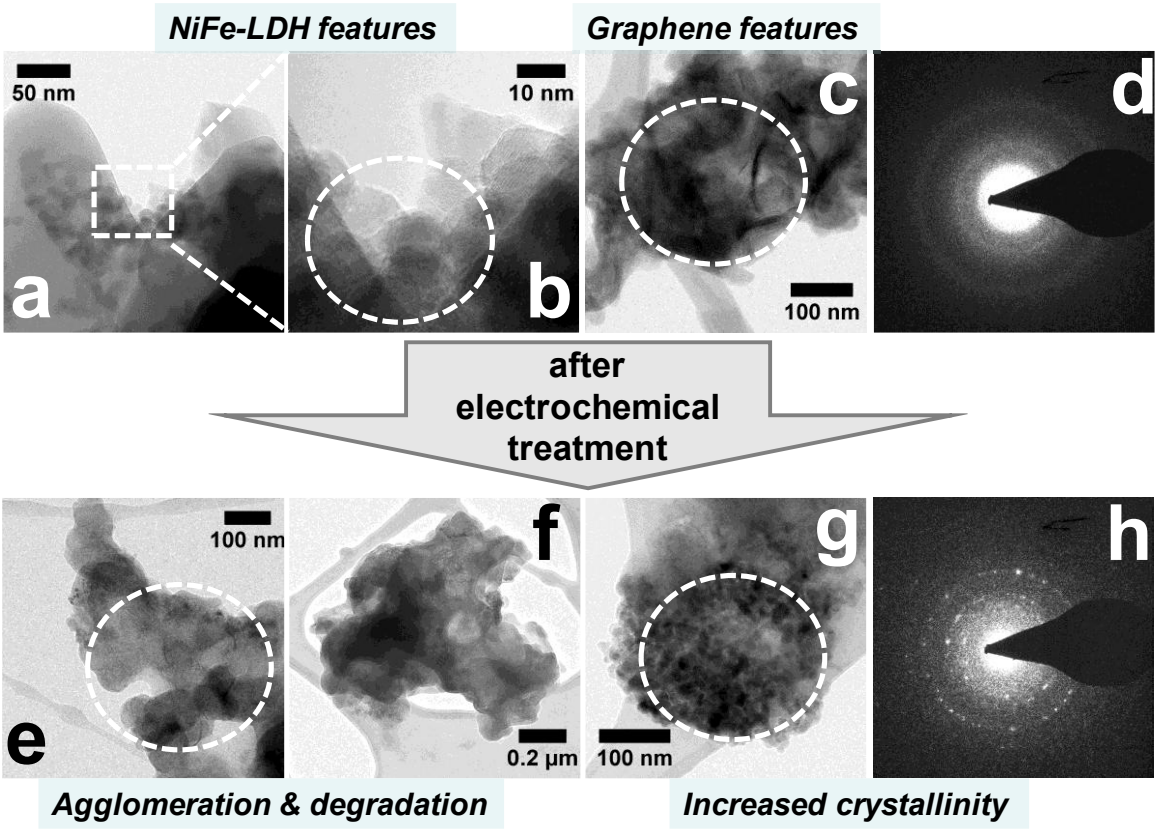

Figure S8: TEM Images of Fe-N-C / NiFe-LDH (3:1) before (a-d) and after (e-h) electrochemical treatment. The SAED spectra (d) and (h) are related to the TEM images (c) and (g). The images are indicating an increased crystallinity nanoparticle formation after electrochemical treatment

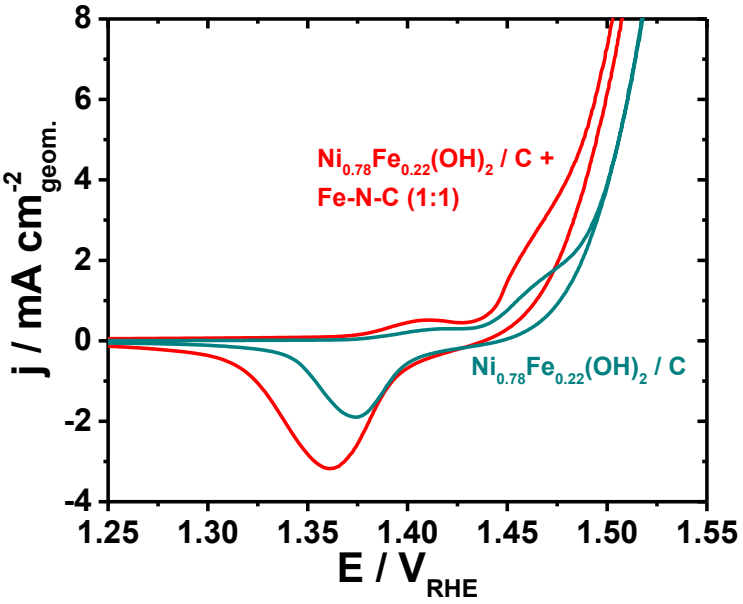

Figure S9: CV of NiFe-LDH and NiFe-LDH + Fe-N-C to 1:1 mixture in O_2 saturated 0.1 M KOH at 50 mV/s . Different size of the $Ni^{2+/3+}$ Redoxpeak may suggest a higher conductivity of the sample or accessibility of the Nickel active sites

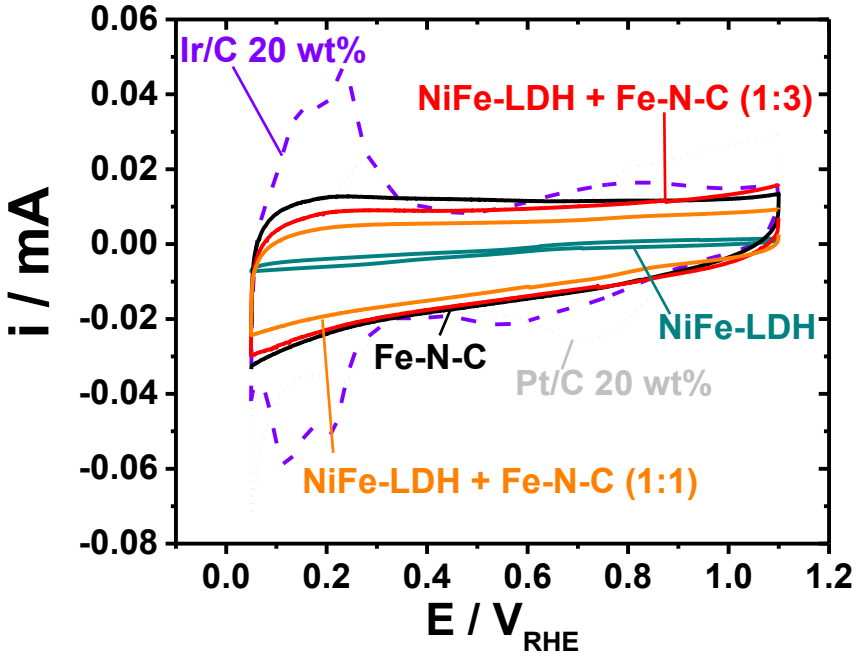

Figure S10: Cyclic voltammogram in N_2 saturated 0.1 M KOH for different catalysts. NiFe-LDH have the shows a CV with the smallest capacitive current

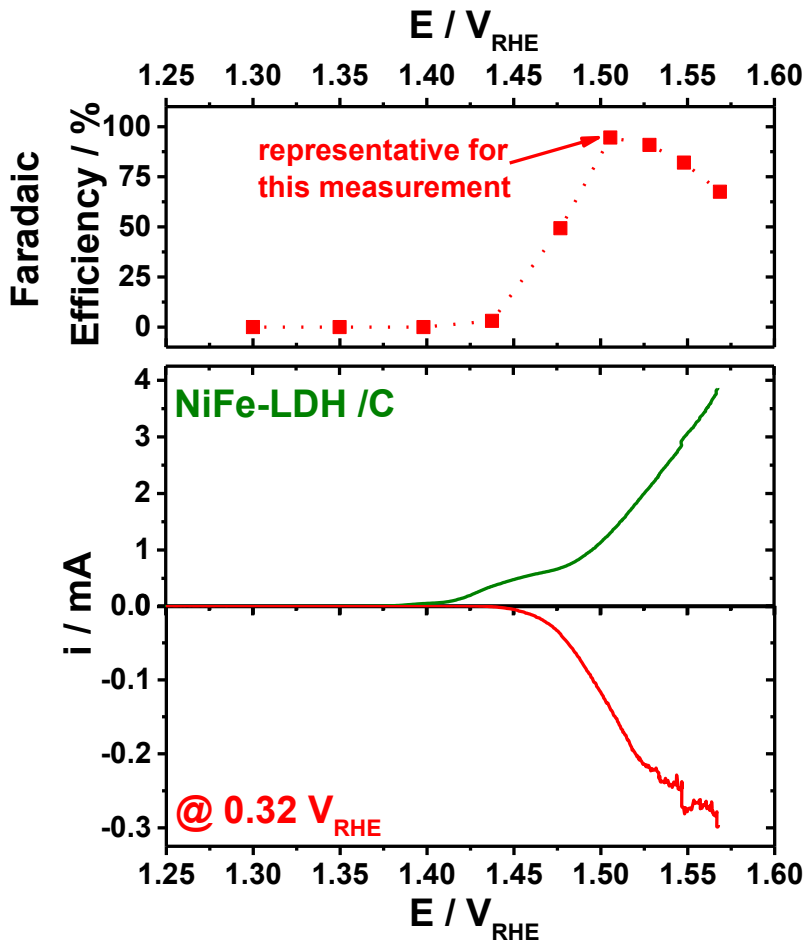

FigureS 11: Faradaic efficiency measurement for Oxygen evolution reactíon

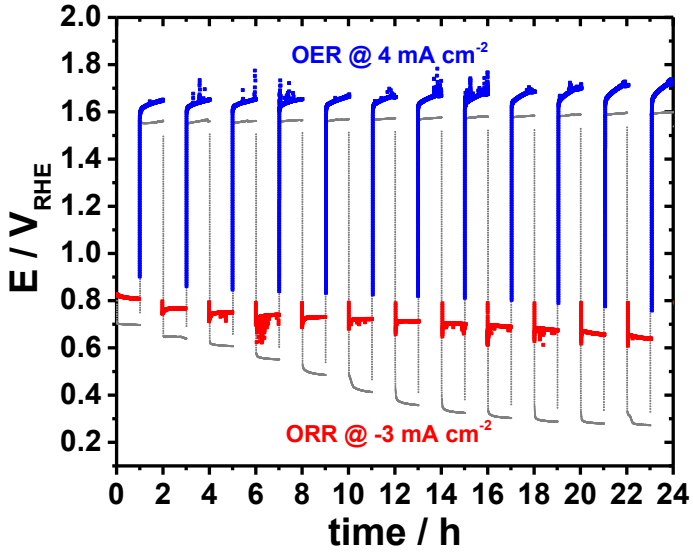

Figure S12: RDE stability measurement over 24 h for Pt/C 20wt% + Ir/C 20 wt% (1:1) mixture (blue @ 4 mA cm^2 and red @ -3 mA cm^2) and NiFe-LDH Fe-N-C (1:3) (grey) in O_2 saturated 0.1 M KOH at 1600 rpm and 0.2 mg cm^{-2} cat loading

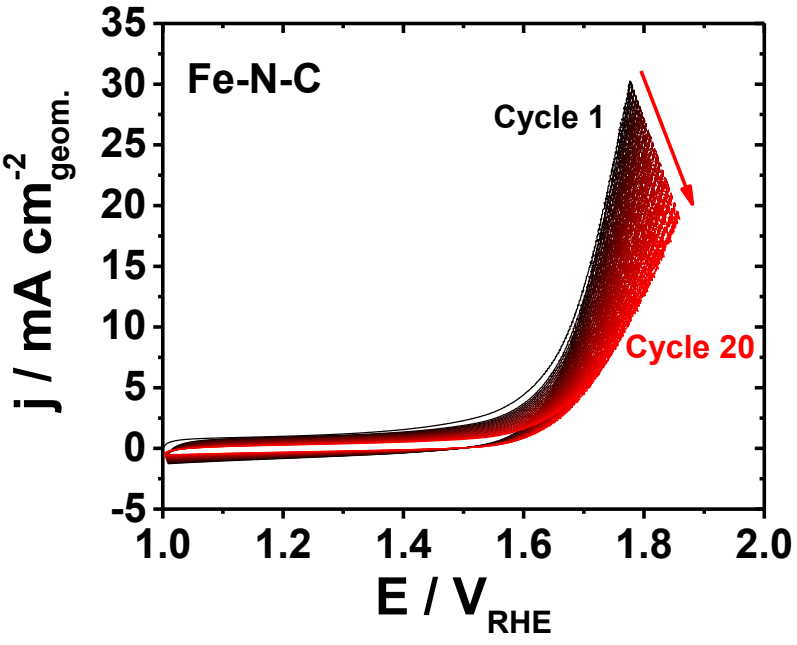

Figure S13: 20 Cycles of Fe-N-C catalyst with 50 mV/s in O_2 saturated 0.1 M KOH. Cycles show the instability of Fe-N-C catalyst during OER potentials. Indicating an oxidation of the catalyst

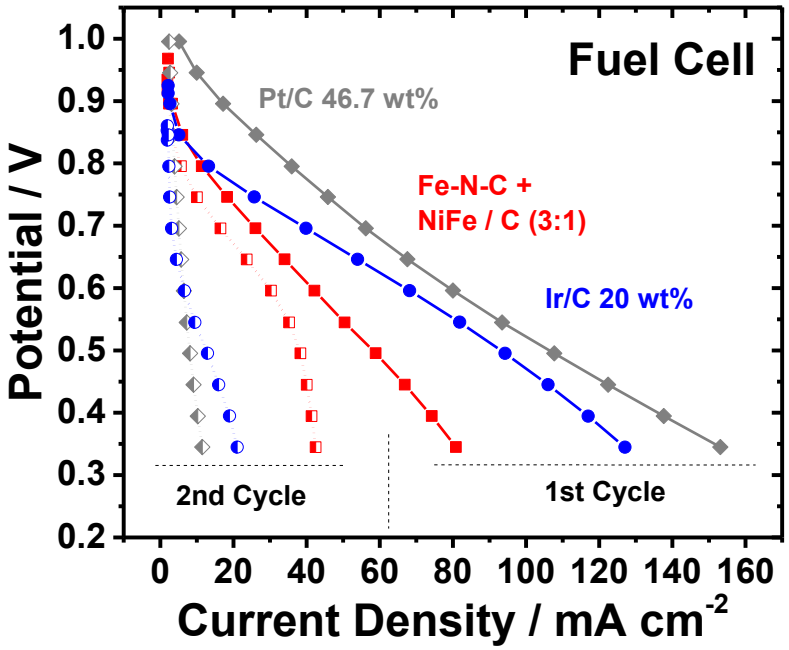

Figure S14: VI-curves for fuel cell testing for different catalysts. The fuel cell activity for the noble materials decreased even more than for the non-noble two component system

Table S1: ORR and OER activities for different catalysts measured in 0.1 M KOH at a rotation rate of 1600 rpm and a catalyst loading of 0.2 mg cm^{-2} .

catalyst	$E_{1/2}$ @ -3 mA cm^{-2} [V]	E @ 10 mA cm^{-2} [V]	ΔE (OER – ORR) [V]	j @ 0.8 V [mA cm^{-2}]	Reference
NiFe-LDH	*0.285 ± 0.056*	*1.550 ± 0.015*	*1.266 ± 0.071*	---	***This study***
Fe-N-C	*0.799 ± 0.009*	*1.736 ± 0.009*	*0.937 ± 0.020*	*3.02 ± 0.218*	***This study***
NiFe-LDH / Fe-N-C (1:1)	*0.728 ± 0.034*	*1.515 ± 0.010*	*0.786 ± 0.044*	*1.52 ± 0.219*	***This study***
NiFe-LDH / Fe-N-C (1:3)	*0.793 ± 0.003*	*1.539 ± 0.006*	*0.747 ± 0.009*	*3.045 ± 0.071*	***This study***
Pt / C 20 wt%	*0.863 ± 0.009*	*1.901 ± 0.01667*	*1.038 ± 0.037*	*5.125 ± 0.125*	***This study***
Ir / C 20 wt%	*0.733 ± 0.010*	*1.586 ± 0.013*	*0.853 ± 0.023*	*1.553 ± 0.052*	***This study***
MnOx	*0.73*	*0.54*	*1.04*	-	[4]
Co/N-C-800	*0.74*	*1.599*	*0.859*	-	[5]
Pt/C to BSCF/C = 4:1	*0.81*	*1.61*	*0.8*	-	[6]
Fe3C@NG800-0.2			*0.78*	-	[7]
/N	*0.83 ± 0.01*	*1.59 ± 0.01*	*0.76 ± 0.02*	-	[8]

Table S2: Obtained loadings for coated Tokuyama A201 membrane

MEA	H_2 load. [mg_{Pt} cm^{-2}]	O_2 load. [$mg_{cat.}$ cm^{-2}]	$j_{geom.}$ @ 0.8 V [mA cm^{-2}]	$j_{geom.}$ @ 1.53 V [mA cm^{-2}]
Pt/C 46.7 wt% / Pt/C 46.7 wt%	*0.51*	*1.35*	*34.93*	*1.45*
Pt/C 46.7 wt% / Ir/C 20 wt%	*0.47*	*2.85*	*12.41*	*40.04*
Pt/C 46.7 wt% / Fe-N-C + NiFe-LDH	*0.58*	*2.50*	*12.79*	*25.24*

Table S3: Used proportion of mixed catalysts

catalyst	NiFe-LDH [%]	Fe-N-C [%]
NiFe-LDH / Fe-N-C (1:1)	*49.9 %*	*50.1 %*
NiFe-LDH / Fe-N-C (1:3)	*25,6 %*	*74,4 %*
NiFe-LDH / Fe-N-C (1:3) (MEA)	*24.7 %*	*75.3 %*

References

1. S. Marcotte, D. Villers, N. Guillet, L. Roué and J. P. Dodelet, *Electrochimica Acta*, 2004, **50**, 179-188.
2. O. Antoine and R. Durand, *Journal of Applied Electrochemistry*, 2000, **30**, 839-844.
3. U. A. Paulus, T. J. Schmidt, H. A. Gasteiger and R. J. Behm, *Journal of Electroanalytical Chemistry*, 2001, **495**, 134-145.
4. Y. Gorlin and T. F. Jaramillo, *Journal of the American Chemical Society*, 2010, **132**, 13612-13614.
5. Y. Su, Y. Zhu, H. Jiang, J. Shen, X. Yang, W. Zou, J. Chen and C. Li, *Nanoscale*, 2014, **6**, 15080-15089.
6. Y. Zhu, C. Su, X. Xu, W. Zhou, R. Ran and Z. Shao, *Chemistry – A European Journal*, 2014, **20**, 15533-15542.
7. H. Jiang, Y. Yao, Y. Zhu, Y. Liu, Y. Su, X. Yang and C. Li, *ACS Applied Materials & Interfaces*, 2015, **7**, 21511-21520.
8. Y. Zhao, K. Kamiya, K. Hashimoto and S. Nakanishi, *The Journal of Physical Chemistry C*, 2015, **119**, 2583-2588.

III. Direct Electrolytic Splitting of Seawater: Activity, Selectivity, Degradation, and Recovery Studied from the Molecular Catalyst Structure to the Electrolyzer Cell Level

This section reprints the following paper

Sören Dresp,[a] Fabio Dionigi,[a] Stefan Loos,[b] Jorge Ferreira de Araujo,[a] Camillo Spöri,[a] Manuel Gliech,[a] Holger Dau,[b]* Peter Strasser[a]*

Adv. Energy Mater., **2018***, p. 1800338; DOI: https://doi.org/10.1002/aenm.201800338*

(30 pages)

ADVANCED ENERGY MATERIALS

www.advenergymat.de

Direct Electrolytic Splitting of Seawater: Activity, Selectivity, Degradation, and Recovery Studied from the Molecular Catalyst Structure to the Electrolyzer Cell Level

Sören Dresp, Fabio Dionigi, Stefan Loos, Jorge Ferreira de Araujo, Camillo Spöri, Manuel Gliech, Holger Dau, and Peter Strasser**

Seawater electrolysis faces fundamental chemical challenges, such as the suppression of highly detrimental halogen chemistries, which has to be ensured by selective catalyst and suitable operating conditions. In the present study, nanostructured NiFe-layered double hydroxide and Pt nanoparticles are selected as catalysts for the anode and cathode, respectively. The seawater electrolyzer is tested successfully for 100 h at maximum current densities of 200 mA cm^{-2} at 1.6 V employing surrogate sea water and compared to fresh water feeds. Different membrane studies are carried out to reveal the cause of the current density drop. During long-term dynamic tests, under simulated day-night cycles, an unusual cell power performance recovery effect is uncovered, which is subsequently harnessed in a long-term diurnal day-night cycle test. The natural day-night cycles of the electrolyzer input power can be conceived as a reversible catalyst materials recovery treatment of the device when using photovoltaic electricity sources. To understand the origin of this reversible recovery on a molecular materials level, in situ extended X-ray absorption fine structure and X-ray near-edge region spectra are applied.

1. Introduction

The progressive global transition to energy systems based on renewable energy is associated with new challenges connected to the fluctuation of energy sources such as wind, sun, and the storage of their frequent surplus in energy supply. Current technologies focusing on splitting water into oxygen and hydrogen (H_2O + energy → ½O_2 + H_2) to use hydrogen as energy carrier. The hydrogen can be reused, for example, in fuel cells to back convert hydrogen into energy and water (½O_2 + H_2 → H_2O + energy). But current water electrolyzer technologies only split either highly alkaline (20–40 wt% KOH) electrolyte obtained from purified freshwater or else purified freshwater alone, if using a membrane-based electrolyzer equipped with a proton exchange membrane (PEM). The direct use of the vastly more abundant seawater supplies as inexhaustible raw water resource could solve the problematics related to scarce water provision and high fresh water demand, which are severe in many arid zones by using a fuel cell to produce electricity and purified water. In 1980, Bennett investigated the electrolysis of seawater into oxygen and hydrogen.[1] Their theoretical study shows the predominance of chlorine evolution reaction (ClER: $2Cl^- \rightarrow Cl_2 + 2e^-$) in unbuffered seawater electrolysis performed in practical operating current conditions, with oxygen evolution reaction (OER: $2H_2O \rightarrow O_2 + 4H^+ + 4e^-$) dominant only at current densities below 1 mA cm^{-2} or at very high current densities where ClER currents reach the mass transfer limitation. Accordingly, the same authors obtained high OER efficiencies by using a porous manganese electrode coating that was formed during seawater electrolysis at low pH.[1] In 1997, Hashimoto and co-workers also investigated different manganese-based electrode materials in acidic environment with high oxygen selectivities at current densities of 1 mA cm^{-2}.[2] Despite the relatively modest number of seawater electrolysis studies,[3] the competition in selectivity between OER and ClER is generating great interest due to the importance of chlorine as chemical and it is currently investigated both theoretically and experimentally.[4] Pioneering these studies, in 1984 Trasatti investigated different catalyst materials and their reactivity toward both anodic OER and ClER. As a conclusion, he revealed that the OER and ClER reactivities of the investigated catalysts scale. Hence, the selectivity for chlorine evolution does not considerably depend on the electrode material.[5] More recently, in 2009 Surendranath et al. published a work using a cobalt-based catalyst splitting seawater in near neutral pH using a potassium phosphate buffer solution.[6]

S. Dresp, Dr. F. Dionigi, J. Ferreira de Araujo, C. Spöri, M. Gliech, Prof. P. Strasser
Department of Chemistry
Technical University Berlin
10623, Berlin, Germany
E-mail: pstrasser@tu-berlin.de
Dr. S. Loos, Prof. H. Dau
Department of Experimental Physics
Free University Berlin
Arnimallee 14 14195, Berlin, Germany
E-mail: holger.dau@fu-berlin.de

The ORCID identification number(s) for the author(s) of this article can be found under https://doi.org/10.1002/aenm.201800338.

DOI: 10.1002/aenm.201800338

Finally, in 2016 Dionigi et al. presented an in-depth analysis of the chemical limitations of seawater electrodes and put forward a general design criterion for selective seawater splitting catalysts. The authors calculated a Pourbaix diagram considering the OER and chloride chemistry and showed that the OER is favored at high pH > 7.5:[7] At these pH values selective OER is thermodynamically possible at overpotentials below 480 mV. The criterion shows the most favorable conditions while it does not exclude that selective OER can be obtained in other conditions. The major competitive anodic reactions at high pH are the OER and hypochlorite formation ($Cl^- + 2OH^- \rightarrow ClO^- + H_2O + 2e^-$). The standard potentials of the OER and of the hypochlorite formation scale parallel resulting in a standard potential difference of $\Delta E = E_{Cl-}{}^0 - E_{OER} = 480$ mV in the pH range from 7.5 to 14. The alkaline electrolyte is additionally advantageous due to the possible use of non-noble metals. Nickel iron mixed layered double hydroxides (NiFe-LDH) are known to be among the most active OER catalyst materials in alkaline medium.[8–11] The origin of their high OER activity that is comparable and in many cases surpassing the one of iridium oxide based catalysts in alkaline media is not clear and object of intense investigation, including advanced in operando methods and theoretical simulations and predictions. At the same time, other works focus on improving the stability,[12] which is a fundamental property for long-term application. Moreover, NiFe-based materials also showed catalytic activity toward the hydrogen evolution reaction (HER) which opens up the possibility to utilize NiFe as bifunctional electrolyzer catalyst.[13] Due to its high OER activity, NiFe LDH was also investigated using rotating disk electrodes (RDE) in electrolytes containing both 0.5 M NaCl to mimic seawater and 0.1 M KOH to operate in alkaline condition.[7] Another member of the LDH family of materials, CoFe LDH, was also recently studied as catalyst for seawater oxidation in different conditions and the work showed a synergistic effect between the different ions in seawater.[14] The herein reported study investigates an anion exchange membrane based electrolyzer operating with alkaline NaCl-containing electrolyte using (highly crystalline) NiFe-LDH as anode material. To the best of our knowledge, this is the first time that this kind of device operating in seawater mimicking condition is reported in literature.

2. Results and Discussion

2.1. Choice of Seawater Electrolyzer Electrode Catalysts

Selective NiFe-LDH electrocatalysts were prepared using a microwave-assisted solvothermal synthesis route following an earlier reported recipe.[15] The obtained Ni/Fe atomic ratio of 3.0 ($Ni_{0.75}Fe_{0.25}$ (OH)) was determined by inductively coupled plasma optical emission spectrometry (ICP-OES). The X-ray diffraction (XRD) pattern, shown in **Figure 1**a, is consistent with data-based reflections of hydrotalcite (JCPDS: 00-014-0191), but with slightly higher interlayer distances.[16] The crystal structure of rhombohedral NiFe-layered double hydroxide with its prismatic P3-R3 oxygen stacking (ABBCCA) is depicted in Figure 1d. The NiFe-LDH has a layered structure with layers consisting of $Ni(II)O_6$ and $Fe(III)O_6$ edge connected octahedrons. The positive charge of the layers is balanced by either intercalated anions between the layers or through deprotonated μ-oxo-bridges or other defects from an ideal crystal structure including boundary effects like terminal coordinated hydroxides. Evaluating the (003) reflection peak and using Scherer equation the crystallite size has shown to be $XS_{003} = 6 \pm 1$ nm. The unit cell interlayer distance is $d_{003} = 7.76$ Å while the metal–metal distance is calculated being $d_{110} = 3.11$ Å that is in agreement with the metal–metal distance of the NiFe-LDH structure shown in literature. The transmission electron microscopy (TEM) images confirmed the sheet structure as shown in Figure 1b,c, even though the very thin flakes appear to agglomerate in big bulk structures.

2.2. The Faradaic Reactivity of Seawater Electrolyzer Cells

A catalyst coated membrane was prepared using a spray-coating method described elsewhere.[17] The test was conducted in an in-house electrolyzer test-stand using a Gamry 3000 potentiostat, a CNL electrolyzer cell, Teflon container as electrolyte reservoir to avoid contamination by glass corrosion, and a peristaltic pump as shown in Figure S1 (Supporting Information). As anion exchange membrane (AEM), a Tokuyama A201 membrane and as ionomer Tokuyama AS-4 was used. As porous transport layer (PTL), a carbon BC 10 GDL for the cathode and a gold-coated Ti mesh for the anode were used. At first, the initial cyclic voltammetry was performed in the electrolyzer setup to verify the typical NiFe-LDH redox behavior as shown in **Figure 2**a. To follow the design criteria for 100% OER selectivity, the maximal potential was set to 1.7 V, equal to an overpotential of 470 mV.[7]

The initial cyclic voltammetry is in agreement with the NiFe-LDH behavior for rotating disk electrode measurements and the typical NiFe-LDH $Ni^{2+\rightarrow 3+/4+}$ redox features were obtained.[9,10] However, after adding 0.5 M NaCl the current density drops even though the resistance of the system slightly decreases. In addition, a hysteresis effect at high electrode potentials was detected (inset in Figure 2a) that may be the consequence of parasitic chloro-chemistry or incomplete redox behavior of the NiFe-LDH in NaCl-containing electrolyte. To better understand the observed voltammetry, rotating disc electrode (RDE) measurements of the oxygen evolution reaction were performed and shown in Figure S2 (Supporting Information). Results showed even higher activity in NaCl-containing electrolyte than in NaCl-free electrolyte, which we attribute to the higher conductivity of the electrolyte. Therefore, this performance drop might be due to the Cl^- influence to the membrane's OH^- conductivity or some competing Cl^- chemistry, which reveals itself at current densities under MEA conditions and not under RDE conditions.

Since the hydrogen electrode may also be influenced by the presence of NaCl, we investigated its influence on the cathodic HER. To achieve this, we tested the Pt/C catalyst in an RDE setup in 0.1 M KOH and 1 M KOH with and without added NaCl. The measurement is shown in Figure S3 (Supporting Information). Increasing the KOH concentration increased the HER activity of the Pt/C catalyst, but no influence of NaCl could be observed. This result suggests that the current drop is likely

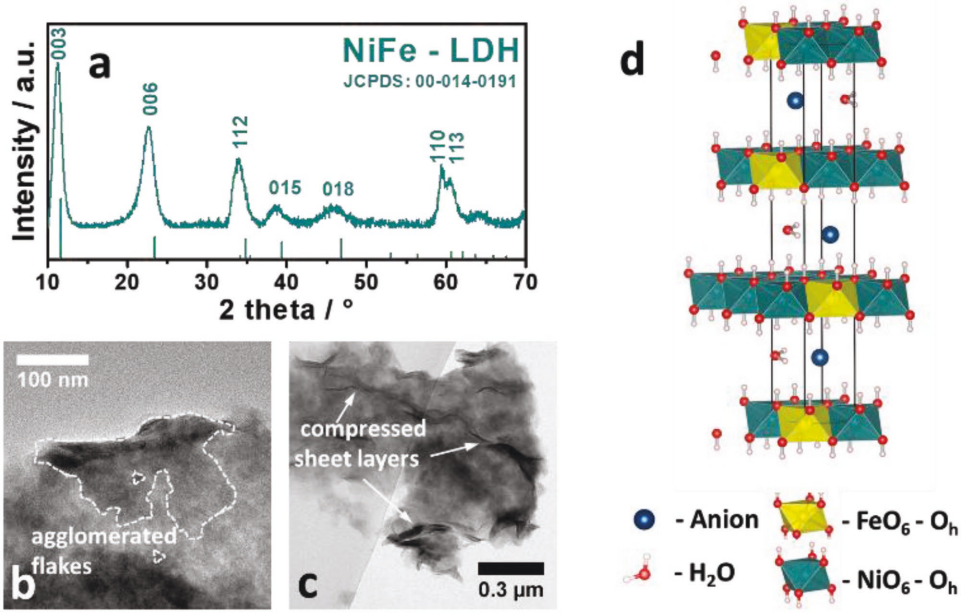

Figure 1. Physicochemical investigations of solvothermal microwave assisted synthesized NiFe-LDH: a) X-ray diffraction pattern, b,c) TEM images, and d) crystal structure of NiFe-LDH with H_2O and CO_3^{2-} ions in the interlayer to compensate the charge of the layer due to Fe^{3+} incorporated in the neutral $Ni(OH)_2$ layers. The nickel and iron are octahedrally (Oh) surrounded by oxygen atoms.

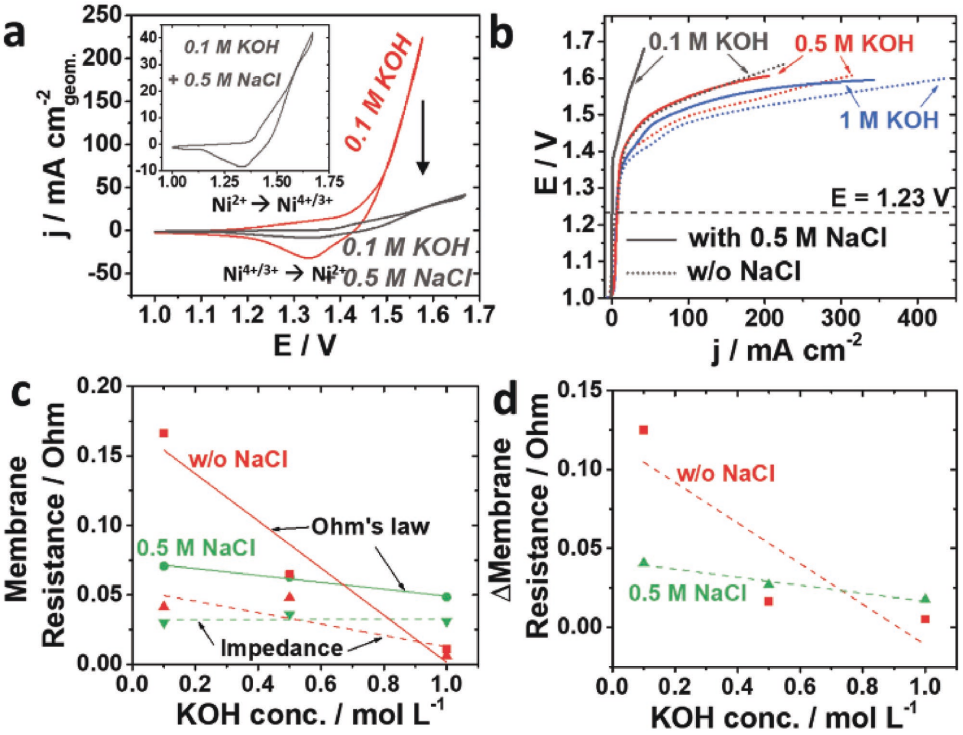

Figure 2. Electrochemical electrolyzer measurement using different electrolytes, NiFe-LDH as anode material, 46.7 wt% Pt on Vulcan (TKK) as cathode material, and Tokuyama A201 as membrane: a) Two-electrode cyclic voltammetry in the cell with 50 mV s^{-1}, electrolyzer anode used as working electrode. b) Polarization curves extracted from the cyclic voltammetry in different electrolytes. c) Membrane resistance in NaCl free (w/o NaCl) and with 0.5 M NaCl in different KOH concentrations determined by a four-probe test cell using a free from capacitive resistance impedance measurement (dashed lines) and an "ohmic" approach that includes the capacitive resistance (solid lines). d) Capacitive resistance of the membrane at different KOH concentrations for NaCl free (w/o) and NaCl containing electrolyte (for more details about the membrane resistance measurement, see the Supporting Information).

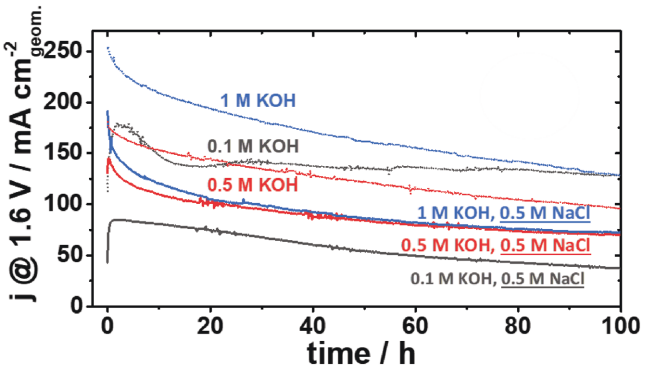

Figure 3. 100 h longtime measurement at +1.6 V in different electrolytes using a loading of 0.5 mg_{Pt} cm^{-2} 46.7 wt% Pt on carbon (TKK) on the cathode and 2.5 mg cm^{-2} NiFe-LDH at the anode, a Tokuyama A201 as membrane in different KOH concentrations with and without 0.5 M NaCl.

due to detrimental chloride effects on the AEM or the ionomer. To study this effect in more detail, we performed two separate series of four-probe measurements in different electrolytes comparing an "ohmic" and an "impedance"-based approach as described in the Experimental Section and in more detail in the Supporting Information (Figures S4–S6, Supporting Information). Most importantly, the impedance estimates the membrane resistance without any capacitive resistance while the ohmic approach delivers the sum of membrane and capacitive resistance.

As shown in Figure 2c, the impedance and ohmic approach show significantly different resistances, being more pronounced at low KOH concentrations. The measured "ohmic" resistance decreased with increasing KOH concentration for the NaCl-containing and NaCl-free electrolyte.

Figure 2d shows the comparably high capacitive resistance and distinctly different behavior of NaCl-free 0.1 M KOH that could also explain the high stability performance of this condition (**Figure 3**). In the other concentration range of 0.5–1 M KOH, the system shows similar capacitive resistances. The impedance measurement does not show significant differences between NaCl-free and NaCl-containing electrolytes. A possible explanation is that the chloride ions compete with the OH^- ion conductivity. Since Cl^- has a finite transfer number and participates in the ion transport through the membrane, the electrochemically determined membrane resistance might not get much affected by the presence of NaCl. Thus, the higher KOH concentration offsets the Cl^- concentration to increase OH^- conductivity resulting in higher current densities. Therefore, according to this scenario, in real seawater splitting electrolyzers a rather high KOH concentration would be preferable, as other chlorides and anions will additionally be present.

Supporting this, seawater electrolyzer polarization curves, presented in Figure 2b, show a clear relation between activity and KOH concentration in the order 0.1 M < 0.5 M < 1 M KOH. The trend is represented for NaCl-containing as well as NaCl-free electrolyte. Note that the performance in NaCl-free electrolyte is always higher, showing the largest difference in 0.1 M KOH electrolyte.

2.3. The Performance Stability of Seawater Electrolyzer Cells

To investigate the practical performance stability of seawater electrolyzer employing the selective NiFe-LDH seawater catalyst system, first, a 100 h test at a constant applied potential of +1.6 V was carried out as shown in Figure 3.

An electrode potential of +1.6 V was chosen to fulfill the "seawater splitting selectivity design criterion" and ensure the selective oxidation to oxygen and avoiding chlorine evolution.[7] Current densities as high as 250 mA cm^{-2} in NaCl-free and record-high 200 mA cm^{-2} in 0.5 M NaCl-containing electrolytes were reproducibly recorded. The presence of NaCl caused a general drop in current density in line with polarization curves of Figure 2b. After an activation time, the current density plateau at 150 mA cm^{-2} for NaCl-free 0.1 M KOH electrolyte was reached and remained almost constant. In other electrolytes, the performance decreased almost instantly after the cell potential reached +1.6 V. The activity decreased nearly proportionally for all other electrolytes, except for the NaCl-free 0.1 M KOH, what we attribute to the membrane behavior.

To get more insight in the origin of the current density losses or possible degradation mechanisms in presence of NaCl, the morphology of the PTL before and after testing in 1 M KOH and 0.5 M NaCl was investigated. Pre/post-testing scanning electron microscopy (SEM) analysis (Figures S7–S9, Supporting Information) revealed negligible corrosion of the current collector mesh indicating a stable PTL material (Figure S7, Supporting Information). SEM cross section and EDX linescans of an as-prepared and a 100 h in 0.5 M KOH + 0.5 M NaCl at 1.6 V treated MEA are shown in Figure S8 (Supporting Information). The as-prepared MEA in Figure S8a (Supporting Information) shows a 14.3 µm Pt/C, a 36 µm NiFe-LDH, and a 28.0 µm membrane layer. Supporting the elemental distribution, EDX mapping of the SEM cross section for the as-prepared MEA is shown in Figure S9 (Supporting Information). Caused by a strong conjunction of the carbon GDL to the Pt/C layer, the GDL remained on the 100 h treated MEA in Figure S8b (Supporting Information). However, the Pt/C layer does not show any significant changes after 100 h, although the layer slightly detaches from the membrane. In contrast, EDX linescan indicates a partial Pt metal diffusion into the carbon GDL (Figure S8c,d, Supporting Information) that might indicate an instability of the Pt in the catalyst layer. Even though the NiFe-LDH catalyst layer decreased after 100 h, this reduced layer thickness cannot be attributed to catalyst corrosion but rather due to mechanical erosion by PTL removal. Supporting this, the layer appears more compressed, which might be due to the induced pressure of the PTL on the catalyst layer in the assembled cell. In top view, the NiFe-LDH particles appear flaky. After 100 h the flake size slightly increased (Figure S10, Supporting Information). This might also be due to the strong compression of the MEA in the assembled electrolyzer cell. In contrast, no significant change of the overall membrane thickness was determined after 100 h. In addition, no elemental diffusion into the membrane was determined. To investigate any membrane changes, the cell impedance after 100 h under all conditions was investigated (Figure S11, Supporting Information). Albeit the NaCl-containing electrolytes showed slightly higher resistances compared to the NaCl-free electrolyte, this

small difference is unable to account for the experimental drop in current density in the NaCl electrolytes. Also, the catalyst material is known to be catalytically stable at this condition as already published in literature elsewhere.[7,9] A reasonable explanation for the sudden loss in current density with NaCl is the deterioration of the ionic OH^- membrane conductivity. Chloride ions lower the OH^- transference numbers across the membrane channels and poison cationic side groups of the ionomer. As a result, there are fewer OH^- ions effectively transported across the membrane to the catalyst layers, which results in a current density decrease. Indeed, the OH^- migration across the anion-conducting membrane appears to be rate limiting and determines the overall catalytic current density. Notably, the stability of the current density in 0.5 M NaCl showed an inverse trend to the initial catalytic activity, as the KOH concentration decreased from 1 to 0.5 M to 0.1 M (Figure S12, Supporting Information). As a result, the final current density is equal for the 0.5 and 1 M KOH but higher for the 0.1 M KOH. We therefore derive a practical design criterion for seawater electrolyzers that the recommended KOH concentration should range at 0.5 M and does not need to be significantly higher. Furthermore, no significant influence of the NiFe-LDH catalyst loading was detected with regard to the stability in 0.1 M KOH and 0.5 M NaCl as shown in Figure S13 (Supporting Information).

2.4. Seawater Electrolyzer Cell Degradation and Activity Recovery Effects

A large-scale operation of water electrolysis might be coupled with the utilization of wind power or solar energy. In more practical terms, this would mean that the electrolyzer will be exposed to alternating loads or even phases of rest. To mimic this intermittent operation under varying loads, the NiFe-LDH deployed anode and its single-cell seawater electrolyzer was subsequently tested after recurring intermittent breaks of 10 min and 1 h. Thereby, a surprising and very important recovery effect was uncovered. After stopping and restarting the electrolysis, a reproducible and robust recovery effect was observed and documented as shown in **Figure 4**a.

The presented data provide clear evidence that the long-term seawater electrolysis cell performance can be significantly improved after stopping the measurement for a period of time and subsequently resetting the electrolysis cell voltage to +1.6 V. A definite mechanistic explanation for this phenomenon is currently unavailable. However, we doubt that any temporary bubble removal from the catalyst surface could explain the sustained recovery at high currents over the course of hours.[18,19] More likely appears an alternative explanation associated with structural and electronic changes of the electrode material upon changing the potential. Resetting the applied electrical

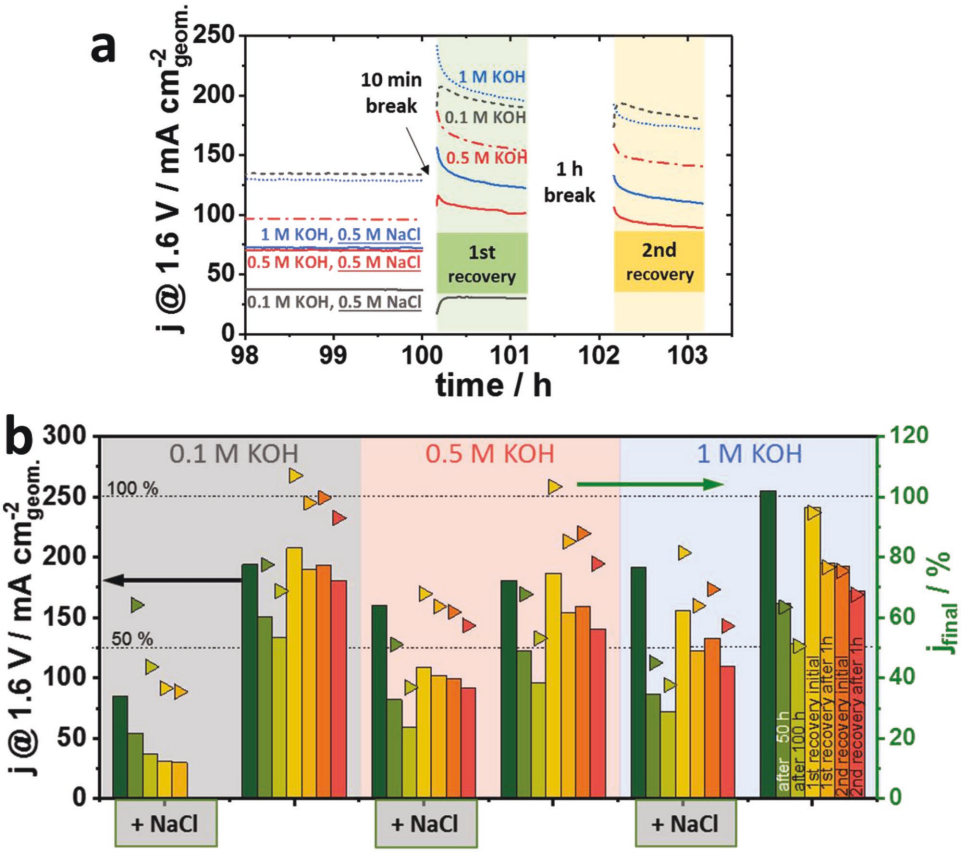

Figure 4. a) Recovery effect after 100 h measurement current density over time after 100 h and restart electrolysis at 1.6 V for two times. The first recovery effect was determined after reapplying the potential after 10 min, the second recovery effect was after 1 h. b) Current density and maximum current related percentage after 50 h, 100 h, initial first recovery effect, after 1 h of first recovery effect, initial second recovery effect, and after 1 h of second recovery effect of NaCl free and the addition of 0.5 M NaCl.

potential could lead to a corresponding partial "chemical resetting" of the metal oxide water splitting catalyst. For instance, the cathodic step to open-circuit potential is likely to reduce the high-valent Ni ion and Fe ion centers to a lower redox state, possibly associated with a reset in the distribution of partially long-range ordered structure phases, such as the γ-NiOOH and α-$Ni(OH)_2$ phase, which differ significantly in their initial OER reactivity. We consider the recovery phenomenon as such an important characteristic that we conducted a more detailed investigation of the stability and the recovery effect (Figure 4b). The bars represent the maximum current density at +1.6 V after selected test times of 50 h, 100 h, and the (maximum) initial and final current density of the first and second recovery (see Figure S14, Supporting Information). The current density values are reported in % relative to the maximum initial current density and are indicated as j_{final} and related to the right γ-axis in Figure 4b.

Generally, higher KOH concentrations lead to higher current densities. In NaCl-free electrolyte, the recovery effect is more pronounced, reaching values of more than 100% of the initial maximum current density. NaCl-free 0.5 M KOH and 1 M KOH show similar trends with recoveries ranging close to 100%. The presence of 0.5 M NaCl resulted in small performance losses even after recovery especially in 0.1 M KOH. Consequently, the 0.5 M NaCl containing tests showed smaller recoveries due to a detrimental chloride effect on either the catalyst or the membrane. For the 0.1 M KOH + 0.5 M NaCl conditions, no recovery was observed, reiterating an effect of the molar Cl^-/OH^- ratio on current density drop and activity recovery. The smaller the molar Cl^-/OH^- ratio, the more the current density recovered.

The second recovery effect is less pronounced. This could in principle be related to the short 1 h potential hold during the first recovery measurement. In other words, the recovery could be a time-dependent phenomenon and is likely that recovery can be observed yet again after an operation of 100 h. In the context of solar/wind input electricity, the recovery of a seawater electrolyzer will be best performed during dark and low-wind phases. This approach would be useful for a system that was shut down during the night or a similar system that is driven by the photovoltage of an integrated photoelectrochemical device.

2.5. Harnessing Cell Performance Recovery Effects

Renewable energy sources are not able to provide constant electricity due to their strong fluctuations. For instance, the diurnal day/night cycle governs photovoltaic solar systems. This is why we tested whether it would be best to harness the recovery effect during intermittent day-night conditions, as illustrated in **Figure 5**.

The test was conducted mimicking 5 d with 20 h daytime, setting a potential of +1.6 V, and 4 h night time at open-circuit potential. The test was conducted in 0.5 M KOH and 0.5 M NaCl in order to operate with the most balanced electrolysis conditions. After each diurnal cycle, a clear recovery was determined, following the results obtained in our preceding preliminary recovery effects. This evidences the possibility for a practical exploitation of the recovery effect. We note that while the

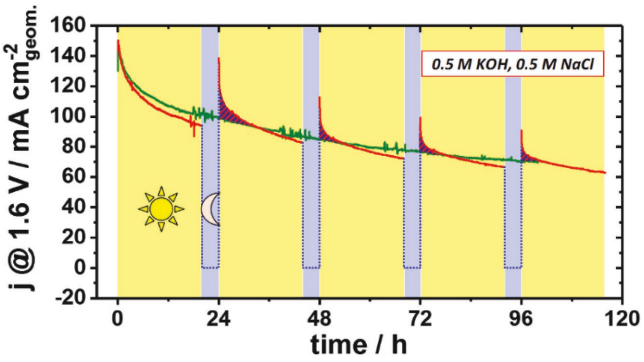

Figure 5. Current density versus electrolysis time for a continuous 100 h measurement (green) and a 20 + 4 h day/night interval measurement (red) mimicking a 4 h night cycle at open circuit potential. The electrolysis potential for the continuous and the day time measurement was kept at 1.6 V. The blue red hatched area expresses the advantageous current density in contrast to the 100 h measurement. A loading of 0.5 mg_{Pt} cm^{-2} 46.7 wt% Pt on carbon (TKK) on the cathode and 2.5 mg cm^{-2} NiFe-LDH at the anode, a Tokuyama A201 as membrane and a 0.5 M KOH and 0.5 M NaCl electrolyte was used.

intermittent 100 h stability is somewhat similar to the continuous 100 h measurement, the former exhibited a much more advantageous current density (reactivity) indicated by the patterned surface areas in Figure 5. In essence, the diurnal day-night cycle can really be used as a natural electrolyzer refreshing treatment and thus might help for a long-time electrolyzer performance.

2.6. The Faradaic Product Efficiency of Seawater Electrolyzer Cells

Seawater electrolyzer cells serve the purpose of electrical energy storage in form of oxygen and hydrogen. Chlorine chemistries are undesired and should therefore be selectively suppressed. To check the chemical and faradic selectivity of the electrolyzer anode, an electrochemical online mass spectrometry at the gas exhaust was used. Constant faradaic currents between 0.05 and 3.0 A were applied for 30 min under 0.5 M KOH with and without 0.5 M NaCl to ensure a steady-state gas concentration. The selectivity results are shown in **Figure 6**.

Consistent with data presented above, the overpotentials in NaCl-free electrolyte are significantly lower (red solid vs black dotted in Figure 6). Apart from a slightly higher noise level for the NaCl-containing electrolyte measurement, the resulting oxygen steady-state concentration levels are basically identical for both electrolytes (cyan and dark blue in Figure 6). Hence, the anodic processes in NaCl-free and NaCl-containing electrolyte show the same chemical selectivities and faradaic efficiencies. Furthermore, no chlorine species were detected. Together, this strongly suggests that chlorine electrochemistry is suppressed and confirms the validity of the general seawater electrolysis selectivity design criterion. For comparison, the oxygen concentration level for a 100% faradaic efficiency (FE) was also added in Figure 6 (green horizontal bars). The oxygen FE values (green% numbers in Figure 6) increased with increasing current, ranging between 73 and 88%. One reason for the efficiency losses is hydrogen and oxygen crossover through the

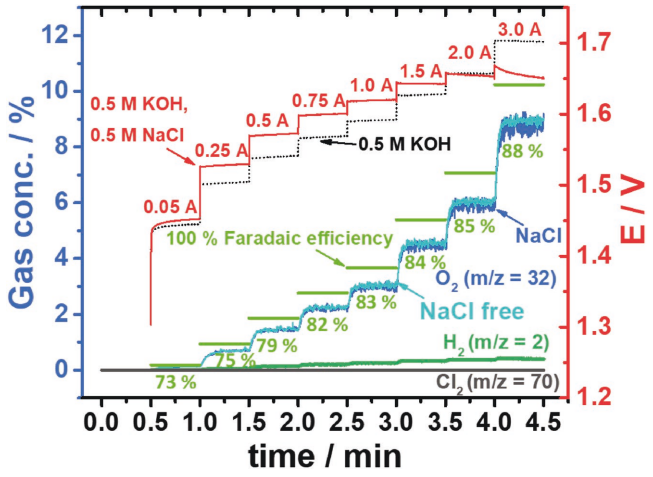

Figure 6. Online selectivity measurements of a 5 cm^2 seawater electrolyzer. The volumetric gas concentration in % of the left (blue) *y*-axis and the cell voltage at the right (red) *y*-axis is plotted against the measurement time, shown at the bottom *x*-axis. The applied currents are given in red numbers over the resulting electrode potentials that are shown for an electrolyte concentration of 0.5 M KOH with 0.5 M NaCl in red and for a concentration of 0.5 M KOH as black dotted line. Concurrent oxygen volumetric concentrations for the NaCl containing are in dark blue and the latter in cyan. The green horizontal bars represent the oxygen level of 100% faradaic efficiencies. The green percent values below the measured gas concentration in green indicate the oxygen faradaic efficiency values at each current. Also shown are the time traces of the chlorine (gray) and hydrogen (dark green) concentrations.

membrane seen in the mass spectrometric profile (H_2 mass signal in Figure 6).

The seawater electrolyzer cell efficiencies were calculated based on the lower heating value (LHV, $\Delta_R H_{LHV} = 241.8$ kJ mol^{-1}) and the higher heating value (HHV, $\Delta_R H_{HHV} = 285.8$ kJ mol^{-1}) of the resulting molecular hydrogen.[20,21] These calorific energy values were translated into a corresponding thermodynamic cell voltage according to

$$U_{\text{LHV or HHV}} = \frac{\Delta_R H_{\text{LHV or HHV}}}{nF} \quad (1)$$

where n is the number of moles of electrons transferred per mole of hydrogen and F is the Faraday constant. With $U_{HHV} = 1.48$ V and $U_{LHV} = 1.25$ V the overall cell energy efficiency as the product of the voltage efficiency and the faradaic efficiency follows as

$$\eta_{\text{cell}} = \left(\frac{U_{\text{LHV or HHV}}}{U_{\text{cell}}}\right) \cdot \eta_{\text{farad}} \quad (2)$$

where η_{farad} is the experimentally determined faradaic efficiency and U_{cell} is the experimental electrolyzer cell potential. The experimental cell efficiencies with and without NaCl at various applied currents are listed in **Table 1** (see further details in Table S1, Supporting Information). Remarkably, the cell voltage at low currents of 0.05 A or 10 mA cm^{-2}, respectively, remained below the voltage of $U_{HHV} = 1.48$ V. This corroborates the high catalytic activity of NiFe-LDH in alkaline media. Consequently, the HHV cell efficiency of 75% at these low currents exceeds the faradaic efficiency of 73%. At high currents of 3.0 A (600 mA cm^{-2}) the cell efficiency decreased to $\eta_{cell} = 77\%$ compared to a much higher faradaic efficiency of $\eta_{farad} = 88\%$.

Table 1. Applied cell currents and the corresponding overall cell energy efficiencies η with respect to the lower heating value (ηLHV) and the higher heating value (ηHHV) in a seawater electrolyzer (NaCl) versus a chloride-free electrolyzer (w/o NaCl), conditions: NiFe-LDH at anode, 46.7 wt% Pt/C at cathode, anion exchange membrane, 0.5 M KOH, and 0.5 M NaCl.

I in [A]	$\eta_{farad.}$	NaCl η_{LHV}	w/o NaCl η_{LHV}	NaCl η_{HHV}	w/o NaCl η_{HHV}
0.05	0.73	0.63	0.63	0.75	0.75
0.25	0.75	0.61	0.63	0.73	0.74
0.50	0.79	0.63	0.64	0.74	0.76
0.75	0.82	0.64	0.65	0.76	0.77
1.00	0.83	0.64	0.65	0.76	0.77
1.50	0.84	0.64	0.64	0.76	0.76
2.00	0.85	0.64	0.64	0.76	0.76
3.00	0.88	0.67	0.65	0.79	0.77

2.7. Relating Electrolyzer Cell Performance to the In Situ Chemical State and Molecular Geometric Structure of the Anode Catalysts

To learn more about the chemical state and local chemical structure of the anode catalysts after long-term seawater electrolysis operation, element-specific structural details of the catalyst at the atomic level were examined by in situ X-ray absorption spectroscopy. Five catalyst samples were selected for the spectroscopic analysis of the redox states by looking at the X-ray near-edge region (XANES) and the analysis of the local geometric chemical structure of the catalysts using the extended X-ray absorption fine structure (EXAFS). More specifically, one freshly prepared, untreated NiFe-LDH catalyst and two NiFe-LDH catalyst samples were characterized under in situ conditions of an operating electrolyzer cell[22] at +1.0 and +1.6 V_{RHE}, one in 0.1 M KOH and one in 0.1 M KOH + 0.5 M NaCl ("seawater"), hence a total of four in situ catalyst measurements were conducted. A lower KOH concentration was used here to uncover potential changes induced by NaCl more clearly. The measurements at fixed potentials were performed after an activation treatment by cycling the cell potential between +1.0 and +1.6 V_{RHE} for ten times.

2.7.1. XANES Analysis of Metal Redox States

XANES spectra (**Figure 7**) indicate a slightly higher oxidation state of the catalyst under operating conditions, as indicated by the positive shift of the energy of the edge position. While the NiFe-LDH water splitting catalyst, when operated at +1.0 V_{RHE} in KOH, had not yet reached the same high oxidation state it attained at +1.6 V_{RHE} in KOH, the NiFe-LDH catalyst operated in seawater took on its highest experimentally observed oxidation state already at +1.0 V_{RHE}. No further oxidation was

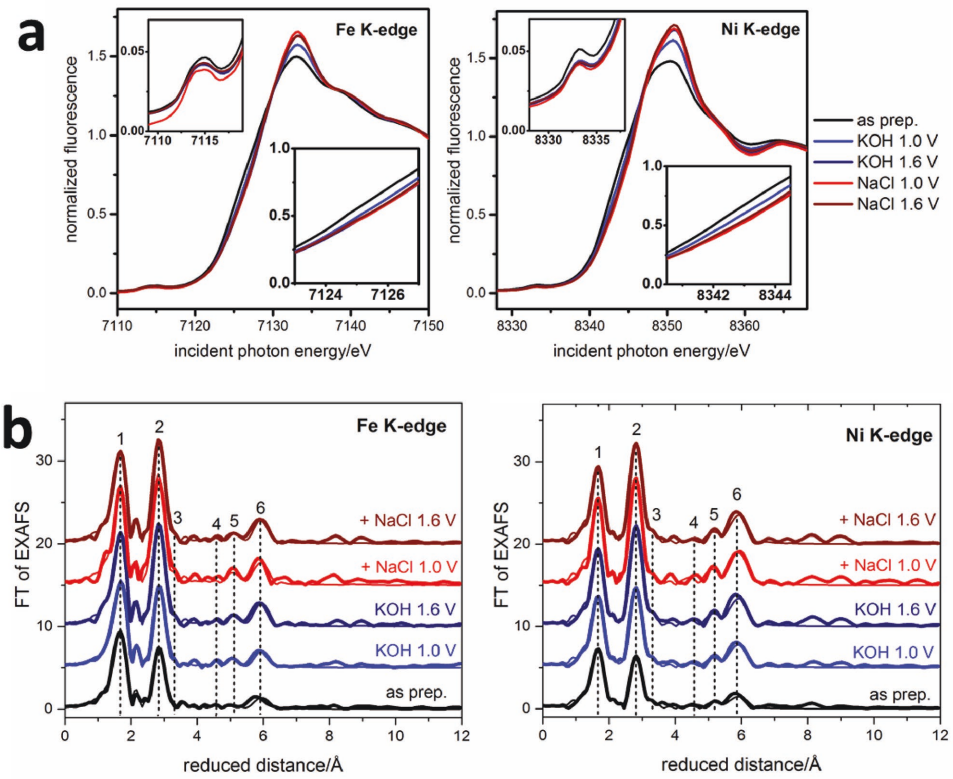

Figure 7. a) XANES spectra at the Ni and the Fe K-edge of NiFe-LDH catalyst materials used in the described electrolyzer system. b) EXAFS spectra of NiFe-LDH catalysts as prepared and under different electrochemical conditions using the quasi in situ freeze-quench approach. Further information about the simulations can be obtained in the Supporting Information. A stacking of +5 (excluding the as-prepared sample) was used for convenience. The chemical structure shown in the Supporting Information represents a fragment of the LDH structure and illustrates different structural motifs that can be derived from the EXAFS spectra (green: metal atoms (Ni/Fe); red: oxygen atoms), it is not showing the dominant structure present. The number of the peaks in the FT refers to the numbering in the structure shown in Figure S16B (Supporting Information).

observed when the potential was increased to +1.6 V_{RHE} in seawater. The fact that the voltammetric Ni reduction peak potential is located more anodic of +1.0 V_{RHE} suggests that the Ni reduction kinetics is relatively slow, in agreement with previous works referring to the insulating character of the reduced phase.[23]

2.7.2. EXAFS Analysis of Local Geometric Structure

All XANES conclusions are in full agreement with the modeling results of the EXAFS functions uncovering, among other things, the local coordination numbers (CN) (see Figure S16, Supporting Information). An increasing oxidation state can cause a higher coordination number for the first metal–oxygen shell. However, as the Ni oxidation state is only slightly increasing we largely attribute the CN trends to an increasing degree of coordinative order for the catalysts characterized under applied electrode potential. The ordering effect is particularly pronounced for the in situ catalyst measurements in comparison to the fresh as-prepared water splitting catalyst.

The EXAFS spectra of all catalysts clearly resemble the layered double-hydroxide structure of the hydrotalcite structure type (see Figure 7b and the layered structure in Figure 1d). At both metal K edges quite similar EXAFS spectra were obtained. The Fe atoms appear to be incorporated inside the LDH structure without any discernible separate Fe oxide phase. Since Fe is present in oxidation state +3, a smaller M–O1 distance is expected for the Fe–O1 shell than for the Ni–O1 shell (peak 1 in the FT). This is indeed observed as the Ni–O1 distance of (2.04–2.05) Å is consistently larger than the Fe–O1 distance of (2.00–2.01) Å throughout the set of samples investigated in this study (Tables S3 and S4, Supporting Information). Peak number 2 in the FT EXAFS plot (Figure 7b) can be assigned to edge-sharing μ-oxo bridged metal atoms (Figure S16B, Supporting Information). Accordingly, the double distance is observed and indicated as peak 6. Peak number 5 emerges as a consequence of M–O_6–octahedra connected via one joint edge, but sitting in different planes with respect to the linearly connected edge-sharing octahedra (see Figure S16B, Supporting Information). Two more oxygen shells were fitted in the EXAFS spectra (peak 3 and peak 4), however the amplitude is small and the uncertainty of the CN large (Tables S3 and S4, Supporting Information). Although spectra of catalysts operated in KOH and seawater appear quite alike, a closer look at the CNs reveals significant difference for the seawater case. After a 15 min operation, the seawater catalysts reached a stable state at +1.0 V_{RHE} which did not significantly change any further at +1.6 V_{RHE}. In contrast, those catalysts operated in KOH only exhibit a continuous trend toward higher CNs

from the fresh catalysts to +1.0 and +1.6 V_{RHE}. This is in full agreement with results from cyclic voltammetry experiments using rotating disk electrodes for these catalysts, where the characteristic metal ion oxidation peak was developing much more rapidly upon cycling in seawater than in pure KOH. The presence of NaCl with its higher ionic strength electrolyte appears to catalyze the molecular oxidation and ordering of the initial LDH structures, enabling higher oxidation states (and related a higher CN value) and more structural order possible at lower electrode potentials. The data further show that under prolonged operation the oxygen evolution catalysts operated in both KOH and seawater eventually attained a virtually identical local structural and oxidation state at +1.6 V_{RHE} suggesting that membrane degradation processes are largely responsible for the experimental losses in catalytic performance observed in the long-time experiments.

3. Conclusions

This study showed a first efficient working alkaline electrolyzer, splitting artificial alkaline seawater selectively into oxygen and hydrogen. The higher the KOH concentration the higher the performance (current density), but the lower the relative stability of the electrolyzer performance. The addition of 0.5 M NaCl to the electrolyte resulted in lower current density that likely is induced by lower OH^- conductivity of the used AEM due to the presence of Cl^- ions. 100 h measurements were successfully performed. While the NaCl-free 0.1 M KOH measurement performed stable after an activation time of 12 h, for all other electrolyte conditions the current density decreased per time. SEM images and impedance investigations indicate a membrane-induced stability loss. However, a recovery effect was identified, which could be exploited in a diurnal day-night cycle. The natural day-night cycles could function as a natural refreshment protocol when using renewable energy sources like photovoltaics or wind power to operate the electrolyzer.

X-ray absorption spectroscopy (XAS) has been conducted to reveal structural integrity of the catalyst after operation in different electrolytes, applying a freeze-quench approach. It confirmed good stability of the LDH catalyst under operating conditions. Additionally, the EXAFS data validate the hypothesis that a major fraction of activity loss is related to chloride ions blocking the membrane, at least hindering the OH^- transport across the membrane. Finally, a selectivity measurement was conducted to determine the faradaic efficiency, which showed faradaic efficiencies up to 88% and cell efficiencies of 64% at high current densities.

4. Experimental Section

Sample Preparation: Highly crystalline NiFe-LDH catalysts were synthesized in a solvothermal one-pot synthesis route using a microwave-assisted autoclave (Anton Paar 300 Monowave), also described elsewhere.[15] In brief, 1200 µL of 0.6 M $Ni(OAc)_2 \times 4H_2O$ (99.998% trace metals basis, Aldrich) and 240 µL of 0.6 M $Fe(NO_3)_3 \times 9H_2O$ (98% trace metals basis, Alfa Aeser) were added to 6 mL DMF and stirred overnight. Afterward, 8 mL ultrapure water (>18 MΩ at room temperature) and 4 mL additional DMF were added to the reaction mixture. The solution was then microwave treated at 120 °C for 60 min and subsequently at 160 °C for 30 min. The final product was collected by centrifuging and subsequently washed using ultrapure water and ethanol.

Preparation of Membrane Electrode Assembly (MEA): The MEA consisting of a Tokuyama A201 membrane, 46.7 wt% Pt on Vulcan XC 72R (TKK) as cathode and synthesized NiFe-LDH as anode material was prepared using a spray-coating method described elsewhere.[17] In short, 50 mg catalyst 50 µL ultrapure water (18.2 MΩ cm), 3 mL i-Prop and 460 mg Ionomer (5 wt% AS-4, Tokuyama) were ultrasonicated for 15 min. The resulting catalyst to ionomer ratio is 7:3. The membrane (A201, Tokuyama) was fixed on a commercial heatable vacuum table at 50 °C (Carbon and FuelCell) equipped with a dry vacuum pump/compressor (Welch 2511) and a temperature controller (Carbon and FuelCell). Typically, 1 mL for the cathode and 2–4 mL for the anode of the ink were spray-coated on the membrane using 1 bar N_2 stream and a Gun Piece SP-2 spray gun (Rich) equipped with a 0.4 mm tip size to achieve a loading of 0.5 mg_{Pt} cm^{-2} for the hydrogen electrode side and 1 – 5 mg(cat) cm^{-2} for the anode side. The spraying was conducted in horizontal and subsequent vertical serpentines to obtain a homogenous 5 cm^2 coating (see Figure S17a, Supporting Information). A protection mask was used to protect the protruding part of the membrane and to ensure the optimal vis-à-vis coating (see Figure S17b, Supporting Information). The catalyst loading was determined by measuring the membrane mass before and after the coating.

Physical and Chemical Characterization: ICP-OES was used for elemental and compositional analysis using a 715-ES-inductively coupled plasma analysis system with CCD detector (Varian). Prior to detecting, the catalyst materials were dissolved in a mixture of $HNO_3/H_2SO_4/HCl$ in a ratio of 1:1:3. XRD measurements were carried out to study the crystallinity using a D8 Advance Diffractometer (Bruker) equipped with a Lynx Eye Detector and KFL Cu 2 K X-ray tube. The diffraction profiles were collected between 2θ angles of 10° and 70° with a step size of 0.039°. The divergence slit was set to 6 mm, the antiscattering slit to 6°, and the Lynx-Iris to 10 mm. Microscopy images were taken using a TEM Tecnai G2 20 S-TWIN microscope operated at 200 kV, equipped with a GATAN MS794 P CCD-detector and a SEM JEOL JSM 7401 F + EDX Bruker Quantax XFlash Detektor 4010 with energy-dispersive X-ray spectroscopy. SEM cross sections were prepared from the full MEA by cutting with asymmetric blade scissors to avoid compression or tear on the investigated cut edges. EDX were conducted to study morphology and composition.

Electrochemical Characterization: The electrolyzer measurement was carried out by using a commercial membrane based electrolyzer assembly (Carbon and FuelCell) consisting of two endplates with gas ports, two current collectors, two bipolar plates (carbon plate for hydrogen side, titanium plate for oxygen side), PTL GDL-10BC (Sigracet GDL) for the cathode side and a gold coated titanium mesh for the anode side, and the prepared MEA (Figure S18, Supporting Information). The screws were tightened with a torque of 5 nm. The measurement was carried out using a peristaltic pump, a Gamry 3000 potentiostat, Teflon tubing, and electrolyte reservoir to avoid glass corrosion induced contaminations and temperature controller to hold the cell temperature at 50 °C (Figure S1, Supporting Information).

Ex situ membrane conductivity was measured by using a four-probe measurement technique. The glass cell was constructed as shown in Figure S4 (Supporting Information). The membrane was fixed between two identical half-cells. The conductivity was measured using 0.1, 0.5, and 1 M KOH with and without additional 0.5 M NaCl. The electrolyte was N_2 saturated to ensure equal conditions. Two Luggin capillaries were located equally close to the membrane, to measure the membrane-induced potential drop, while a current was set between the two platinum mesh electrodes acting as working and counter electrodes. The connection of the electrodes is presented in Figure S5 (Supporting Information).

Ohm's Law Approach: In Ohm's law approach, the potential drop at 1, 2, 3, 4, 5, 10, 20, 50, 100, 200, and 230 mA were measured with and without the membrane. The slope of the potential drop and the current

density represent the resistance shown in Figure S6a (Supporting Information). The difference of the membrane-free resistance and the resistance with membrane results into an apparent membrane resistance, which includes the capacitive resistance as shown in the equivalent circuit in the inset of Figure S6a (Supporting Information). After the Ohm's law approach the impedance was measured at OCV between 50 and 200 kHz (impedance spectroscopy approach). With this method the resistance of the membrane is obtained without the contribution of the capacitive resistance.[24]

For the experiments aimed at calculating the Faradaic efficiencies for the electrolyzer anode, an in-house electrolyzer test station equipped with a mass flow controlled N_2 flow (100 sccm) through the electrolyte reservoir and a mass spectrometer (Pfeiffer Thermostar: GSD 320 TC2) equipped with a (150/220 µm) fused silica tubing was used. To ensure a constant gas concentration level the constant current was hold for 30 min. To determine the faradaic efficiency the average concentration level of oxygen of the last 5 min was taken. For a detailed calculation see the Supporting Information. All electrochemical potentials discussed here are given versus RHE.

XAS Sample Preparation and Measurements: The XANES and EXAFS measurements were carried out at the BESSY synchrotron radiation source operated by the Helmholtz-Zentrum Berlin. The measurements were performed at the KMC-3 bending-magnet beamline at 20 K in a helium-flow cryostat (Oxford-Danfysik). The incident beam energy was selected by a Si(111) double-crystal monochromator. The measurements at the nickel and iron K-edge were performed in fluorescence mode using a 13-element energy-resolving Ge detector (Canberra) cooled with liquid nitrogen. The extracted spectra were weighted by k^3 and simulated in k-space ($E_0 = 7112$ eV for iron and 8333 eV for nickel). The k^3-weighted spectra are available in Figure S15 (Supporting Information). All EXAFS simulations were performed using in-house software (SimXLite) after calculation of the phase functions with the FEFF program (version 8.4, self-consistent field option activated). The data range used in the simulation of the EXAFS spectra was $k = (3–13)$ Å^{-1}.

The EXAFS simulation was optimized by a minimization of the error sum obtained by summation of the squared deviations between measured and simulated values (least-squares fit). The fit was performed using the Levenberg–Marquardt method with numerical derivatives. The error ranges of the fit parameters were estimated from the covariance matrix of the fit. Further details are given elsewhere. The amplitude reduction factor S_0^2 was kept constant at 0.9. Energy calibration was carried out by simultaneous measurement of the X-ray absorption spectrum of 10 µm thick metal foils (Ni and Fe, Good Fellow 99.99%).

Catalysts for XAS experiments were prepared on glassy carbon substrates. Samples for quasi in situ XAS-spectroscopy were prepared via a freeze-quench approach as described elsewhere.[22] Before freezing they were operated for 15 min at the potential indicated.

Supporting Information

Supporting Information is available from the Wiley Online Library or from the author.

Acknowledgements

Financial support by the German Research Foundation (DFG) through Grant Reference No. STR 596/8-1 and the Federal Ministry of Education and Research (BMBF) grant 03SF0433A "MEOKATS" are gratefully acknowledged. The authors also acknowledge the ZELMI for making the TEM image.

Conflict of Interest

The authors declare no conflict of interest.

Keywords

alkaline electrolyzer, NiFe-LDH, seawater splitting

Received: January 30, 2018
Revised: April 15, 2018
Published online:

[1] J. E. Bennett, *Int. J. Hydrogen Energy* **1980**, *5*, 401.
[2] a) Z. Kato, M. Sato, Y. Sasaki, K. Izumiya, N. Kumagai, K. Hashimoto, *Electrochim. Acta* **2014**, *116*, 152; b) K. Izumiya, E. Akiyama, H. Habazaki, N. Kumagai, A. Kawashima, K. Hashimoto, *Mater. Trans. JIM* **1997**, *38*, 899; c) K. Izumiya, E. Akiyama, H. Habazaki, N. Kumagai, A. Kawashima, K. Hashimoto, *Electrochim. Acta* **1998**, *43*, 3303; d) K. Fujimura, T. Matsui, K. Izumiya, N. Kumagai, E. Akiyama, H. Habazaki, A. Kawashima, K. Asami, K. Hashimoto, *Mater. Sci. Eng., A* **1999**, *267*, 254; e) K. Fujimura, T. Matsui, H. Habazaki, A. Kawashima, N. Kumagai, K. Hashimoto, *Electrochim. Acta* **2000**, *45*, 2297; f) H. Habazaki, T. Matsui, A. Kawashima, K. Asami, N. Kumagai, K. Hashimoto, *Scr. Mater.* **2001**, *44*, 1659; g) N. A. Abdel Ghany, N. Kumagai, S. Meguro, K. Asami, K. Hashimoto, *Electrochim. Acta* **2002**, *48*, 21; h) A. A. El-Moneim, N. Kumagai, K. Hashimoto, *Mater. Trans.* **2009**, *50*, 1969; i) A. A. El-Moneim, J. Bhattarai, Z. Kato, K. Izumiya, N. Kumagai, K. Hashimoto, *ECS Trans.* **2010**, *25*, 127; j) Z. Kato, J. Bhattarai, N. Kumagai, K. Izumiya, K. Hashimoto, *Appl. Surf. Sci.* **2011**, *257*, 8230.
[3] S. Fukuzumi, Y.-M. Lee, W. Nam, *ChemSusChem* **2017**, *10*, 4264.
[4] a) T. Arikawa, Y. Murakami, Y. Takasu, *J. Appl. Electrochem.* **1998**, *28*, 511; b) V. Petrykin, K. Macounova, O. A. Shlyakhtin, P. Krtil, *Angew. Chem., Int. Ed.* **2010**, *49*, 4813; c) K. S. Exner, J. Anton, T. Jacob, H. Over, *Angew. Chem., Int. Ed.* **2014**, *53*, 11032; d) R. K. B. Karlsson, H. A. Hansen, T. Bligaard, A. Cornell, L. G. M. Pettersson, *Electrochim. Acta* **2014**, *146*, 733; e) R. K. B. Karlsson, A. Cornell, *Chem. Rev.* **2016**, *116*, 2982; f) I. Sohrabnejad-Eskan, A. Goryachev, K. S. Exner, L. A. Kibler, E. J. M. Hensen, J. P. Hofmann, H. Over, *ACS Catal.* **2017**, *7*, 2403; g) J. G. Vos, M. T. M. Koper, *J. Electroanal. Chem.* **2017**.
[5] S. Trasatti, *Electrochim. Acta* **1984**, *29*, 1503.
[6] Y. Surendranath, M. Dincă, D. G. Nocera, *J. Am. Chem. Soc.* **2009**, *131*, 2615.
[7] F. Dionigi, T. Reier, Z. Pawolek, M. Gliech, P. Strasser, *ChemSusChem* **2016**, *9*, 962.
[8] a) D. A. Corrigan, *J. Electrochem. Soc.* **1987**, *134*, 377; b) M. Gong, Y. Li, H. Wang, Y. Liang, J. Z. Wu, J. Zhou, J. Wang, T. Regier, F. Wei, H. Dai, *J. Am. Chem. Soc.* **2013**, *135*, 8452; c) M. W. Louie, A. T. Bell, *J. Am. Chem. Soc.* **2013**, *135*, 12329; d) J. A. Haber, C. Xiang, D. Guevarra, S. Jung, J. Jin, J. M. Gregoire, *ChemElectroChem* **2014**, *1*, 524; e) Y.-F. Li, A. Selloni, *ACS Catal.* **2014**, *4*, 1148; f) J. Y. C. Chen, L. Dang, H. Liang, W. Bi, J. B. Gerken, S. Jin, E. E. Alp, S. S. Stahl, *J. Am. Chem. Soc.* **2015**, *137*, 15090; g) O. Diaz-Morales, I. Ledezma-Yanez, M. T. M. Koper, F. Calle-Vallejo, *ACS Catal.* **2015**, *5*, 5380; h) D. Friebel, M. W. Louie, M. Bajdich, K. E. Sanwald, Y. Cai, A. M. Wise, M.-J. Cheng, D. Sokaras, T.-C. Weng, R. Alonso-Mori, R. C. Davis, J. R. Bargar, J. K. Nørskov, A. Nilsson, A. T. Bell, *J. Am. Chem. Soc.* **2015**, *137*, 1305; i) M. K. Bates, Q. Jia, H. Doan, W. Liang, S. Mukerjee, *ACS Catal.* **2016**, *6*, 155; j) B. M. Hunter, W. Hieringer, J. R. Winkler, H. B. Gray, A. M. Muller, *Energy Environ. Sci.* **2016**, *9*, 1734; k) M. Goerlin, J. Ferreira de Araújo, H. Schmies, D. Bernsmeier, S. Dresp, M. Gliech, Z. Jusys, P. Chernev, R. Kraehnert, H. Dau, P. Strasser, *J. Am. Chem. Soc.* **2017**; l) M. Görlin, P. Chernev, J. Ferreira de Araújo, T. Reier, S. Dresp, B. Paul, R. Krähnert, H. Dau,

P. Strasser, *J. Am. Chem. Soc.* **2016**, *138*, 5603; m) C. C. L. McCrory, S. Jung, J. C. Peters, T. F. Jaramillo, *J. Am. Chem. Soc.* **2013**, *135*, 16977; n) L. Trotochaud, S. L. Young, J. K. Ranney, S. W. Boettcher, *J. Am. Chem. Soc.* **2014**, *136*, 6744.

[9] F. Dionigi, P. Strasser, *Adv. Energy Mater.* **2016**, 1600621.

[10] M. Görlin, M. Gliech, J. F. de Araújo, S. Dresp, A. Bergmann, P. Strasser, *Catal. Today* **2016**, *262*, 65.

[11] L. Wang, F. Dionigi, N. T. Nguyen, R. Kirchgeorg, M. Gliech, S. Grigorescu, P. Strasser, P. Schmuki, *Chem. of Mater.* **2015**, *27*, 2360.

[12] S. Barwe, C. Andronescu, J. Masa, W. Schuhmann, *Curr. Opin. Electrochem.* **2017**, *4*, 4.

[13] a) Y. Jia, L. Zhang, G. Gao, H. Chen, B. Wang, J. Zhou, M. T. Soo, M. Hong, X. Yan, G. Qian, J. Zou, A. Du, X. Yao, *Adv. Mater.* **2017**, *29*; b) Y. Gu, S. Chen, J. Ren, Y. A. Jia, C. Chen, S. Komarneni, D. Yang, X. Yao, *ACS Nano* **2018**, *12*, 245.

[14] F. Cheng, X. Feng, X. Chen, W. Lin, J. Rong, W. Yang, *Electrochim. Acta* **2017**, *251*, 336.

[15] S. Dresp, P. Strasser, *ECS Trans.* **2016**, *75*, 1113.

[16] M. Gabrovska, D. Crisan, N. Stanica, D. Nikolova, L. Bilyarska, M. Crisan, R. Edreva-Kardjieva, *Rev. Roum. Chim.* **2014**, *59*, 447.

[17] S. Dresp, F. Luo, R. Schmack, S. Kuhl, M. Gliech, P. Strasser, *Energy Environ. Sci.* **2016**, *9*, 2020.

[18] X. Lu, C. Zhao, *Nat Commun.* **2015**, *6*, 6616.

[19] J. Luo, J.-H. Im, M. T. Mayer, M. Schreier, M. K. Nazeeruddin, N.-G. Park, S. D. Tilley, H. J. Fan, M. Grätzel, *Science* **2014**, *345*, 1593.

[20] P. K. Pahwa, G. K. Pahwa, *Hydrogen Economy*, Energy and Resources Institute **2014**.

[21] N. R. Council, N. A. o. Engineering, *The Hydrogen Economy: Opportunities, Costs, Barriers, and R&D Needs*, The National Academies Press, Washington, DC **2004**.

[22] I. Zaharieva, D. González-Flores, B. Asfari, C. Pasquini, M. R. Mohammadi, K. Klingan, I. Zizak, S. Loos, P. Chernev, H. Dau, *Energy Environ. Sci.* **2016**, *9*, 2433.

[23] A. S. Batchellor, S. W. Boettcher, *ACS Catal.* **2015**, *5*, 6680.

[24] E. Fontananova, W. Zhang, I. Nicotera, C. Simari, W. van Baak, G. Di Profio, E. Curcio, E. Drioli, *J. Membr. Sci.* **2014**, *459*, 177.

Supporting Information

Direct alkaline seawater electrolysis: Performance, selectivity, and degradation studied from the molecular catalyst structure to the single electrolyzer cell level

Sören Dresp,[a] Fabio Dionigi,[a] Stefan Loos,[b] Jorge Ferreira de Araujo,[a] Camillo Spöri,[a] Manuel Gliech,[a] Holger Dau,[b] Peter Strasser[a]**

[a] *Department of Chemistry, Technical University Berlin, 10623 Berlin, Germany*

[b] *Department of Experimental Physics, Free University Berlin, Arnimallee 14, 14195 Berlin, Germany*

E-mail: pstrasser@tu-berlin.de, holger.dau@fu-berlin.de

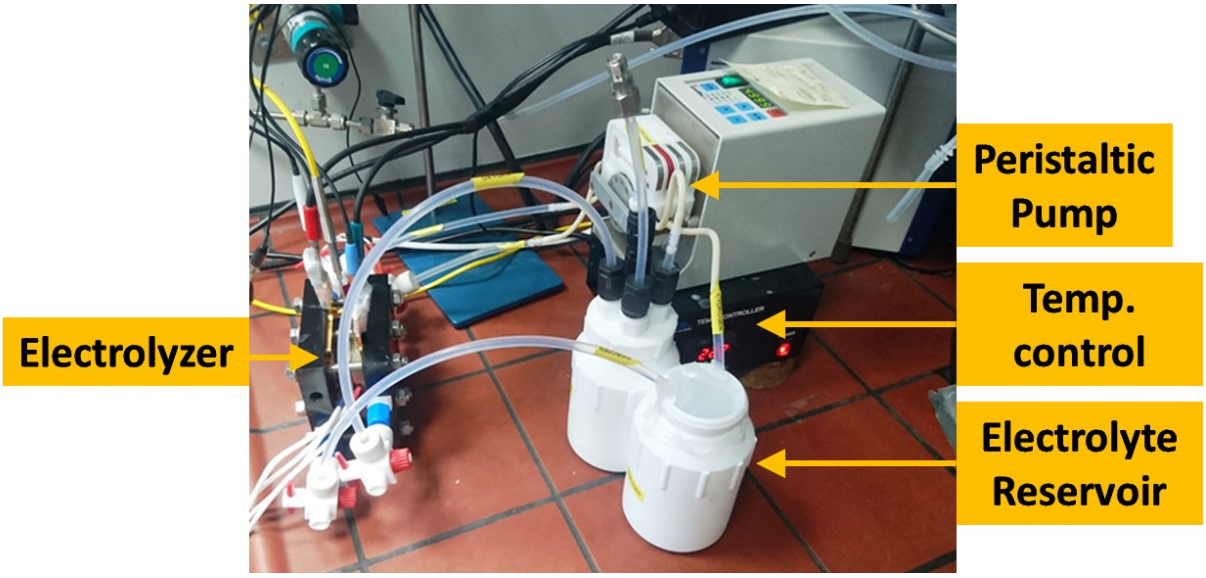

Figure S1: Image of seawater electrolyzer set-up

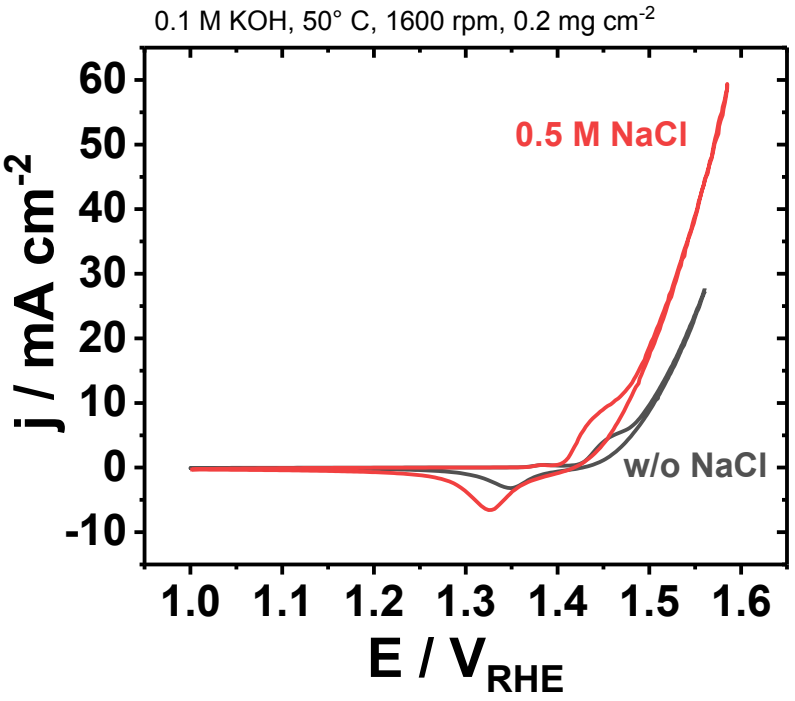

Figure S2: Cyclic voltammogramm of NiFe-LDH with a cat loading of 0.2 mg cm^{-2} in 0.1 M KOH with and without (w/o) 0.5 M NaCl at 1600 rpm and at 50 °C

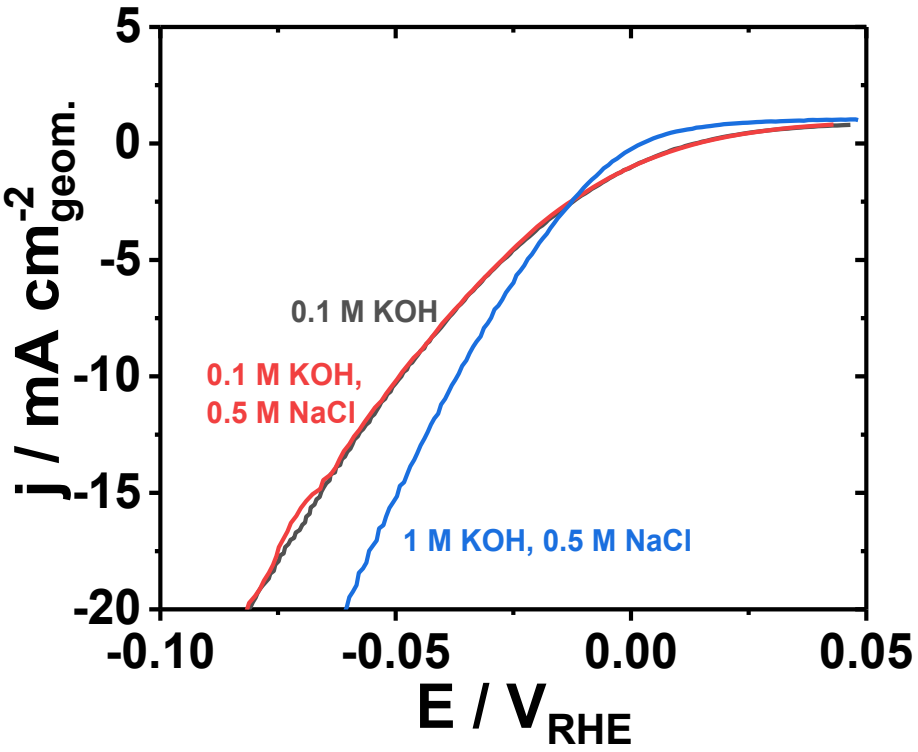

Figure S3: Cyclic voltammetry of Pt on Vulcan XC 72R (46.7 wt%, TKK), with a catalyst loading of 0.2 mg cm^{-2} at 1600 rpm, a scan rate of 20 mV s^{-1} in different alkaline electrolytes to determine the influence of NaCl towards the hydrogen evolution reaction using a three-electrode cell consisting of reversible Hydrogen electrode (RHE, Gaskatel) as reference, a Pt mesh as counter and Glassy carbon (GC) disk electrode (PINE) as working electrode. The 0.1 M KOH was prepared by using KOH pellets (>99.97 % trace metals basis, sigma aldrich) and Millipure water (> 18 mΩ at room temperature). The electrode potentials are IR-corrected and given in respect to the reversible Hydrogen electrode (RHE).

4-Probe Conductivity Measurement

The ohm's law approach is a technique to measure the membrane conductivity. It estimates the conductivity by measuring the potential drop at a specific current with and without the membrane in a set up shown in figure S1. The slope of the potential drop against the current directly yielded the resistance of the membrane system. Subtracting the resistance without the membrane yields in a resistance including the capacitive and the membrane resistance (Figure S3a).

In parallel, the **high frequency impedance** of the system was measured. Due to the alternating potential, the impedance is free of any capacitive resistances[1] and could provide additional conductivity data.

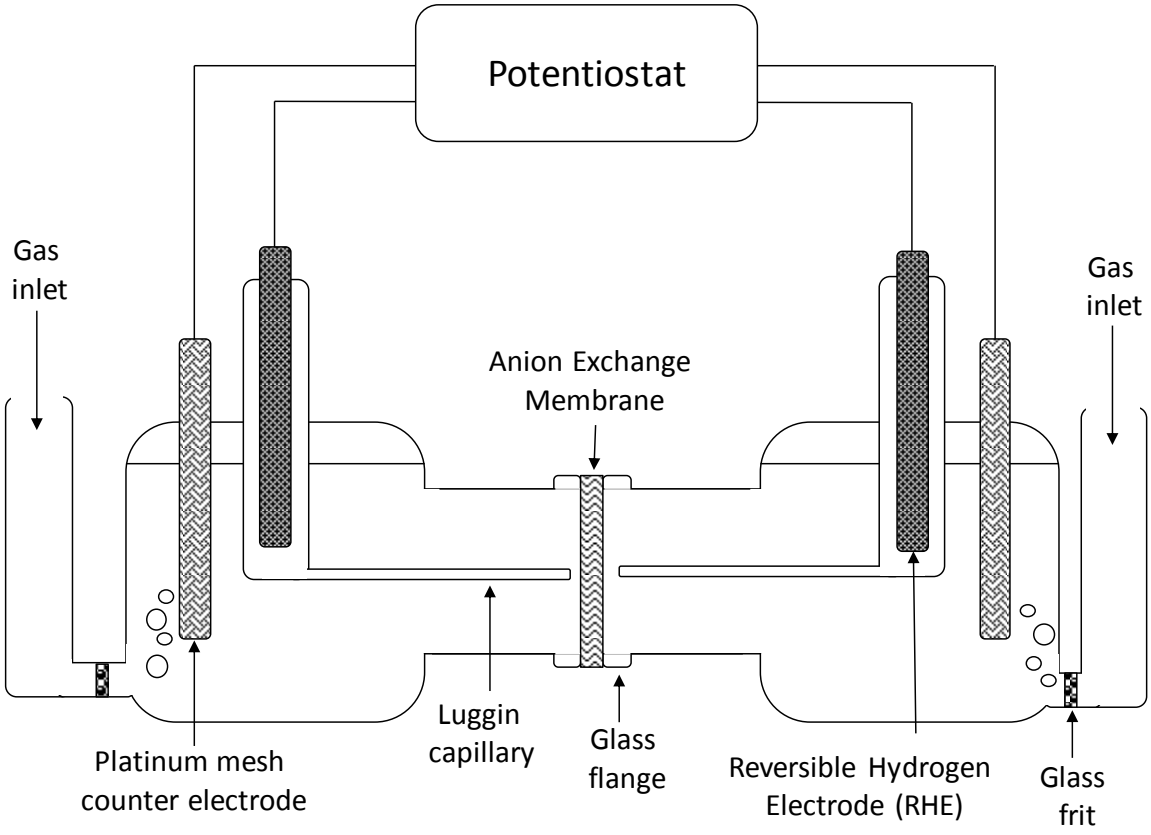

Figure S4: Sketch of 4 probe membrane conductivity measurement cell. The cell has a heating coat

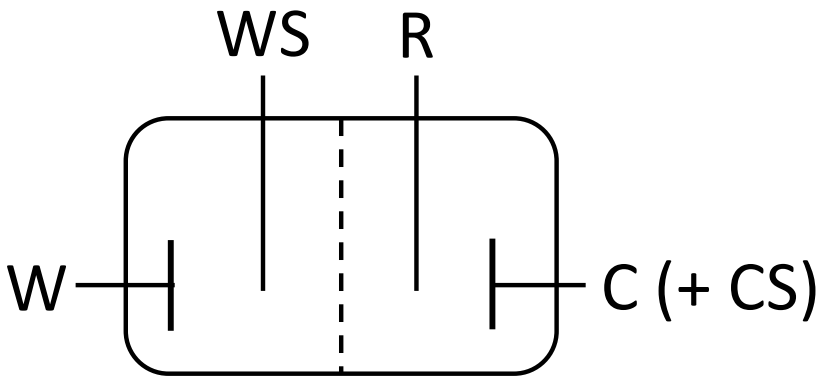

Figure S5: Scheme of working electrode (W), Working sense (WS), Reference electrode (R), Counter sense and counter electrode connection with the cell

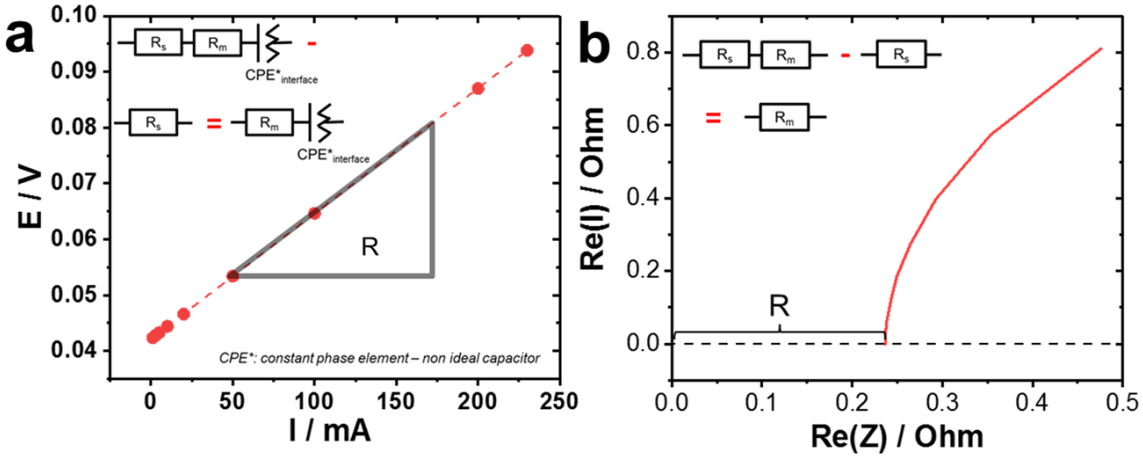

Figure S6: Determination of membrane resistance **(a)** Ohm‘s law approach **(b)** Impedance approach

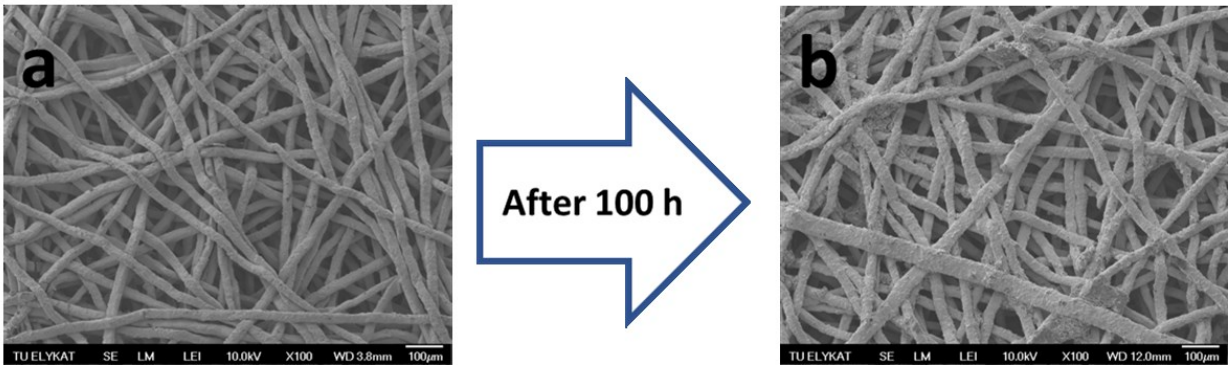

Figure S7: SEM image of Au coated Ti mesh porous transport layer before and after 100 h at 1.6 V in 1 M KOH and 0.5 M NaCl.

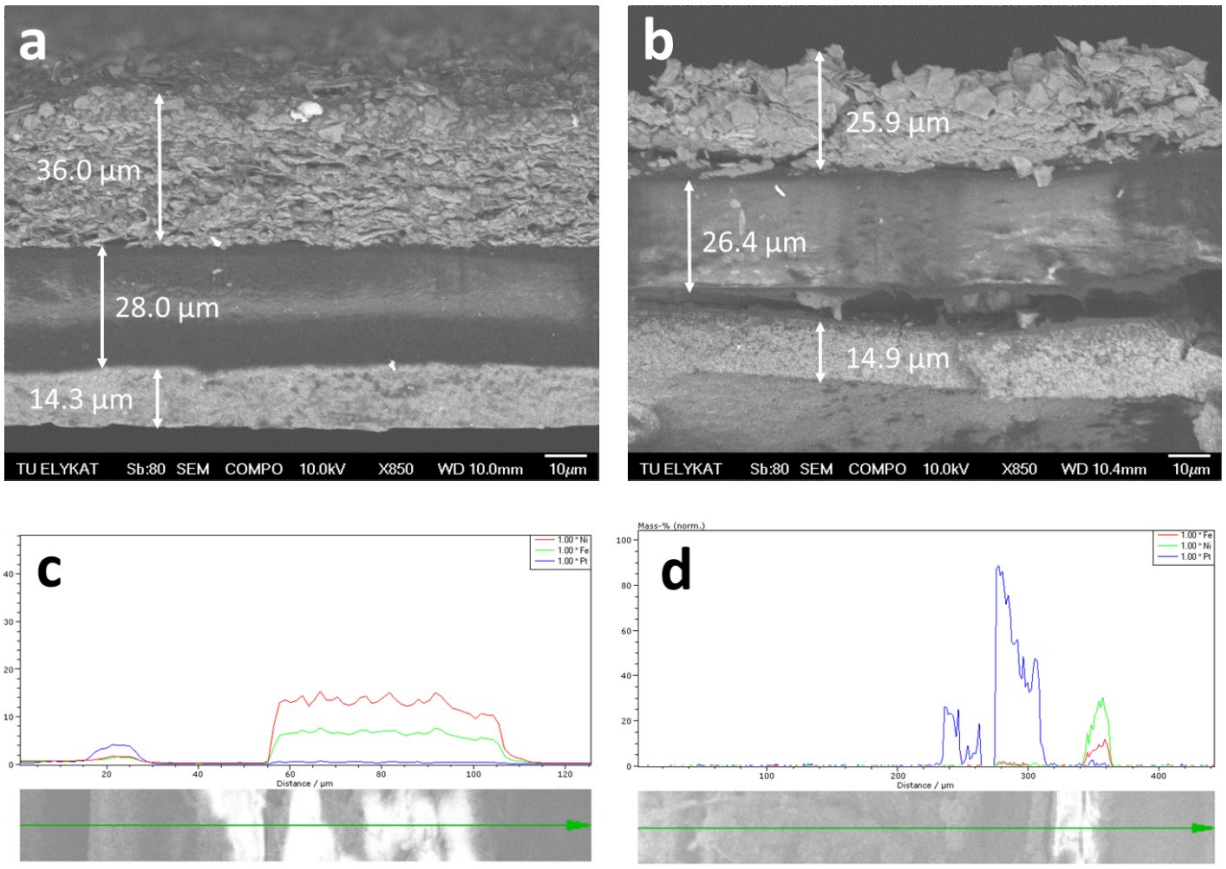

Figure S8: SEM cross-section image in compo mode of 2.5 mg cm^{-2} NiFe-LDH coated and 0.5 mg cm^{-2} coated Tokuyama A201 membrane (a-b) with the corresponding linescans **(a,c)** as prepared and **(b,d)** after 100 h at 1.6 V in 0.5 M KOH and 0.5 M NaCl. Note: linescans are not at the same magnification as the displayed cross-sections in order to include more of the PTL in the linescan

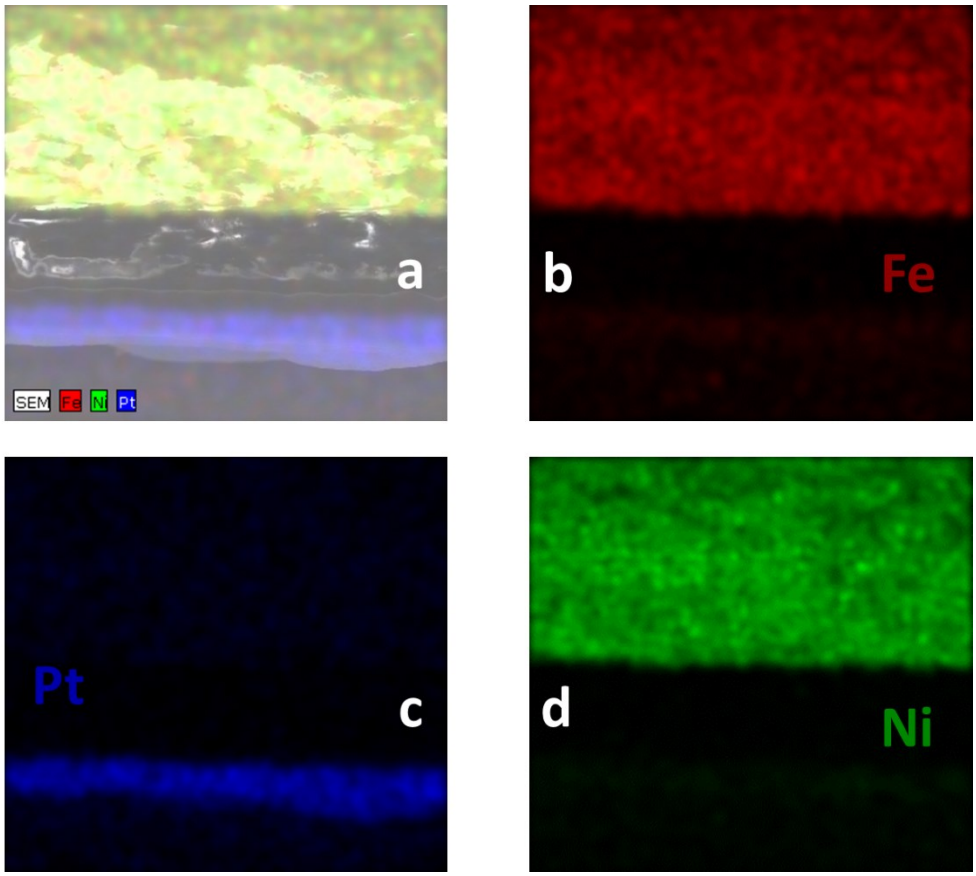

Figure S9: EDX mapping of an as prepared membrane electrode assembly (MEA) cross section with 2.5 mg cm^{-2} NiFe-LDH and 0.5 mg_{Pt} cm^{-2} 46.7 wt% Pt/C TKK catalyst

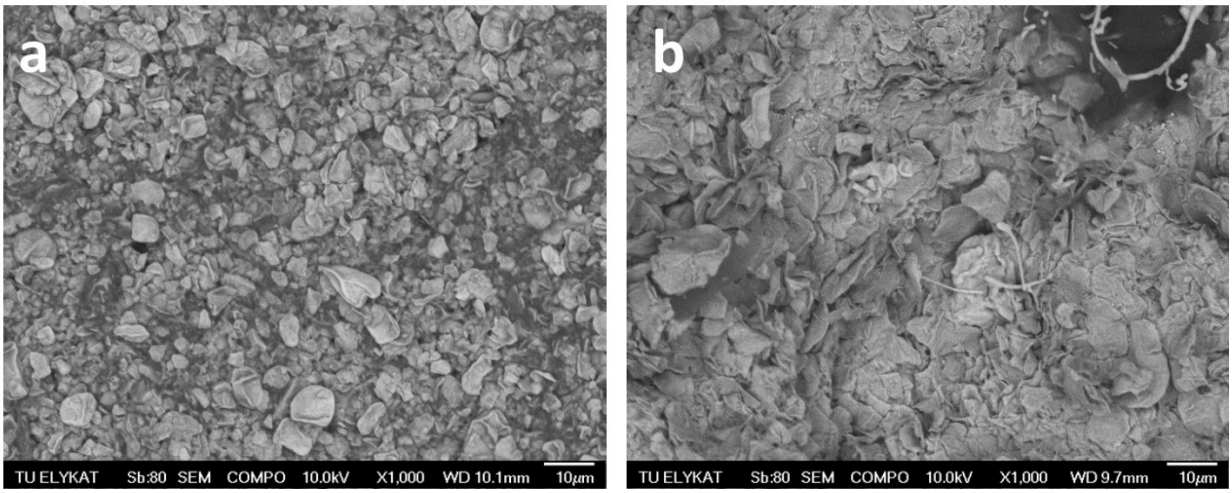

Figure S10: SEM image in compo mode of NiFe-LDH coated Tokuyama A201 membrane **(a)** as prepared and **(b)** after 100 h at 1.6 V in 0.5 M KOH and 0.5 M NaCl

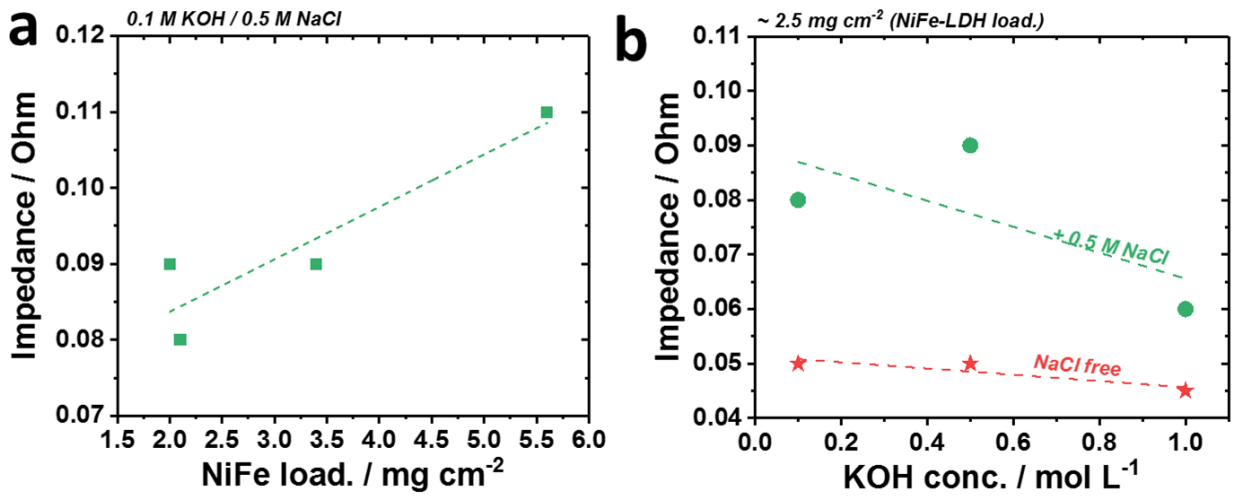

Figure S11: Impedance measurement of the electrolyzer cell after 100 h measurement at 1.6 V in different electrolyte compositions and catalyst loadings

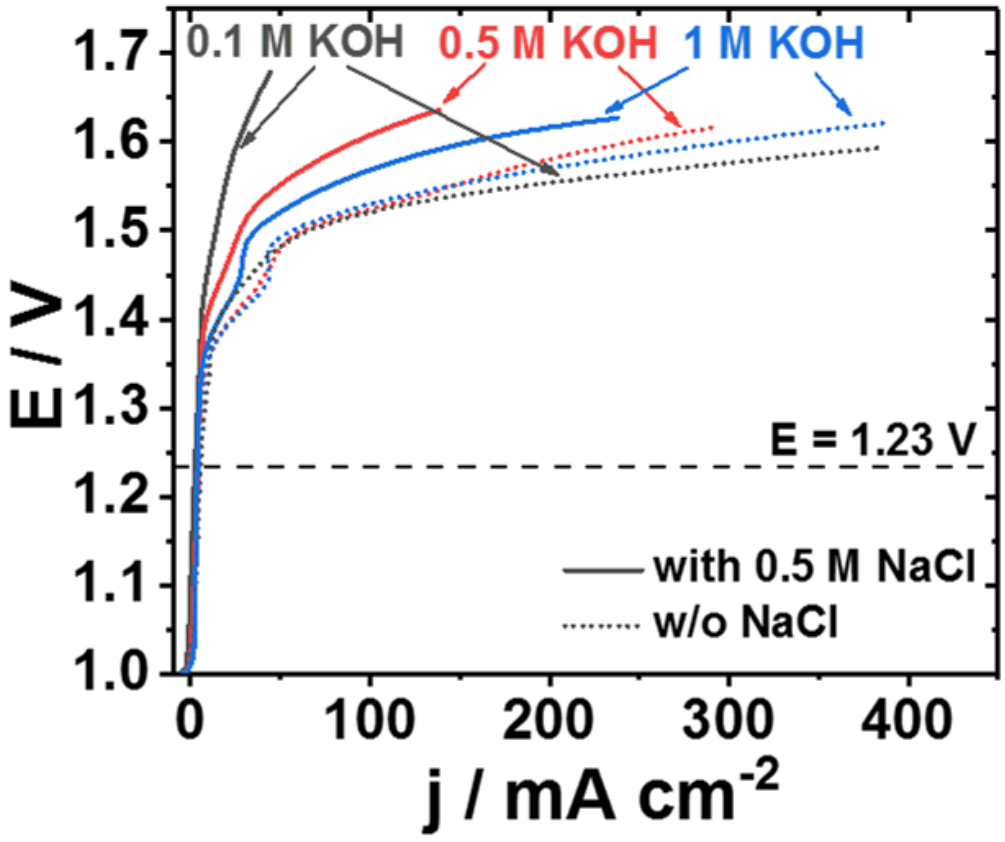

Figure S12: Polarization curves after 100 h in different electrolytes

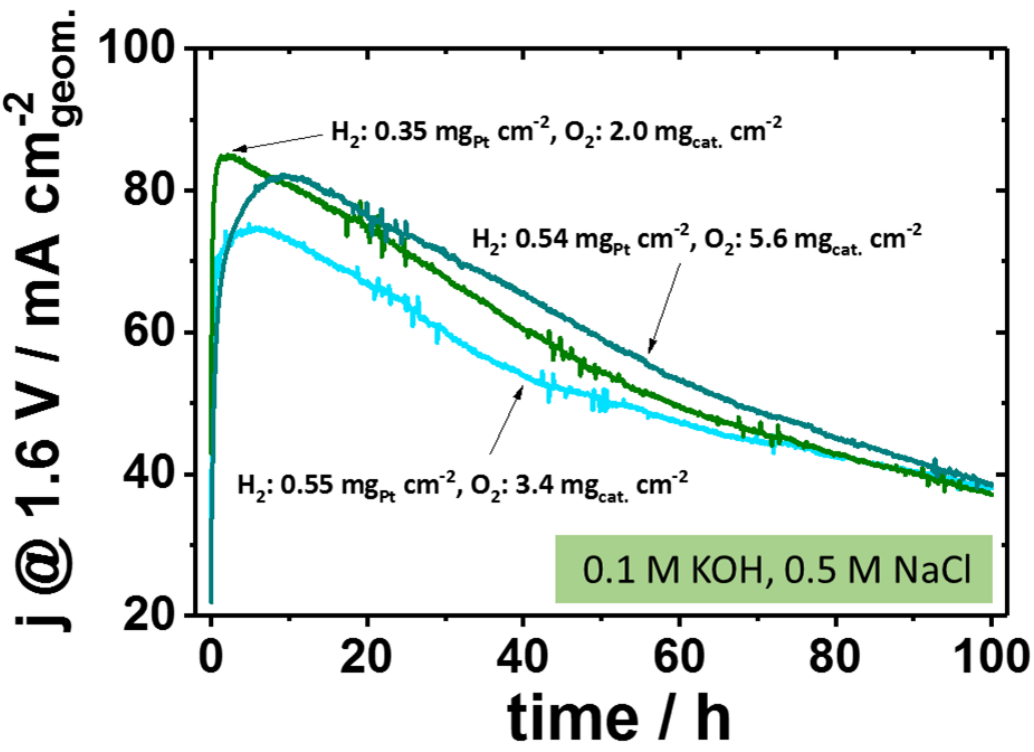

Figure S13: 100 h seawater electrolyzer measurement in 0.1 M KOH, 0.5 M NaCl with different catalyst loadings at the cathode (H_2) and anode (O_2)

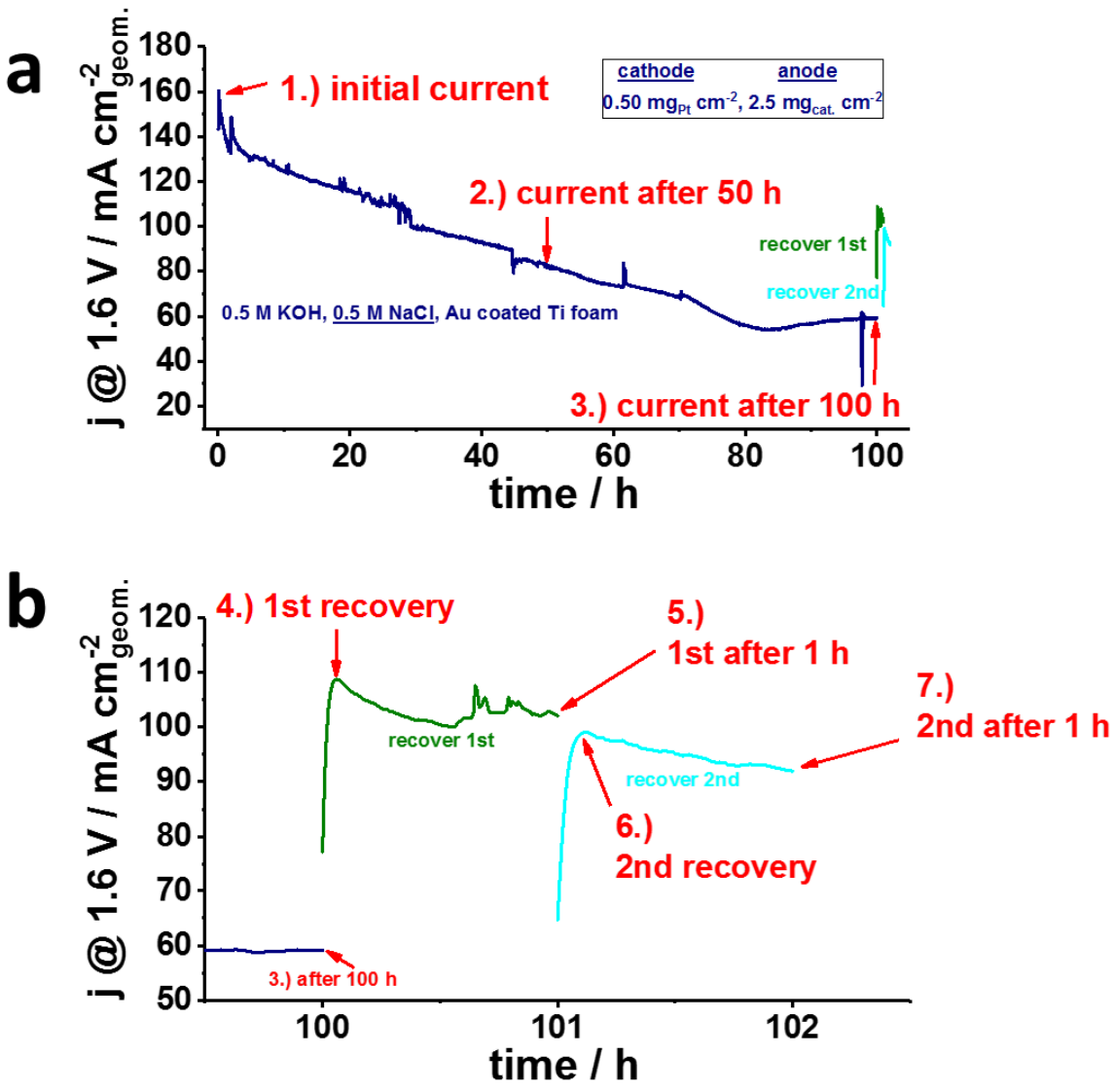

Figure S14: Recovery effect: (a) Determination of 100 h stability (b) Determination of recovery effect

Faradaic Efficiency calculations

The theoretical oxygen evolution stream $\dot{n}_{O_2}$ in [mol s^{-1}] for a 100 % faradaic efficiency was calculated using a modified faradaic equation (1) with z = 4 as the electrons transferred per ion; F = 96485.33 s A mol^{-1} as faradaic constant and I as the corresponding current in [A].:

$$\dot{n}_{O_2} = \frac{I}{z \cdot F} \tag{1}$$

The mass flow controlled N_2 stream (100 ml min^{-1}) is converted to a mole stream $\dot{n}_{N_2}$ in [mol s^{-1}] using a modified ideal Gas equation (2) with R = 8.314 kg m^2 s^{-2} mol^{-1} K^{-1} as ideal Gas constant; T = 298.15 K as Temperature; p = 101000 Pa as atmospheric pressure and $\dot{V}_{N_2}$ as the corresponding Volume stream in [m^3 s^{-1}]:

$$\dot{n}_{N_2} = \frac{\dot{V}_{N_2} \cdot p}{R \cdot T} \tag{2}$$

The obtained streams were used to obtain the theoretical gas concentrations in [%] for a 100 % faradaic efficiency using equation (3):

$$c_{gas_{theor.}}[\%] = \left(\frac{\dot{n}_{O_2}}{\dot{n}_{N_2} + \dot{n}_{O_2}}\right) \cdot 100 \tag{3}$$

The faradaic efficiency (FE) in [%] was calculated using the theoretical $c_{gas_{theor.}}$ and the nominal measured $c_{gas_{nominal}}$ in equation (4). The nominal gas concentration is the average value of the last 5 min of the 30 min step.

$$FE[\%] = \left(\frac{c_{gas_{nominal}}}{c_{gas_{theor.}}}\right) \cdot 100 \tag{4}$$

Cell Efficiencies

The cell efficiencies are calculated using equation (5):

$$\eta_{cell} = \left(\frac{U_{LHV\,or\,HHV}}{U_{Cell}} \right) x\, \eta_{farad.} \qquad (5)$$

Where $\eta_{farad.}$ is the determined faradaic efficiency that is equal to the current efficiency $U_{LHV\ or\ HHV}$ is the representative potential for the water splitting towards the lower heating value (1.25 V) or the higher heating value (1.48 V) and U_{cell} is the actual measured cell potential.

Table S1: Applied cell currents, faradaic efficiencies and corresponding cell potentials and cell efficiencies in respect to the lower heating value (LHV: 1.25 V) or the higher heating value (HHV:1.48 V) for the anode reaction in an electrolyzer using NiFe-LDH as anode and 46.7 wt% Pt/C as cathode material and a Tokuyama A201 as anion exchange membrane

I in [A]	$\eta_{farad.}$	**E_{cell} in [V] NaCl**	**E_{cell} w/o NaCl**	**η LHV NaCl**	**η LHV w/o NaCl**	**η HHV NaCl**	**η HHV w/o NaCl**
0.05	0.73	1.45	1.44	0.63	0.63	0.75	0.75
0.25	0.75	1.53	1.50	0.61	0.63	0.73	0.74
0.50	0.79	1.57	1.54	0.63	0.64	0.74	0.76
0.75	0.82	1.60	1.57	0.64	0.65	0.76	0.77
1.00	0.83	1.62	1.59	0.64	0.65	0.76	0.77
1.50	0.84	1.64	1.63	0.64	0.64	0.76	0.76
2.00	0.85	1.65	1.66	0.64	0.64	0.76	0.76
3.00	0.88	1.65	1.70	0.67	0.65	0.79	0.77

X-ray absorption spectroscopy

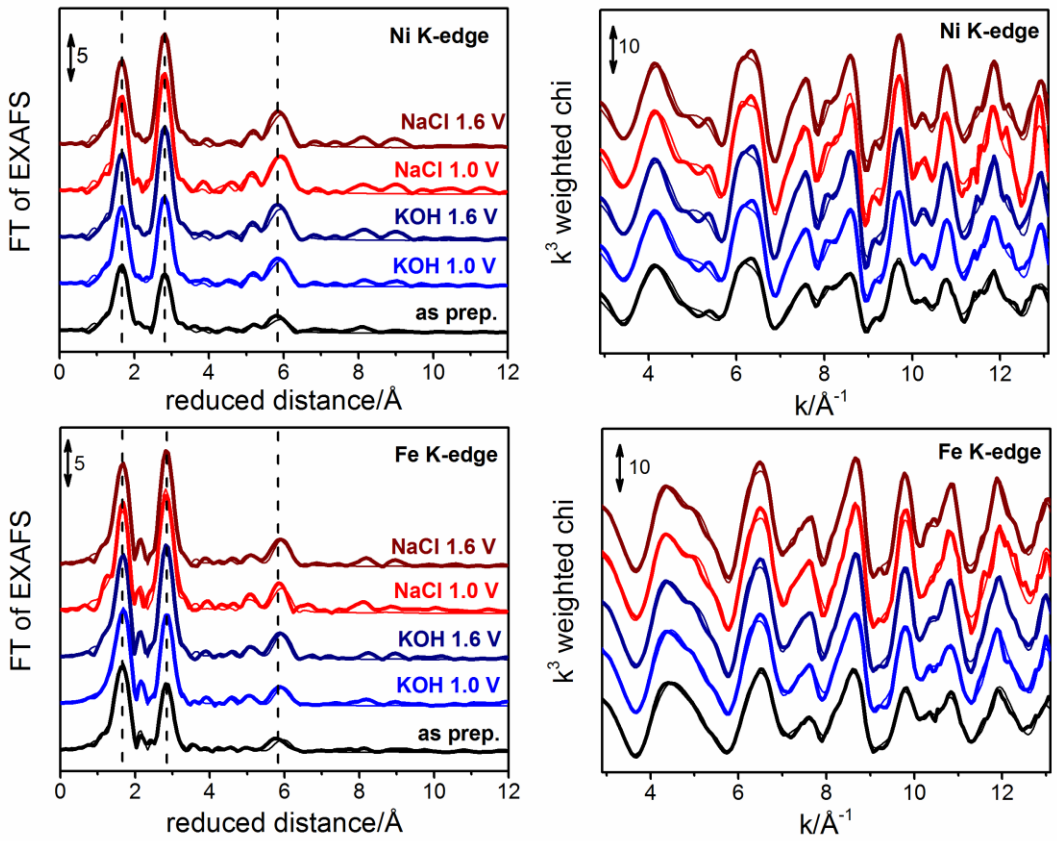

Figure S15: Fourier transforms (left) and k^3-weighted χ (right) EXAFS spectra of layered double hydroxides at the Ni and Fe K edge. Thin lines represent the simulation of the experimental data. Simulation parameters are given in table S3 and S4. A stacking of +10 (k^3-weighted χ) and +5 (FT) was used for clarity. Amplitudes for the FT and the k^3-weighted χ are indicated by the arrow inside the graphs.

EXAFS simulations

An EXAFS spectrum $\chi(k)$ is given by the sum of the contributions of n_{shell} 'atomic shells'. A 'shell' is a group of elements with identical atomic number and similar distances from the X-ray absorbing atom. The EXAFS equation is mathematically defined by the following equation:

$$\chi(k) = {S_o}^2 \sum_{i}^{n_{shell}} A(R_i, k)_i N_i \exp\left(-2{\sigma_i}^2 k^2\right) \sin(2kR_i + \phi_i)$$

where ${S_o}^2$ is the amplitude reduction factor, $A(R_i, k)_i$ is a factor that includes the scattering amplitude and mean-free-path of the photo-electron, ϕ_i the phase correction, N_i the number of atoms in the i^{th} atomic shell, σ_i the Debye-Waller parameter of the i^{th} atomic shell, and R_i the (average) distance between the X-ray absorbing atom and the atoms of the i^{th} atomic shell. The functions A and ϕ were obtained herein from ab-initio calculations using Feff 9.05[2], using coordinates from a fragment of the $Ni(OH)_2$ structure.

For conversion of the energy axis to a k-vector axis, an E_0 of 7112 eV (Fe) and 8333 eV (Ni) was used. Curve-fitting of the data was accomplished within a k-range of 3 $Å^{-1}$ to 13 $Å^{-1}$. The amplitude reduction factor, ${S_o}^2$, was 0.9. The error ranges of the fit parameters were estimated from the covariance matrix of the fit and represent the 68% confidence intervals (error calculations as described in reference b)). Cosine windows covering 10 % of the low k-side and 10 % of the high k-side of the spectra were applied before calculation of the Fourier transforms.

The average oxidation state of the absorbing atom was determined by calibration with reference compounds (assuming linear dependence of the energy of the edge position on the oxidation state in this range)[3].The edge position has been determined using a step integral method as described elsewhere[4-10].

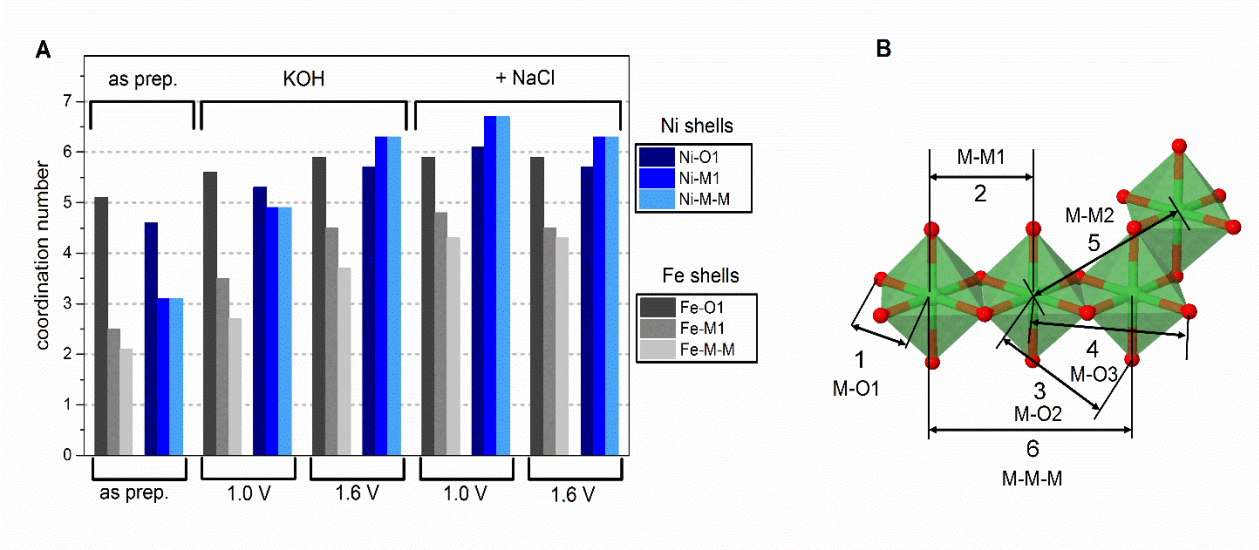

Figure S16: Coordination numbers of selected shells as provided from the EXAFS simulation (A) and assignment of structural motifs within the LDH-structure. The numbering of the distances in (B) refers to the number of the peaks in the FT in figure 7b.

Table S2: Edge positions and corresponding oxidation states deduced from the edge position of the Ni-K-edge and from EXAFS simulations (calculated oxidation state from the bond valence sum in parentheses)

sample	**edge position Fe/eV**	**oxidation state Fe (BVS)**	**edge position Ni/eV**	**oxidation state Ni (BVS)**
NiFe LDH as prep.	7125.1	3.2 (2.6)	8342.4	1.9 (1.7)
NiFe LDH 1.0 V KOH	7125.5	3.3 (2.8)	8342.7	2.1 (1.9)
NiFe LDH 1.6 V KOH	7125.7	3.3 (3.0)	8343.1	2.3 (2.1)
NiFe LDH 1.0 V NaCl	7125.7	3.3 (3.1)	8343.1	2.3 (2.2)
NiFe LDH 1.6 V NaCl	7125.6	3.3 (3.1)	8343.0	2.3 (2.1)

Table S3: Simulation parameters for EXAFS fitting at the Fe K-edge

sample	shell	R/Å	CN	σ/Å	R_f
	Fe-O1	2.01 ± 0.01	5.1 ± 0.2	0.0671*	
	Fe-M1	3.11 ± 0.01	**2.5 ± 0.2**	0.050*	
	Fe-O2	3.83 ± 0.06	1.7 ± 1.5	0.0671*	
as prepared	Fe-O3	4.82 ± 0.10	1.7 ± 3.0	0.0671*	15.5
	Fe-M2	5.38 ± 0.06	0.9 ± 0.7	0.050*	
	Fe-M-M	6.14 ± 0.06	2.1*	0.050*	
	Fe-M (ms)	3.05 ± 0.03	2.1*	0.050*	
	Fe-O1	2.02 ± 0.01	5.6 ± 0.2	0.0671*	
	Fe-M1	3.11 ± 0.01	3.5 ± 0.2	0.050*	
	Fe-O2	3.73 ± 0.04	2.2 ± 1.3	0.0671*	
KOH 1.0 V	Fe-O3	4.78 ± 0.06	2.9 ± 2.8	0.0671*	14.1
	Fe-M2	5.35 ± 0.02	1.8 ± 0.7	0.050*	
	Fe-M-M	6.15 ± 0.09	2.7*	0.050*	
	Fe-M (ms)	3.08 ± 0.02	2.7*	0.050*	
	Fe-O1	2.01 ± 0.01	5.9 ± 0.2	0.0671*	
	Fe-M1	3.11 ± 0.01	4.5 ± 0.2	0.050*	
	Fe-O2	3.73 ± 0.03	3.7 ± 1.4	0.0671*	
KOH 1.6 V	Fe-O3	4.77 ± 0.08	2.4 ± 2.9	0.0671*	12.0
	Fe-M2	5.38 ± 0.02	2.2 ± 0.8	0.050*	
	Fe-M-M	6.15 ± 0.08	3.7*	0.050*	
	Fe-M (ms)	3.08 ± 0.02	3.7*	0.050*	
	Fe-O1	2.00 ± 0.01	5.9 ± 0.2	0.0671*	
	Fe-M1	3.10 ± 0.01	4.8 ± 0.2	0.050*	
	Fe-O2	3.73 ± 0.02	4.5 ± 1.4	0.0671*	
+ NaCl 1.0 V	Fe-O3	4.78 ± 0.20	0.8 ± 2.9	0.0671*	16.8
	Fe-M2	5.37 ± 0.02	2.7 ± 0.8	0.050*	
	Fe-M-M	6.12 ± 0.09	4.3*	0.050*	
	Fe-M (ms)	3.06 ± 0.03	4.3*	0.050*	
	Fe-O1	2.01 ± 0.01	5.9 ± 0.2	0.0671*	
	Fe-M1	3.11 ± 0.01	4.5 ± 0.2	0.050*	
	Fe-O2	3.73 ± 0.03	3.5 ± 1.3	0.0671*	
+ NaCl 1.6 V	Fe-O3	4.76 ± 0.09	2.2 ± 2.9	0.0671*	12.4
	Fe-M2	5.38 ± 0.02	2.2 ± 0.8	0.050*	
	Fe-M-M	6.15 ± 0.07	4.3*	0.050*	
	Fe-M (ms)	3.08 ± 0.02	4.3*	0.050*	

* Debye Waller parameter (σ) that were fixed to the same value in the global fit approach. Unless indicated the Debye-Waller Parameter, coordination number (CN) and distances (R) were kept unrestricted. The CN for the M-M double distances were kept smaller or equal than the M-M CN. Cn for the multiple scattering contribution was fixed to be equal to the CN of the M-M double distance. R_f is the filtered R-factor (6.3 Å).

Table S4: EXAFS simulation parameters for the Ni K-edge (fitted k-range: 3-13 Å).

sample	shell	R/Å	CN	σ/Å	R_f
	Ni-O1	2.04 ± 0.01	4.6 ± 0.3	0.0707*	
	Ni-M1	3.08 ± 0.01	3.1 ± 0.2	0.0671*	
	Ni-O2	3.68 ± 0.04	2.6 ± 1.4	0.0707*	
as prepared	Ni-O3	4.82 ± 0.07	3.1 ± 3.3	0.0707*	17.0
	Ni-M2	5.38 ± 0.03	2.2 ± 1.1	0.0671*	
	Ni-M-M	6.16 ± 0.12	3.1*	0.0671*	
	Ni-M (ms)	3.10 ± 0.02	3.1*	0.0671*	
	Ni-O1	2.04 ± 0.01	5.3 ± 0.3	0.0707*	
	Ni-M1	3.08 ± 0.01	4.9 ± 0.2	0.0671*	
	Ni-O2	3.69 ± 0.03	3.4 ± 1.4	0.0707*	
KOH 1.0 V	Ni-O3	4.82 ± 0.05	4.3 ± 3.2	0.0707*	14.1
	Ni-M2	5.37 ± 0.02	3.3 ± 1.1	0.0671*	
	Ni-M-M	6.17 ± 0.07	4.9*	0.0671*	
	Ni-M (ms)	3.10 ± 0.01	4.9*	0.0671*	
	Ni-O1	2.04 ± 0.01	5.7 ± 0.3	0.0707*	
	Ni-M1	3.08 ± 0.01	6.3 ± 0.2	0.0671*	
	Ni-O2	3.70 ± 0.02	4.6 ± 1.4	0.0707*	
KOH 1.6 V	Ni-O3	4.82 ± 0.04	5.7 ± 3.2	0.0707*	12.0
	Ni-M2	5.37 ± 0.01	4.4 ± 1.1	0.0671*	
	Ni-M-M	6.17 ± 0.01	6.3*	0.0671*	
	Ni-M (ms)	3.10 ± 0.01	6.3*	0.0671*	
	Ni-O1	2.04 ± 0.01	6.1 ± 0.3	0.0707*	
	Ni-M1	3.08 ± 0.01	6.7 ± 0.2	0.0671*	
	Ni-O2	3.69 ± 0.03	3.8 ± 1.4	0.0707*	
+ NaCl 1.0 V	Ni-O3	4.81 ± 0.03	7.4 ± 3.2	0.0707*	17.3
	Ni-M2	5.36 ± 0.01	5.6 ± 1.1	0.0671*	
	Ni-M-M	6.18 ± 0.01	6.7*	0.0671*	
	Ni-M (ms)	3.11 ± 0.01	6.7*	0.0671*	
	Ni-O1	2.05 ± 0.01	5.7 ± 0.3	0.0707*	
	Ni-M1	3.08 ± 0.01	6.3 ± 0.2	0.0671*	
	Ni-O2	3.69 ± 0.02	4.2 ± 1.4	0.0707*	
+ NaCl 1.6 V	Ni-O3	4.82 ± 0.05	4.2 ± 3.2	0.0707*	12.6
	Ni-M2	5.38 ± 0.01	4.2 ± 1.1	0.0671*	
	Ni-M-M	6.18 ± 0.05	6.3*	0.0671*	
	Ni-M (ms)	3.11 ± 0.01	6.3*	0.0671*	

* Debye Waller parameter (σ) that were fixed to the same value in the global fit approach. Unless indicated the Debye-Waller parameter, coordination number (CN) and distances (R) were kept unrestricted. The CN for the M-M double distances were kept smaller or equal than the M-M CN. Cn for the multiple scattering contribution was fixed to be equal to the CN of the M-M double distance. R_f is the filtered R-factor (6.3 Å).

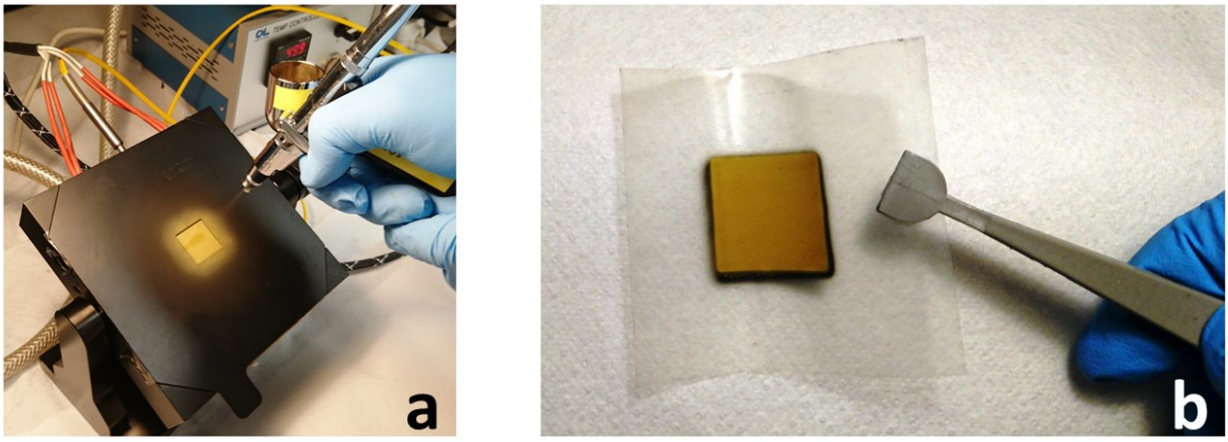

Figure S17: (a) Spraycoating method using a heatable vacuum table (50 °C), a protection mask (5 cm^2) and a Gun Piece SP-2 spray gun (Rich) equipped with a 0.4 mm tip (b) Catalyst coated membrane (CCM)

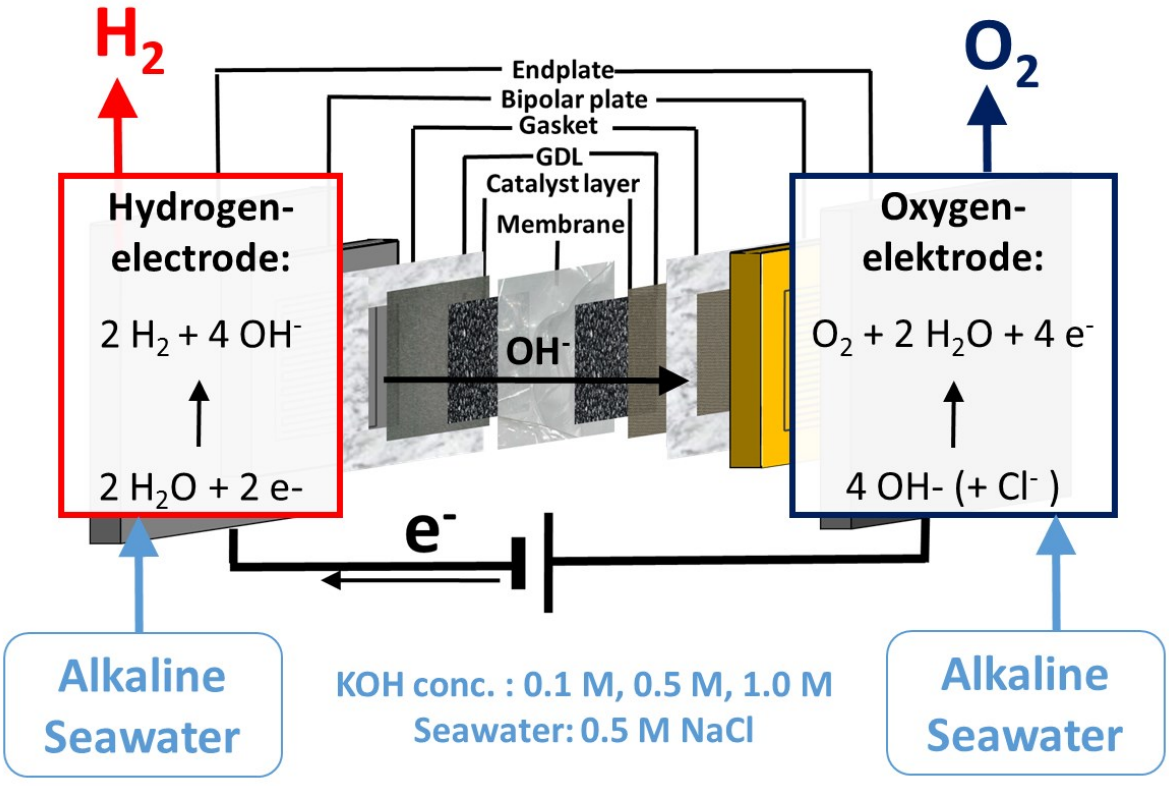

Figure S18: Sketch of alkaline seawater electrolyzer

References

1. E. Fontananova, W. Zhang, I. Nicotera, C. Simari, W. van Baak, G. Di Profio, E. Curcio and E. Drioli, *Journal of Membrane Science*, 2014, **459**, 177-189.
2. A. L. Ankudinov, B. Ravel, J. J. Rehr and S. D. Conradson, *Physical Review B*, 1998, **58**, 7565-7576.
3. M. Görlin, P. Chernev, J. Ferreira de Araújo, T. Reier, S. Dresp, B. Paul, R. Krähnert, H. Dau and P. Strasser, *Journal of the American Chemical Society*, 2016, **138**, 5603-5614.
4. H. Dau, P. Liebisch and M. Haumann, *Anal Bioanal Chem*, 2003, **376**, 562-583.
5. I. Zaharieva, P. Chernev, M. Risch, K. Klingan, M. Kohlhoff, A. Fischer and H. Dau, *Energy & Environmental Science*, 2012, **5**, 7081-7089.
6. A. Bergmann, I. Zaharieva, H. Dau and P. Strasser, *Energy & Environmental Science*, 2013, **6**, 2745-2755.
7. D. Shevchenko, M. F. Anderlund, S. Styring, H. Dau, I. Zaharieva and A. Thapper, *Phys. Chem. Chem. Phys.*, 2014, **16**, 11965-11975.
8. A. Bergmann, E. Martinez-Moreno, D. Teschner, P. Chernev, M. Gliech, J. F. de Araújo, T. Reier, H. Dau and P. Strasser, *Nature Communications*, 2015, **6**, 8625.
9. M. Risch, F. Ringleb, M. Kohlhoff, P. Bogdanoff, P. Chernev, I. Zaharieva and H. Dau, *Energy & Environmental Science*, 2015, **8**, 661-674.
10. I. Zaharieva, D. Gonzalez-Flores, B. Asfari, C. Pasquini, M. R. Mohammadi, K. Klingan, I. Zizak, S. Loos, P. Chernev and H. Dau, *Energy & Environmental Science*, 2016, **9**, 2433-2443.

IV. Simplified Microwave Assisted Solvothermal One Pot Synthesis of Highly Active Nickel-Iron Layered Double Hydroxide as Oxygen Evolution Reaction Catalyst

This section reprints the following paper

Dresp, S., *Strasser, P.**

ECS Transactions, **2016**, *75(14): p. 1113-1119. DOI: https://doi.org/10.1149/07514.1113ecst*

(7 pages)

ECS Transactions, 75 (14) 1113-1119 (2016)
10.1149/07514.1113ecst ©The Electrochemical Society

Simplified microwave assisted solvothermal one pot synthesis of highly active Nickel-Iron layered double hydroxide as oxygen evolution reaction catalyst

Sören Dresp[a], Peter Strasser[a]

[a] Department of Chemistry, Technische Universität Berlin, Berlin 10623, GERMANY

Nickel-Iron layered double hydroxides (NiFe-LDH), a known highly active material for the oxygen evolution reaction (OER) in alkaline media, needs better and simpler synthesis routes. Due to high energy efficiency of microwave heating, microwave assisted solvothermal synthesis could play a major role in environmental friendly synthesis routes. This approach could also be a key step for sustainable production of highly active materials like electro-catalysts. Therefore, we developed a simplified and shortened solvothermal microwave assisted one pot synthesis to produce highly active NiFe-LDH supported on Vulcan XC-72R. The synthesis was studied for reproducibility in loading, composition and activity using inductively coupled plasma optical emission spectrometry (ICP-OES), X-ray diffraction and rotating ring disk electrodes (RDE) in a three electrode set-up.

Introduction

For a world based on sustainable energy coupled with its cycles of energy consumption and production many problems remain unsolved. One persisting challenge is saving the surplus electricity produced by renewable energy sources like wind and solar power. An approach is storing the excess energy in water electrolyzers, and electrochemically split water into hydrogen and oxygen ($H_2O \rightarrow O_2 + H_2$). The reaction mechanism in alkaline media is divided into a 4e- oxygen evolution reaction (OER) at the anode [1] and a $2e^-$ hydrogen evolution reaction (HER) at the cathode [2] (1):

$$\text{OER:} \quad 4OH^- \rightarrow O_2 + H_2O + 4e^- \quad [1]$$

$$\text{HER:} \quad 2H_2O \rightarrow H_2 + 2OH^- + 2e^- \quad [2]$$

The produced hydrogen serves as energy carrier and can be used vice versa in fuel cells to produce electricity. But the proposed hydrogen economy (2) still poses major problems in terms of catalyst materials. It is necessary to develop cheap, highly active and stable materials for these reactions. Especially OER catalysis remains a challenge due to sluggish 4 e^- kinetics (3). However, one of the most promising materials in alkaline media is Nickel-Iron layered double hydroxide (NiFe-LDH). This material is already widely investigated, but it is synthesized primarily by electro-deposition or other time consuming synthesis routes (4-7). In contrast, microwave assisted solvothermal synthesis routes are known to be highly efficient and environmental friendly, since the energy transfer is much more efficient (8). This could be a key step to synthesize new and highly active catalyst materials in a sustainable way.

This study presents a simple, fast and reproducible microwave assisted solvothermal synthesis route to produce highly active NiFe-LDH supported on Vulcan XC72R.

Experimental

Synthesis of NiFe-LDH / C

Inspired by Hongjie Dai (5), we prepared highly OER active NiFe-LDH supported on Vulcan XC-72r by a simplified and shortened microwave assisted solvothermal one pot synthesis route, as shown in Figure 1.

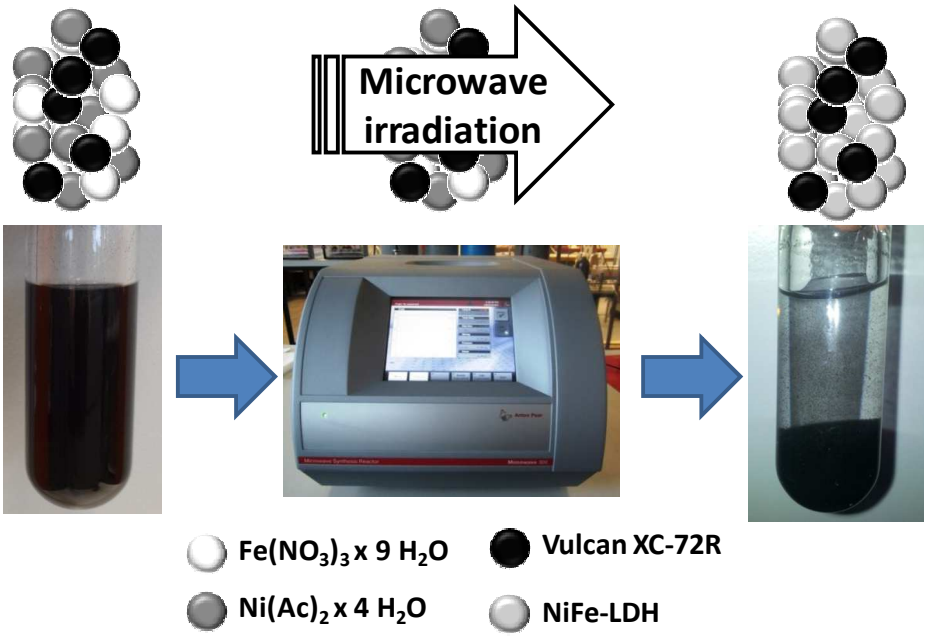

Figure 1. Synthesis scheme of NiFe-LDH / C. Before the microwave treatment of the mixture of Vulcan XC72R, $Ni(OAc)_2$ x 4 H_2O, $Fe(NO_3)_3$ x 9 H_2O in DMF and water it was stirred for 4 h at 80 °C.

Initially, we dispersed 6 mg Vulcan XC-72R for a high loading (hl) and 23 mg for a low loading (ll) sample in 6 ml Dimethylformamid (DMF) for 15 min using an ultra-sonication bath. Then, 1200 µl 0.2 M $Ni(OAc)_2$ x 4 H_2O (Sigma Aldrich, 99.998 %) for hl- and 330 µl for ll-sample and 240 µl 0.2 M $Fe(NO_3)_3$ x 9 H_2O (Alfa Aesar, 98.0 - 101 %) for hl- and 70 µl for ll-samples were added to the dispersion. After stirring for 4 h at 80 °C 8 ml H_2O and 4 ml DMF were added to the solution. The mixture is then heated using a microwave (Anton Paar Monowave 300) to 120 °C for 60 min and subsequently heated to 160 °C and held for 30 min. The product was then collected in a centrifuge at 8500 rpm and washed several times with ultrapure water and ethanol.

Elemental Analysis by Inductively Coupled Plasma Optical Emission Spectrometry (ICP-OES)

The metal content was determined by inductively coupled plasma optical emission spectrometry (ICP-OES) using a Varian 715-ES spectrometer with a CCD detector. The sample were digested in a mixture of concentrated HNO_3:H_2SO_4:HCl in a ratio of 1:1:3 using a Discover SP-D Plus microwave. The concentrated acid digestion was subsequently diluted with ultrapure water (18 mΩ).

Crystal Structure Analysis by X-ray Diffraction (XRD)

The crystal structure was determined by x-ray diffraction using a Bruker D8 advance powder diffractometer (Bragg-Brentano geometry) equipped with a Cu K_a source, a variable divergence slit and a Lynx eye detector. The divergence slit was set to 6 mm, the anti-scattering slit to 6° and the Lynx-Iris to 10 mm. Data were recorded between 10° to 70° 2Ѳ with a step size of 0.039°.

Electrochemical Characterization by Rotating Disc Electrode Measurement (RDE)

Electrochemical measurement was determined by rotating disk measurement using a Biologic SP 200 in a three electrode set-up consisting of a Pt-mesh as counter electrode, RHE as reference electrode and a glassy carbon (d = 0.5 mm) as working electrode. All measurements were conducted in N_2 saturated 0.1 M KOH. The catalyst loading was 0.2 mg cm^{-2} using a drop coating method. The ink consists of Nafion, i-Propanol and water in a ratio of 4:25:96 to aim a final concentration of 4 $mg_{cat.}$ ml^{-1}. All electrochemical measurements are iR-corrected and in respect to the RHE potential scale.

Results and Discussion

In this study we prepared NiFe-LDH supported on Vulcan XC-72R using a simple microwave assisted solvothermal synthesis route. As shown in Figure 2A the layered double hydroxide structure is confirmed by x-ray diffraction. The diffraction pattern can be compared to hydrotalcite structure (JCPDS: 00-014-0191), but with slightly higher interlayer distances. ICP-OES revealed high reproducibility towards the metal loading of the catalyst as presented in Figure 2B.

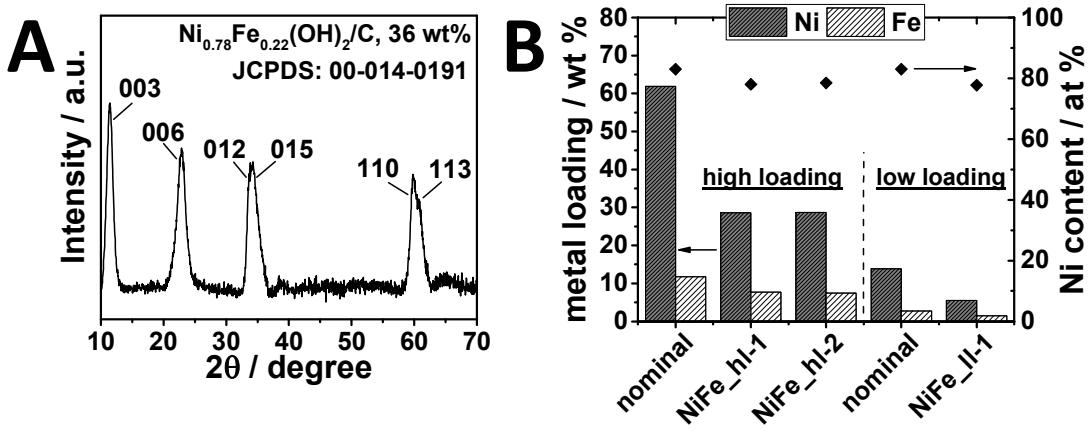

Figure 2. Results of the NiFe-LDH / C samples **(A)** x-ray diffraction pattern of NiFe-LDH / C and **(B)** ICP-OES date of different synthesis batches of NiFe-LDH high loading (NiFe-hl) and low loading (NiFe-ll)

As expected, we see a loss of about 50 % in metal loading on Vulcan XC-72R. For the high loading (hl), the nominal value of 74 wt% is reduced to 36 wt%, and for the low loading (ll) 17 wt% to 7 %. This metal loss is explained by incorporating oxygen in the crystal structure. The larger reduction in loading for the ll-sample might indicate a higher oxygen incorporation level, since at lower concentrations the layered double hydroxides

are more accessible. The ratio of Ni and Fe, however, remained constant at about 3.5 or $Ni_{0.78}Fe_{0.22}$.

We tested the electrochemical properties using rotating ring disk electrode (RDE) measurements in N_2 saturated 0.1 M KOH at 1600 rpm as shown in Figure 3.

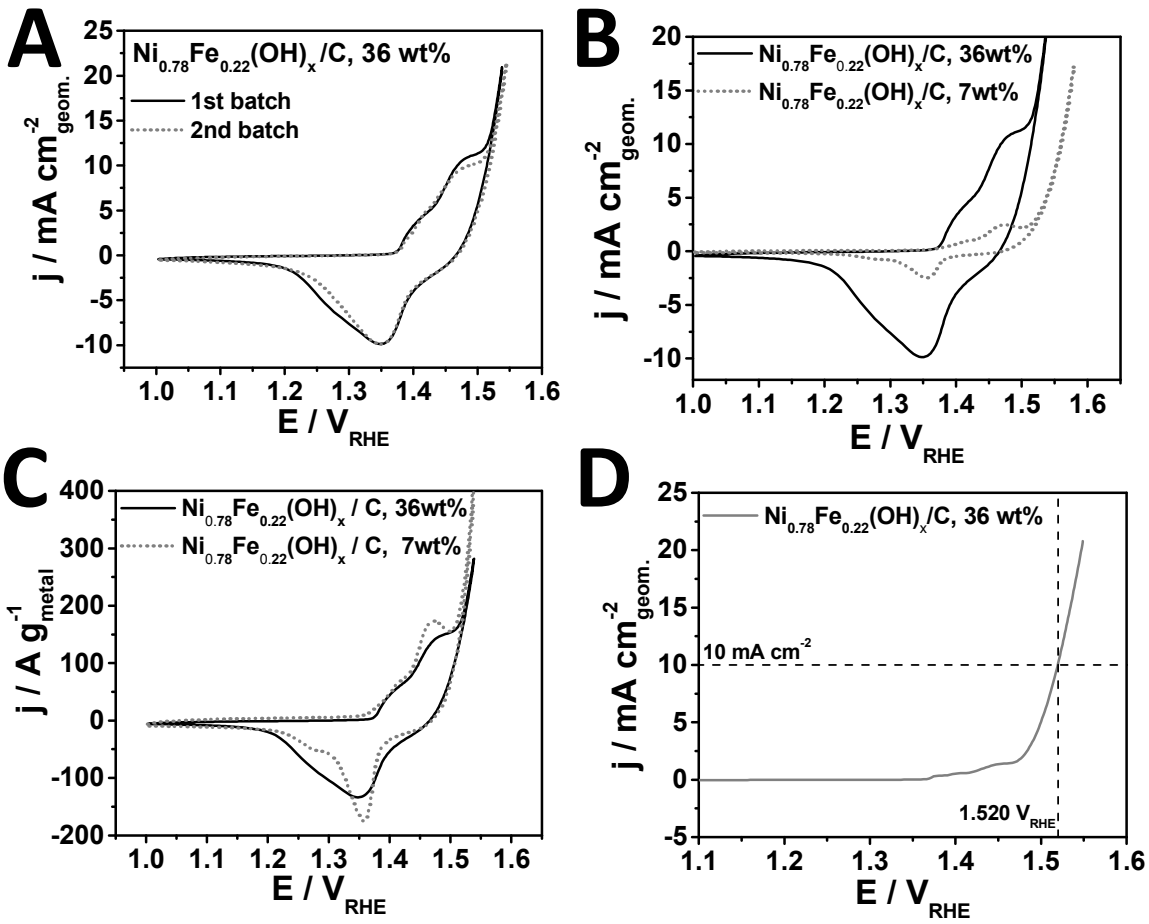

Figure 3. RDE measurement of different NiFe-LDH / C batches in N_2 saturated 0.1 M KOH at 1600 rpm and 0.2 mg cm^{-2} catalyst loading **(A)** Cyclic voltammogram of the 50's cycle with a scan rate of 50 mV/S of the first and the second batch **(B)** cyclic voltammogram of the 50's cycle with a scan rate of 50 mV/s of the high loading and the low loading sample normalized to the geometric surface area **(C)** cyclic voltammogram with a scan rate of 50 mV/s of the high loading and the low loading sample normalized to the metal mass (D) Linear sweep voltammogram after the activation cycles with a scan rate of 5 mV/s

The redox behaviour of NiFe-LDH system is well known: in 1987, Corrigan et al. investigated the influence of the oxygen evolution on nickel electrodes in alkaline electrolytes with iron impurities (9-11). Current research is more focused on revealing the active site for OER using techniques such as synchrotron radiation beam and conductivity measurements (12-15) The redox peaks in the cyclic voltammogram (CV) in Figure 3 are attributed to the Ni^{2+} /$Ni^{3+/4+}$ system. The real oxidation state of Nickel during OER is a matter of debate in the scientific community (13).

The various NiFe-LDH / C samples showed excellent reproducibility. The shape of the CVs in Figure 3A are similar showing good batch-to-batch reproducibility. In Figure 3B the CV of the NiFe-LDH /C 7 wt% shows a similar shape to the 36 wt%, but with current of significantly lower magnitude. If the current is normalized to metal loading, as shown in Figure 3C, the CVs are much more similar, but the higher loading sample is smoother. The smoothness may be due to better accessibility of surface sites on the low loading sample. The better accessibility may result in an easier interaction of the catalyst at the three phase boundary. Higher loadings would result consequently in a higher chemical inertia, although the overall OER mass activity is the same.

In Figure 3D linear sweep voltammetry at low scan rates (5 mV/s) demonstrates the expected promising geometric OER activity. In respect to 1.23 V OER standard potential, the overpotential of the material is only $\eta = 290$ mV. The high OER activity is of course already known for this material which is claimed to be one of the most OER active materials in alkaline media (16).

To study the stability we carried out galvanostatic measurement at 5 mA cm^{-2} as presented in Figure 4. Every hour the measurement was stopped to measure a CV and an impedance measurement. After this the galvanostatic measurement was started again. In contrast to the usual 10 mA cm^{-2} a low current density of 5 mA cm^{-2} was chosen to avoid strong bubble formation.

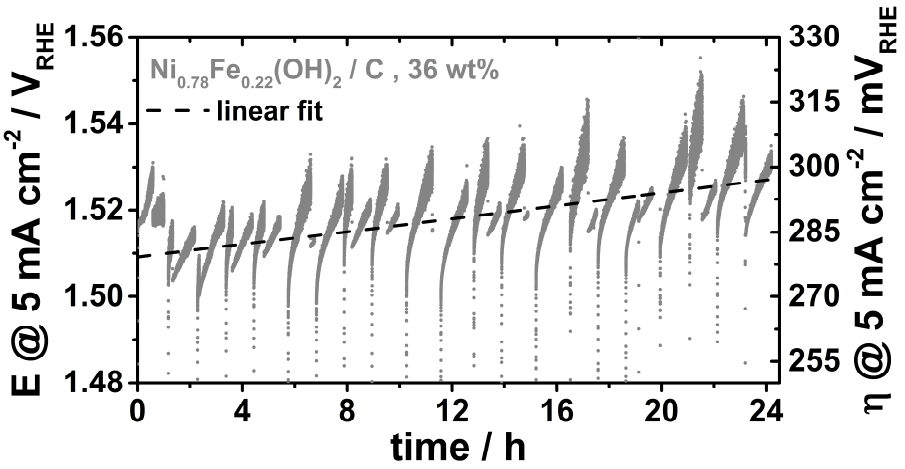

Figure 4. Stability measurement of NiFe-LDH / C 36wt% in N_2 saturated 0.1 M KOH at 1600 rpm and a cat loading of 0.2 mg cm^{-2}; After every hour the measurement was stopped to measure the impedance at open circuit potential and cyclic voltammogram.

The stability of the sample is, however, relatively stable in a range of 15 mV, although the overpotential at 5 mA cm^{-2} is obviously constantly decreasing over time. But interestingly a reactivation of the NiFe-LDH / C material after each stop is discovered. After a CV and impedance measurement the overpotential dropped and a reactivation takes place. This activity recovery was already discovered by Grätzel et al. (17). Furthermore, the strongest activity increase is presented after an initial phase of 2 hours. An additionally activity decrease could also be related to bubble formation at the electrode surface. After bubble removal the activity immediately recovers as well. This phenomenon was also presented by Zhao et al. (18). To determine the overall change of

the overpotential we include a linear fit to the longtime measurement. This fit results in an overall activity loss of 17 mV in 24 h including 24 start/stop cycles.

Conclusion

In conclusion we presented a simple and fast route to produce highly active NiFe-LDH supported on Vulcan XC-72R. The synthesis was highly reproducible for metal loading and atomic composition. Furthermore, the OER activities in N_2 saturated 0.1 M KOH of different batches are compatible. The materials synthesized by this synthesis route also showed consistent mass activity for a wide range of metal loading. This work also characterized the high stability of the materials. It was observed, that when the OER measurement is stopped, the activity recovers to the initial activity. However, after 24 h and 24 start/stop cycles the overpotential increased by 17 mV.

Acknowledgments

Financial support by the German Research Foundation (DFG) through grant reference number STR 596/8-1 and the Federal Ministry of Education and Research (BMBF) grant 03SF0433A ‘‘MEOKATS’’ are grateful acknowledged.

References

1. J. Rossmeisl, A. Logadottir and J. K. Norskov, *Chemical Physics*, **319**, 178 (2005).
2. M. Ball and M. Weeda, *International Journal of Hydrogen Energy*, **40**, 7903 (2015).
3. H. Dau, C. Limberg, T. Reier, M. Risch, S. Roggan and P. Strasser, *Chemcatchem*, **2**, 724 (2010).
4. F. Dionigi, T. Reier, Z. Pawolek, M. Gliech and P. Strasser, *ChemSusChem*, **9**, 962 (2016).
5. M. Gong, Y. Li, H. Wang, Y. Liang, J. Z. Wu, J. Zhou, J. Wang, T. Regier, F. Wei and H. Dai, *Journal of the American Chemical Society*, **135**, 8452 (2013).
6. M. S. Burke, L. J. Enman, A. S. Batchellor, S. Zou and S. W. Boettcher, *Chemistry of Materials*, **27**, 7549 (2015).
7. L. Trotochaud, J. K. Ranney, K. N. Williams and S. W. Boettcher, *Journal of the American Chemical Society*, **134**, 17253 (2012).
8. J. Zhao and W. Yan, in *Modern Inorganic Synthetic Chemistry*, R. Xu, W. Pang and Q. Huo Editors, p. 173, Elsevier, Amsterdam (2011).
9. D. A. Corrigan, *Journal of the Electrochemical Society*, **134**, 377 (1987).
10. D. A. Corrigan and R. M. Bendert, *Journal of the Electrochemical Society*, **136**, 723 (1989).
11. D. A. Corrigan and S. L. Knight, *Journal of the Electrochemical Society*, **136**, 613 (1989).
12. L. Trotochaud, S. L. Young, J. K. Ranney and S. W. Boettcher, *Journal of the American Chemical Society*, **136**, 6744 (2014).
13. M. Görlin, P. Chernev, J. Ferreira de Araújo, T. Reier, S. Dresp, B. Paul, R. Krähnert, H. Dau and P. Strasser, *Journal of the American Chemical Society*, **138**, 5603 (2016).

14. D. Friebel, M. W. Louie, M. Bajdich, K. E. Sanwald, Y. Cai, A. M. Wise, M.-J. Cheng, D. Sokaras, T.-C. Weng, R. Alonso-Mori, R. C. Davis, J. R. Bargar, J. K. Nørskov, A. Nilsson and A. T. Bell, *Journal of the American Chemical Society*, **137**, 1305 (2015).
15. M. Görlin, M. Gliech, J. F. de Araújo, S. Dresp, A. Bergmann and P. Strasser, *Catalysis Today*, **262**, 65 (2016).
16. C. C. L. McCrory, S. Jung, J. C. Peters and T. F. Jaramillo, *Journal of the American Chemical Society*, **135**, 16977 (2013).
17. J. Luo, J.-H. Im, M. T. Mayer, M. Schreier, M. K. Nazeeruddin, N.-G. Park, S. D. Tilley, H. J. Fan and M. Grätzel, *Science*, **345**, 1593 (2014).
18. X. Lu and C. Zhao, *Nat Commun*, **6**, 6616 (2015).

V. Direct electrolytic splitting of seawater – Opportunities and challenges

This section reprints the following paper

***Dresp, S.**, Dionigi F., Klingenhof, M., Strasser, P,*

ACS Energy Letters, 2019, 4, 933-942, DOI: https://doi.org/10.1021/acsenergylett.9b00220

(24 pages)

ACS Energy LETTERS

Cite This: ACS Energy Lett. 2019, 4, 933−942

http://pubs.acs.org/journal/aelccp

PERSPECTIVE

Direct Electrolytic Splitting of Seawater: Opportunities and Challenges

Sören Dresp, Fabio Dionigi, Malte Klingenhof, and Peter Strasser*

Department of Chemistry, Chemical Engineering Division, Technical University Berlin, Straße des 17. Juni 124, 10623 Berlin, Germany

Supporting Information

ABSTRACT: Hot, coastal, hyper-arid regions with intense solar irradiation and strong on- and off-shore wind patterns are ideal locations for the production of renewable electricity using wind turbines or photovoltaics. Given ample access to seawater and scarce freshwater resources, such regions make the direct and selective electrolytic splitting of seawater into molecular hydrogen and oxygen a potentially attractive technology. The key catalytic challenge consists of the competition between anodic chlorine chemistry and the oxygen evolution reaction (OER). This Perspective addresses some aspects related to direct seawater electrolyzers equipped with selective OER and hydrogen evolution reaction (HER) electrocatalysts. Starting from a historical background to the most recent achievements, it will provide insights into the current state and future perspectives of the topic. This Perspective also addresses prospects of the combination of direct seawater electrolysis with hydrogen fuel cell technology (reversible seawater electrolysis) and discusses its suitability as combined energy conversion−freshwater production technology.

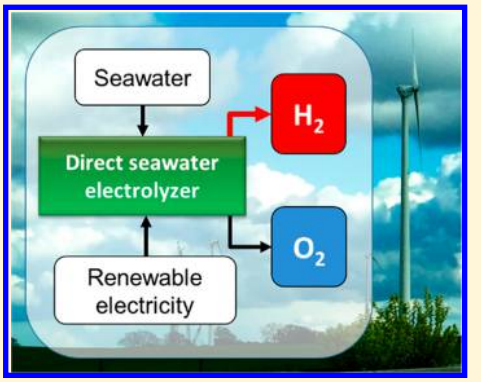

To combat climate change and secure energy for our planet, the concept of the hydrogen economy has been extensively discussed as one possible future scenario, in which renewable electricity combined with water electrolyzers may one day produce ample amounts of molecular or chemically bound hydrogen as primary or intermediate energy vectors. Hydrogen as a sustainable energy carrier can be further converted either electrochemically in hydrogen fuel cells or thermochemically in chemical reactors for the production of synthetic fuels, like methane, methanol, or synthetic higher hydrocarbons or oxygenates. For the purpose of electrolytic hydrogen production, scientists have been pursuing a set of different technologies in order to increase the electrolyzer performance and lower their overall costs, such as the quite mature liquid-electrolyte alkaline electrolysis, the high-temperature solid oxide electrolysis, the emerging proton exchange membrane (PEM) electrolysis, and the still quite immature anion exchange membrane (AEM) electrolysis.[1−3] The two things these electrolyzers have in common are the cathode where the hydrogen evolution reaction (HER) occurs and the anode for the oxygen evolution reaction (OER).

One of the less-discussed requirements of low-temperature water electrolyzer technologies is the availability of highly pure water feeds. While readily available in the laboratory, larger quantities of freshwater feeds may become a bottleneck if hydrogen electrolyzer technology will be deployed more widely in hot arid regions around the world that have limited access to freshwater yet plenty of access to ocean seawater. Seawater and the oceans represent 96.5% of the total water reserves of the planet,[4] which is why seawater, unlike freshwater, is an almost unlimited resource. Coastal Arid zones of the world possess both the potential for ample photovoltaic electricity and the potential for ample wind power-based electricity. This is why they could become preferred locations for production of electrolytic hydrogen from renewable electricity. The world's arid desert regions are located in the Middle East, South Africa, the west coast of the Americas, Australia, and the west of China, while coastal wind power is concentrated at the north coast of Europe, south coast of Alaska, the tip of South America, Greenland, and some other small coastal sections in Australia and Asia. This calls

While readily available in the laboratory, larger quantities of freshwater feeds may become a bottleneck if hydrogen electrolyzer technology will be deployed more widely in hot arid regions around the world that have limited access to freshwater yet plenty of access to ocean seawater.

Received: January 29, 2019
Accepted: March 19, 2019
Published: March 19, 2019

DOI: 10.1021/acsenergylett.9b00220
ACS Energy Lett. 2019, 4, 933−942

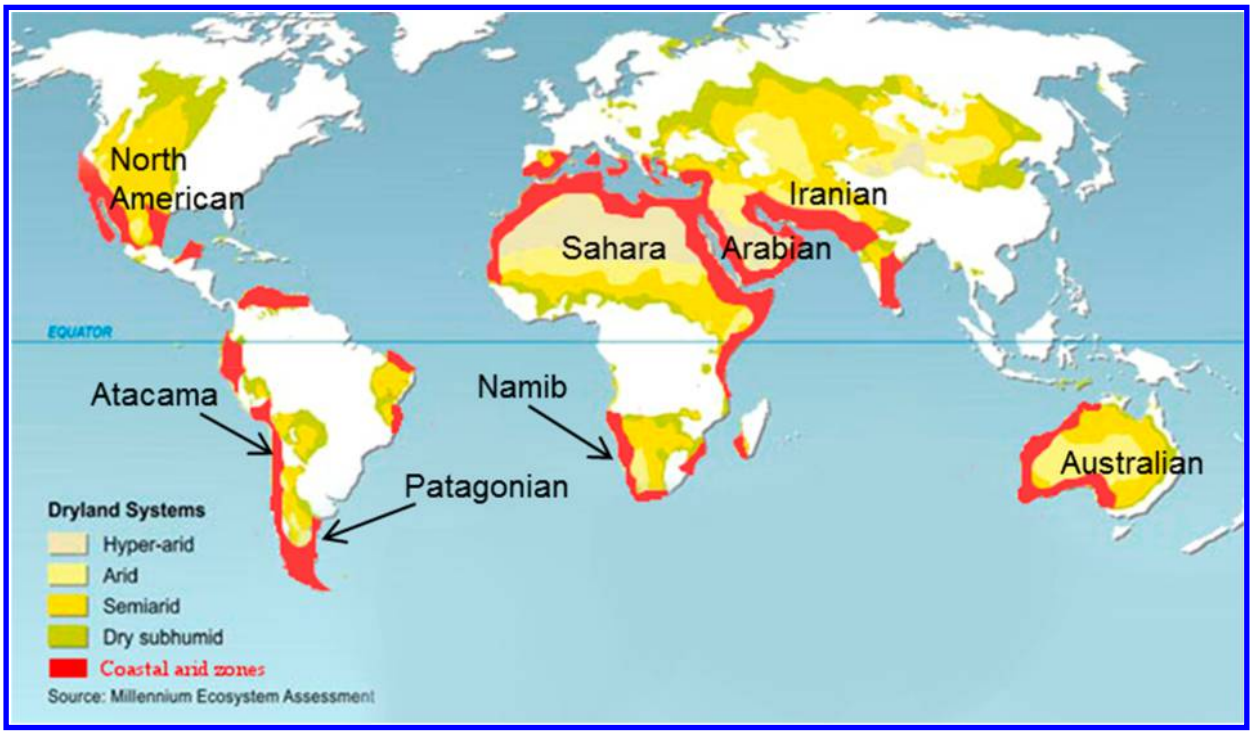

Figure 1. Dryland areas of the earth highlighting the coastal arid zones in red. Reprinted and modified with permission from ref 5. Copyright 2005 World Resources Institute.

for the generation of hydrogen directly from seawater using surplus renewable electricity of arid desert zones located near ocean coastlines, as shown in Figure 1.

The deep-red areas represent coastal hyper-arid or arid zones[6] where direct seawater electrolysis would be the most suitable and effective technology for solar hydrogen production. While available in ample amounts in the red areas of Figure 1, seawater is not a suitable feed for current electrolyzer technologies, because it contains electrochemically active anions that would interfere and compete with the water-splitting electrocatalysis. Table 1 shows the typical composition of ocean seawater species with the corresponding redox reactions and the electrochemical standard potential E^0 at alkaline and acidic pH.

Although the composition of seawater varies from region to region, the average overall salt concentration of all ions ranges at about 3.5 wt % with pH ∼ 8.[9−12] Taking into account all ions with their corresponding standard redox potentials from Table 1, the oxidation of bromide and chloride would compete with the oxidation of water. However, the low concentration of Br^- means its competing oxidation is typically neglected as a first approximation and in comparison with chloride oxidation in seawater electrolyzer studies. Clearly, the dominant ions are Na^+ and Cl^-, which is why an aqueous 0.5 M NaCl solution can be considered a reasonable surrogate of natural seawater.

Oxidation of Seawater: OER versus ClER. Early work on selective electrolysis of seawater into hydrogen and oxygen was conducted by Bennett.[13] Interested in a selective working electrolyzer anode, he conducted electrolysis in unbuffered seawater and showed a predominance of the chlorine evolution reaction (ClER: $2\,Cl^- \rightarrow Cl_2 + 2e^-$) at realistic larger current densities. The desired OER (OER: $2H_2O \rightarrow O_2 + 4\,H^+ + 4\,e^-$) was dominant only at current densities below 1 mA cm^{-2} or at very high current densities in which ClER mass-transfer limitations become noticeable which, in turn, favor the OER. This is shown in Figure 2a.

Bennet used a porous manganese-based electrode, which he estimated as an ideal candidate for selective OER using acidic seawater as electrolyte.[13] Seventeen years later, in 1997, Hashimoto and co-workers started to investigate selective OER electrodes using initially a low-pH 0.5 M NaCl electrolyte.[16] The, they modified manganese-based electrode materials and gained high oxygen efficiencies while testing their catalyst in 0.5 M NaCl at pH 8. However, in later work they focused on selective OER at pH 1, but similarly to Bennett, Hashimoto and co-workers choose comparably low current densities of 1 mA cm^{-2}.[16−25] At higher currents of 100 mA cm^{-2}, El-Monheim tested an electrode made of Mn−Mo−W, which was electrochemically deposited on a Ti/IrO_2 net.[26] Using a two-compartment electrochemical cell equipped with a three-electrode setup, this electrode was analyzed for up to 3500 h in a 0.5 M NaCl solution at pH 8.7. An initial OER efficiencies of 99% were reported. They proposed an OER mechanism based on MnO_x as active catalyst material. In contrast and most recently, Vos et al. found that rather the deposition of MnO_x onto IrO_x enhances the OER selectivity by a blocking effect, in which the MnO_2 prevents Cl^- from reaching the catalytically active IrO_x.[27,28]

In addition to the interest in an OER selective water electrolyzer anode, the chlorine industry was generating great interest, and the community started to investigate the anodic behavior in theory and experimentally.[29−37] Starting in 1984, Trasatti pioneered the reactivity of different catalyst materials toward the OER and the ClER activity. He revealed a parallel activity scaling for both reactions in either alkaline or acidic solutions and that it was independent of the electrode material, as shown in Figure 2b.[14] It took several years until another material for the selective splitting of seawater was identified. In 2009, Surendranath et al.[38] used a cobalt-based Co−Pi catalyst material for splitting 0.5 M NaCl in near neutral pH using an additional potassium phosphate buffer and reached selectivities

DOI: 10.1021/acsenergylett.9b00220
ACS Energy Lett. 2019, 4, 933−942

Table 1. Standard Mean Chemical Composition of Seawater Species with the Corresponding Redox Reaction and Electrochemical Standard Potential E^0 at Different pH[7,8]

species	conc. [mol $kg_{H_2O}^{-1}$]	conc. [g $kg_{H_2O}^{-1}$]	reaction[8] Red. ⇌ Ox at pH 0	E^0 [V_{SHE}][8]	reaction[8] Red. ⇌ Ox at pH 14	E^0 [V_{SHE}][8]
H_2O			$2H_2O \rightleftharpoons O_2 + 4H^+ + 4e^-$	1.229	$H_2 + 2OH^- \rightleftharpoons 2H_2O + 2e^-$	−0.828
Cl^-	0.56576	20.0579	$2Cl^- \rightleftharpoons Cl_2(g) + 2e^-$	1.358	$Cl^- + 4OH^- \rightleftharpoons ClO_2^- + 2H_2O + 4e^-$	0.76
			$Cl^- + 4H_2O \rightleftharpoons ClO_4^- + 8H^+ + 8e^-$	1.389	$Cl^- + 2OH^- \rightleftharpoons ClO^- + H_2O + 2e^-$	0.89
			$Cl^- + 3H_2O \rightleftharpoons ClO_3^- + 6H^+ + 6e^-$	1.451	$2Cl^- \rightleftharpoons Cl_2(g) + 2e^-$	1.358
			$Cl^- + H_2O \rightleftharpoons HClO + H^+ + 2e^-$	1.482		
			$Cl^- + 2H_2O \rightleftharpoons HClO_2 + 3H^+ + 4e^-$	1.570		
SO_4^{2-}	0.02927	2.8117	$S_2O_6^{2-} + 2H_2O \rightleftharpoons 2SO_4^{2-} + 4H^+ + 2e^-$	−0.22	$SO_3^{2-} + 2OH^- \rightleftharpoons SO_4^{2-} + H_2O + 2e^-$	−0.93
			$H_2SO_3 + H_2O \rightleftharpoons SO_4^{2-} + 4H^+ + 2e^-$	0.172	$2SO_4^{2-} \rightleftharpoons S_2O_8^{2-} + 2e^-$	2.010
			$2SO_4^{2-} \rightleftharpoons S_2O_8^{2-} + 2e^-$	2.010		
Br^-	0.00087	0.0695	$2Br^- \rightleftharpoons Br_2(aq) + 2e^-$	1.0873	$Br^- + 6OH^- \rightleftharpoons BrO_3^- + 3H_2O + 6e^-$	0.61
			$Br^- + H_2O \rightleftharpoons HBrO + H^+ + 2e^-$	1.331	$Br^- + 2OH^- \rightleftharpoons BrO^- + H_2O + 2e^-$	0.761
			$Br^- + 3H_2O \rightleftharpoons BrO_3^- + 6H^+ + 6e^-$	1.423	$2Br^- \rightleftharpoons Br_2(aq) + 2e^-$	1.0873
F^-	0.00007	0.0013	$2F^- \rightleftharpoons F_2 + 2e^-$	2.866	$2F^- \rightleftharpoons F_2 + 2e^-$	2.866
Na^+	0.48616	11.1768	$Na \rightleftharpoons Na^+ + e^-$	−2.71	$Na \rightleftharpoons Na^+ + e^-$	−2.71
Mg^{2+}	0.05475	1.3307	$Mg \rightleftharpoons Mg^{2+} + 2e^-$	−2.372	$Mg \rightleftharpoons Mg^{2+} + 2e^-$	−2.372
Ca^{2+}	0.01065	0.4268	$Ca \rightleftharpoons Ca^{2+} + 2e^-$	−2.868	$Ca \rightleftharpoons Ca^{2+} + 2e^-$	−2.868
K^+	0.01058	0.4137	$K \rightleftharpoons K^+ + e^-$	−2.931	$K \rightleftharpoons K^+ + e^-$	−2.931
Sr^{2+}	0.00009	0.0079	$Sr \rightleftharpoons Sr^{2+} + 2e^-$	−2.899	$Sr \rightleftharpoons Sr^{2+} + 2e^-$	−2.899
$B(OH)_3$	0.00033	0.0204	$B(OH)_3 + 7H^+ + 8e^- \rightleftharpoons BH_4^- + 3H_2O$	−0.481		
$B(OH)_4^-$	0.00010	0.0079				
CO_2*	0.00001	0.0004				
HCO^{3-}	0.00183	0.1117				
CO_3^{2-}	0.00027	0.0162				
OH^-	0.00001	0.0002			$4OH^- \rightleftharpoons O_2 + 2H_2O + 4e^-$	0.401
H^+			$H_2 \rightleftharpoons 2H^+ + 2e^-$	0.0		

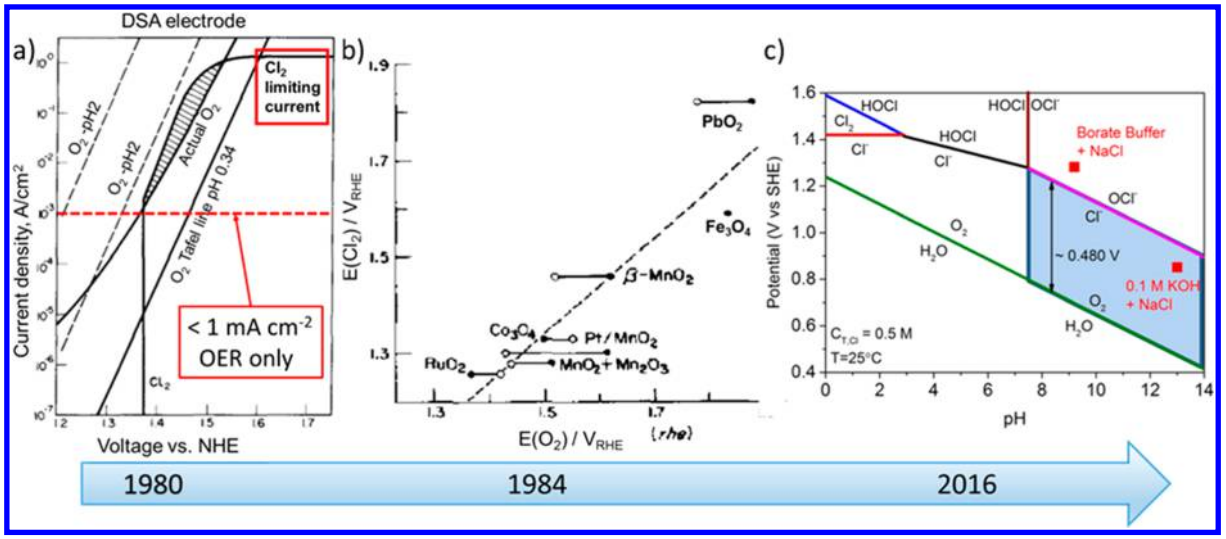

Figure 2. Theoretical evolution of seawater anode chemistry knowledge and concepts. (a) Log current vs voltage for chlorine and oxygen in seawater. Reprinted with permission from ref 13. Copyright 1980 Elsevier. (b) Potential of ClER vs OER at the same current density for a number of oxides (○) and alkaline (●) acidic electrolytes. Reprinted with permission from ref 14. Copyright 1984 Elsevier. (c) Pourbaix diagram of oxygen evolution reaction and chloride chemistry. Reprinted with permission from ref 15. Copyright 2015 Wiley-VCH.

DOI: 10.1021/acsenergylett.9b00220
ACS Energy Lett. 2019, 4, 933−942

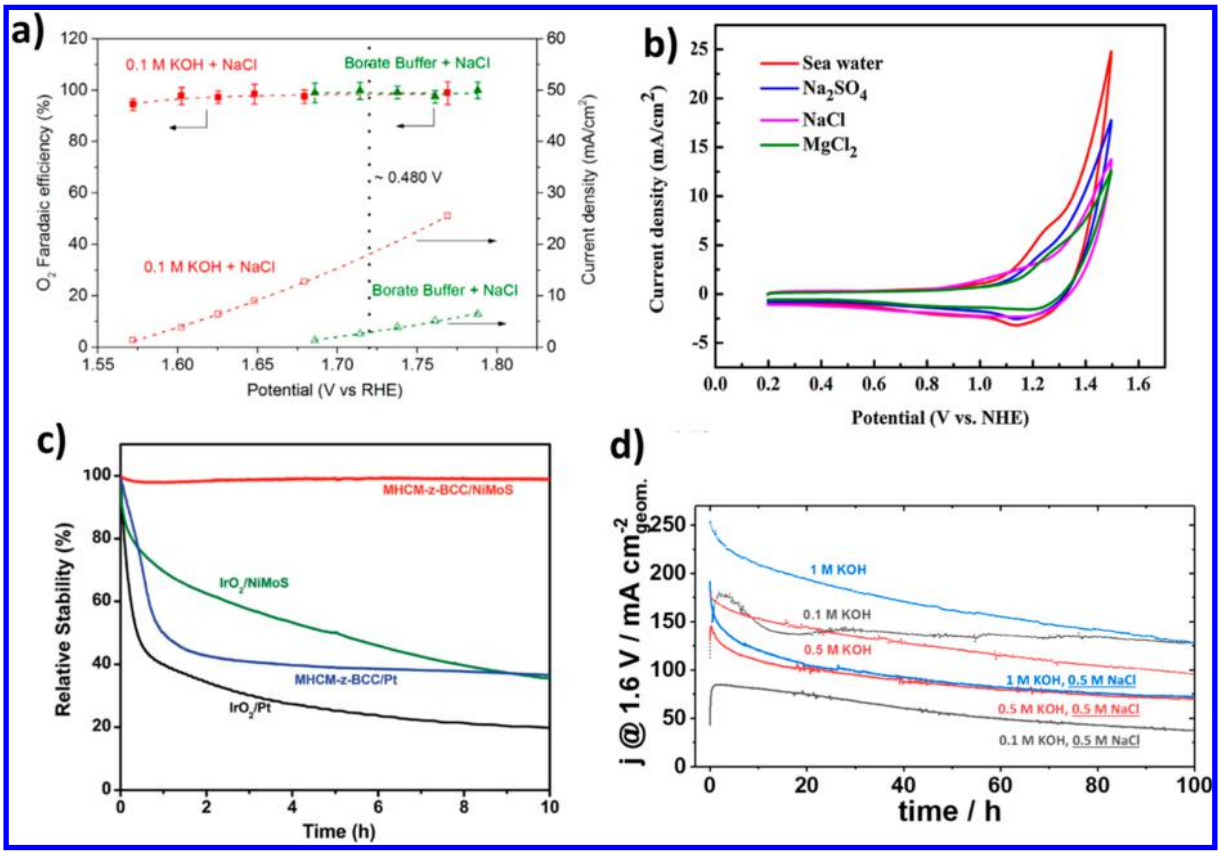

Figure 3. (a) Selectivity measurement in neutral pH borate buffered and 0.1 M KOH with the addition of 0.5 M NaCl. Reprinted with permission from ref 15. Copyright 2015 Wiley-VCH. (b) CV curves of Co−Fe LDH/GCEs in seawater and aqueous solutions including $MgCl_2$, NaCl, or Na_2SO_4 as electrolytes. Scan rate: 100 mV s^{-1}. Reprinted with permission from ref 59. Copyright 2017 Elsevier. (c) Relative 10 h galvanostatic stability test at 2.1 V in a two-electrode configuration with different electrode combinations and an electrolyte. Reprinted with permission from ref 60. Copyright 2015 Wiley-VCH. (d) 100 h seawater electrolyzer measurement in different electrolyte conditions using NiFe-LDH as anode material and Pt/C as cathode. Reprinted with permission from ref 61. Copyright 2015 Wiley-VCH.

about 100%. One year later, on the basis of DFT calculations, the group of Krtil reported a selective working nanocrystalline RuO_2:Zn electrode showing current densities of 0.012 mA cm^{-2}.[30]

Building on the former theoretical considerations of Bennett and Trasatti, Dionigi et al. presented an in-depth analysis of the anodic seawater electrolyzer chemistry and their limitations in 2016, in which they calculated based on the literature a Pourbaix diagram including the chloride and the oxygen chemistry, as shown in Figure 2c.[15] On the basis of this, the chlorine evolution reaction (ClER) at low pH and the hypochlorite formation in high pH solution are the main OER competing reactions.[31,32] Equations 1 and 2 show the corresponding chloride chemistry reactions at low and at high pH, respectively:

ClER:

$$2Cl^- \rightarrow Cl_2 + 2e^- \quad E^0 = 1.36\ \text{V vs SHE, pH 0} \tag{1}$$

Hypochlorite:

$$Cl^- + 2OH^- \rightarrow ClO^- + H_2O + 2e^-$$

$$E^0 = 0.89\ \text{V vs SHE, pH 14} \tag{2}$$

More recently, a more detailed ClER mechanism was presented in 2016 by Exner et al. proposing a Volmer−Heyrovsky mechanism on RuO_2 surfaces.[33,39] Involved in the mechanism, Exner describes an on-top oxygen (O_{ot}) that caps all undercoordinated ruthenium sites (Ru_{cus}) of a RuO_2(110) surface.

Volmer:

$$O_{ot} + 2Cl^- \rightarrow O_{ot}{-}Cl + e^- + Cl^- \tag{3}$$

Heyrovsky:

$$O_{ot}{-}Cl + Cl^- \rightarrow O_{ot} + Cl_2 + e^- \tag{4}$$

In detail, the mechanism consists of a Cl^- adsorption on the O_{ot} combined with a discharge of the anion (eq 3). This adsorption is followed by a direct recombination of the adsorbed chlorine species O_{ot}−Cl with a Cl^- anion from the electrolyte to finally evolve Cl_2 (eq 4). In contrast to the sluggish 4 e^- transfer reaction of the OER, the chloride chemistry involves only 2 e^-. Even though the thermodynamics favors the OER, the kinetics are much faster for the chloride reactions, which leads to smaller overpotentials. Consequently, maximizing the thermodynamic potential difference of both reactions will result in a convenient high potential window for selective OER. This is given for pH > 7.5, where the maximum potential difference is maximized ΔE = 480 mV. On the basis of this, high pH values facilitate the selective splitting of seawater. For validation, Dionigi et al. successfully tested nickel iron mixed layered double hydroxides (NiFe-LDH)[40] as catalyst material in 0.5 M NaCl solution at different pH values. High OER selectivity was confirmed for

DOI: 10.1021/acsenergylett.9b00220
ACS Energy Lett. 2019, 4, 933−942

both the borate buffered and 0.1 M KOH chloride-containing electrolytes, as shown in Figure 3a.[15] The high current densities are obtained by the NiFe-LDH, which is known to be the most active OER catalyst material in an alkaline medium.[40−55]

Despite the ideal solution of a direct seawater electrolyzer, reaching high current densities in typical liquid-based electrolyzer cells leads to a dramatic pH decrease at the anode.[56] Even though carbonate and borate ions are present in seawater (see Table 1), their average concentration is too low to sustain proton handling at high currents. Hence, seawater cannot be used without a buffer or additives with current seawater electrolyzer technology, but other solutions like membranes or different cell designs might be possible to overcome this local pH change. Considering this, in 2010, Esswein et al. tested a cobalt phosphate and borate-based catalyst material in a potassium phosphate buffered (pH 7), a potassium borate buffered (pH 9.2), and a mixed potassium hydroxide (pH 14) natural seawater electrolyte.[38,57] In contrast to typical Ni electrodes, the Co−Bi on the ITO electrode showed comparably high activity even at neutral pH. In contrast, the previously mentioned work reported by El-Monheim et al. did not consider any pH.[23,24,26]

In 2017, Cheng et al. studied the influence of different electrolyte salts on CoFe LDH as seawater oxidizing catalyst and revealed a synergistic effect between the ions of natural seawater and the catalyst, as shown in Figure 3b.[58]

Comparable to the work of Esswein et al.,[57] Cheng et al. determined an enhanced activity of CoFe-LDH in natural seawater than in plane NaCl solutions, revealing an additional influence of the not considered components of natural seawater, which makes the usage of natural water resources desirable for future tests. In 2018, Hsu et al. published a work using transition-metal hexacyanometallates (MHCMs) with a conductive core of basic cobalt carbonate (BCC). They present reaching high stability in neutral pH buffered natural seawater electrolyte (Figure 3c).[60] Additionally, they combined their experimental study with DFT calculations in which they gained deeper insights about the competing OER and ClER using their model catalyst. Combined with a single III−V triple-junction solar cell, they even realized a photolysis system and reported a solar-to-hydrogen efficiency of 17.9%.

In the same year, Dresp et al. presented a first working membrane-based alkaline seawater electrolyzer, using also NiFe-LDH as anode material and a Tokuyama A201 membrane as anion exchange membrane (AEM). Using different KOH concentrated synthetic seawater (0.5 M NaCl) electrolytes,[61] they obtained a high oxygen selectivity. Furthermore, they tested the seawater electrolyzer cell for 100 h at 1.6 V (Figure 3d). In contrast to the results of Dionigi et al., addition of 0.5 M NaCl to different KOH concentrated electrolytes (0.1−1.0 M KOH) resulted in the current density being significantly lower for the NaCl-containing electrolyte. They believed in a membrane-caused performance loss, because separated electrochemical tests of the catalysts and electrodes did not show any negative influence of NaCl. They assumed that Cl^- ions rather block the OH^- transfer capabilities of the membrane, resulting in a mass-transfer limitation phenomenon associated with a performance drop. Supporting the catalyst stability, quasi in situ extended X-ray absorption fine structure (EXAFS) and X-ray absorption near-edge spectroscopy (XANES) measurements showed high stability for the NiFe-LDH phase structure before and after potential treatment.

In addition to the success in catalyst research, which reports highly active and selective materials, the anion exchange membranes seem to be the bottleneck for future AEM seawater electrolyzers. Also, the group of Boettcher highlighted the importance of a novel and stable anion exchange membrane for future alkaline electrolyzer cells, pointing out the strong performance and stability difference to much more advanced proton exchange membranes.[62] Still, contaminating cations such as Na^+, Mg^{2+}, and Ca^{2+} also decrease the performance of proton exchange membranes (PEMs).[63] Consequently, current PEM electrolyzers require highly purified water to sustain their long-term performance. This might also apply for AEM, because the additional anions of seawater (Cl^-, Br^-, SO_4^{2-}, etc.) might negatively influence the membrane performance. This again highlights the importance for novel ion exchange membranes for future seawater electrolyzers. Alternatively, a Zirfon diaphragm as a more robust system could satisfy the required performance stability. However, in this case, the conductivity of the electrolyte would become more important, because diaphragm separators fail to have functional ion exchange groups so that the conductivity is dependent on the ion migration within the electrolyte.[64]

In addition to the success in catalyst research, which reports highly active and selective materials, the anion exchange membranes seem to be the bottleneck for future AEM seawater electrolyzers.

To overcome the membrane-based difficulties, novel approaches for alternative hydrogen production routes from seawater are reported.[65] One approach is photocatalytic splitting.[10,12,66] In 2007, Ji et al. demonstrated photocatalytic hydrogen production from natural seawater using a $La_2Ti_2O_7$ suspension under ultraviolet light, CdS/TiO_2 suspension under visible light, and Fe_2O_3 film under photoelectrochemical conditions. In all cases, no chlorine evolution could be detected.[10] In addition, Maeda et al. modified a $(Ga_{1-x}Zn_x)$-$(N_{1-x}O_x)$ with either $Rh_{2-y}Cr_yO_3$ or RuO_2 nanoparticles as cocatalysts for overall water splitting under visible light ($\lambda > 400$ nm) and tested it in seawater.[12] Luo et al. presented Mo-doped $BiVO_4$ photoanode to improve the solar to energy efficiency and the catalytic stability and also tested it in seawater.[66] Additional loading with RhO_2 as cocatalyt further increased the photo stability in seawater. A completely novel approach was presented in 2016 from the group of Spurgeon, in which they used seawater vapor to circumvent problematic catalyst fouling in PEM electrolyzers.[67]

Hydrogen Evolution Reaction Using Seawater as Electrolyte. While the previous investigations focused primarily on seeking high-performance OER selective catalyst for the anode, the catalyst material and the chemistry at the cathode seems more straightforward, because the thermodynamic potentials for electrochemical deposition or competing reactions are not as close as for the OER and ClER. However, the catalytic activity in natural seawater with its interfering ions and the near-neutral pH seems also challenging.

In 2015, Gao et al. found a Co,N-codoped nanocarbon for electrocatalytic hydrogen production from natural seawater. Supporting the above-mentioned local pH change of unbuffered

DOI: 10.1021/acsenergylett.9b00220
ACS Energy Lett. 2019, 4, 933−942

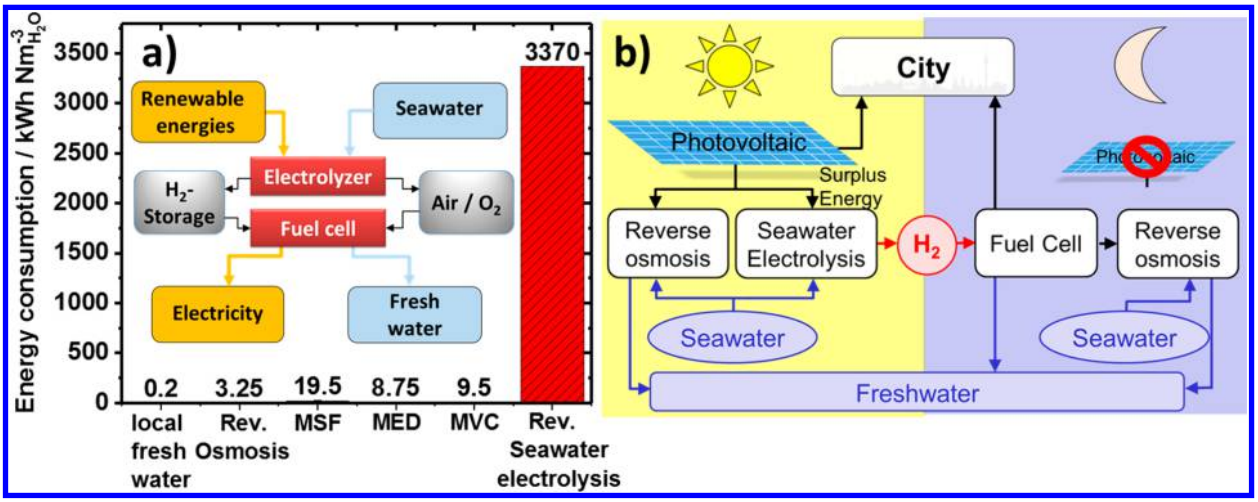

Figure 4. (a) Energy consumption of various desalination technologies and the local water treatment supplier per Nm^3. MSF, multistage flash distillation; MED, multieffect distillation; and MVC, mechanical vapor compression.[74,75] The reversible seawater electrolysis is based on realistic conditions assuming 79% electrolyzer and 50% fuel cell efficiencies. Inset: Sketch for reversible seawater electrolysis based on renewable energy. (b) Process scheme of freshwater production based on seawater electrolysis.

seawater, the catalyst activity showed a higher overpotential in unbuffered seawater than in buffered seawater.[68] In 2016, Martindale and Reisner found an Fe-based bifunctional OER/HER catalyst working in alkalinized synthetic seawater (0.6 M NaCl).[69] One year later in 2017, Ma et al. showed a CoMoP catalyst that is incorporated into a N-doped carbon shell (CoMoP@C). At high overpotentials and pH conditions between 2.0−14.0, this material showed even superior HER activity compared to Pt/C 20 wt %.[70] For their tests, they used several electrolyte conditions including artificial and natural seawater at pH values of 8.2 and 8.35, respectively. In contrast to the Pt/C catalyst, the catalytic HER performance of the CoMoP@C catalyst remained for almost 10 h, which they explained by the carbon shell protecting the catalyst core from etching and poisoning in seawater. In contrast, in 2018 Lu et al. found a manganese doped nickel/nickel foam electrode for the HER in natural seawater without using any buffer.[71] Using natural seawater, they identified a slight deposition of Na, Ca, and Mg on the electrode, which was attributed to an electrode performance loss, but can be easily removed by a mild acid washing. Zhao et al. showed in 2018 a novel $CoSe_xO_y$ catalyst material with high bifunctional HER/OER activity in 1.0 M KOH. They showed further high activity using CoSe1 at the anode and CoSe4 at the cathode using buffered (pH 7.4) and natural seawater, exceeding the activity of Ir−C/Pt−C electrodes.[72] Most recently in 2018, Guan et al. presented unassisted photocatalytic overall seawater splitting using a p-type (In)GaN nanowire array, reaching even higher H_2 evolution rates in seawater than in pure water.[73]

Freshwater Production Using Reversible Seawater Electrolysis. An interesting aspect of direct seawater electrolysis consists of the production of freshwater when back converting the produced hydrogen and oxygen into electricity and water, as indicated in the inset in Figure 4a. This can be achieved in one single device, termed a reversible seawater electrolyzer, or in two separated subsequent combined fuel cell and electrolyzer devices. Considering realistic electrolyzer/fuel cell efficiencies and calculating the required energy to produce 1 Nm^3 of H_2O, a reversible seawater electrolyzer would require an energy input of roughly 3370 kWh for every $Nm^3_{H_2O}$ water produced (see the Supporting Information for more detailed energy consumption and efficiency calculations). Compared to other established technologies, such as reverse osmosis, multistage flash distillation, multieffect distillation, and mechanical vapor compression, the energy consumption of a reversible seawater electrolyzer to desalinate 1 $Nm^3_{H_2O}$ is several orders of magnitude higher, as shown in Figure 4a.[74,75]

Although the water produced in the fuel cell process is perfectly purified water, reverse osmosis is currently by far the most efficient technology for the production of freshwater. However, reverse osmosis entails a number of drawbacks, like the frequent maintenance of the membrane and the exhaust saltwater feed's harm to the environment. Only the water treatment of the local freshwater supplier consumes less energy per $Nm^3_{H_2O}$.

Nevertheless, 1 $Nm^3_{H_2O}$ produces under realistic conditions H_2 equivalent to 2200 kWh (see the Supporting Information), which is equal to the annual electricity demand of an average one-person household in Europe. On the one hand, this illustrates the high energy content of hydrogen and underlines the importance of electrolyzer technologies to store surplus renewable electricity. On the other hand, 1 Nm^3 amounts to the cumulative yearly recommended intake of freshwater of 2−3 L. However, one person consumes significantly more water than 1 $Nm^3_{H_2O}$ per year. As a result, reversible seawater electrolysis should be perceived more as an energy storage technology than a freshwater production technology when transforming the hydrogen back into electricity and water by using the fuel cell. One possible process scheme providing constant and sustainable freshwater production through a combination of photovoltaics with reverse osmosis, a direct seawater electrolyzer and a fuel cell, is shown in Figure 4b.

During the day, the photovoltaic device supplies the electricity for both water purification by reverse osmosis and the stationary power demand (city). Thus, the reverse osmosis desalinates seawater and provides potable freshwater, while the power demand is met by photovoltaics. Excess solar electricity drives the direct seawater electrolyzer, producing solar hydrogen, which is stored locally. At night, in the absence of solar

DOI: 10.1021/acsenergylett.9b00220
ACS Energy Lett. 2019, 4, 933−942

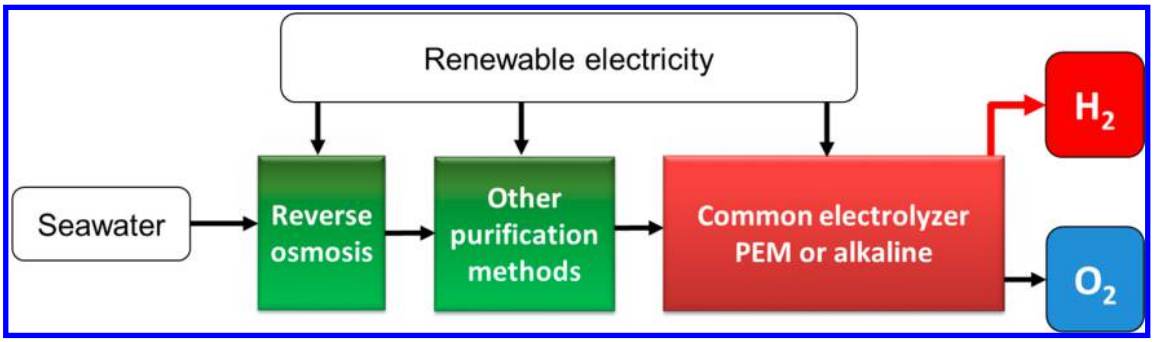

Figure 5. Sketch of alternative seawater electrolysis design with common technologies.

electricity, the hydrogen fuel cell system supplies electrical stationary power and produces freshwater directly by the fuel cell and indirectly by powering the reverse osmosis.

In conclusion, in specific environments and under certain conditions, reversible seawater electrolysis offers advantages for the storage of surplus electricity in the form of molecular hydrogen and for the collateral purification of seawater in combination with a fuel cell device.

Direct Seawater Electrolysis Compared to Established Electrolysis Technologies. Splitting seawater by using today's established technologies requires careful water prepurification, as shown in the process diagram of Figure 5.

After basic filtering, seawater is purified in a first step by reverse osmosis (RO). The purification of 9 kg of H_2O via RO requires about 0.03 kWh (see the Supporting Information). Consequently, even assuming an input power excess with a factor of 10, the resulting energy consumption of RO for the production of 1 kg of H_2 amounts to a mere 0.3 kWh, which appears negligible against the typical energy input per kilogram of H_2 (~47−66 kWh $kg_{H_2}^{-1}$). Table 2 compares published energy and efficiency values of established electrolysis technologies and the direct seawater electrolysis for the production of 1 kg of H_2. Here, the conventional electrolysis scheme offers slight advantages in terms of energy consumption. However, in many cases, the resulting purity of RO water still does not reach the required purity level of membrane-based freshwater electrolysis.[76] This is why an additional purification step will be required. PEM membranes, in particular, require, in parts, ion exchanged ultrapurified (18 MΩ cm) water for sustained operation. Hence, seawater-splitting schemes using those conventional membrane electrolyzers do require additional energy, space, and investment.

Table 2. Performance Indicators of Different Technologies for the Production of 1 kg of Hydrogen from Freshwater (PEM and Alkaline) or Seawater (Direct Seawater Electrolysis)[a]

technology	specific energy consumption (stack) [kWh $kg_{H_2}^{-1}$]	voltage efficiency based on HHV [%]	reference
PEM electrolysis	47−63	67−82	77
liquid alkaline electrolysis	47−66	62−82	77
direct seawater electrolysis	50−53	75−79	61

[a]Data is taken and converted from refs 61 and 77.

Catalysts and separators of liquid alkaline electrolyzers, on the other hand, tend to be more tolerant for electrolyte impurities than membrane-based electrolyzers. However, they require ample amounts of concentrated KOH solutions (20−40 wt %).[78] More importantly, under the highly alkaline conditions at common electrolyzer potentials (1.8−2.4 V),[77] traces of chloride ions would be electro-oxidized to hypochlorite ions, harming the catalyst and limiting the long-term stability of the system.

Even though the conventional PEM and liquid alkaline electrolyzer schemes display slight energetic advantages over direct seawater electrolyzers, under certain conditions, the latter may still prove superior on the system level for hydrogen production applications in spatially constrained offshore or mobile maritime applications. Thus, even though the conventional PEM and liquid alkaline electrolyzer schemes display slight energetic advantages over direct seawater electrolyzers, under certain conditions, the latter may still prove superior on the system level for hydrogen production applications in spatially constrained offshore or mobile maritime applications.

Even though the conventional PEM and liquid alkaline electrolyzer schemes display slight energetic advantages over direct seawater electrolyzers, under certain conditions, the latter may still prove superior on the system level for hydrogen production applications in spatially constrained offshore or mobile maritime applications.

The compact seawater electrolyzer concepts presented and demonstrated at the lab-bench level by Dionigi et al.[15] and Dresp et al.,[61] for instance, are designed in such a way that the formation of chlorine or hypochlorite can be suppressed by careful adjustment of the seawater pH and the catalytic selectivity of the electrodes employed. As a downside, the corrosive effect of seawater might reduce the lifetime of the direct seawater electrolyzers compared to conventional electrolyzers. However, the purification methods such as RO are also exposed to seawater, which limits equally the lifetime of conventional electrolyzers with prepurification, so that at larger scales, such single direct seawater electrolyzer devices with their compact design are projected to feature minimal investment and maintenance costs.

DOI: 10.1021/acsenergylett.9b00220
ACS Energy Lett. 2019, 4, 933−942

Summary and Future Outlook. The planet's oceans supply almost unlimited quantities of seawater, while freshwater is becoming a more and more precious resource. Against this global backdrop, in selected locations and special environments, direct seawater electrolysis is an increasingly attractive electricity/hydrogen conversion and storage technology of the future. It will be most effective in regions with ample surplus renewable electricity, little access to freshwater, and yet sufficient access to ocean seawater. It also offers advantages for mobile maritime and offshore hydrogen-based power applications. Examples include powering underwater, unmanned maritime vehicles for maintenance of offshore installations. Range and refueling time of hydrogen-powered vehicles greatly outperform those of comparable battery-based vehicles. Because of the compact design, direct seawater electrolyzers are expected to pose fewer system engineering challenges compared to multistep schemes. The key chemical challenge is the design of robust and selective electrodes in order to suppress undesired electrochemical processes that are associated with the contaminants, primarily chloride chemistry. A number of active and selective catalysts have been identified as selective and active anode and cathode materials. However, advanced membranes and novel separator concepts appear critical to increase stability of direct seawater electrolyzer devices. Even though standard RO purification of seawater requires limited amounts of energy, it may be insufficient to reach the necessary levels of water purity. The necessary multiple consecutive purification steps are likely to reduce the overall robustness of the seawater electrolyzer system, because all additional devices, such as reverse osmosis systems, require frequent and additional maintenance compared with a single direct seawater-splitting device.

In combination with a hydrogen fuel cell, a reversible seawater electrolysis scheme is possible that holds promise for the storage of surplus electricity in the form of molecular hydrogen, and more as a collateral process, purified water is formed during the fuel cell reaction. Based on the energy efficiency of reversible electrolyzer−fuel cell schemes, the resulting freshwater production may remain limited with respect to more conventional freshwater technologies. Here, a new process concept for a sustained freshwater supply based on the combination of RO water purification and direct seawater electrolysis was developed and suggested. Offshore wind parks and solar energy-rich coastal desert regions would benefit the most from this combined process technology, where molecular hydrogen is transformed back into electricity and water.

■ ASSOCIATED CONTENT

Supporting Information

The Supporting Information is available free of charge on the ACS Publications website at DOI: 10.1021/acsenergylett.9b00220.

Calculation of the energy consumption for a reversible electrolyzer (PDF)

■ AUTHOR INFORMATION

Corresponding Author

*E-mail: pstrasser@tu-berlin.de.

ORCID

Peter Strasser: 0000-0002-3884-436X

Notes

The authors declare no competing financial interest.

Biographies

Sören Dresp is a post-doctoral researcher in the "The Electrochemical Energy, Catalysis, and Materials Science Group" of Prof. Peter Strasser. He received his Ph.D. in electrochemistry in 2018 from the Technische Universität Berlin. His research focuses on reversible seawater electrolyzers, including selective non-noble bifunctional OER/ORR catalysts and membrane-based reversible electrolyzer devices.

Fabio Dionigi completed his Ph.D. in Physics in 2012 at Danmarks Tekniske Universitet, Denmark and continued as a postdoc. In 2013, he joined the group of Prof. Strasser at Technische Universität Berlin, Germany. His work focuses on Pt-based alloy nanoparticles for the oxygen reduction reaction and non-noble metal-based catalysts for the oxygen evolution reaction.

Malte Klingenhof received his Bachelor of Science in 2014 and a Master of Science in 2016 at the Technical University of Berlin (TUB), Germany. In 2017, he started his Ph.D. in the group of Prof. Strasser at TUB, where he is currently studying non-noble metal-based bifunctional electrocatalysts for reversible seawater electrolyzers.

Prof. Peter Strasser is a chaired professor of Chemistry and Chemical Engineering heading the "Electrochemical Materials and Catalysis Laboratory" at the Technical University Berlin. He was awarded the Otto-Hahn Research Medal, the Otto-Roelen medal, the Ertl Prize, and the Sir William Grove Award.

■ ACKNOWLEDGMENTS

Financial support by the German Research Foundation (DFG) through Grant Reference Number STR 596/8-1 and the federal ministry for economic affairs and energy (Bundesministerium für Wirtschaft und Energie, BMWi) under Grant Number 03EIV041F in the collaborative research project "MethQuest" in the group "MethFuel" are gratefully acknowledged.

■ REFERENCES

(1) Shaner, M. R.; Atwater, H. A.; Lewis, N. S.; McFarland, E. W. A comparative technoeconomic analysis of renewable hydrogen production using solar energy. *Energy Environ. Sci.* **2016**, *9* (7), 2354−2371.

(2) Buttler, A.; Spliethoff, H. Current status of water electrolysis for energy storage, grid balancing and sector coupling via power-to-gas and power-to-liquids: A review. *Renewable Sustainable Energy Rev.* **2018**, *82*, 2440−2454.

(3) Vincent, I.; Bessarabov, D. Low cost hydrogen production by anion exchange membrane electrolysis: A review. *Renewable Sustainable Energy Rev.* **2018**, *81*, 1690−1704.

(4) Shiklomanov, I. In *Water in crisis: a guide to the world's fresh water resources*; 1993; Chapter 2.

(5) Insititute, W. R. *Millennium Ecosystem Assessment: Appendix A*; Island press: Washington, DC, 2005.

(6) Feng, S.; Fu, Q. Expansion of global drylands under a warming climate. *Atmos. Chem. Phys.* **2013**, *13* (19), 10081−10094.

(7) Dickson, A. G.; Goyet, C. *Handbook of methods for the analysis of the various parameters of the carbon dioxide system in sea water; version 2.*; San Diego, ORNL/DCIAC-74, 1994.

(8) Vanysek, P. Electrochemical series. In *CRC handbook of chemistry and physics*; Lide, D. R., Ed.; CRC Press: Boca Raton, FL, 2005.

(9) Cuartero, M.; Crespo, G.; Cherubini, T.; Pankratova, N.; Confalonieri, F.; Massa, F.; Tercier-Waeber, M.-L.; Abdou, M.; Schäfer, J.; Bakker, E. In Situ Detection of Macronutrients and Chloride in Seawater by Submersible Electrochemical Sensors. *Anal. Chem.* **2018**, *90* (7), 4702−4710.

(10) Ji, S. M.; Jun, H.; Jang, J. S.; Son, H. C.; Borse, P. H.; Lee, J. S. Photocatalytic hydrogen production from natural seawater. *J. Photochem. Photobiol., A* **2007**, *189* (1), 141−144.

DOI: 10.1021/acsenergylett.9b00220
ACS Energy Lett. 2019, 4, 933−942

(11) Kester, D. R.; Duedall, I. W.; Connors, D. N.; Pytkowicz, R. M. Preparation of artificial seawater. *Limnol. Oceanogr.* **1967**, *12* (1), 176−179.
(12) Maeda, K.; Masuda, H.; Domen, K. Effect of electrolyte addition on activity of $(Ga_{1-x}Zn_x)(N_{1-x}O_x)$ photocatalyst for overall water splitting under visible light. *Catal. Today* **2009**, *147* (3), 173−178.
(13) Bennett, J. E. Electrodes for generation of hydrogen and oxygen from seawater. *Int. J. Hydrogen Energy* **1980**, *5* (4), 401−408.
(14) Trasatti, S. Electrocatalysis in the anodic evolution of oxygen and chlorine. *Electrochim. Acta* **1984**, *29* (11), 1503−1512.
(15) Dionigi, F.; Reier, T.; Pawolek, Z.; Gliech, M.; Strasser, P. Design Criteria, Operating Conditions, and Nickel−Iron Hydroxide Catalyst Materials for Selective Seawater Electrolysis. *ChemSusChem* **2016**, *9* (9), 962−972.
(16) Izumiya, K.; Akiyama, E.; Habazaki, H.; Kumagai, N.; Kawashima, A.; Hashimoto, K. Effects of additional elements on electrocatalytic properties of thermally decomposed manganese oxide electrodes for oxygen evolution from seawater. *Mater. Trans., JIM* **1997**, *38* (10), 899−905.
(17) Kato, Z.; Sato, M.; Sasaki, Y.; Izumiya, K.; Kumagai, N.; Hashimoto, K. Electrochemical characterization of degradation of oxygen evolution anode for seawater electrolysis. *Electrochim. Acta* **2014**, *116* (0), 152−157.
(18) Izumiya, K.; Akiyama, E.; Habazaki, H.; Kumagai, N.; Kawashima, A.; Hashimoto, K. Anodically deposited manganese oxide and manganese−tungsten oxide electrodes for oxygen evolution from seawater. *Electrochim. Acta* **1998**, *43* (21−22), 3303−3312.
(19) Fujimura, K.; Matsui, T.; Izumiya, K.; Kumagai, N.; Akiyama, E.; Habazaki, H.; Kawashima, A.; Asami, K.; Hashimoto, K. Oxygen evolution on manganese−molybdenum oxide anodes in seawater electrolysis. *Mater. Sci. Eng., A* **1999**, *267* (2), 254−259.
(20) Fujimura, K.; Matsui, T.; Habazaki, H.; Kawashima, A.; Kumagai, N.; Hashimoto, K. The durability of manganese−molybdenum oxide anodes for oxygen evolution in seawater electrolysis. *Electrochim. Acta* **2000**, *45* (14), 2297−2303.
(21) Habazaki, H.; Matsui, T.; Kawashima, A.; Asami, K.; Kumagai, N.; Hashimoto, K. Nanocrystalline manganese-molybdenum-tungsten oxide anodes for oxygen evolution in seawater electrolysis. *Scr. Mater.* **2001**, *44* (8−9), 1659−1662.
(22) Abdel Ghany, N. A.; Kumagai, N.; Meguro, S.; Asami, K.; Hashimoto, K. Oxygen evolution anodes composed of anodically deposited Mn−Mo−Fe oxides for seawater electrolysis. *Electrochim. Acta* **2002**, *48* (1), 21−28.
(23) El-Moneim, A. A.; Kumagai, N.; Hashimoto, K. Mn-Mo-W Oxide Anodes for Oxygen Evolution in Seawater Electrolysis for Hydrogen Production. *Mater. Trans.* **2009**, *50* (8), 1969−1977.
(24) El-Moneim, A. A.; Bhattarai, J.; Kato, Z.; Izumiya, K.; Kumagai, N.; Hashimoto, K. Mn-Mo-Sn Oxide Anodes for Oxygen Evolution in Seawater Electrolysis for Hydrogen Production. *ECS Trans.* **2009**, *25* (40), 127−137.
(25) Kato, Z.; Bhattarai, J.; Kumagai, N.; Izumiya, K.; Hashimoto, K. Durability enhancement and degradation of oxygen evolution anodes in seawater electrolysis for hydrogen production. *Appl. Surf. Sci.* **2011**, *257* (19), 8230−8236.
(26) El-Moneim, A. A. Mn−Mo−W-oxide anodes for oxygen evolution during seawater electrolysis for hydrogen production: Effect of repeated anodic deposition. *Int. J. Hydrogen Energy* **2011**, *36* (21), 13398−13406.
(27) Vos, J. G.; Wezendonk, T. A.; Jeremiasse, A. W.; Koper, M. T. M. MnOx/IrOx as Selective Oxygen Evolution Electrocatalyst in Acidic Chloride Solution. *J. Am. Chem. Soc.* **2018**, *140* (32), 10270−10281.
(28) Vos, J. G.; Koper, M. T. M. Measurement of competition between oxygen evolution and chlorine evolution using rotating ring-disk electrode voltammetry. *J. Electroanal. Chem.* **2018**, *819*, 260−268.
(29) Arikawa, T.; Murakami, Y.; Takasu, Y. Simultaneous determination of chlorine and oxygen evolving at RuO_2/Ti and RuO_2−TiO_2/Ti anodes by differential electrochemical mass spectroscopy. *J. Appl. Electrochem.* **1998**, *28* (5), 511−516.
(30) Petrykin, V.; Macounova, K.; Shlyakhtin, O. A.; Krtil, P. Tailoring the Selectivity for Electrocatalytic Oxygen Evolution on Ruthenium Oxides by Zinc Substitution. *Angew. Chem., Int. Ed.* **2010**, *49* (28), 4813−4815.
(31) Menzel, N.; Ortel, E.; Mette, K.; Kraehnert, R.; Strasser, P. Dimensionally Stable Ru/Ir/TiO_2-Anodes with Tailored Mesoporosity for Efficient Electrochemical Chlorine Evolution. *ACS Catal.* **2013**, *3* (6), 1324−1333.
(32) Man, I. C.; Su, H.; Calle-Vallejo, F.; Hansen, H. A.; Martínez, J. A.; Inoglu, N. G.; Kitchin, J.; Jaramillo, T. F.; Nørskov, J. K.; Rossmeisl, J. Universality in Oxygen Evolution Electrocatalysis on Oxide Surfaces. *ChemCatChem* **2011**, *3*, 1159−1165.
(33) Exner, K. S.; Anton, J.; Jacob, T.; Over, H. Controlling Selectivity in the Chlorine Evolution Reaction over RuO_2-Based Catalysts. *Angew. Chem., Int. Ed.* **2014**, *53* (41), 11032−11035.
(34) Karlsson, R. K. B.; Hansen, H. A.; Bligaard, T.; Cornell, A.; Pettersson, L. G. M. Ti atoms in $Ru_{0.3}Ti_{0.7}O_2$ mixed oxides form active and selective sites for electrochemical chlorine evolution. *Electrochim. Acta* **2014**, *146* (Supplement C), 733−740.
(35) Karlsson, R. K. B.; Cornell, A. Selectivity between Oxygen and Chlorine Evolution in the Chlor-Alkali and Chlorate Processes. *Chem. Rev.* **2016**, *116* (5), 2982−3028.
(36) Sohrabnejad-Eskan, I.; Goryachev, A.; Exner, K. S.; Kibler, L. A.; Hensen, E. J. M.; Hofmann, J. P.; Over, H. Temperature-Dependent Kinetic Studies of the Chlorine Evolution Reaction over RuO2(110) Model Electrodes. *ACS Catal.* **2017**, *7* (4), 2403−2411.
(37) Vos, J. G.; Koper, M. T. M. Measurement of competition between oxygen evolution and chlorine evolution using rotating ring-disk electrode voltammetry. *J. Electroanal. Chem.* **2018**, *819*, 260.
(38) Surendranath, Y.; Dincá, M.; Nocera, D. G. Electrolyte-Dependent Electrosynthesis and Activity of Cobalt-Based Water Oxidation Catalysts. *J. Am. Chem. Soc.* **2009**, *131* (7), 2615−2620.
(39) Exner, K. S.; Anton, J.; Jacob, T.; Over, H. Full Kinetics from First Principles of the Chlorine Evolution Reaction over a RuO_2(110) Model Electrode. *Angew. Chem., Int. Ed.* **2016**, *55* (26), 7501−7504.
(40) Dionigi, F.; Strasser, P. NiFe-Based (Oxy)hydroxide Catalysts for Oxygen Evolution Reaction in Non-Acidic Electrolytes. *Adv. Energy Mater.* **2016**, *6*, 1600621.
(41) Corrigan, D. A. The Catalysis of the Oxygen Evolution Reaction by Iron Impurities in Thin Film Nickel Oxide Electrodes. *J. Electrochem. Soc.* **1987**, *134* (2), 377−384.
(42) Gong, M.; Li, Y.; Wang, H.; Liang, Y.; Wu, J. Z.; Zhou, J.; Wang, J.; Regier, T.; Wei, F.; Dai, H. An Advanced Ni−Fe Layered Double Hydroxide Electrocatalyst for Water Oxidation. *J. Am. Chem. Soc.* **2013**, *135* (23), 8452−8455.
(43) Louie, M. W.; Bell, A. T. An Investigation of Thin-Film Ni−Fe Oxide Catalysts for the Electrochemical Evolution of Oxygen. *J. Am. Chem. Soc.* **2013**, *135* (33), 12329−12337.
(44) Haber, J. A.; Xiang, C.; Guevarra, D.; Jung, S.; Jin, J.; Gregoire, J. M. High-Throughput Mapping of the Electrochemical Properties of (Ni-Fe-Co-Ce)Ox Oxygen-Evolution Catalysts. *ChemElectroChem* **2014**, *1* (3), 524−528.
(45) Li, Y.-F.; Selloni, A. Mechanism and Activity of Water Oxidation on Selected Surfaces of Pure and Fe-Doped NiOx. *ACS Catal.* **2014**, *4* (4), 1148−1153.
(46) Chen, J. Y. C.; Dang, L.; Liang, H.; Bi, W.; Gerken, J. B.; Jin, S.; Alp, E. E.; Stahl, S. S. Operando Analysis of NiFe and Fe Oxyhydroxide Electrocatalysts for Water Oxidation: Detection of Fe^{4+} by Mössbauer Spectroscopy. *J. Am. Chem. Soc.* **2015**, *137* (48), 15090−15093.
(47) Diaz-Morales, O.; Ledezma-Yanez, I.; Koper, M. T. M.; Calle-Vallejo, F. Guidelines for the Rational Design of Ni-Based Double Hydroxide Electrocatalysts for the Oxygen Evolution Reaction. *ACS Catal.* **2015**, *5* (9), 5380−5387.
(48) Friebel, D.; Louie, M. W.; Bajdich, M.; Sanwald, K. E.; Cai, Y.; Wise, A. M.; Cheng, M.-J.; Sokaras, D.; Weng, T.-C.; Alonso-Mori, R.; Davis, R. C.; Bargar, J. R.; Nørskov, J. K.; Nilsson, A.; Bell, A. T. Identification of Highly Active Fe Sites in (Ni,Fe)OOH for Electrocatalytic Water Splitting. *J. Am. Chem. Soc.* **2015**, *137* (3), 1305−1313.

DOI: 10.1021/acsenergylett.9b00220
ACS Energy Lett. 2019, 4, 933−942

(49) Bates, M. K.; Jia, Q.; Doan, H.; Liang, W.; Mukerjee, S. Charge-Transfer Effects in Ni−Fe and Ni−Fe−Co Mixed-Metal Oxides for the Alkaline Oxygen Evolution Reaction. *ACS Catal.* **2016**, *6* (1), 155−161.
(50) Hunter, B. M.; Hieringer, W.; Winkler, J. R.; Gray, H. B.; Muller, A. M. Effect of interlayer anions on [NiFe]-LDH nanosheet water oxidation activity. *Energy Environ. Sci.* **2016**, *9* (5), 1734−1743.
(51) Goerlin, M.; Ferreira de Araújo, J.; Schmies, H.; Bernsmeier, D.; Dresp, S.; Gliech, M.; Jusys, Z.; Chernev, P.; Kraehnert, R.; Dau, H.; Strasser, P. Tracking catalyst redox states and reaction dynamics in Ni-Fe oxyhydroxide oxygen evolution reaction (OER) electrocatalysts: The role of catalyst support and electrolyte pH. *J. Am. Chem. Soc.* **2017**, *139* (5), 2070−2082.
(52) Görlin, M.; Chernev, P.; Ferreira de Araújo, J.; Reier, T.; Dresp, S.; Paul, B.; Krähnert, R.; Dau, H.; Strasser, P. Oxygen Evolution Reaction Dynamics, Faradaic Charge Efficiency, and the Active Metal Redox States of Ni−Fe Oxide Water Splitting Electrocatalysts. *J. Am. Chem. Soc.* **2016**, *138* (17), 5603−5614.
(53) Görlin, M.; Gliech, M.; de Araújo, J. F.; Dresp, S.; Bergmann, A.; Strasser, P. Dynamical changes of a Ni-Fe oxide water splitting catalyst investigated at different pH. *Catal. Today* **2016**, *262*, 65−73.
(54) McCrory, C. C. L.; Jung, S.; Peters, J. C.; Jaramillo, T. F. Benchmarking Heterogeneous Electrocatalysts for the Oxygen Evolution Reaction. *J. Am. Chem. Soc.* **2013**, *135* (45), 16977−16987.
(55) Trotochaud, L.; Young, S. L.; Ranney, J. K.; Boettcher, S. W. Nickel−Iron Oxyhydroxide Oxygen-Evolution Electrocatalysts: The Role of Intentional and Incidental Iron Incorporation. *J. Am. Chem. Soc.* **2014**, *136* (18), 6744−6753.
(56) Kuhn, A. T.; Chan, C. Y. pH changes at near-electrode surfaces. *J. Appl. Electrochem.* **1983**, *13* (2), 189−207.
(57) Esswein, A. J.; Surendranath, Y.; Reece, S. Y.; Nocera, D. G. Highly active cobalt phosphate and borate based oxygen evolving catalysts operating in neutral and natural waters. *Energy Environ. Sci.* **2011**, *4* (2), 499−504.
(58) Cheng, F.; Feng, X.; Chen, X.; Lin, W.; Rong, J.; Yang, W. Synergistic action of Co-Fe layered double hydroxide electrocatalyst and multiple ions of sea salt for efficient seawater oxidation at near-neutral pH. *Electrochim. Acta* **2017**, *251* (Supplement C), 336−343.
(59) Cheng, F.; Feng, X.; Chen, X.; Lin, W.; Rong, J.; Yang, W. Synergistic action of Co-Fe layered double hydroxide electrocatalyst and multiple ions of sea salt for efficient seawater oxidation at near-neutral pH. *Electrochim. Acta* **2017**, *251*, 336−343.
(60) Hsu, S. H.; Miao, J.; Zhang, L.; Gao, J.; Wang, H.; Tao, H.; Hung, S. F.; Vasileff, A.; Qiao, S. Z.; Liu, B. An Earth-Abundant Catalyst-Based Seawater Photoelectrolysis System with 17.9% Solar-to-Hydrogen Efficiency. *Adv. Mater.* **2018**, *30* (18), No. 1707261.
(61) Dresp, S.; Dionigi, F.; Loos, S.; Ferreira de Araujo, J.; Spöri, C.; Gliech, M.; Dau, H.; Strasser, P. Direct Electrolytic Splitting of Seawater: Activity, Selectivity, Degradation, and Recovery Studied from the Molecular Catalyst Structure to the Electrolyzer Cell Level. *Adv. Energy Mater.* **2018**, *8* (22), 1800338.
(62) Oener, S. Z.; Ardo, S.; Boettcher, S. W. Ionic Processes in Water Electrolysis: The Role of Ion-Selective Membranes. *ACS Energy Lett.* **2017**, *2* (11), 2625−2634.
(63) Kienitz, B. L.; Baskaran, H.; Zawodzinski, T. A. Modeling the steady-state effects of cationic contamination on polymer electrolyte membranes. *Electrochim. Acta* **2009**, *54* (6), 1671−1679.
(64) Lavorante, M. J.; Reynoso, C. Y.; Franco, J. I. Water electrolysis with Zirfon® as separator and NaOH as electrolyte. *Desalin. Water Treat.* **2015**, *56* (13), 3647−3653.
(65) Fukuzumi, S.; Lee, Y.-M.; Nam, W. Fuel Production from Seawater and Fuel Cells Using Seawater. *ChemSusChem* **2017**, *10* (22), 4264−4276.
(66) Luo, W.; Yang, Z.; Li, Z.; Zhang, J.; Liu, J.; Zhao, Z.; Wang, Z.; Yan, S.; Yu, T.; Zou, Z. Solar hydrogen generation from seawater with a modified BiVO4 photoanode. *Energy Environ. Sci.* **2011**, *4* (10), 4046−4051.
(67) Kumari, S.; Turner White, R.; Kumar, B.; Spurgeon, J. M. Solar hydrogen production from seawater vapor electrolysis. *Energy Environ. Sci.* **2016**, *9* (5), 1725−1733.
(68) Gao, S.; Li, G.-D.; Liu, Y.; Chen, H.; Feng, L.-L.; Wang, Y.; Yang, M.; Wang, D.; Wang, S.; Zou, X. Electrocatalytic H_2 production from seawater over Co, N-codoped nanocarbons. *Nanoscale* **2015**, *7* (6), 2306−2316.
(69) Martindale, B. C. M.; Reisner, E. Bi-Functional Iron-Only Electrodes for Efficient Water Splitting with Enhanced Stability through In Situ Electrochemical Regeneration. *Adv. Energy Mater.* **2016**, *6* (6), 1502095.
(70) Ma, Y.-Y.; Wu, C.-X.; Feng, X.-J.; Tan, H.-Q.; Yan, L.-K.; Liu, Y.; Kang, Z.-H.; Wang, E.-B.; Li, Y.-G. Highly efficient hydrogen evolution from seawater by a low-cost and stable CoMoP@C electrocatalyst superior to Pt/C. *Energy Environ. Sci.* **2017**, *10* (3), 788−798.
(71) Lu, X.; Pan, J.; Lovell, E.; Tan, T. H.; Ng, Y. H.; Amal, R. A sea-change: manganese doped nickel/nickel oxide electrocatalysts for hydrogen generation from seawater. *Energy Environ. Sci.* **2018**, *11* (7), 1898−1910.
(72) Zhao, Y.; Jin, B.; Zheng, Y.; Jin, H.; Jiao, Y.; Qiao, S.-Z. Charge State Manipulation of Cobalt Selenide Catalyst for Overall Seawater Electrolysis. *Adv. Energy Mater.* **2018**, *8* (29), 1801926.
(73) Guan, X.; Chowdhury, F. A.; Pant, N.; Guo, L.; Vayssieres, L.; Mi, Z. Efficient Unassisted Overall Photocatalytic Seawater Splitting on GaN-Based Nanowire Arrays. *J. Phys. Chem. C* **2018**, *122* (25), 13797−13802.
(74) Desai, D.; Beh, E. S.; Sahu, S.; Vedharathinam, V.; van Overmeere, Q.; de Lannoy, C. F.; Jose, A. P.; Völkel, A. R.; Rivest, J. B. Electrochemical Desalination of Seawater and Hypersaline Brines with Coupled Electricity Storage. *ACS Energy Lett.* **2018**, *3* (2), 375−379.
(75) Epri, P. A. *Water & Sustainability (Vol. 4): U.S. Electricity Consumption for Water Supply & Treatment - The Next Half Century*; Palo Alto, CA, 2000; p 1006787.
(76) Hanrahan, G. Chapter 5 - Water Treatment and Related Technologies. In *Key Concepts in Environmental Chemistry*; Hanrahan, G., Ed.; Academic Press: Boston, 2012; pp 155−176.
(77) Carmo, M.; Fritz, D. L.; Mergel, J.; Stolten, D. A comprehensive review on PEM water electrolysis. *Int. J. Hydrogen Energy* **2013**, *38* (12), 4901−4934.
(78) Smolinka, T.G. M., Garche, J. *NOW-Studie: Stand und Entwicklungspotenzial der Wasserelektrolyse zur Herstellung von Wasserstoff aus regenerativen Energien.*; Fraunhofer ISE, 2011.

DOI: 10.1021/acsenergylett.9b00220
ACS Energy Lett. 2019, 4, 933−942

Supporting Information

Direct electrolytic splitting of seawater: Opportunities and challenges

Sören Dresp,[a] Fabio Dionigi,[a], Malte Klingenhof, [a] Peter Strasser[a]*

[a] *Department of Chemistry, Technical University Berlin, 10623 Berlin, Germany*

E-mail: pstrasser@tu-berlin.de

Roundtrip energy efficiency of a reversible (seawater) electrolyzer

This section provides a simple estimate of the energy requirement in kWh (i.e. the energy loss) for turning 1 Nm^3 seawater into 1 Nm^3 fresh water, assuming perfect conservation of mass inside the device. The schematic mass/energy equation of the exergonic water splitting process and the corresponding masses of the reactants and products as well as the relevant reaction energies with respect to 1 mole water is[1]

H_2O	+	Energie	→	½ O_2↑	+	H_2↑
18 g/mol	+	285.8 kJ/mol ($\Delta_R H^0$) 237.1 kJ/mol ($\Delta_R G^0$)	→	16 g/mol	+	2 g/mol

(S1)

Here, $\Delta_R H^0$ is the reaction enthalpy and $\Delta_R G^0$ is the free enthalpy. Water density at room temperature is $\rho = 0.997\ kg \cdot L^{-1}$, so that 1 Nm^3 of H_2O weights about 997 kg. Thus, the number of moles water in 1 Nm^3 water at room temperature are:

$$n\ (H_2O) = \frac{\rho(H_2O)}{M(H_2O)} = \frac{997\ kg\ m^{-3}}{0.018\ kg\ mol^{-1}} = 55389\ mol\ m^{-3} \quad \text{(S2)}$$

The reaction enthalpy $\Delta_R H^0 = +285.8$ kJ is the required overall thermal plus electric energy to split 1 mole of H_2O at standard conditions into its elemental gaseous components which are also taken to be in standard conditions. The necessary combined electrical and thermal energy E to split 1 Nm^3 of water $\left(1\ Nm^3_{H_2O}\right)$ at 100 % electrolyzer efficiency is

$$E\left[kJ \cdot Nm^{-3}_{H_2O}\right] = n_{H_2O} \cdot \Delta_R H^0 = 15\ 830\ 144\ kWh \cdot Nm^{-3}_{H_2O} \quad \text{(S3)}$$

$$E\left[kWh \cdot Nm_{H_2O}^{-3}\right] = 15\,830\,144\ \text{kJ} \cdot 0.000278\ kWh \cdot Nm_{H_2O}^{-3} \quad \text{(S4)}$$

$$= 4400\ kWh \cdot Nm_{H_2O}^{-3}$$

For a realistic calculation, we assume 79 % efficiency for the direct seawater electrolyzer from Table 2, which results in a required overall energy E of

$$E\left[kWh \cdot Nm_{H_2O}^{-3}\right] = \frac{4400\ kWh \cdot Nm_{H_2O}^{-3}}{0.79} = 5{,}570\ kWh \cdot Nm_{H_2O}^{-3} \quad \text{(S5)}$$

to split 1 Nm^3 of salinated water. So, the electrolyzer function causes an energy loss of $1{,}170\ kWh \cdot Nm_{H_2O}^{-3}$. The thermodynamic (or theoretical) efficiency of the water formation process in a hydrogen-oxygen fuel cell is the ratio between the free enthalpy $\Delta_R G^0$ and the reaction enthalpy $\Delta_R H^0$ under standard conditions:

$$\eta_{theoretical} = \frac{\Delta_R G^0}{\Delta_R H^0} = \frac{237.1\ kJ\ mol^{-1}}{285.8\ kJ\ mol^{-1}} \approx 83\% \quad \text{(S6)}$$

Thus, at least 17 % of the input chemical energy will be lost during the fuel cell process, which corresponds to

$$4{,}400\ \frac{kWh}{Nm_{H_2O}^3} \cdot 0.17\ \% = 748\ kWh \cdot Nm_{H_2O}^{-3} \quad \text{(S7)}$$

The remaining energy content of the hydrogen and oxygen gas amounts to about 3,653 kWh, which could theoretically be converted into useful electric work. However, realistic efficiencies of proton exchange membrane (PEM) fuel cells range around 50 % , perhaps in alkaline fuel cells around 70 %.[2] Assuming 50 % efficiency for the PEM fuel cell, the expected energy loss in the water formation process is

$$4{,}400\ \frac{kWh}{Nm^3_{H_2O}} \cdot 0.50\ \% = 2{,}200\ kWh \cdot Nm^{-3}_{H_2O} \quad \text{(S8)}$$

In sum, a realistic combined water electrolyzer/ hydrogen fuel cell device that splits 1 Nm^3 salinated seawater and produces 1 Nm^3 of purified H_2O requires (suffers an overall energy loss of) about 3,370 $kWh \cdot Nm^{-3}_{H_2O}$.

Calculation of the energy consumption for the production of 1 kg H_2 using a combination of desalination followed by water electrolysis

According to equation S1, 9 kg of water are necessary to produce 1 kg of H_2. Water deionization by Reverse Osmosis (RO) requires $E_{\text{Rev. Osmosis}} = 3.25\ kWh\ \cdot Nm^{-3}_{H_2O}$ for the desalination of 1 Nm^3 seawater.[3] We note that this energy consumption is associated with a RO process that does not necessarily generates the usual 18.0 MΩ distilled water quality, that is used in research work, and hence may be actually insufficient in purity for conventional PEM water electrolyzers. The resulting desalinated water has a density of 997 $kg\ \cdot Nm^{-3}_{H_2O}$ at room temperature. The energy needed for a pre-desalination step via reverse osmosis prior to electrolysis to obtain the 9 kg of purified water necessary which will result in 1 kg H_2 amounts to a mere

$$E\left[\frac{kWh}{kg_{H_2}}\right] = \frac{3.25\ kWh \cdot Nm^{-3}_{H_2O}}{997\ kg_{H_2O} \cdot Nm^{-3}_{H_2O}} \cdot 9\ kg_{H_2O} \cdot kg^{-1}_{H_2} = 0.03\ kWh\ \cdot\ kg^{-1}_{H_2} \quad \text{(S6)}$$

Hence, compared to the overall energy (~ 47 – 66 kWh $kg^{-1}{}_{H2}$) [4, 5] used by the electrolyzer-system to produce 1 kg of H_2 , the RO based pre-desalination energy requirements are essentially negligible.

References

1. P. D. V. M. Schmidt, in *Elektrochemische Verfahrenstechnik*, 2003, DOI: doi:10.1002/3527602143.ch1.
2. Z. Salameh, in *Renewable Energy System Design*, ed. Z. Salameh, Academic Press, Boston, 2014, DOI: https://doi.org/10.1016/B978-0-12-374991-8.00004-0, pp. 201-298.
3. P. A. EPRI, *Water & Sustainability (Volume 4): U.S. Electricity Consumption for Water Supply & Treatment - The Next Half Century*, Palo Alto, CA, 2000.
4. M. Carmo, D. L. Fritz, J. Mergel and D. Stolten, *Int. J. Hydrogen Energy*, 2013, **38**, 4901-4934.
5. S. Dresp, F. Dionigi, S. Loos, J. Ferreira de Araujo, C. Spöri, M. Gliech, H. Dau and P. Strasser, *Advanced Energy Materials*, 2018, **8**, 1800338.

AUTHOR CONTRIBUTIONS

SD [I] Dresp, S. and Strasser, P. *ChemCatChem*. 2018, 10, 4162 - 4171. https://doi.org/10.1002/cctc.201800660

S.D. planned the outline, did the literature research, and conducted the synthesis, all experiments, the data evaluation and the design of the figures. S.D. wrote the manuscript with support of P.S.. All authors discussed and agreed on the final version of the manuscript.

SD [II] S. Dresp, F. Luo, R. Schmack, S. Kühl, M. Gliech, P. Strasser, *Energy Environ. Sci.* 2016, 9, 2020-2024. https://doi.org/10.1039/C6EE01046F

S.D. planned the study and did the literature research. F.L. synthesized the Fe-N-C catalysts. S.D. prepared the NiFe-LDH samples. S.D. performed the XRD measurement did all electrochemical measurements including RDE, RRDE, MEA preparation, assembled the reversible electrolyzer and measured the cell in fuel cell and electrolyzer mode. M.G. and R.S. conducted TEM images supported by S.D.. S.D. did the data evaluation and the design of the figures. S.D. wrote the manuscript with support of all authors. All authors discussed and agreed on the final version of the manuscript.

SD [III] S. Dresp, F. Dionigi, S. Loos, J. Ferreira de Araujo, C. Spöri, M. Gliech, H. Dau, P. Strasser, *Adv. Energy Mater.* 2018, 8, 1800338. https://doi.org/10.1002/aenm.201800338

S.D. planned the study with support of F.D. and P.S.. S.D. conducted the synthesis, performed and analyzed the XRD measurements, did the electrochemical measurements including MEA preparation, assembled the electrolyzer and planned and constructed the in-house seawater electrolyzer set-up including the selectivity measurement. J.F.d.A. set the mass spectrometer. S.D. and F.D. planned the electrochemical testing protocol. S.L. measured EXAFS and XANES at the BESSY II synchrotron facility and evaluated the data supported by H.D.. S.D. prepared the EXAFS and XANES samples supported by F.D.. C.S. did additional SEM measurements and M.G. did additional TEM measurements supported by S.D.. S.D. wrote the manuscript with support of all authors. All authors discussed and agreed on the final version of the manuscript.

SD [IV] Dresp, S. and Strasser, P., *ECS Transactions*, 2016. **75**(14): p. 1113-1119. https://doi.org/10.1149/07514.1113ecst

S.D. planned the outline, did the literature research, and conducted the synthesis, all experiments, the data evaluation and the design of the figures. S.D. wrote the manuscript with support of P.S.. All authors discussed and agreed on the final version of the manuscript.

SD [V] Dresp, S., Dionigi F., Klingenhof M. and Strasser P., ACS Energy Letters, 2019, 4, 933-942, https://doi.org/10.1021/acsenergylett.9b00220

S.D. planned the outline, did the literature research, and calculated all values and designed the figures. S.D. wrote the manuscript with support of all authors. All authors discussed and agreed on the final version of the manuscript.